# IRE Transactions

## n Microwave Theory and Techniques

Volume MTT-6 **OCTOBER, 1958** Number 4

### In This Issue





PUBLISHED BY THE

essional Group on Microwave Theory and Techniques

## IRE TRANSACTIONS®

**on Microwave Theory and Techniques**

Published by the Institute of Radio Engineers, Inc., for the Professional Group on Microwave Theory and Techniques, at 1 East 79th Street, New York 21, New York. Responsibility for the contents rests upon the authors, and not upon the IRE, the Group, or its members. Price per copy: IRE PGMTT members, $2.50; IRE members, $3.75, nonmembers, $7.50. Annual subscription price: IRE members, $8.50; colleges and public libraries, $12.75; nonmembers, $17.00.

Address all manuscripts to K. Tomiyasu, PGMTT Editor, General Electric Microwave Laboratory, 601 California Ave., Palo Alto, Calif. Submission of three copies of manuscripts, including figures, will expedite the review.

# IRE Transactions on Microwave Theory and Techniques

Volume MTT-6 OCTOBER, 1958 Number 4



## TABLE OF CONTENTS

# Eugene G. Fubini

Eugene G. Fubini (A'36–SM'46–F'54) was born on April 19, 1913 in Turin, Italy. He received the Ph.D. degree from the University of Rome, Italy, in 1933. Associated with the National Electric Institute of Italy from 1936 to 1938, he also worked prior to World War I, in the Short-Wave Division, General Engineering Department, of the Columbia Broadcasting System.

In 1943 and 1944 Dr. Fubini was a research associate at the Radio Research Laboratory at Harvard University, Cambridge, Mass., a technical observer in countermeasure work with the United States Army and Navy in Italy, Corsica, and Africa, and director of Operational Analysis, Radar Countermeasures Section, with the United States Eighth Air Force in England. He was also a special consultant for countermeasures in the Air Communications Office, United States War Department, and was awarded a Presidential Certificate of Merit.

In 1945 Dr. Fubini joined Airborne Instruments Laboratory and served as supervising engineer of the Special Devices Section before he became codirector of the Research and Engineering Division in 1955. While at AIL he has worked on many concepts and developments in electronics. He also has lectured at Harvard University on electromagnetic and microwave phenomena.

# A Plea for Simplification

EUGENE G. FUBINI†

HANDBOOK engineering is becoming more and more common in our laboratories and the distance is increasing between the engineer faced with the practical problem and the professional theoretical man. The widening of the practice-theory gap seems to be universal throughout our industry: our efficiency is reduced and progress made more difficult. The people who are compelled to the steady use of handbook formulas regret this fact and have an intense thirst for knowledge.

A drive toward a middle ground between complicated theory and practice is needed intensively in our field, and such a middle ground does exist. History shows that problems are solved in ways which appear esoteric at the time they are introduced and then drift down the scale of difficulties, appearing to become in a mysterious way easier and easier to understand. It was not so long ago when Boolean algebra, Fourier series, operational calculus were at the frontiers of mathematical knowledge. Even such abstruse concepts as those of general relativity are beginning to be understood by thousands of people when just about forty years ago they appeared comprehensible by only a few outstanding brains.

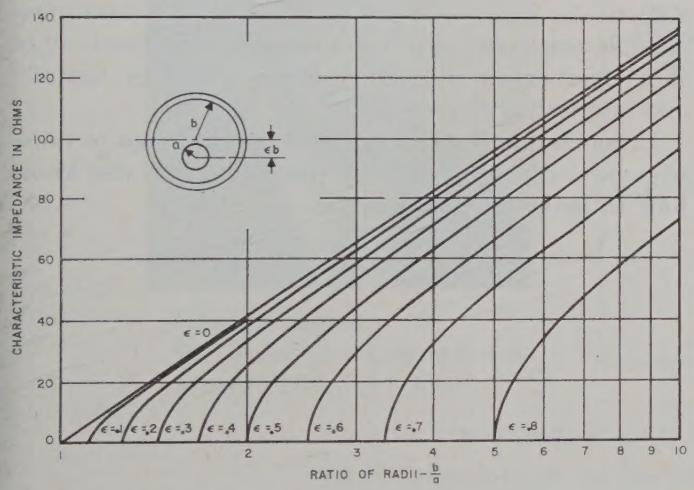


Fig. 1—Characteristic impedance of an eccentric coaxial line (from an exact computation).

This is a plea for a determined effort toward simplification of concepts, to reach a middle ground between abstract mathematical theory and the blind use of someone else's formulas. Poincaré, a great mathematician, used to say that there are two ways of understanding a concept. The first way, through mathematics, is the easier but not the more useful; the second way is that of understanding without resorting to mathematical crutches. The latter is more difficult, but it is the only real way of understanding the concept.

As a corollary to the above, we should strive toward simpler, even if not accurate, methods of analysis. We should have papers listing rough approximations to complicated problems, and simple theoretical limitations on the optimum possible performance of different devices.

As an example consider Fig. 1: it gives the characteristic impedance $Z_0$ of an eccentric coaxial line. The formula from which the curves of Fig. 1 have been computed can be obtained from a solution of a boundary-value problem of a well-known type. It is interesting, however, to show that the results of Fig. 1 can be obtained purely from an intuitive basis and with a surprising degree of accuracy.[1] In Fig. 2, the ordinate and abscissa axes are the normalized characteristic impedance $Z(\epsilon)/Z_0$ and $\epsilon/\epsilon_{max}$, respectively. $Z(\epsilon)$ is the characteristic impedance of an eccentric line and $Z_0$ is the characteristic impedance of a concentric line having the same conductors. $\epsilon/\epsilon_{max}$ is the ratio between the ec-

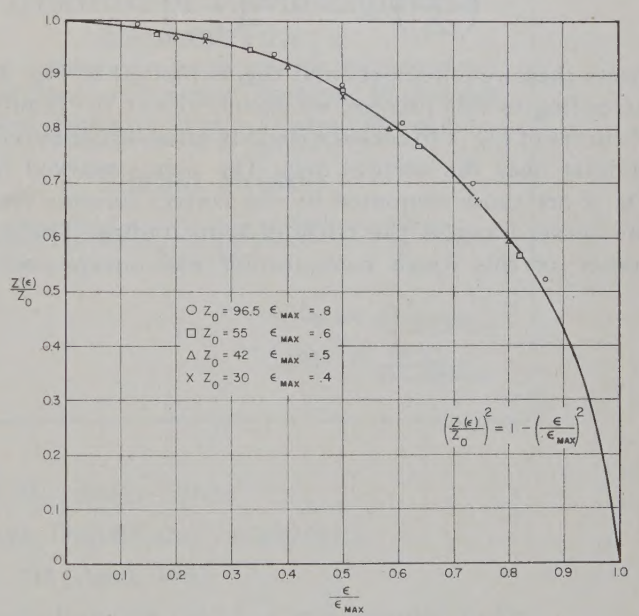


Fig. 2—Normalized characteristic impedance of an eccentric coaxial line. Comparison between approximation (solid curve) and exact theory.

† Airborne Instruments Lab., Div. Cutler-Hammer, Inc., Mineola, N. Y.

[1] I am deeply indebted to Harold A. Wheeler for having inspired this desire for semirigorous considerations and for having, in many years of mutual discussions, supplied me with innumerable examples of this approach.

centricity $\epsilon$, defined in Fig. 1, and the maximum eccentricity $\epsilon_{max}$.

We could now plot in Fig. 2 a set of curves which would correspond to the set shown in Fig. 1. Before doing this, however, we should point out that, due to the choice of the coordinate system, all of the curves must pass through the unity points on the ordinate and abscissa axes, since for $\epsilon = 0$ the characteristic impedance of all the lines is equal to that of the concentric line and for $\epsilon = \epsilon_{max}$ the inner and outer conductors are shorted and the characteristic impedances are zero. Furthermore, since the impedance must be an even function of the eccentricity, the impedance curve for small eccentricity must be of the type $1 - K\epsilon^2$. For large eccentricities the capacitance near the point where the two conductors almost touch must change roughly with the square root of the distance, because the "useful" area of the conductors decreases while the distance decreases. The following equation which yields a circle of unity radius,

$$\left(\frac{Z(\epsilon)}{Z_0}\right)^2 = 1 - \left(\frac{\epsilon}{\epsilon_{max}}\right)^2$$

meets these requirements and this is plotted in Fig. 2. According to this process, we should expect the family of curves of Fig. 1 to coalesce roughly into a single curve, at least near the vertical axis. The points marked in Fig. 2 are those computed by the correct formula and the curve drawn is the circle of unity radius. The accuracy of this rough computation was unexpectedly good, but the reader should not expect such good results every time!

Consider as another example the effect of losses in a waveguide. The problem can be solved by using boundary value concepts or by applying elementary impedance methods to the zig-zag concept of wave propagation.

Almost as powerful as the simplified treatment of important phenomena is the establishment of upper and lower limits to design capabilities. To know how close one is to a theoretical optimum is essential information for a designer. A few years ago the author spent several months trying in vain to improve a filter which was, without his knowledge, within a few per cent of the theoretical optimum.

Unfortunately, not all these limits have found a place in the minds of the engineers. Take the cases of the minimum delay in an amplifier of a given gain, the maximum sensitivity in a receiver whose antenna partially sees the earth, the fastest rise time for a given bandwidth, the minimum $Q$ for a given amount of supergain, the minimum phase shift required by a given amplitude response, the maximum bandwidth over which a particular impedance can be matched, the maximum possible sensitivity of a direct detection receiver—all of these limitations and many others could be usefully and interestingly presented.

In conclusion, let special credit and glory go to those who not only solve difficult problems but also know how to make difficult solutions appear easy.

# Microwave Prize

*The Professional Group on Microwave Theory and Techniques has established the Microwave Prize to recognize annually a significant paper which appeared in the* IRE TRANSACTIONS ON MICROWAVE THEORY AND TECHNIQUES. *In selecting the paper, consideration is given primarily to the subject of the contribution and secondarily to its presentation. All members and affiliates of* PGMTT *are eligible for the award. The award consists of a certificate, a monetary sum of $100, and a feature publication in these* TRANSACTIONS. *If the paper has more than one author, the monetary sum is divided equally among the authors.*

*—The Editor*

HAROLD SEIDEL
Bell Telephone Laboratories
Murray Hill, New Jersey

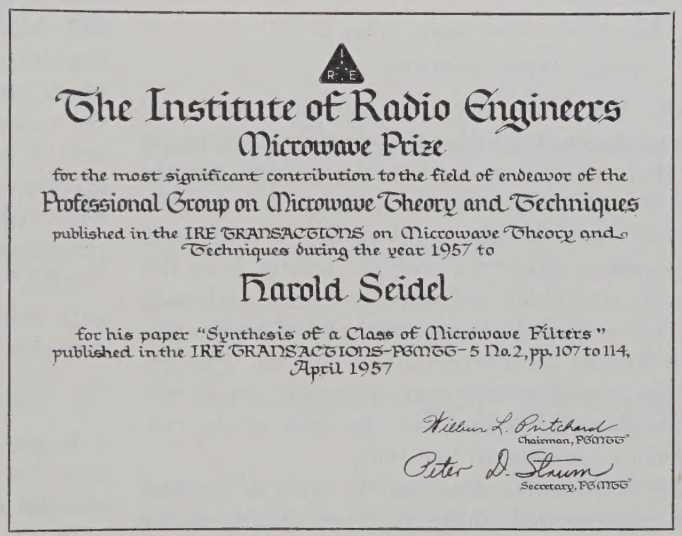

The Institute of Radio Engineers
Microwave Prize
for the most significant contribution to the field of endeavor of the
Professional Group on Microwave Theory and Techniques
published in the IRE TRANSACTIONS on Microwave Theory and Techniques during the year 1957 to
Harold Seidel
for his paper "Synthesis of a Class of Microwave Filters" published in the IRE TRANSACTIONS-PGMTT-5 No.2, pp. 107 to 114, April 1957
William L. Pritchard
Chairman, PGMTT
Peter D. Strum
Secretary, PGMTT

"Synthesis of a Class of Microwave Filters"

IRE TRANSACTIONS ON MICROWAVE THEORY AND TECHNIQUES

Vol. MTT-5, pp. 107–114; April, 1957

It is a pleasure to announce that the Microwave Prize for 1957 has been awarded to Dr. Harold Seidel for the above paper. This paper is an ingenious extension of Darlington's procedure for the synthesis of lumped element networks to the synthesis of networks involving distributed line elements. A new model for a class of microwave filters is set forth from which a wide variety of structural realizations is obtainable.

The Awards Committee, composed this year of representatives of all the PGMTT Chapters in the United States, believes that Dr. Seidel's paper represents an important advance in microwave network theory.

We congratulate Dr. Seidel on his excellent work.

W. L. PRITCHARD, *Chairman*
PGMTT Administrative Committee

# General Treatment of Klystron Resonant Cavities*

KAZUO FUJISAWA†

*Summary*—Klystron resonant cavities are treated for general cases and their equivalent circuits are theoretically determined, which allows a fairly accurate estimate of resonant properties. It is shown that a reentrant cavity is expressed as a low-frequency series $LCR_{se}$ circuit or a shunt $LCR_{sh}$ circuit, taking $L$ as the inductance of a toroidal coil with one turn and with a cross section the same as the cavity, $C$ as the gap capacitance plus the equivalent capacitance of the cavity, and $R_{se}$ or $R_{sh}$ as the equivalent series or shunt resistance of the cavity at resonance. The introduction of the equivalent cavity capacitance has proved to be very effective.

The formulas derived here enable one to calculate the resonant frequency within an error of a few per cent and the shunt resistance and the $Q$ within an error of several tenths of a per cent in most cases, and thus should prove to be very useful to the designer of microwave circuits.

## Introduction

SO FAR, there has been no general theory on klystron resonant cavities of the reentrant type, so that their shapes and dimensions were mainly determined by cut-and-try method. There is an empirical statement[1] that the reentrant cavity is expressed as a low-frequency shunt $LC$ circuit, taking $L$ as the inductance of a toroidal coil with one turn and with the same cross section as the cavity, and $C$ as the gap capacitance formed by plane parallel plates. The accuracy of this empirical statement is insufficient to rely upon for designing. It is said that the error of the resonant frequency exceeds 20 per cent.

As for the reentrant coaxial cavity with a toroidal rectangular cross section, there have been many works initiated by Hansen, and now we can utilize various charts to obtain its resonant frequency.[2–4] The unloaded $Q$ and the shunt resistance of this type of cavity are also calculated and tabulated in some cases,[5] and are studied in detail by Ginzton and Nalos.[6]

However, in practice, the purely coaxial reentrant cavity is seldom used, so we need some more general calculating methods in order to design practical klystron cavities.

In this paper, an arbitrary reentrant cavity is generally treated using the theory of Green's functions. The formula for the input admittance at the gap is derived, and then its low-frequency equivalent circuit is determined in general form. Thus we can estimate its resonant properties with considerable accuracy and determine its dimensions at least in the earlier stages of designing.

The low-frequency equivalent circuit derived here theoretically has proved to be almost the same as the above mentioned empirical circuit, except for the addition of an equivalent capacitance of the cavity to the gap capacitance. By the introduction of this cavity capacitance, the accuracy of the equivalent circuit is much improved. By means of this method the error of the resonant frequency is ordinarily within a few per cent in its region of validity. The region of applicability of this equivalent circuit is estimated by comparisons with experiments and with other calculated results on the coaxial reentrant cavity.

Also, for the special reentrant cavity with an aperture gap, equivalent circuit parameters are given here with considerable accuracy.

## General Theory of a Reentrant Cavity

In this Section, a reentrant cavity is generally treated, and the general expression for its input admittance at the gap is derived.

In Fig. 1, the cross section of a reentrant cavity is shown, and the cylindrical coordinates $r$, $\phi$, and $z$ are used as shown. In this cavity, the fundamental $E$-type mode with axial symmetry is excited and its field components are given by

$$E_z = \frac{1}{j\omega\epsilon_0}\frac{1}{r}\frac{\partial u}{\partial r}, \quad E_r = -\frac{1}{j\omega\epsilon_0}\frac{1}{r}\frac{\partial u}{\partial z}, \quad u = rH_\phi, \tag{1}$$

where mks units are used. $u$ satisfies the following wave equation

$$\frac{\partial}{\partial r}\left(\frac{1}{r}\frac{\partial u}{\partial r}\right)+\frac{\partial}{\partial z}\left(\frac{1}{r}\frac{\partial u}{\partial z}\right)+\frac{k^2}{r}u \equiv L(u)+\frac{k^2}{r}u = 0, \tag{2}$$

under the boundary condition

$$\text{on } c_1 \quad \frac{\partial u}{\partial n} = 0, \tag{3}$$

where $c_1$ is the wall part of the boundary $c$ of $D$, $D$ being the hatched region of the cavity cross section, and $k^2 = \omega^2\epsilon_0\mu_0$.

* Manuscript received by the PGMTT, July 3, 1957; revised manuscript received, May 2, 1958.

† Dept. of Elec. Eng., Kobe Univ., Nagata, Kobe, Japan.

[1] F. E. Terman, "Radio Engineer's Handbook," McGraw-Hill Book Co., Inc., New York, N. Y., p. 263; 1943.

[2] A. E. Harrison, "Klystron Tubes," McGraw-Hill Book Co., Inc., New York, N. Y., pp. 253–262; 1947.

[3] T. Moreno, "Microwave Transmission Design Data," McGraw-Hill Book Co., Inc., New York, N. Y., pp. 230–238; 1948.

[4] D. R. Hamilton, J. K. Knipp, and J. B. H. Kuper, "Klystrons and Microwave Triodes," McGraw-Hill Book Co., Inc., New York, N. Y., pp. 73–75; 1948.

[5] *Ibid.*, pp. 77–79.

[6] E. L. Ginzton and E. J. Nalos, "Shunt impedance of klystron cavities," IRE Trans. on Microwave Theory and Techniques, vol. MTT-3, pp. 4–7; October, 1955.

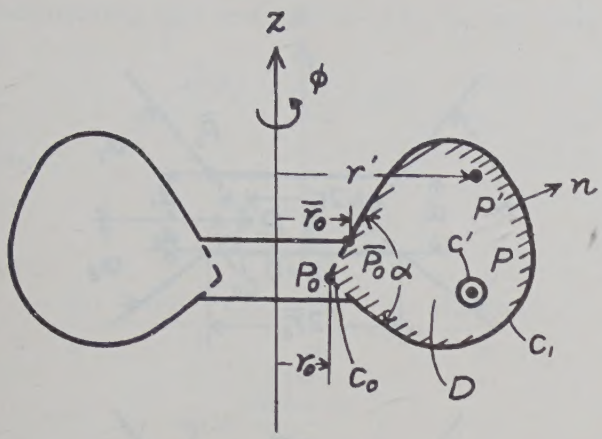


Fig. 1—Cross section of a reentrant cavity.

To solve this boundary-value problem, let us introduce Green's function $G(P, P'; k^2)$ for two points $P$ and $P'$ in $D$, which has the following properties.[7,8]

1) $G$, regarded as a function of $P'$, satisfies the wave equation

$$L'(G) + \frac{k^2}{r'} G = 0, \tag{4}$$

everywhere in $D$ except at $P$. The dashed symbols all refer to the point $P'$ throughout this paper.

2) When $P'$ is on $c$

$$\frac{\partial G}{\partial n'} = 0, \tag{5}$$

where $n'$ is the outward normal to $D$ at $P'$.

3) When the distance $PP' \simeq 0$ and $P$ lies in $D$, $G$ is written

$$G(P, P'; k^2) = -\frac{r'}{2\pi} \ln PP' + g(P, P'; k^2), \tag{6}$$

where $g$ is a regular function everywhere in $D$. So, taking $c'$ as an infinitesimal circle aroung $P$, we have

$$\oint_{c'} \frac{\partial G}{\partial n'} \frac{ds'}{r'} = 1, \tag{7}$$

where $n'$ is the inward normal to $c'$, and $ds'$ is the increment of length along $c'$.

For a point $P$ on the boundary $c$, $G$ may be written

$$G(P, P'; k^2) = -\frac{r'}{\alpha} \ln PP' + g(P, P'; k^2), \tag{8}$$

where $\alpha$ is the angle subtended by $c$ at $P$. The rigorous proof of this equation may be difficult, but we can confirm it by several examples.[9] Assuming (8) and taking now $c'$ as the part in $D$ of an infinitesimal circle around $P$, (7) remains valid.

4) If we denote the $i$th eigenvalue of the boundary-value problem, (4) and (5), as $k_i$, and the $i$th normalized eigenfunction as $v_i$, the following relations exist:

$$\int_D v_i(P')v_j(P') \frac{dS'}{r'} = \begin{cases} 0, & \text{if } i \neq j, \\ 1, & \text{if } i = j, \end{cases} \tag{9}$$

$$i, j = 0, 1, 2, \cdots,$$

where $dS'$ is the increment of area at $P'$. Particularly, for $i = 0$

$$\left.\begin{aligned} k_i &= k_0 = 0, \\ v_i^2 &= v_0^2 = \text{const} = \frac{1}{\displaystyle\int_D dS'/r'} \end{aligned}\right\}. \tag{10}$$

Using these eigenvalues and eigenfunctions, $G$ is expanded as

$$G(P, P'; k^2) = \sum_{i=0}^{\infty} \frac{v_i(P)v_i(P')}{k_i^2 - k^2}. \tag{11}$$

Then, by Green's theorem, we have

$$u(P) = rH_\phi(P) = j\omega\epsilon_0 \int_{c_0} G(P, P'; k^2)\boldsymbol{E}' \cdot d\boldsymbol{s}', \tag{12}$$

where the line integral is taken counter-clockwise around $D$, on the boundary section $c_0$ in the gap region, and $\boldsymbol{E}'$ is the electric field at $P'$ on $c_0$.

Now, for simplicity, let us consider the case when the unit gap voltage is applied; then we have

$$\int_{c_0} \boldsymbol{E}' \cdot d\boldsymbol{s}' = -1. \tag{13}$$

Thence, the input admittance of the cavity at the gap edge $\bar{P}_0$ is given by

$$\begin{aligned} \vec{Y}(\bar{P}_0) &= -2\pi u(\bar{P}_0) \\ &= -j\omega\epsilon_0 2\pi \int_{c_0} G(\bar{P}_0, P'; k^2)\boldsymbol{E}' \cdot d\boldsymbol{s}'. \end{aligned} \tag{14}$$

Let us consider here how to take the cavity cross section $D$ for the ease of practical applications. At a glance, one is liable to take $D$ as shown in Fig. 2(a) and 2(b).

[7] A. Sommerfeld, "Die Greensche Funktion der Schwingungsgleichung," *Jahrb. Deut. Math.-Ver.*, Bd. 21, pp. 309–353; March, 1912.

[8] R. Courant and D. Hilbert, "Methoden der Mathematischen Physik I," Julius Springer, Berlin, pp. 302–337; 1931.

[9] K. Fujisawa, "Theory of slotted cylindrical cavities with transverse electric field," *Tech. Reps. Osaka Univ.*, vol. 1, pp. 69–87; March, 1951.

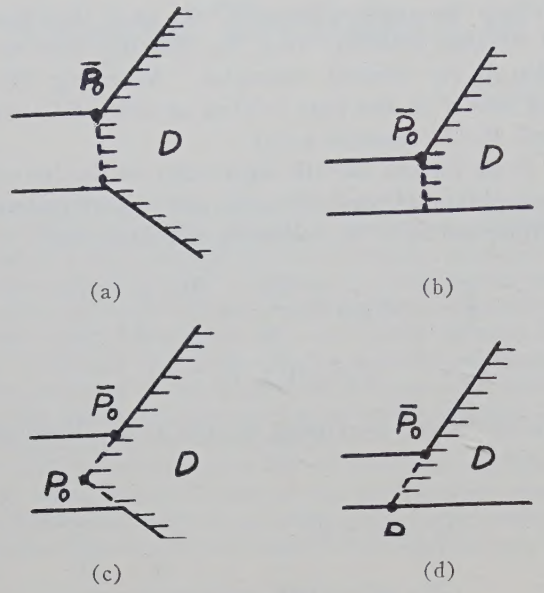


Fig. 2—Determination of the cavity region $D$. (a) and (b) are unsuitable, and (c) and (d) are suitable, for practical applications.

But for these regions, which have two vertexes on their boundaries at the gaps, it is almost impossible to evaluate the Green's function $G$. So, for practical applications, it is better to take $D$ as shown in Fig. 2(c) and 2(d), and take the reference point at the vertex $P_0$ rather than $\bar{P}_0$ to evaluate the Green's function.

Accordingly, we rewrite using (12)

$$\vec{Y}(\bar{P}_0) = 2\pi[u(P_0) - u(\bar{P}_0)] - j\omega\epsilon_0 2\pi \int_{c_0} G(P_0, P'; k^2)\boldsymbol{E}' \cdot d\boldsymbol{s}'. \quad (15)$$

This formula is suitable for practical applications. In the next Section, approximate approaches are given.

## General Equivalent Circuit of a Reentrant Cavity

For a reentrant cavity, the resonant wavelength is much greater than the cavity dimensions, so we can put

$$k \ll k_i, \quad i = 1, 2, 3, \cdots. \quad (16)$$

Hence we have, from (11)

$$G(P, P'; k^2) \simeq -\frac{v_0^2}{k^2} + G_1(P, P'), \quad (17)$$

where

$$G_1(P, P') = \sum_{i=1}^{\infty} \frac{v_i(P)v_i(P')}{k_i^2}. \quad (18)$$

Obviously, $G_1$ is the Green's function for the static

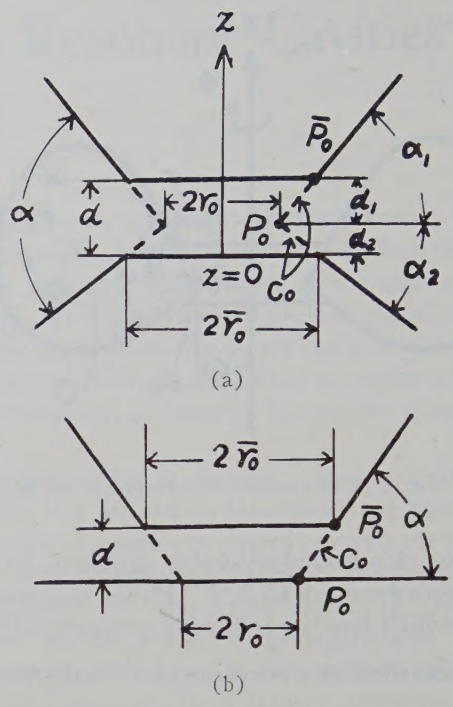


Fig. 3—General shapes of the cavity near the gap.

problem $L'(G_1) = 0$ under the same boundary condition as (5). So, it may be written as

$$G_1(P_0, P') = -\frac{r'}{\alpha} \ln P_0P' + g_1(P_0, P'), \quad (19)$$

where $g_1$ is a regular function everywhere in $D$. And it must satisfy

$$\int_D G_1(P_0, P') \frac{dS'}{r'} = 0, \quad (20)$$

by the orthogonality of $v_i$ to $v_0$ (a constant) in (18). So, substituting (19) in (20), and regarding $g_1$ as a constant, we can write as

$$G_1(P_0\ P') \simeq -\frac{r'}{\alpha} \ln \frac{P_0P'}{l_M}, \quad \text{for } P_0P' \simeq 0, \quad (21)$$

taking $l_M$ as the mean distance of $D$ to $P_0$.

Hence, we have finally

$$G(P_0, P'; k^2) \simeq -\frac{1}{k^2 \int_D dS'/r'} - \frac{r'}{\alpha} \ln \frac{P_0P'}{l_M}, \quad \text{for } P_0P' \simeq 0. \quad (22)$$

For the fields in the gap region (Fig. 3), we assume spatially constant electric fields and obtain

$$E_z = \frac{1}{d}, \quad E_r = 0, \quad u = j\omega\epsilon_0 \frac{r^2}{d}. \quad (23)$$

Substituting (22) and (23) in (15), we can write

$$\overrightarrow{Y}(\overline{P}_0) = \frac{1}{i\omega L} + j\omega C_1, \tag{24}$$

where

$$L = \frac{\mu_0}{2\pi}\int_D \frac{dS'}{r'}, \tag{25}$$

$$\frac{C_1}{\epsilon_0} = \frac{\pi(r_0^2 - \bar{r}_0^2)}{d} + \frac{2\pi}{\alpha d}\left( r_0 d_1 \ln\frac{el_M \sin\alpha_1}{d_1} + \gamma_0 d_2 \ln\frac{el_M \sin\alpha_2}{d_2} + \frac{d_1^2 \cot\alpha_1}{2}\ln\frac{\sqrt{e}l_M \sin\alpha_1}{d_1} + \frac{d_2^2 \cot\alpha_2}{2}\ln\frac{\sqrt{e}l_M \sin\alpha_2}{d_2}\right), \tag{26a}$$

[for the gap shown in Fig. 3(a)],

$$\frac{C_1}{\epsilon_0} = \frac{\pi(r_0^2 - \bar{r}_0^2)}{d} + \frac{2\pi}{\alpha}\left( r_0 \ln\frac{el_M \sin\alpha}{d} + \frac{d\cot\alpha}{2}\ln\frac{\sqrt{e}l_M \sin\alpha}{d}\right), \tag{26b}$$

[for the gap shown in Fig. 3(b)], where $e = 2.718$.

As for the gap capacitance, we assume a gap formed by plane parallel plates instead of the actual gridded gap, and obtain

$$C_0 = \epsilon_0 \frac{\pi \bar{r}_0^2}{d}. \tag{27}$$

If we cannot neglect the effect of grids, the value of $C_0$ from the above equation should be modified by multiplication by a capacitance reduction factor.

Accordingly, we have, as the total equivalent capacitance of the cavity

$$C = C_0 + C_1. \tag{28}$$

It is very interesting that $L$, given by (25), is equal to the inductance of a toroidal coil with one turn and with a cross section the same as $D$. This agrees with the usual empirical statement.[1] But the new introduction of $C_1$ is found to be very effective.

$C_1$ is the equivalent capacitance of the cavity region $D$, and is mainly formed by the capacitance between the side walls of the posts [in Fig. 3(a)], or by that between the side wall of the post and the end plate [in Fig. 3(b)]. It is very interesting to compare the nature of $C_1$ with those of the usual discontinuity capacitances in transmission lines.

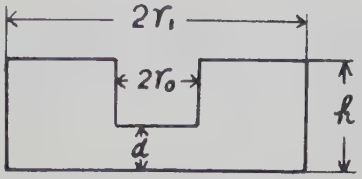


Fig. 4—Reentrant coaxial cavity.

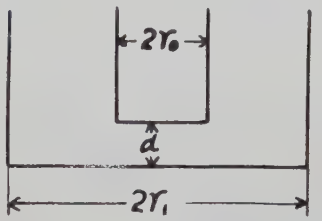


(a)

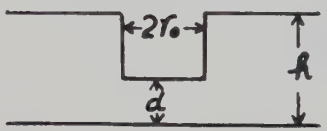


(b)

Fig. 5—(a) Coaxial line terminated by a gap; (b) step discontinuity in a radial line.

For this purpose, let us take a reentrant coaxial cavity shown in Fig. 4, for example. In this case, we have

$$C_1 = 4\epsilon_0 r_0 \ln\frac{e\sqrt{(r_1 - r_0)^2 + h^2}}{2d}. \tag{26c}$$

The discontinuity capacitance (excluding the gap capacitance) of the coaxial line terminated by a gap shown in Fig. 5(a), is easily obtained by a little manipulation as[10]

$$C_d = 4\epsilon_0 r_0 \ln\frac{r_1 - r_0}{d}, \qquad (r_1 - r_0 \gg d). \tag{29}$$

The step discontinuity capacitance in the radial line shown in Fig. 5(b), is easily obtained as[11]

$$C_d = 4\epsilon_0 r_0 \ln\frac{eh}{4d}, \qquad (h \gg d). \tag{30}$$

Comparing the above three capacitances, it is found that $C_1$ is closely related with the usual discontinuity capacitances in transmission lines, and is slightly greater than

[10] N. Marcuvitz, "Waveguide Handbook," McGraw-Hill Book Co., Inc., New York, N. Y., p. 178; 1951.

[11] C. G. Montgomery, R. H. Dicke, and E. M. Purcell, "Principles of Microwave Circuits," McGraw-Hill Book Co., Inc., New York, N. Y., p. 274; 1948.

these. The difference may be due to the contribution of the electric field in the cavity region far from the gap.

To evaluate $C_1$ actually, we must know the value of $l_M$. This is given by

$$l_M = P_0P_M = \frac{1}{S}\int_D P_0P' \cdot dS', \tag{31}$$

taking $S$ as the area of $D$, and $P_M$ as its center. Also, $l_M$ is obtained graphically by the following procedure.

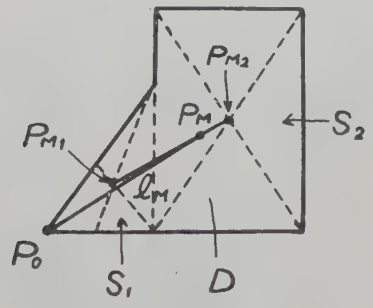


Fig. 6—Graphical determination of $l_M$.

Given a cavity cross section $D$ as in Fig. 6, for example, we divide it into two regions of simple shapes, and determine the centers of the respective regions, and denote it as $P_{M1}$ and $P_{M2}$, respectively. Then the center $P_M$ of $D$ is obtained as the dividing point of $P_{M1}P_{M2}$ in inverse proportion to the respective areas, and $l_M$ is found by measuring the distance $P_0P_M$.

Now, let us turn to the calculation of wall loss. Clearly, the equivalent shunt resistance of the cavity at the gap is given by

$$\frac{1}{R_{sh}} = \int_{c_1} \frac{|2\pi u(P')|^2}{2\pi\delta\sigma}\frac{ds'}{r'}, \tag{32}$$

where $\sigma$ is the conductivity of the cavity wall and $\delta$ is its skin depth.

For a point $P'$ not so close to the gap, we have, from (12) and (13)

$$u(P') \simeq -j\omega\epsilon_0 G(P', P_0; k^2). \tag{33}$$

Substituting (33) in (32), and using (22), we obtain

$$\frac{1}{R_{sh}} \simeq \frac{1}{2\pi\delta\sigma}\frac{1}{\omega^2L^2}\int_{c_1}\frac{ds'}{r'} + \frac{2}{\alpha\delta\sigma}\frac{\epsilon_0}{L}\int_{c_1}\ln\frac{P_0P'}{l_M}ds'$$

$$\simeq \frac{1}{2\pi\delta\sigma}\frac{1}{\omega^2L^2}\int_{c_1}\frac{ds'}{r'}, \tag{34}$$

where we neglected the square of the second term in (22). So, the equivalent series resistance of the cavity at the gap is given by

$$R_{se} = \frac{\omega^2L^2}{R_{sh}} \simeq \frac{1}{2\pi\delta\sigma}\int_{c_1}\frac{ds'}{r'}. \tag{35}$$

Clearly, this is equal to the high-frequency resistance of a toroidal coil with one turn and with a cross section the same as $D$.

Using these equivalent circuit constants and the equivalent circuits shown in Fig. 7, we can estimate the resonant properties of the reentrant cavities with ease.

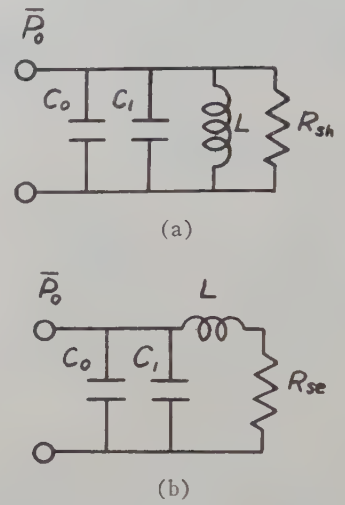


Fig. 7—Equivalent circuits of a reentrant cavity at the gap.

For practical applications, calculated results on typical reentrant cavities are summarized in Table I opposite. The regions of validity of these formulas are discussed in the next Section.

## The Ranges of Validity of the Formulas

Generally, the main parameters which affect the validity of the formulas are summarized as the following three:

$l_M/\lambda_0$—this shows the relative size of the cavity compared to the resonant wavelength. As referred before, the accuracy is better for smaller $l_M/\lambda_0$.

$P_0P_V/l_M$—taking $P_V$ as the nearest vertex to $P_0$ on $c_1$ this affects the validity of (21). The accuracy is better for larger $P_0P_V/l_M$.

$r_0/l_M$—this shows the relative size of the post compared to the cavity. The accuracy is better for larger $r_0/l_M$.

From the following examples, let us now find the ranges of parameters over which the formulas are valid. In Fig. 8 (p. 350) comparisons are made between the calculations from the formulas and those by Hansen, of the resonant wavelengths of the sixty cavities[4] shown in Fig. 9, which, according to his calculations, have the value of $\lambda_0 = 3.2$ cm within an error of 3 per cent. In the figure, the cavities are represented as points in the

TABLE I

(a)

$$\frac{L}{\mu_0}=\frac{h}{2\pi}\ln\frac{r_1}{r_0},\qquad \frac{C_0}{\epsilon_0}=\frac{\pi r_0^2}{d},\qquad \frac{C_1}{\epsilon_0}=4r_0\ln\frac{el_M}{d},\qquad l_M=\frac{\sqrt{(r_1-r_0)^2+h^2}}{2},$$
$$\frac{\omega^2L^2}{R_{sh}}=\frac{1}{2\pi\delta\sigma}\left(\frac{h-d}{r_0}+\frac{h}{r_1}+2\ln\frac{r_1}{r_0}\right),\qquad \lambda=2\pi\sqrt{r_0h\left(\frac{r_0}{2d}+\frac{2}{\pi}\ln\frac{el_M}{d}\right)\ln\frac{r_1}{r_0}}$$

(b)

$$\frac{L}{\mu_0}=\frac{1}{2\pi}\left(h_1\ln\frac{r_1}{r_0}+h_2\ln\frac{r_2}{r_1}\right),\qquad \frac{C_0}{\epsilon_0}=\frac{\pi r_0^2}{d},\qquad \frac{C_1}{\epsilon_0}=4r_0\ln\frac{el_M}{d},$$
$$l_M=\frac{1}{2}\,\frac{\sqrt{\{(r_1-r_0)h_1^2+(r_2-r_1)h_2^2\}^2+\{(r_1-r_0)^2h_1+(r_2-r_1)(r_1+r_2-2r_0)h_2\}^2}}{(r_1-r_0)h_1+(r_2-r_1)h_2},$$
$$\frac{\omega^2L^2}{R_{sh}}=\frac{1}{2\pi\delta\sigma}\left(\frac{h_1-d}{r_0}+\frac{h_2-h_1}{r_1}+\frac{h_2}{r_2}+2\ln\frac{r_2}{r_0}\right)$$

(c)

$$\frac{L}{\mu_0}=\frac{1}{2\pi}\left[h_1\ln\frac{r_0+2a}{r_0}+\pi\left(r_0+a-\sqrt{r_0(r_0+2a)}\right)\right],\qquad \frac{C_0}{\epsilon_0}=\frac{\pi r_0^2}{d},\qquad \frac{C_1}{\epsilon_0}=4r_0\ln\frac{el_M}{d},$$
$$l_M=\sqrt{a^2+\left[\frac{h_1}{2}+\left(\frac{4a}{3\pi}+\frac{h_1}{2}\right)\frac{\pi a}{\pi a+4h_1}\right]^2},$$
$$\frac{\omega^2L^2}{R_{sh}}=\frac{1}{2\pi\delta\sigma}\left[\frac{h_1-d}{r_0}+\frac{h_1}{r_0+2a}+\frac{\pi a}{\sqrt{r_0(r_0+2a)}}+\ln\frac{r_0+2a}{r_0}\right]$$

(d)

$$\frac{L}{\mu_0}=\frac{1}{2\pi}\left\{\left[h_1-(h_2-h_1)\frac{r_0}{r_1-r_0}\right]\ln\frac{r_1}{r_0}+h_2\ln\frac{r_2}{r_1}+h_2-h_1\right\},\qquad \frac{C_0}{\epsilon_0}=\frac{\pi r_0^2}{d},\qquad \frac{C_1}{\epsilon_0}=4r_0\ln\frac{el_M}{d},$$
$$l_M=\frac{1}{3}\,\frac{\sqrt{\{(r_1-r_0)(h_1^2+h_2^2+h_1h_2)+3h_2^2(r_2-r_1)\}^2+\{(r_1-r_0)^2(2h_2+h_1)+3h_2(r_2-r_1)(r_1+r_2-2r_0)\}^2}}{h_1(r_1-r_0)+h_2(2r_2-r_1-r_0)},$$
$$\frac{\omega^2L^2}{R_{sh}}=\frac{1}{2\pi\delta\sigma}\left[\frac{h_1-d}{r_0}+\frac{h_2}{r_2}+\ln\frac{r_2^2}{r_0r_1}+\frac{\sqrt{(r_1-r_0)^2+(h_2-h_1)^2}}{r_1-r_0}\ln\frac{r_1}{r_0}\right]$$

(e)

$$\frac{L}{\mu_0}=\frac{h}{2\pi}\left(\ln\frac{er_2}{r_1}-\frac{r_0}{r_1-r_0}\ln\frac{r_1}{r_0}\right),\qquad \frac{C_0}{\epsilon_0}=\frac{\pi\bar r_0^2}{d},$$
$$\frac{C_1}{\epsilon_0}=\frac{\pi(r_0^2-\bar r_0^2)}{d}+\frac{2\pi}{\alpha}\left[r_0\ln\frac{el_M\sin\alpha}{d}+\frac{d\cot\alpha}{2}\ln\frac{\sqrt{e}l_M\sin\alpha}{d}\right],$$
$$l_M=\frac{1}{3}\,\frac{\sqrt{\{2(r_1-r_0)^2+3(r_2-r_1)(r_1+r_2-2r_0)\}^2+h^2(3r_2-2r_1-r_0)^2}}{2r_2-r_1-r_0},$$
$$\frac{\omega^2L^2}{R_{sh}}=\frac{1}{2\pi\delta\sigma}\left(\frac{h}{r_2}+\ln\frac{r_2^2}{\bar r_0r_1}+\sec\alpha\ln\frac{r_1}{\bar r_0}\right)$$

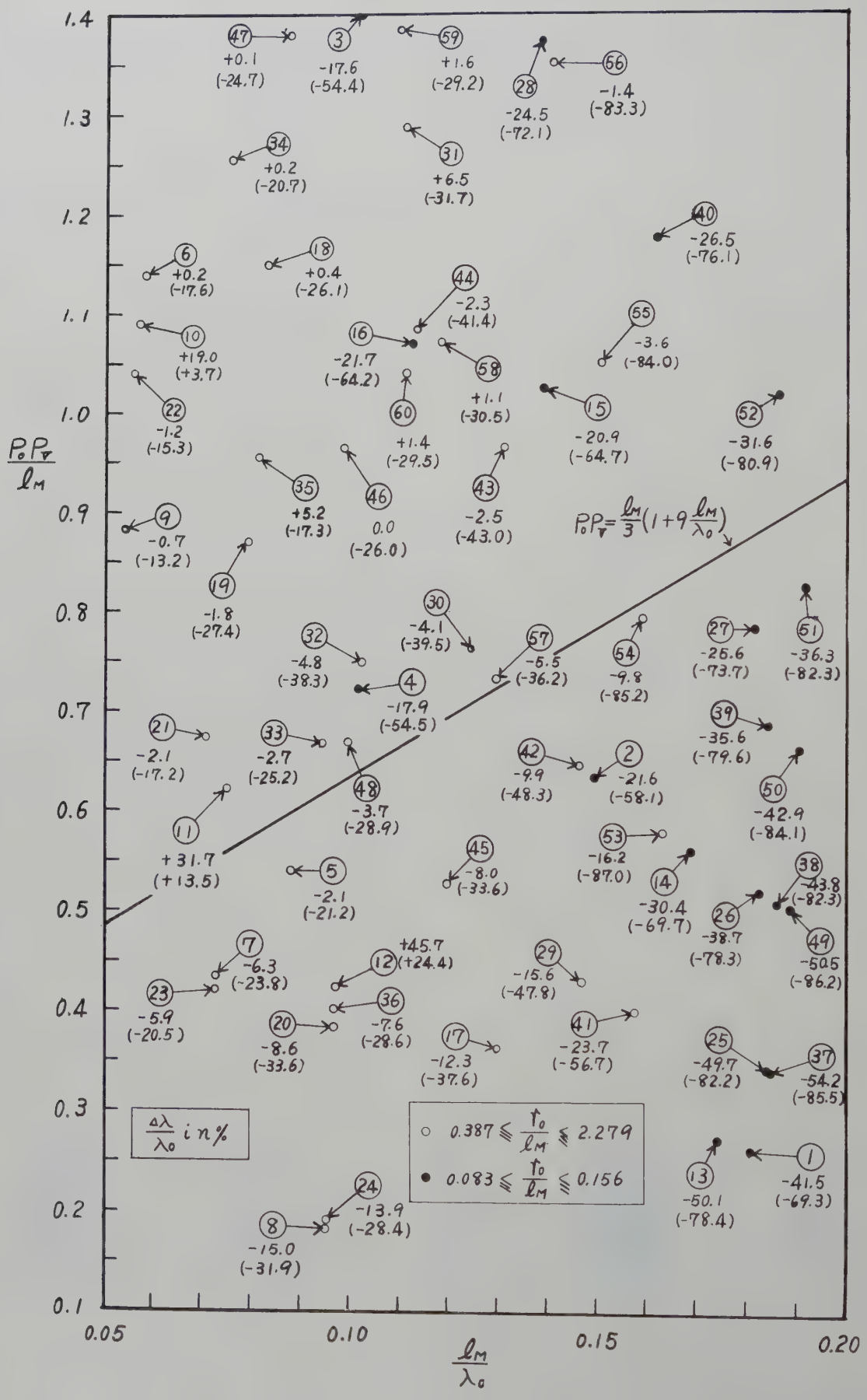


Fig. 8—Percentage differences between the calculations from the formulas and those of Hansen, of the resonant wavelengths of the cavities shown in Fig. 9.

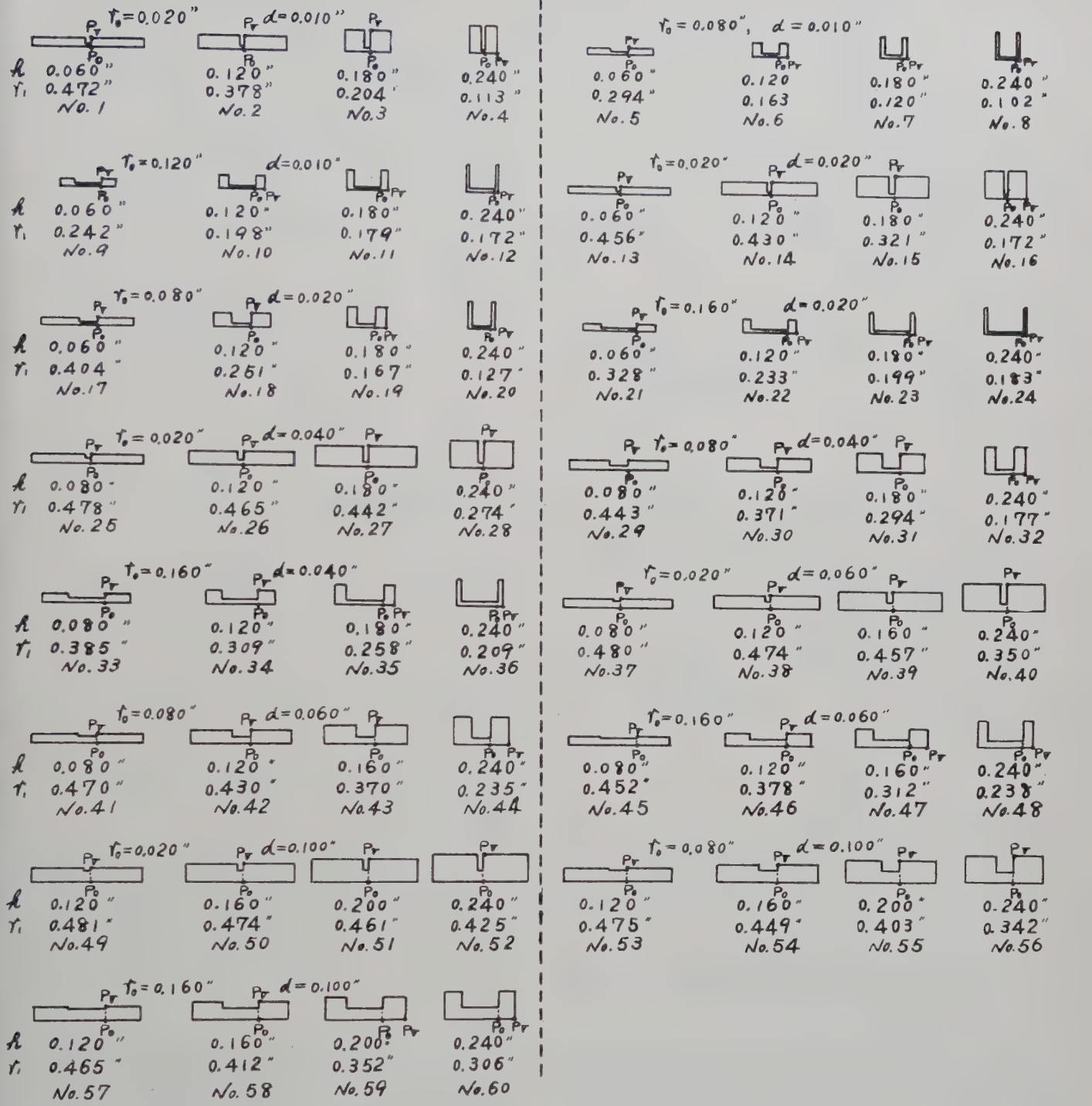


Fig. 9—Reentrant coaxial cavities that have the resonant wavelength of 3.2 cm according to Hansen.

$l_M/\lambda_0$-$P_0P_V/l_M$ plane, according to the values of their parameters, and the percentage differences between the two calculations of their resonant wavelengths are indicated. The values in parentheses show the percentage differences between the calculations by the formulas excepting $C_1$ and those by Hansen.

Clearly, the introduction of $C_1$ is very effective, and the accuracy is much improved. Also, it is found that the cavities are classified into two groups according to their values ot $r_0/l_M$. For the one group with smaller $r_0/l_M(r_0/l_M \leqq 0.156)$, the formulas are not applicable, and for the other with larger $r_0/l_M(r_0/l_M \geqq 0.387)$, they are valid within an error of about 5 per cent, in the region above the straight line indicated in the figure.[12]

[12] Three cavities, Nos. 10, 11 and 12, show extraordinarily great and unusually directed errors. Since some misprints probably may be included in Hamilton, Knipp, and Kuper, *op. cit.*, these three cavities are to be omitted.

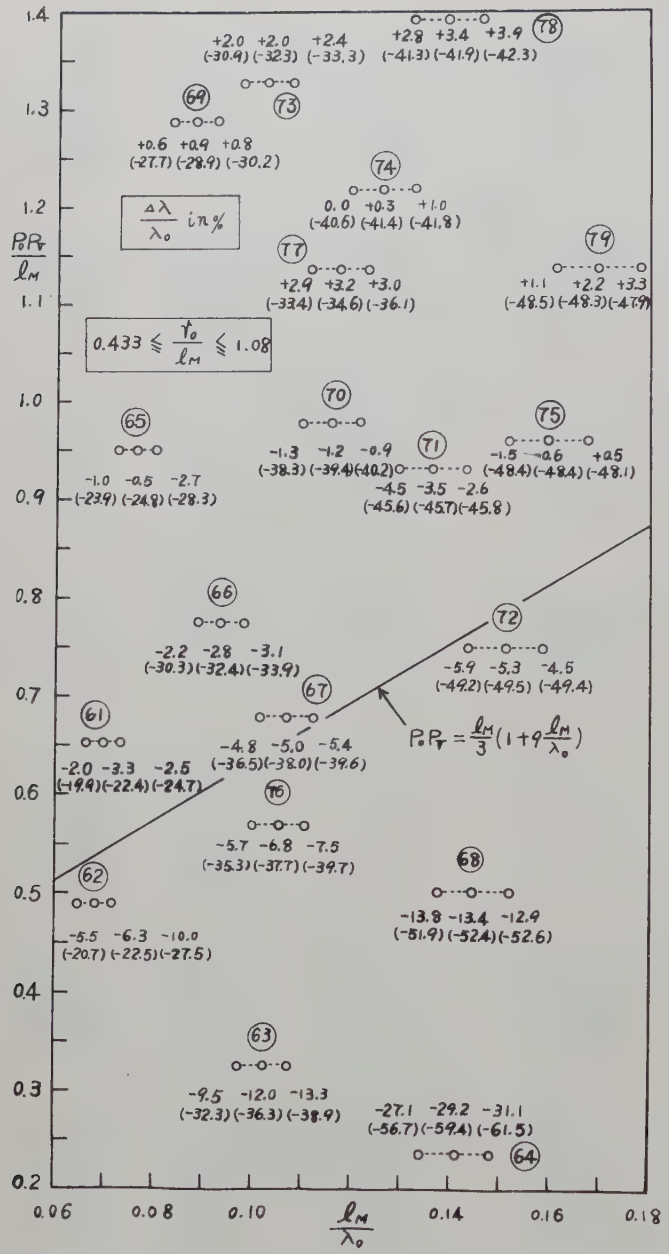


Fig. 10—Percentage errors of the calculated resonant wavelengths of the cavities shown in Fig. 13.

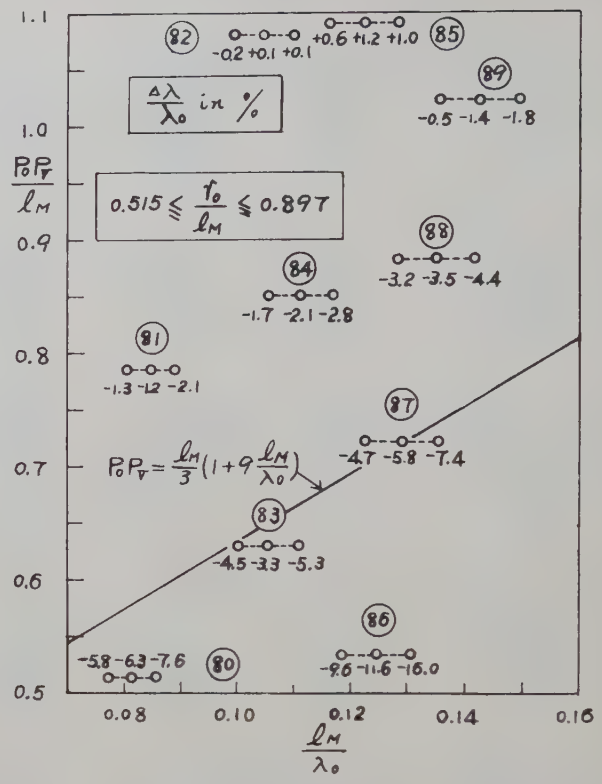


Fig. 11—Percentage errors of the calculated resonant wavelengths of the cavities shown in Fig. 14.

In Figs. 10–12, the calculated resonant wavelengths obtained by the formulas are compared with results of the experiments of the cavities (Figs. 13–15, pp. 354–355), and their percentage errors are given. These cavities all have the resonant frequencies of 3800, 4000, and 4200 mc at the gap distances indicated (the smaller gap distance corresponds to the lower resonant frequency). The values in parentheses in Fig. 10 show the percentage errors of the calculated resonant wavelengths by the formulas excepting $C_1$.

Here also the effectiveness of $C_1$ is proved. Fig. 17 shows the percentage errors of the calculated resonant wavelengths compared with results of experiments of the cavities[13] shown in Fig. 16. In these cases, the resonant wavelengths are varied from about 13 cm to about 32 cm.

The experimental values of the resonant wavelengths are affected by the external loads through the loop coupling, so they contain some errors probably smaller than a few per cent.

From these figures, it is concluded that the introduction of $C_1$ is very effective, and the resonant frequency may be calculated by the formulas to within an error of about 5 per cent in the following ranges of parameters:

$$r_0/l_M \geqq 1/3, \tag{36}$$

and

$$P_0P_V/l_M \geqq 1/3 + 3l_M/\lambda_0. \tag{37}$$

This condition applies for the case when the boundary $c_1$ subtends a right angle at the vertex $P_V$. If the angle at $P_V$ is larger than a right angle, the bend at $P_V$ affects the validity of (21) less, so that the formulas are applicable to smaller values of $P_0P_V/l_M$ than are given by (37). This is understood from the data of the cavities Nos. 110 and 111 in Fig. 17.

As for the shunt resistance and the unloaded $Q$, comparisons were made between the values of the formulas

[13] The cavities Nos. 108 and 109 are the doubly-scaled cavity models of the klystron 2K56 and 2K54.

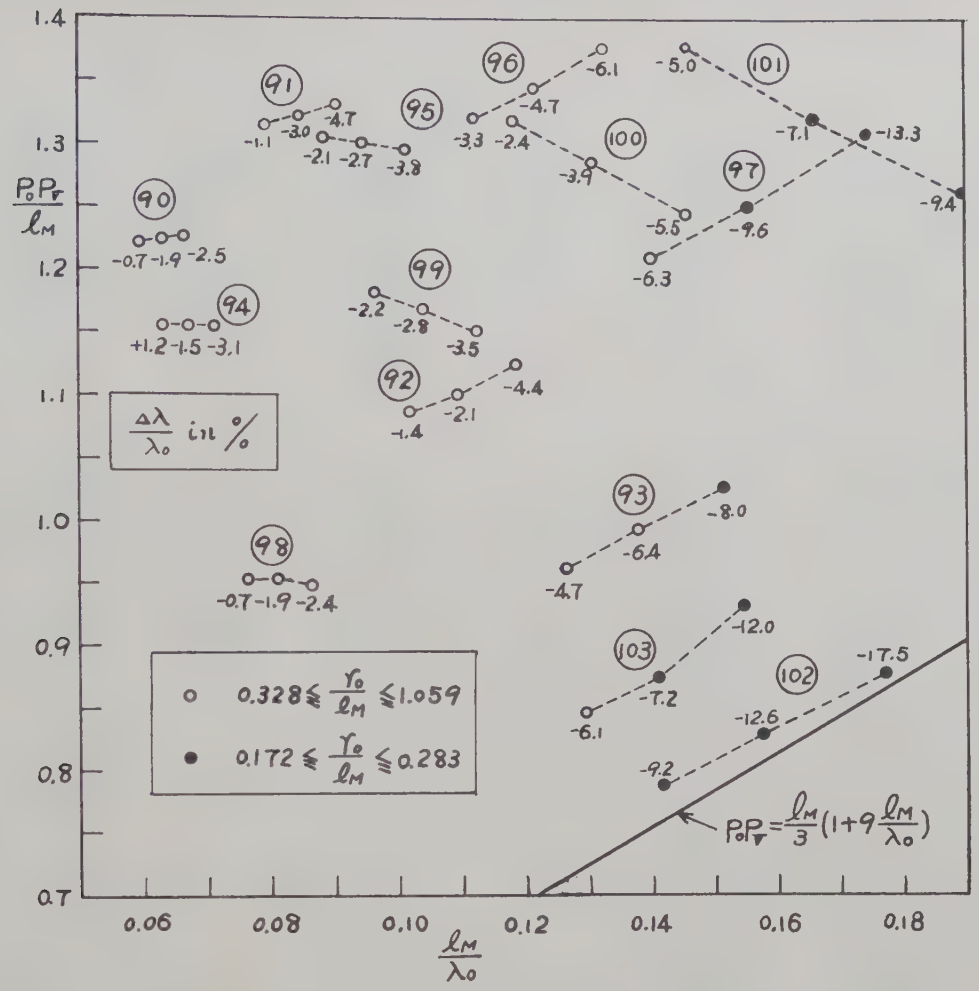


Fig. 12—Percentage errors of the calculated resonant wavelengths of the cavities shown in Fig. 15.

and those of Hansen, for the sixty cavities shown in Fig. 9. The percentage differences between the two calculations are smaller than about 50 per cent,[14] but their values distribute irregularly and it seems impossible to find any rules for the resonant frequency. This may be due to the fact that both calculations contain considerable errors,[15] and we have no standard values to compare them with.

Also, the shunt impedance $R_{sh}/Q_0$ of the reentrant coaxial cavity with a square cross section was calculated by the formulas and compared with the results of Ginzton and Nalos.[16]

The values according to the formulas are in close agreement with their calculated values based on a mean value between coaxial and radial field approximation, and are accurate to 15 per cent for values of $kr_0$ up to 0.6 provided that $kd<0.5$.

From the above discussions, it is concluded that the formulas may give the shunt resistance and the unloaded $Q$ to within an error of several tens of per cent in most cases.

## Special Cases

### *Case 1—A Reentrant Cavity with a Gridless Gap*

So far, we have considered only reentrant cavities with a gridded gap. But, for high power and for extremely high frequency, one uses klystrons with a gridless gap. In Fig. 18, such a gap is shown, which is formed by a cylinder of inner radius $\bar{r}_i$ and outer radius $\bar{r}_0$ and an end plate with an aperture of radius $\bar{r}_i$, at a distance $d$ apart. We assume here that the end plate has a thickness greater than the aperture radius, so that the aperture behaves as a cylinder for the gap fields. The gap fields excite a cutoff $E$-type mode with axial symmetry in the cylinders.

Such a problem was solved in detail by Wang.[17]

[14] Here also the cavities Nos. 10, 11 and 12 were omitted.

[15] The calculations by W. W. Hansen of the shunt resistance and the $Q$ are believed to be accurate to 10 per cent for cavities highly reentrant and to 25 per cent for those that are less so.

[16] Ginzton and Nalos, *op. cit.*, p. 5, Fig. 5.

[17] C. C. Wang, "Electromagnetic field inside a cylinder with a gap," *J. Appl. Phys.*, vol. 16, pp. 351–366; June, 1945.

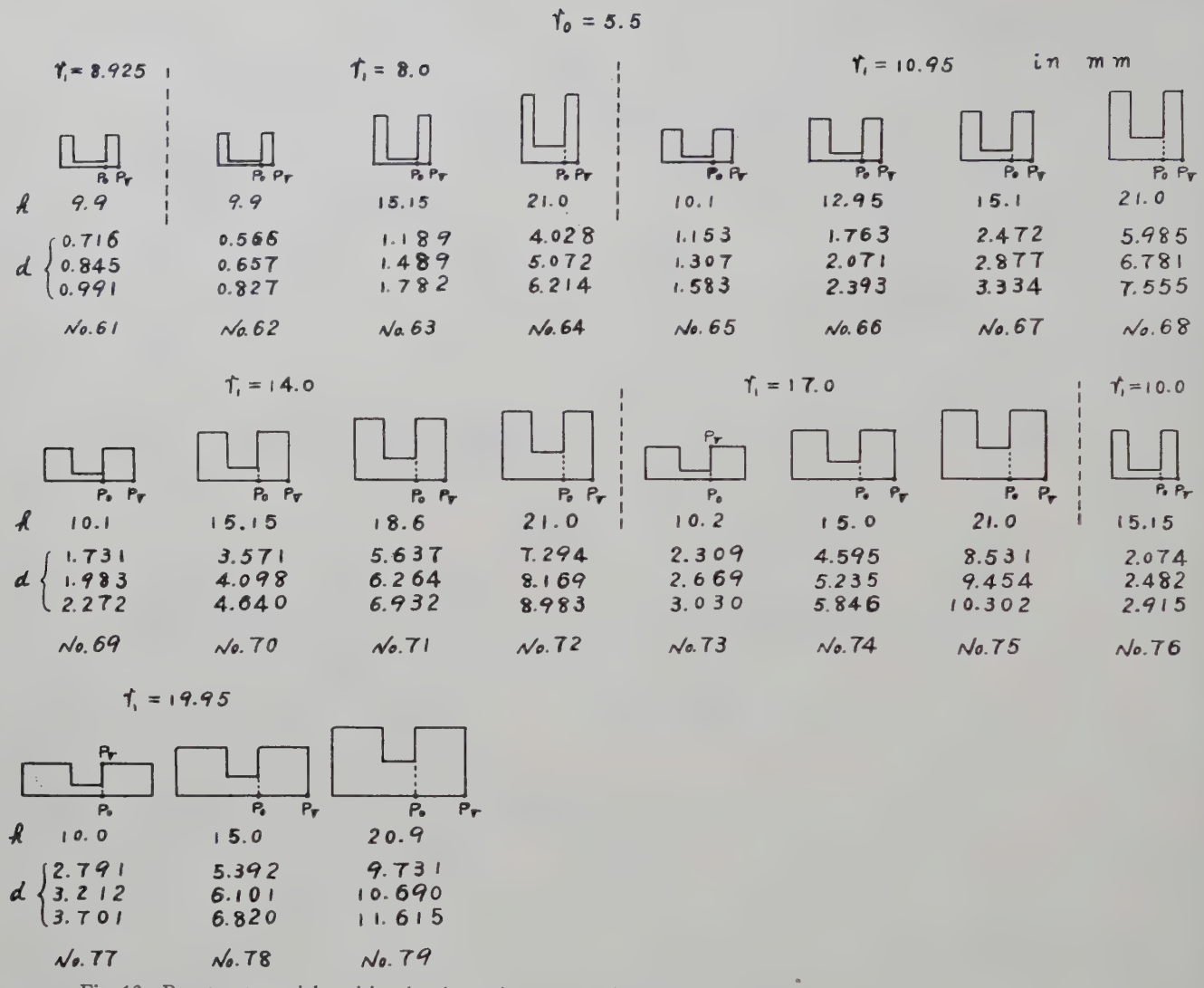


Fig. 13—Reentrant coaxial cavities that have the resonant frequencies of 3800, 4000, and 4200 mc experimentally.

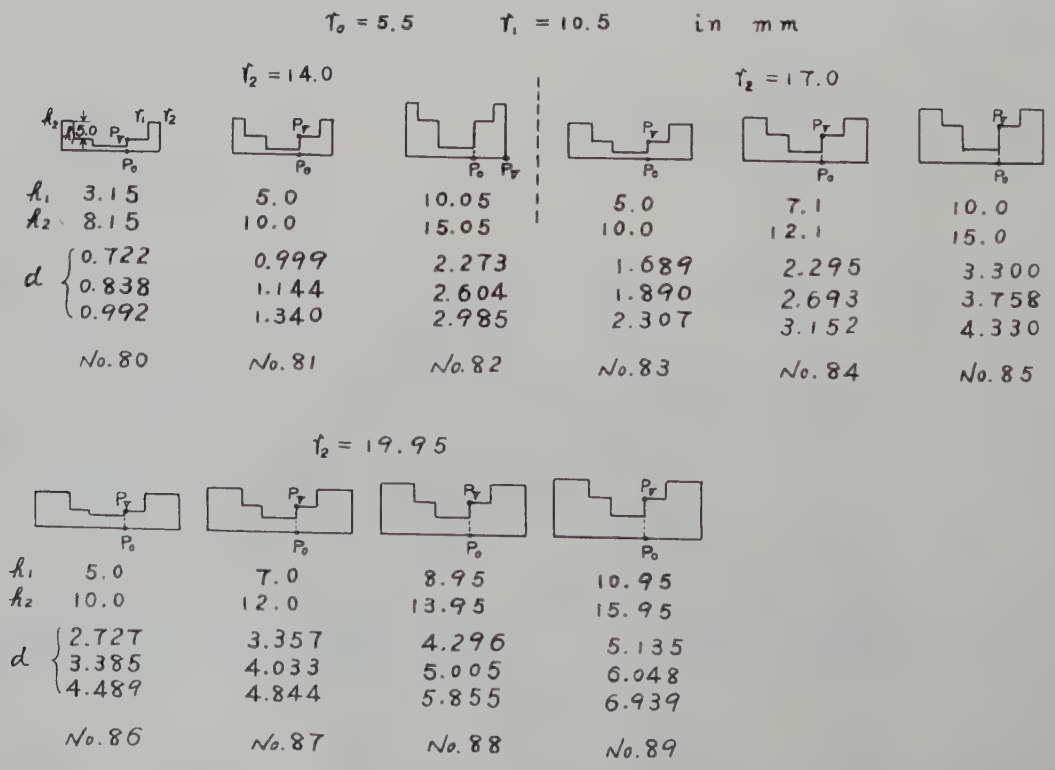


Fig. 14—Reentrant cavities with stepped posts that have the resonant frequencies of 3800, 4000, and 4200 mc experimentally.

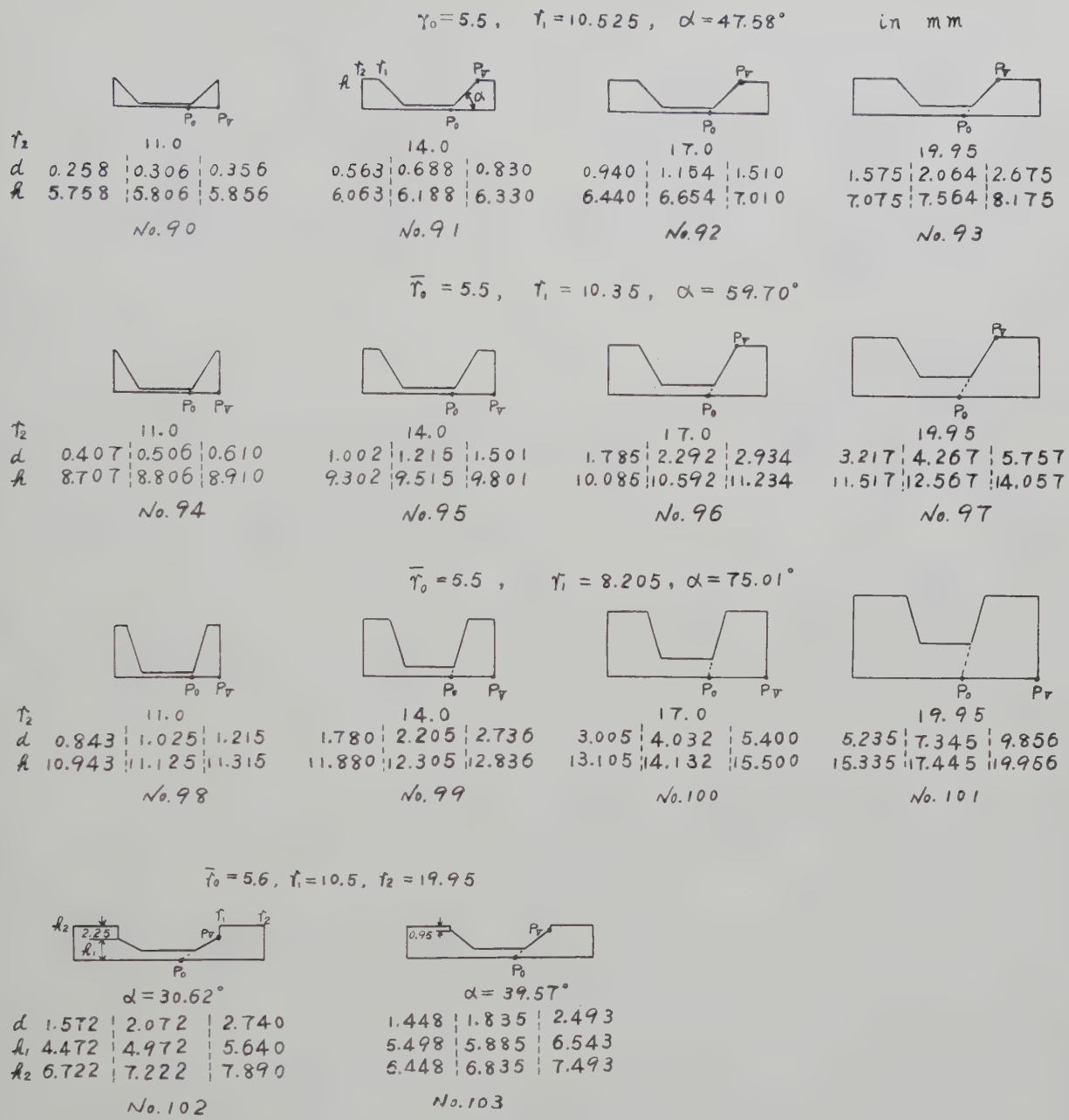


Fig. 15—Reentrant cavities that have the resonant frequencies of 3800, 4000, and 4200 mc experimentally.

Later, it was treated by the author independently, and the following results are derived.[18]

Assuming a space constant electric field on the cylindrical surface $r=\bar{r}_i$ in the gap region, and expressing the fields in Fourier integrals of the elementary waves in the cylinders, the equivalent gap capacitance $C_0$ is obtained as

$$C_0 = \epsilon_0 \frac{\pi(\bar{r}_\theta^2 - \bar{r}_i^2)}{d} + \epsilon_0 \frac{\pi \bar{r}_i^2}{d} \gamma\left(\frac{d}{\bar{r}_i}, \; k\bar{r}_i\right). \quad (38)$$

Clearly, $\gamma$ is a capacitance reduction factor for the gridless gap as compared with the gridded one, and its values are given in Fig. 19, p. 357.

[18] K. Fujisawa, "Gridless modulation gap of a klystron," *J. Inst. Elec. Comm. Eng. Japan*, vol. 36, pp. 613–617; November, 1953.

Substituting (38) for (27), all the former relations remain valid in the same ranges of parameters given by (36) and (37).

*Case 2—A Reentrant Cavity with a Post Stepped near the Tip*

Such a cavity is shown in Fig. 20. By taking the cavity cross section $D$ as shown in Fig. 20(a), as usual, we sometimes have more small values of $P_0P_V/l_M$ than are given by (37), and cannot apply the formulas. In such cases, by taking $D$ as shown in Fig. 20(b), the conditions (36) and (37) are often satisfied, and the formulas become applicable in certain conditions.

In Fig. 20(b), the equivalent gap capacitance consists of the capacitances of the plane parallel plates of the circular and annular areas and the discontinuity capacitance at $r=r_0$ given by (30). So it is written as

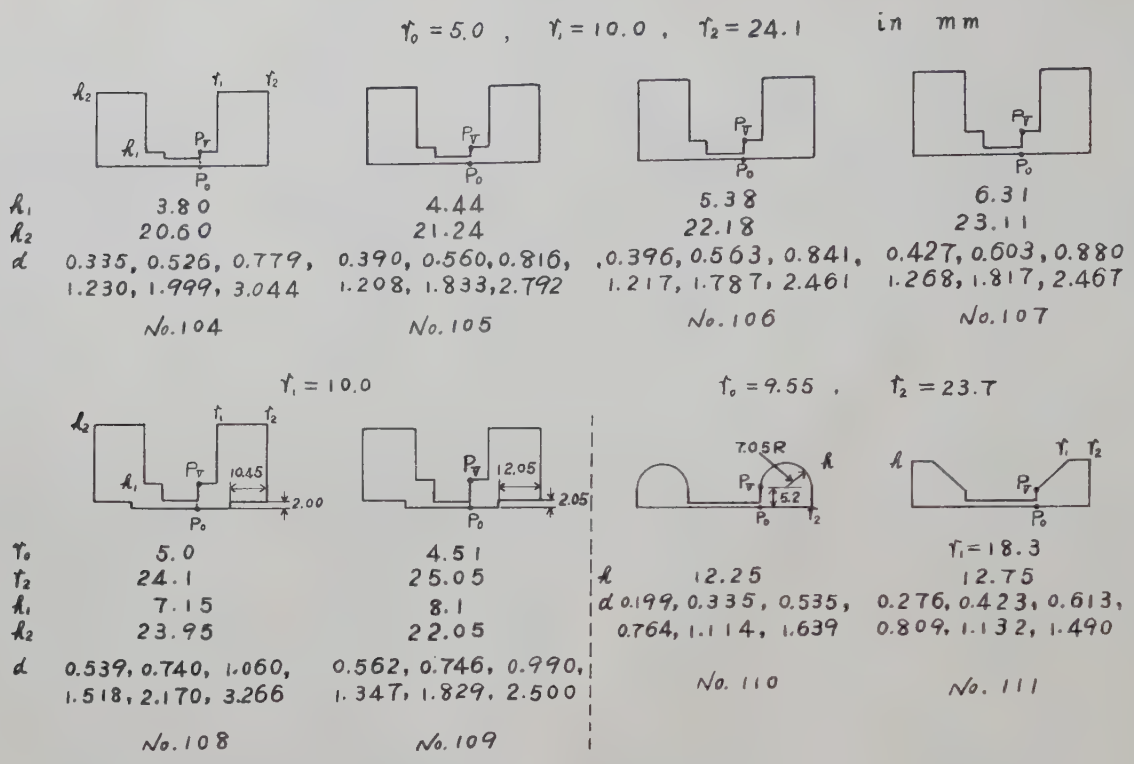


Fig. 16—Various reentrant cavities that have the resonant wavelengths between 13 cm and 32 cm.

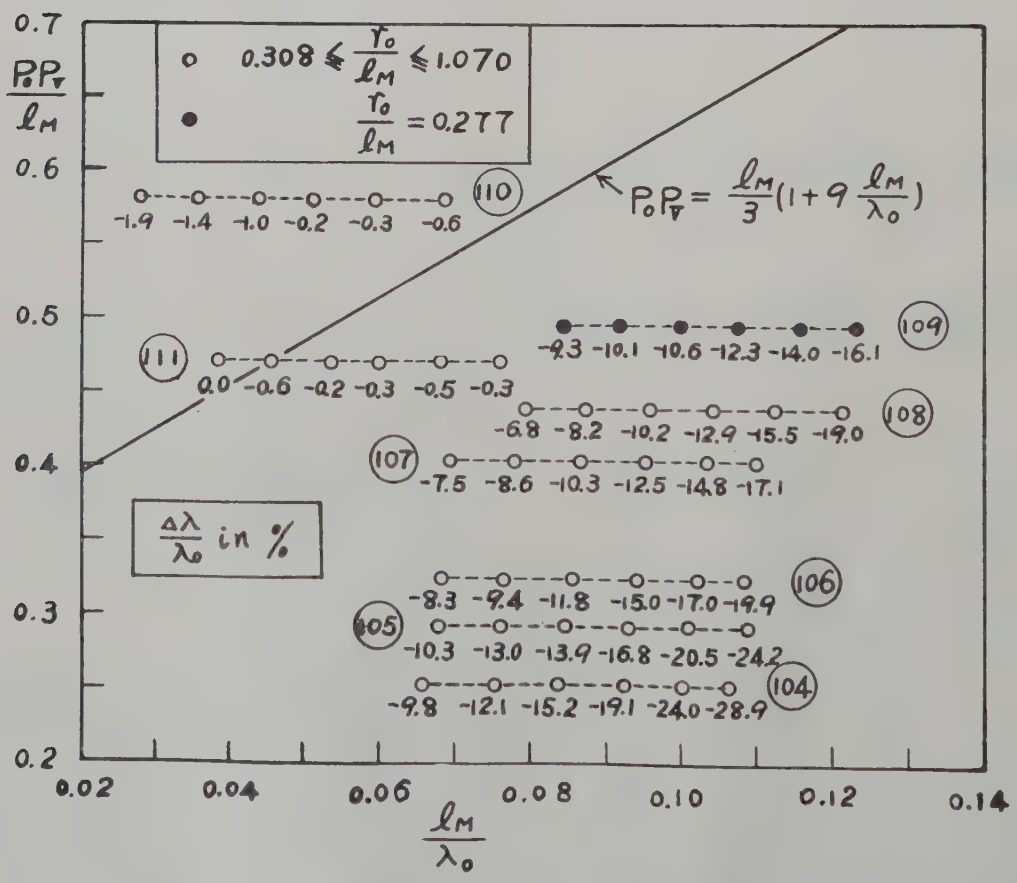


Fig. 17—Percentage errors of the calculated resonant wavelengths of the cavities shown in Fig. 16.

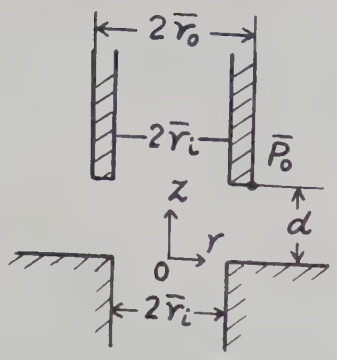


Fig. 18—Typical gridless gap.

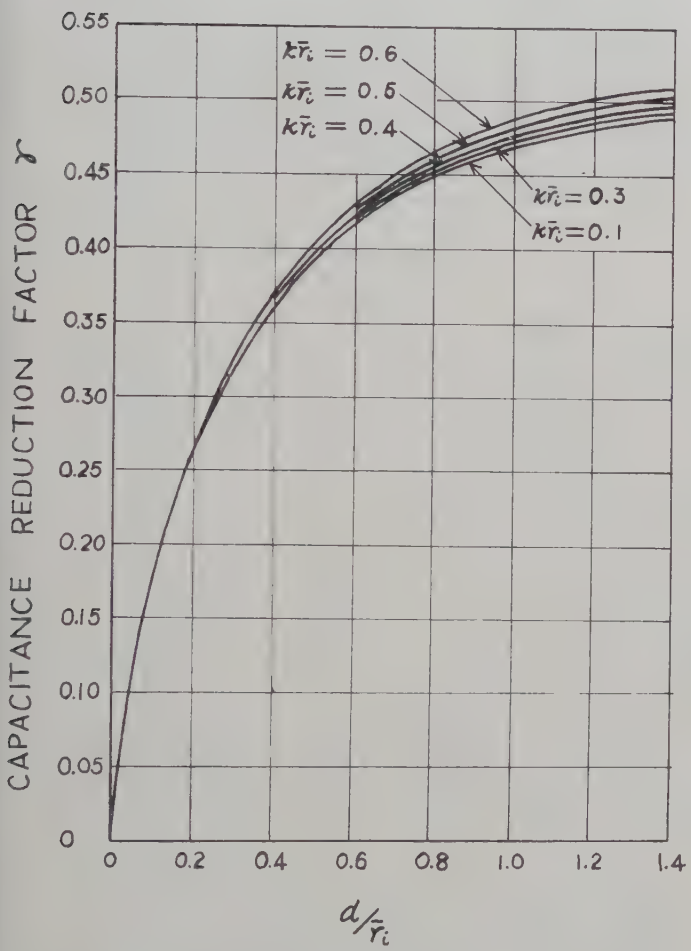


Fig. 19—Capacitance reduction factor for the gridless gap as compared with the gridded one.

$$C_0 = \epsilon_0 \frac{\pi r_0^2}{d} + \epsilon_0 \frac{\pi(r_1^2 - r_0^2)}{h_1} + 4\epsilon_0 r_0 \ln \frac{eh_1}{4d} \cdot \quad (39)$$

Substituting (39) for (27), all the resonance properties are calculable.

By this method, the resonant wavelengths of several cavities were calculated, and their percentage errors compared with experiments are given in Fig. 21 (p. 358). Formerly, these cavities were treated by taking $D$ as usual, and the percentage errors of their calculated resonant wavelengths are given in Figs. 11 and 17. Comparing these data, it is concluded that by this method some cavities are brought into the applicable regions of the formulas [(36) and (37) are satisfied], and their resonant frequencies are calculable within an error of 5 per cent, when the following additional condition is satisfied for the new cavity region $D$:

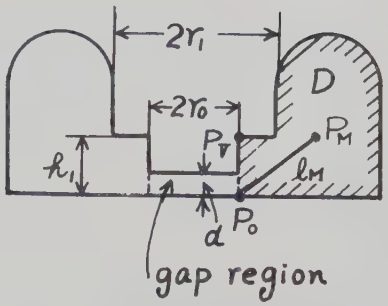


(a)

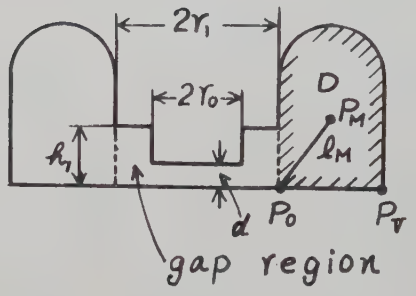


(b)

Fig. 20—Two methods of taking the cavity region $D$ for a cavity with a stepped post.

$$\frac{d}{h_1} \geqq \frac{4}{5}\left(\frac{h_1}{l_M} - \frac{1}{5}\right). \quad (40)$$

## Conclusion

In this paper, general formulas for calculating the equivalent circuit constants of a reentrant cavity are derived, which enable one to calculate the resonant frequency within an error of 5 per cent, in the ranges of parameters given by (36) and (37), and the shunt resistance and the $Q$ within an error of several tens of per cent in most cases. For practical klystron cavities, the conditions (36) and (37) are usually satisfied, so that the formulas are applicable for most klystron cavities.

## Acknowledgment

This work was carried out partly at Osaka University, and partly at Kobe University following the author's transfer to Kobe University in 1954.

The author expresses his sincere thanks to Prof. S. Kumagai for his support and encouragement at Osaka University. He also wishes to acknowledge the valuable assistance of T. Yuwamoto and S. Otsuka at Osaka University and of T. Kaneko and T. Takashima at Kobe University.

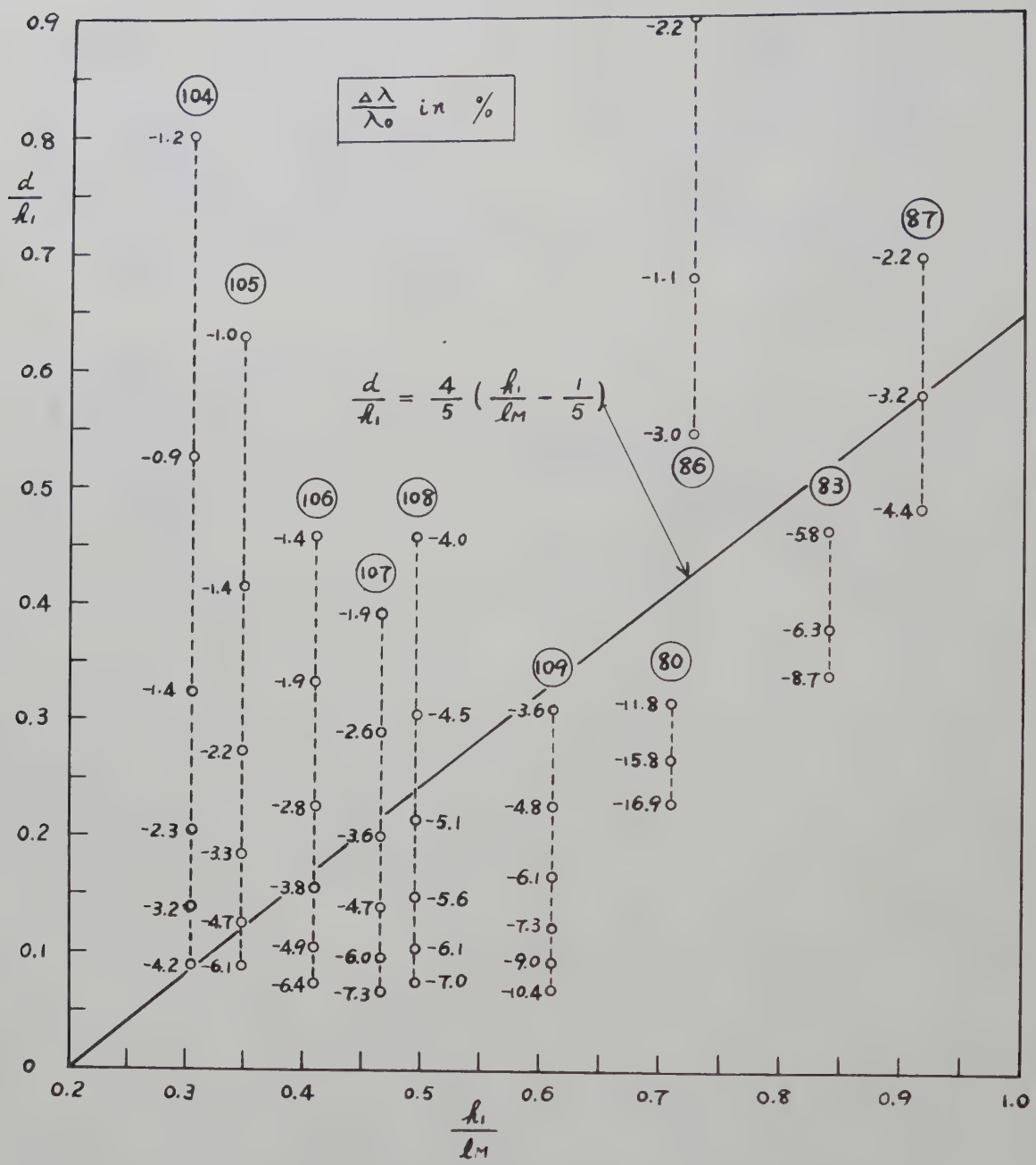


Fig. 21—Percentage errors of the resonant wavelengths calculated by taking $D$ as in Fig. 20(b).

# A Unified Discussion of High-$Q$ Waveguide Filter Design Theory*

HENRY J. RIBLET†

*Summary*—For the general design of conventional, high-$Q$, direct-coupled waveguide filters to be based on the frequency behavior of a classical ladder network prototype, it is necessary and sufficient that the reflecting elements of the filter be replaceable by admittance inverters and that the lengths of transmission line be replaceable by resonant elements. The error due to the latter assumption is of the order of twice the square of the percentage bandwidth measured in guide wavelengths, and the classical synthesis problem is a limiting case of a solvable transmission line problem. In this limit, an exact equivalence is established between the design of a direct-coupled filter and the design of a quarter-wave-coupled filter based on the same ladder network prototype. Design formulas for equal ripple and maximally flat performance are given for the VSWR's of the reflecting elements in terms of dimensionless quantities. Detailed comparison of previous formulas is made.

## Introduction

THIS PAPER is concerned with the general design of filters which consist of a cascade of large, lossless, similar, reflecting elements, often shunt inductances, spaced in a regular manner on a uniform waveguide. Lawson and Fano[1] have given general synthesis procedures for two types of filters distinguished as "quarter-wave-coupled" and "direct-coupled." For both types of filters, they give explicit synthesis procedures based on the use of a ladder network prototype having a prescribed insertion loss function. Southworth[2] has given the design parameters for direct-coupled, maximally flat filters without, however, any supporting synthesis procedure. Mumford[3] has given the design parameters for quarter-wave-coupled, maximally flat filters, and has improved on the approximation used by Lawson and Fano for the interconnecting, quarter wavelength of waveguide. He has used the synthesis procedure proposed by Lawson and Fano. Recently, Cohn[4] has given design parameters for direct-coupled filters, for equal ripple, and for maximally flat response. He has employed a ladder network prototype explicitly and has used a frequency transformation which improves the approximation for shunt inductances.

A general synthesis procedure for the design of direct-coupled filters has been given by Riblet[5] but since it is not based on the use of a ladder network prototype, it is not within the scope of this paper.

The multiplicity of papers in the literature which are concerned with the design of direct-coupled filters (Fig. 1), is a source of confusion to the design engineer. Lawson and Fano,[1] Cohn,[4] and presumably Southworth,[2] base their assumptions on the same ladder network prototype (Fig. 2). In spite of this similarity, Cohn has indicated how different results are obtained in each of these papers. Actually the situation is not difficult to understand when one considers the number of approximations involved in the synthesis procedure and realizes that little effort has been made to justify any of them rigorously.

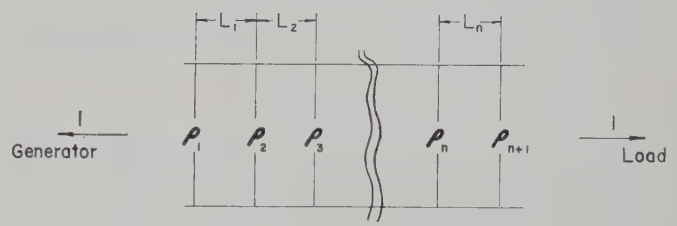


Fig. 1—Schematic of a direct-coupled filter.

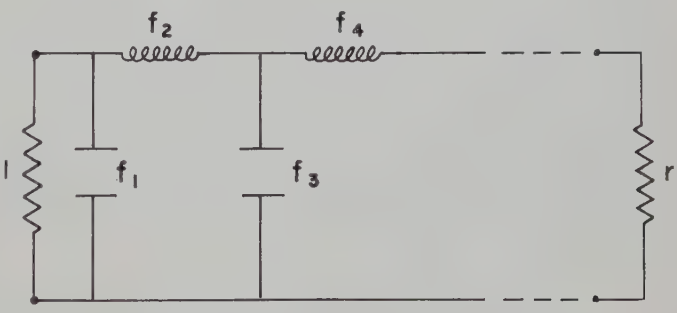


Fig. 2—Ladder network prototype.

The fact that the differences observed by Cohn are minor suggests that the methods used are the same in principle. It is the object of this paper to show that this is the case and to unify the whole problem by putting the approximations required for the existence of a general synthesis procedure, based on a ladder network prototype, on a formal basis. By way of justification it will be indicated how the approximate synthesis is a limiting

* Manuscript received by the PGMTT, November 29, 1957; revised manuscript received, July 10, 1958. Presented before the URSI meeting, Washington, D. C., May, 1957.

† Microwave Development Lab., Wellesley, Mass.

[1] A. W. Lawson and R. M. Fano, "The design of microwave filters," in "Microwave Transmissions Circuits," M.I.T. Rad. Lab. Ser., McGraw-Hill Book Co., Inc., New York, N. Y., vol. 9, pp. 661–706; 1948.

[2] G. C. Southworth, "Principles and Applications of Waveguide Transmission," D. Van Nostrand Co., Inc., New York, N. Y., pp. 297–298; 1950.

[3] W. W. Mumford, "Maximally-flat filters in waveguide," *Bell Sys. Tech. J.*, vol. 27, pp. 684–713; October, 1948.

[4] S. B. Cohn, "Direct-coupled resonator filters," PROC. IRE, vol. 45, pp. 187–196; February, 1957.

[5] H. J. Riblet, "Synthesis of narrow-band direct-coupled filters," PROC. IRE, vol. 40, pp. 1219–1223; October, 1952.

form of an exact transmission-line synthesis. As by-products, we obtain 1) a quantitative estimate of the error involved in the ladder network approximation, 2) slightly more concise formulas than previously given, and 3) a demonstration of an exact equivalence between direct-coupled filters and quarter-wave-coupled filters using Mumford's approximation for the quarter wavelength of line. Finally, the general synthesis given by Lawson and Fano[1] is derived, and it is shown how our formulas for the case of direct-coupled filters may be obtained as special cases from their formulas.

## Formal Theory

This section considers the consequences of the following two simplifying assumptions.

1) The admittance transformation of the reflecting elements, which relates the input voltage and current, $v_i$ and $i_i$ to the output voltage and current, $v_0$ and $i_0$, may be written

$$\begin{aligned} i_i &= 0 \cdot i_0 + j\sqrt{\rho}\, v_0 \\ v_i &= \frac{j}{\sqrt{\rho}} \cdot i_0 + 0 \cdot v_0, \end{aligned} \tag{1}$$

where $\rho$[6] is a positive real constant, to be called the inversion factor.

2) The admittance transformation of the interconnecting half wavelengths of waveguide, may be written

$$\begin{aligned} i_i &= 1 \cdot i_0 + 0 \cdot v_0 \\ v_i &= p \cdot i_0 + 1 \cdot v_0. \end{aligned} \tag{2}$$

where $p = j \sin \theta$ with $\theta = 2\pi l/\lambda_g$.

Now the interest in 1) and 2) arises from the fact that they are, as will be shown in a very broad sense, necessary and sufficient for the existence of a general synthesis procedure for direct-coupled filters based on a ladder-network prototype. Accordingly, differences in previous results[1,2,4] must arise from the approximations used in relating $\rho$ and $p$ to reactance and frequency.

How this can be demonstrated is outlined in Appendix I. First, the possibility of connecting the reflecting elements with transmission line sections having the admittance transformation,

$$\begin{aligned} i_i &= \cos \theta i_0 + j \sin \theta v_0 \\ v_i &= j \sin \theta i_0 + \cos \theta v_0 \end{aligned} \tag{3}$$

is considered and then excluded when it is found that, in general, the input admittance of such a cascade cannot have the form required by ladder network prototypes. (Note that the coefficients of (1)–(3) are transfer matrices[7] rearranged in DCBA form.) When (3) is replaced by (2) such a synthesis can be carried out if, and only if, the general circuit parameters of the reflecting elements, assumed to be analytic in $p$, simplify to the form in (1). Eq. (2) is justified further in Appendix II, where it is shown that if the admittance inverters, designed on the basis of a ladder network prototype, are equally spaced on a uniform transmission line, and and if the inversion factors are allowed to become arbitrarily large so as to preserve the form of the insertion loss function, though not its bandwidth, then $\cos \theta$ tends to unity and the upper-corner $\sin \theta$ tends to zero, and (2) is exact. Of course, the validity of (1) remains to be established in each application.

To show that a direct-coupled filter consisting of a cascade of alternate (1) and (2) matrices corresponds to every ladder network prototype readily follows with the help of the equalities,

$$f_i \begin{pmatrix} 1 & f_i p \\ 0 & 1 \end{pmatrix} = \begin{pmatrix} 0 & f_i \\ 1 & 0 \end{pmatrix} \begin{pmatrix} 1 & 0 \\ p & 1 \end{pmatrix} \begin{pmatrix} 0 & f_i \\ 1 & 0 \end{pmatrix} \tag{4}$$

and

$$\begin{pmatrix} 0 & f_i f_k \\ 1 & 0 \end{pmatrix} = \begin{pmatrix} 0 & f_i \\ 1 & 0 \end{pmatrix} \begin{pmatrix} 0 & 1 \\ 1 & 0 \end{pmatrix} \begin{pmatrix} 0 & f_k \\ 1 & 0 \end{pmatrix}. \tag{5}$$

Consider a ladder network prototype which can be written in matrix form as

$$\begin{pmatrix} 1 & f_1 p \\ 0 & 1 \end{pmatrix} \begin{pmatrix} 0 & 1 \\ 1 & 0 \end{pmatrix} \begin{pmatrix} 1 & f_2 p \\ 0 & 1 \end{pmatrix} \cdots \begin{pmatrix} 0 & 1 \\ 1 & 0 \end{pmatrix} \begin{pmatrix} 0 & f_n p \\ 1 & 0 \end{pmatrix}, \tag{6}$$

since the first and alternate matrices are the admittance transformations of shunt resonant elements and the remaining matrices are the admittance inverters that correspond to changing from shunt to series. Applying (4)[8] to the resonant elements of (6) and eliminating the unity admittance inverters by means of (5) results in the matrix product,

$$\begin{pmatrix} 0 & f_1 \\ 1 & 0 \end{pmatrix} \begin{pmatrix} 1 & 0 \\ p & 1 \end{pmatrix} \begin{pmatrix} 0 & f_1 f_2 \\ 1 & 0 \end{pmatrix} \begin{pmatrix} 1 & 0 \\ p & 1 \end{pmatrix} \cdots \begin{pmatrix} 0 & f_n \\ 1 & 0 \end{pmatrix}, \tag{7}$$

which is of the required form if

$$\rho_1 = f_1,\ \rho_2 = f_1 \cdot f_2,\ \cdots,\ \rho_n = f_n \cdot f_{n-1},\ \rho_{n+1} = f_n. \tag{8}$$

The converse is not generally true, but if we terminate the direct-coupled filter, we can always find a terminated ladder network prototype with the same input admittance function. Accordingly, it is convenient to carry through a general synthesis procedure for the determination of the $\rho$'s without requiring the $f$'s. We now consider the admittances seen at various points of the network assuming a known terminating admittance. If $Y_i = N_i/D_i$, where $N_i$ and $D_i$ are polynomials in $p$, is the admittance preceding

$$\begin{pmatrix} 0 & \rho_i \\ 1 & 0 \end{pmatrix} \begin{pmatrix} 1 & 0 \\ p & 1 \end{pmatrix}, \tag{9}$$

[6] $\rho$ is the coupling reactance, $X^{-2}$, of Lawson and Fano, *op. cit.* We have chosen to denote it by $\rho$ to emphasize that it is, for $\rho \geq 1$, numerically equal to VSWR of the reflecting element.

[7] E. A. Guillemin, "Communication Networks," John Wiley and Sons, Inc., New York, N. Y., vol. 2, pp. 144–152; 1935.

[8] Any common multiplicative factors may be ignored because they cancel out of numerator and denominator once a terminating admittance is selected and the input admittance is determined.

and $Y_{i-1}=N_{i-1}/D_{i-1}$ is the admittance into which it is transformed by (9), then

$$N_{i-1} = \rho_i p N_i + \rho_i D_i; \qquad D_{i-1} = N_i. \tag{10}$$

If the admittance, $Y_{n+1}$, terminating the cascade is a constant, then $Y_n$ is a first degree polynomial in $p$. In particular, the degree of $N_n$ is one higher than the degree of $D_n$. This is true for all admittances looking into the admittance inverters. For, if it is true for $N_i$ and $D_i$ in (10), it is certainly true for $N_{i-1}$ and $D_{i-1}$. Thus the input admittance of a cascade of the form of (7) is a rational function of $p$ whose denominator is of degree $n$ in $p$ while its numerator is of degree $n-1$. It is, of course, positive real in the sense of Brune.[9] Of course the input impedance of the network can be determined from the given insertion loss function by the method of Darlington.[10] Then the $\rho_i$ associated with $Y_{i-1}$ can always be determined by dividing the coefficient of the highest power of $p$ in its numerator by the coefficient of the highest power of $p$ in the denominator. This follows from (10). We also see that $Y_i$ equals the denominator, $D_{i-1}$, of $Y_{i-1}$ divided by the remainder when $N_{i-1}/\rho_i$ is divided by $D_{i-1}$.

This procedure can be summarized in a continued fraction expansion for the input admittance, $Y_0$, of the cascade terminated in an admittance, $R$.

$$Y_0 = \rho_1 p + \cfrac{\rho_1}{\rho_2 p + \cfrac{\rho_2}{\ddots \cfrac{}{\rho_n p + \cfrac{\rho_n}{(\rho_{n+1})/R}}}} \tag{11}$$

The use of the continued fraction expansion simplifies certain manipulations once it is clear that the value of $Y_0$ is unchanged when one multiplies the quantities directly above and below any of the fraction bars by the same quantity. Thus in (10), we may replace the second $\rho_1$ by 1, if we divide both $\rho_2$'s below it by $\rho_1$. Thus $Y_0$ can be written

$$Y_0 = \rho_1 p + \cfrac{1}{(\rho_2/\rho_1) p + \cfrac{1}{\left(\frac{\rho_1\rho_3}{\rho_2}\right) p + \cfrac{1}{\ddots \cfrac{}{\left(\frac{\rho_n\rho_{n-2}\cdots}{\rho_{n-1}\rho_{n-3}\cdots}\right) p + \cfrac{\rho_n\rho_{n-2}\cdots R}{\rho_{n+1}\rho_{n-1}\cdots}}}}} \tag{12}$$

Thus, for every terminated direct-coupled filter there is a corresponding terminated ladder network prototype having the same input impedance, although the terminations are not in general the same. This is precisely the equivalence used by Lawson and Fano[1] to give a general synthesis procedure for direct-coupled filters. This discussion, however, avoids the troublesome reactances, $X_S$ and $X_L$ which were invoked by them.

In general, the values of $p$ which are of practical interest are small, whereas the formulas due to Bennett[11] and Belevitch (modified by Orchard)[12] for the element values, $f_i$, of the ladder network prototypes yielding maximally flat and Tchebycheff performance assume that the value of the frequency variable $\omega$ is equal to unity at the edges of the pass band. Accordingly, we consider the effect of replacing $p$ in (11) by $tp$. We then find that the form of the continued fraction can be preserved, if we multiply numerator and denominator of each fraction bar by $t$. The resulting continued fraction is

$$Y_0 = \rho_1 t p + \cfrac{\rho_1 t}{\rho_2 t^2 p + \cfrac{\rho_2 t^2}{\ddots \cfrac{}{\rho_n t^2 p + \cfrac{\rho_n t^2}{(\rho_{n+1})r/R}}}}. \tag{13}$$

Thus a narrowing of the frequency scale by a factor of $1/t$ is accomplished by multiplying the inversion factors at each end of the filter by $t$ and all of the other inversion factors by $t^2$.

For narrow-band filters, the dimensional tolerances are relaxed by replacing some or all of the half wavelengths of waveguide by sections an integral number of half wavelengths long. Increasing the length of a filter in this way also increases its peak power handling ability. In fact, it is readily shown, by the methods of this section, that for fixed band-pass characteristics the maximum voltage in a given cavity section varies

[9] O. Brune, "Synthesis of a finite two-terminal network whose driving point impedance is a prescribed function of frequency," *J. Math. Phys.*, vol. 10, pp. 191–236; October, 1931.

[10] S. Darlington, "Synthesis of reactance 4-poles," *J. Math Phys.*, vol. 18, pp. 257–353; September, 1939

[11] W. R. Bennett, U. S. Patent No. 1,849,656; March 15, 1932.

[12] V. Belevitch, "Tchebyshev filters and amplifiers networks," *Wireless Eng.*, vol. 29, pp. 106–107; April, 1952.
H. J. Orchard, "Formulae for ladder filters," *Wireless Eng.*, vol. 30, pp. 3–5; January, 1953.

inversely with the square root of its length measured in half wavelengths. The change in (19)–(22) required to give the same pass-band characteristic when the length of a given transmission line section is increased to $n$ half wavelengths is readily seen from (11). Here, if the corresponding $p$ is replaced by $np$, no change in $Y_0$ results when the adjacent inversion factors are divided by $n$.

This section is concluded by establishing the exact equivalence between a direct-coupled filter and a quarter-wave-coupled filter (Fig. 3) employing Mumford's approximation for a quarter wavelength of waveguide.

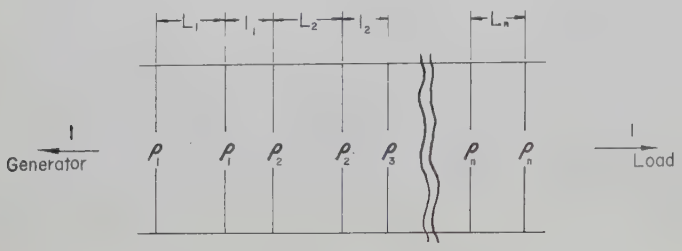


Fig. 3—Schematic of a quarter-wave-coupled filter.

First, the admittance transformation,

$$\begin{pmatrix} kp & 1+(kp)^2 \\ 1 & kp \end{pmatrix}, \tag{14}$$

for $k=\frac{1}{2}$ (quarter-wave coupling), 3/2 (three-quarter-wave coupling), etc., is that used by Mumford[3] to approximate sections of waveguide an odd number of quarter wavelengths long. We are required to show that a matrix product of the form,

$$\begin{pmatrix} 1 & (f_1-k)p \\ 0 & 1 \end{pmatrix}\begin{pmatrix} kp & 1+(kp)^2 \\ 1 & kp \end{pmatrix}\begin{pmatrix} 1 & (f_2-2k)p \\ 0 & 1 \end{pmatrix} \cdots \begin{pmatrix} 1 & (f_n-k)p \\ 0 & 1 \end{pmatrix}, \tag{15}$$

is precisely equivalent to (7), since we have already seen how in (4), the matrices involving the $f_i$'s are the admittance transformations of resonant cavities, except for a multiplicative factor. This is done by replacing the first and last terms with the help of the identities,

$$\begin{pmatrix} 0 & f_i \\ 1 & 0 \end{pmatrix}\begin{pmatrix} 1 & 0 \\ p & 1 \end{pmatrix}\begin{pmatrix} 0 & f_i \\ 1 & -kp \end{pmatrix} = f_i\begin{pmatrix} 1 & (f_i-k)p \\ 0 & 1 \end{pmatrix} = \begin{pmatrix} -kp & f_i \\ 1 & 0 \end{pmatrix}\begin{pmatrix} 1 & 0 \\ p & 1 \end{pmatrix}\begin{pmatrix} 0 & f_i \\ 1 & 0 \end{pmatrix}, \tag{16}$$

and the other terms involving $f$'s by using the identity,

$$\begin{pmatrix} -kp & f_i \\ 1 & 0 \end{pmatrix}\begin{pmatrix} 1 & 0 \\ p & 1 \end{pmatrix}\begin{pmatrix} 0 & f_i \\ 1 & -kp \end{pmatrix} = f_i\begin{pmatrix} 1 & (f_i-2k)p \\ 0 & 1 \end{pmatrix}. \tag{17}$$

Then the matrices involving $1+(kp)^2$ are eliminated using the identity,

$$\begin{pmatrix} 0 & f_if_{i+1} \\ 1 & 0 \end{pmatrix} = \begin{pmatrix} 0 & f_i \\ 1 & -kp \end{pmatrix}\begin{pmatrix} kp & 1+(kp)^2 \\ 1 & kp \end{pmatrix}\begin{pmatrix} -kp & f_{i+1} \\ 1 & 0 \end{pmatrix}. \tag{18}$$

This equivalence, of course, only operates in one direction. For a direct-coupled filter network there is no equivalent quarter-wave-coupled filter network, in general, without specifying the termination.

## Design Formulas

When expressions for $f_i$,[11,12] are substituted in (8) and suitable allowance is made, according to (13), for a change in frequency scale, general formulas are obtained for the VSWR's of the reflecting elements of maximally flat or equal ripple, direct-coupled filters. The equivalence between (15) and (7), results in similar formulas for the VSWR's of the reflecting elements of quarter-wave-coupled filters. Table I gives these formulas together with the figures, equations, and definitions required for design purposes.

Table II gives formulas for the line lengths separating the reflecting elements, together with an equation and the definitions required for design. These formulas are conventional except for the allowance for end effects. This addition has been made because the author's experience shows that in some applications end effect correction must be taken into account in order to avoid significant experimental error.

The use of Table I formulas requires the determination of $h$ (for equal-ripple performance), $n$, $\omega_0$, and $t$ in that order. The value of $h$ is readily obtained from the tolerance given for the pass-band ripple or VSWR. Selection of $n$ is made to yield the desired skirt steepness. The formulas for $P_L$ are used for this purpose where $\omega$ equals a frequency scale factor multiplied by the departure of the frequency from the filter midband. For quick estimates this can be done in terms of frequency but for greater accuracy the use of guide wavelengths is recommended. Once $n$ and $h$ are fixed, $\omega_0$ is found from the corresponding expression for $P_L$. For example, if a two-section maximally flat filter is specified to have 10-db loss at frequencies corresponding to $\lambda_{g_1}$ and $\lambda_{g_2}$, then $P_L=10=1+\omega_0^4$, so that $\omega_0=\sqrt[4]{3}$. Where the bandwidth of a maximally flat filter is specified at the 3-db points $\omega_0=1$; if the bandwidth of an equal ripple filter is specified at the extremes of the equal ripple tolerance, $\omega_0=1$. The $t$ occurring in the formulas is a generalization of the notion of total $Q$ introduced by Mumford. It is determined by the requirement that $t \sin\theta=\omega_0$ for the two specified guide wavelengths $\lambda_{g_1}$, and $\lambda_{g_2}$ at which symmetrical behavior is expected.

## Definitions for Table I

The VSWR of the reflecting element is $\rho$. $P_L$ is the insertion loss function obtained by dividing the avail-

TABLE I

INVERSION FACTOR FORMULAS

| | Equal Ripple | Maximally Flat |
|---|---|---|
| Direct-Coupled Filter | $\rho_1 = t \cdot \dfrac{2 \sin \dfrac{\pi}{2n}}{\gamma}$<br>$\rho_2 = t^2 \cdot \dfrac{4 \sin \dfrac{3\pi}{2n} \cdot \sin \dfrac{\pi}{2n}}{\gamma^2 + \sin^2 \dfrac{\pi}{n}}$<br>$\vdots$<br>$\rho_i = t^2 \cdot \dfrac{4 \sin \dfrac{(2i-1)\pi}{2n} \cdot \sin \dfrac{(2i-3)\pi}{2n}}{\gamma^2 + \sin^2 \dfrac{(i-1)\pi}{n}}$<br>$\vdots$<br>$\rho_{n+1} = \rho_1$ (19) | $\rho_1 = t \cdot 2 \sin \dfrac{\pi}{2n}$<br>$\rho_2 = t^2 \cdot 4 \sin \dfrac{3\pi}{2n} \cdot \sin \dfrac{\pi}{2n}$<br>$\vdots$<br>$\rho_i = t^2 \cdot 4 \sin \dfrac{(2i-1)\pi}{2n} \cdot \sin \dfrac{(2i-3)\pi}{2n}$<br>$\vdots$<br>$\rho_{n+1} = \rho_1$ (20) |

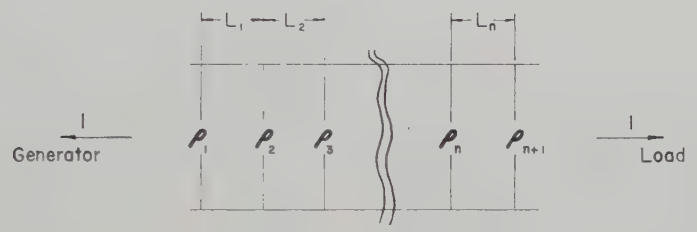


| | | |
|---|---|---|
| Quarter-Wave-Coupled Filter | $\rho_1 = t \cdot \dfrac{2 \sin \dfrac{\pi}{2n}}{\gamma} - k$<br>$\rho_2 = t \cdot \dfrac{2 \sin \dfrac{3\pi}{2n} \cdot \gamma}{\gamma^2 + \sin^2 \dfrac{\pi}{n}} - 2k$<br>$\vdots$<br>$= t \cdot \dfrac{2 \sin \dfrac{(2i-1)\pi}{2n} \cdot \left(\gamma^2 + \sin^2 \dfrac{\pi}{n}\right) \cdots}{\gamma \cdot \left(\gamma^2 + \sin^2 \dfrac{2\pi}{n}\right) \cdots} - 2k$<br>$\vdots$<br>$\rho_n = \rho_1$<br>($n$ odd only) (21) | $\rho_1 = t \cdot 2 \sin \dfrac{\pi}{2n} - k$<br>$\rho_2 = t \cdot 2 \sin \dfrac{3\pi}{2n} - 2k$<br>$\vdots$<br>$\rho_i = t \cdot 2 \sin \dfrac{(2i-1)\pi}{2n} - 2k$<br>$\vdots$<br>$\rho_n = \rho_1$ (22) |

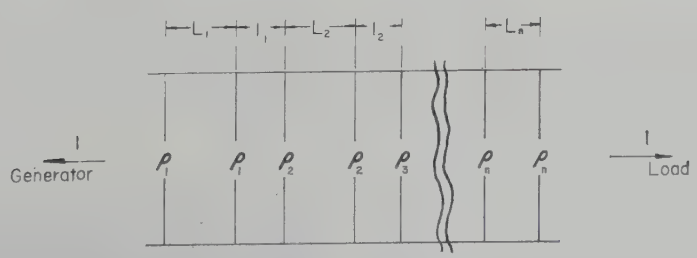


TABLE I *Cont'd next page*

TABLE I (*Cont'd*)

| | Defining Equations | |
|---|---|---|
| | $P_L = 1 + [hT_n(\omega)]^2$ <br> $\gamma = \sinh \frac{1}{n} \sinh^{-1} \frac{1}{h}$ (23) | $P_L = 1 + \omega^{2n}$ |
| | $t = \omega_0 \csc \frac{\pi(\lambda_{g_1} - \lambda_{g_2})}{\lambda_{g_1} + \lambda_{g_2}}$ (24) | |

TABLE II
LINE LENGTH FORMULAS

$$L_i = \frac{\lambda_{g_1} \cdot \lambda_{g_2}}{\lambda_{g_1} + \lambda_{g_2}} - \left(\frac{\phi_i}{2} + \frac{\phi_{i+\epsilon}}{2}\right) - T_i - T_{i+\epsilon}$$
$$\doteq \frac{\lambda_{g_1} + \lambda_{g_2}}{4} - \left(\frac{\phi_i}{2} + \frac{\phi_{i+\epsilon}}{2}\right) - T_i - T_{i+\epsilon}. \quad (25)$$
$$l_i = k \cdot \frac{\lambda_{g_1} \cdot \lambda_{g_2}}{\lambda_{g_1} + \lambda_{g_2}} - \left(\frac{\phi_i}{2} + \frac{\phi_{i+1}}{2}\right) - T_i - T_{i+1}.$$

DEFINING EQUATION

$$\rho_i = \cot^2 \frac{\phi_i}{2}. \quad (26)$$

able power by the power into the load. The number of resonant sections is $n$. The pass-band, insertion-loss tolerance is given by $h$ and is related to the maximum, pass-band VSWR, $\rho_{\max}$, by

$$h = (\rho_{\max} - 1)/(2\sqrt{\rho_{\max}}).$$

In the expression for $t$, $\lambda_{g_1}$ and $\lambda_{g_2}$ are the guide wavelengths at which the skirt insertion loss is specified and $\omega_0$ is the corresponding value of $\omega$ determined from $P_L$. $k = \frac{1}{2}$ (quarter-wave coupling), and 3/2 (three-quarter wave coupling), etc. $\omega$ is equal to $t \cdot \sin(\pi\lambda_{g_0}/\lambda_g)$, where $\lambda_{g_0}$ is the mean guide wavelength given by $2\lambda_{g_1} \cdot \lambda_{g_2}/(\lambda_{g_1} + \lambda_{g_2}) \doteq (\lambda_{g_1} + \lambda_{g_2})/2$.

## DEFINITIONS FOR TABLE II

$\epsilon$ is unity for direct-coupled filters and zero for quarter-wave-coupled filters. $T_i$ is the end effect error associated with the $i$th reflecting element. $\phi$ is positive for series capacities and shunt inductances, and negative for series inductances and shunt capacities.

## COMPARISON WITH PREVIOUS RESULTS

*Lawson and Fano*[1]

Neglecting $X_S$ and $X_L$, comparison of their (146) with (11) of this paper indicates that $\rho_i = X_i^{-2}$. We note that (8) can be written, with a suitable frequency transformation

$$\rho_1 = tC_1,\ \rho_2 = t^2 C_1 L_2,\ \rho_3 = t^2 L_2 C_3,\ \cdots,\ \rho_{n+1} = t \cdot (C_n \text{ or } L_n). \quad (27)$$

Since our $t$ is defined to be the reciprocal value of $\sin\theta$ at the band edges, and $p$ is equivalent to $Z$ in their (145), we have $t = 1/Lw$. Hence their (156) to (159) are seen to be equivalent to (26), except for the subscript on $L$ which should be a superscript. Consequently (19) and (20) are essentially special cases of general formulas given in their paper.

Eqs. (160) to (163)[1] can also be obtained. According to Lawson and Fano, $w$ is the frequency bandwidth for unity value of $\omega'$ so that our value of $\omega_0 = 1$. Thus by (24),

$$t = \csc \frac{\pi(\lambda_{g_1} - \lambda_{g_2})}{\lambda_{g_1} + \lambda_{g_2}} \doteq \frac{\lambda_{g_1} + \lambda_{g_2}}{\pi(\lambda_{g_1} - \lambda_{g_2})} \doteq \frac{2\lambda_{g_0}}{\pi\Delta\lambda_g}, \quad (28)$$

where $\Delta\lambda_g = \lambda_{g_1} - \lambda_{g_2}$ and $\lambda_{g_0}$ is the mean guide wavelength. Now

$$\Delta\lambda_g \doteq \frac{\lambda_{g_0}^3}{\lambda_0^3} \Delta\lambda \doteq \frac{\lambda_{g_0}^3 w}{\lambda_0^2 \omega_0}$$

so that

$$t \doteq \frac{2\lambda_0^2 \omega_0}{\lambda_{g_0}^2 \cdot w}, \quad (29)$$

and finally since $(\lambda_0/\lambda_{g_0})^2 = 1 - (\omega_c/\omega_0)^2$ we have

$$t \doteq \frac{2}{\pi} \frac{\omega_0}{w} \left\{1 - \left(\frac{\omega_c}{\omega_0}\right)^2\right\}. \quad (30)$$

Since

$$|b_i| = \rho_i^{1/2} - \rho_i^{-1/2} \doteq \rho_i^{1/2}, \quad (31)$$

we obtain their (160) except that $\omega$ should be $w$. In their (161) and (162), $C_1$ should be taken outside of the radical sign.

*Southworth*[2]

If we put $C_1 = f_1 = 2 \sin \pi/2n$ in (160) of Lawson and Fano,[1] we immediately obtain (9.2-7) of Southworth. His (9.2-8) is immediately obtained from (20), if we use the above approximation for $t$, put $|\overline{B}_m| = \sqrt{\rho_m}$ and replace the product of sines by the difference in cosines.

*Mumford*[3]

It is clear from (A10) of Mumford[3] and (27) of this paper that in the narrow-band limit, $Q_t$ is approximately equal to $\pi t/2$ when $\omega_0$ is chosen to be unity. Now the $f_i$'s that occur in (6) when multiplied by $\pi/4$

are precisely the $Q_i$'s in his (15) in the small angle limit. Thus (22) can be written:

$$Q_1 = \pi/4\rho_1 = \frac{\pi}{4}\cdot\left\{\frac{4}{\pi}Q_t \sin\frac{\pi}{2n} - k\pi\ 4\right\}$$

$$Q_i = \pi/4\rho_i = \frac{\pi}{4}\cdot\left\{\frac{4}{\pi}Q_t \sin\frac{(2i-1)\pi}{2n} - \frac{k\pi}{2}\right\}$$

$$\vdots$$

$$Q_n = Q_1.$$

These are precisely Mumford's results when the selectivities of the coupling lines are included.

If assumption 1 is satisfied by the reflecting elements, then the above remarks concerning Mumford's paper are true. This condition, though sufficient for a synthesis of quarter-wave-coupled filters, in terms of a ladder network prototype is not necessary. As explained in Appendix I, it is possible to define the $Q$ of a cavity terminated in more general reflecting elements. For such cases, the characteristics of the reflecting elements can be determined from the required $Q$'s by means of formulas derived for each case. For the cases of usual interest, three such formulas have been given in Riblet and Reed.[13] There it was pointed out by Reed that the formula relating to the case of constant susceptance is equivalent to Mumford's. It is also indicated that the formula for the inductive case is equivalent to that given by Reed.[14]

Eq. (22) gives the value of $\rho_i$ directly since it can be shown for the inductive case, that the error in approximating $Q_i$ by $\pi/4\rho_i$ is of the order of $\phi_0^3/5$.

*Cohn*[4]

The value of $L$ in Fig. 5 of Cohn[4] is the same as the $t^{-1}$ used in this paper except for a typographical ambiguity and the use of the small angle approximation. The values of $X_{i,i+1}$, except possibly for sign, follow from

$$|X_{i,i+1}| = |b_i|^{-1} = \frac{(\rho_i)^{-1/2}}{1-(\rho_i)^{-1}}.$$

For completeness, the frequency transformation due to Cohn[4] is derived at this point. In the limit of large susceptances, $\rho_i = b_i^2$. From (13), we see that a frequency variation common to the inversion factors can be included in the frequency variable. Now, if $\rho_i = \bar{\rho}_i f^2(p)$ with $\bar{\rho}_i$ constant, the theory is applicable when we replace $p$ by $f(p)\cdot p$ except for a relatively small error in the end elements. For inductances which vary directly as $\lambda_g$ (this is approximated by waveguide irises), $f(p) = \lambda_g/\lambda_{g0}$, where $\lambda_{g0}$ is the midband guide wavelength. Then

$$p = j\lambda_g/\lambda_{g0}\sin(\pi\lambda_{g0}/\lambda_g). \tag{32}$$

Using the small angle approximation for $\sin\theta$, we have

$$p \doteq j\pi(\lambda_g/\lambda_{g0} - 1),$$

with $\lambda_{g0} = (\lambda_{g1}+\lambda_{g2})/2$, where $\lambda_{g1}$ and $\lambda_{g2}$ are the guide wavelengths at the band edges.

This frequency variable has, as Cohn has pointed out, the important property that the response curve of the filter is symmetrical in $\lambda_g$ rather than in $1/\lambda_g$. Curiously, (24) for $t$ is not altered by this transformation, a statement which is not true for capacitive irises. The principal effect of this transformation on the design procedure is to alter the midband guide wavelength which enters into the determination of $L$ and $l$ in (25). For bandwidths as great as 10 per cent, and difference between the two formulas for $L$, due to this transformation, is generally less than the error due to the neglect of $T_i$, and so we have given the formula for the mean guide wavelength which is a rigorous consequence of (1) and (2). The approximate formula is simpler for computation and is to be recommended accordingly for design purposes whenever inductive irises are used.

*Riblet*[5]

Riblet[5] is concerned with a first order equivalence between direct-coupled filters and quarter-wave-coupled filters in contrast to the zero order equivalence established in (14)–(17). Its interest lies in the fact that a synthesis in terms of quarter-wave-coupled cavities requires less restrictive assumptions on the nature of the reflecting elements (see Appendix I) than is required for a direct-coupled filter synthesis, based on a ladder network prototype. Accordingly, the procedure is capable of a high degree of accuracy and generality when used with the recommended frequency transformation.

## Comments on Assumption 1

The applicability of this assumption to practical waveguide reflecting elements must be justified by consideration of their properties or by the construction of experimental filters. Admittance transformations for shunt susceptances have been given[13] which are constant and which vary inversely and directly with $\lambda_g$. These are correct to the first order in a frequency variable, $\Omega$, where $\Omega \doteq jp/\pi$. Written in the form of (1), these become

$$\begin{bmatrix} \dfrac{k_2\Omega}{\sin\phi_0} & j\sqrt{\dfrac{1+\cos\phi_0}{1-\cos\phi_0}}\left(1-\dfrac{k_1\Omega}{\sin\phi_0}\right) \\ j\sqrt{\dfrac{1-\cos\phi_0}{1+\cos\phi_0}}\cdot\left(1+\dfrac{k_1\Omega}{\sin\phi_0}\right) & \dfrac{k_2\Omega}{\sin\phi_0} \end{bmatrix}, \tag{33}$$

where

$$k_1 = \pm\sin^2\phi_0\cos\phi_0$$

$$k_2 = \phi_0 \pm \sin\phi_0\cdot\cos\phi_0,$$

[13] J. Reed and H. J. Riblet, "Discussion on synthesis of narrow-band direct-coupled filters," Proc. IRE, vol. 41, pp. 1058–1059; August, 1953. See (4).

[14] J. Reed, "Low $Q$ microwave filters," Proc. IRE, vol. 38, pp. 793–796; July, 1950. See p. 794.

and the upper signs are used with inductances, the lower signs are used with capacities, and they are replaced by zero for constant susceptances. Of course $\phi_0$ is the value of $\phi$, previously defined, when $\Omega=0$. For inductances, the terms on the principal diagonal tend to zero with increasing susceptance. Accordingly the theory is particularly applicable to this case, as Cohn[4] has pointed out.

### Comments on Assumption 2

The principal justification is the following theorem:

The matrix product,

$$\cos^n\theta \begin{pmatrix} 0 & c_1\sqrt{t} \\ \dfrac{1}{c_1\sqrt{t}} & 0 \end{pmatrix} \begin{pmatrix} 1 & \bar{p} \\ p & 1 \end{pmatrix} \begin{pmatrix} 0 & c_2 t \\ \dfrac{1}{c_2 t} & 0 \end{pmatrix} \begin{pmatrix} 1 & \bar{p} \\ p & 1 \end{pmatrix} \cdots \begin{pmatrix} 0 & c_n t \\ \dfrac{1}{c_n t} & 0 \end{pmatrix} \begin{pmatrix} 1 & \bar{p} \\ p & 1 \end{pmatrix} \begin{pmatrix} 0 & c_{n+1}\sqrt{t} \\ \dfrac{1}{c_{n+1}\sqrt{t}} & 0 \end{pmatrix}, \tag{34}$$

has the form

$$\cos^n\theta \begin{pmatrix} D(pt, \bar{p}/t) & C(pt, \bar{p}/t) \\ B(pt, \bar{p}/t) & A(pt, \bar{p}/t) \end{pmatrix}, \tag{35}$$

where $A$, $B$, $C$, and $D$ are polynomials in $pt$ and $\bar{p}/t$, and the only $n$th degree terms are $(pt)^n$ and $(\bar{p}/t)^n$. That is, terms of the form $p^k\bar{p}^{n-k}$ do not occur.

When $\bar{p}=p=j\tan\theta$, the matrix product of the theorem represents the exact admittance transformation of a cascade of admittance inverters, equally spaced on a uniform transmission line, whose dependence on $t$ is consistent with the form obtained in (13) from a ladder network prototype. Moreover the determinant of (35) is unchanged by replacing $\bar{p}$ by zero, and cos $\theta$ by one.

Comparison of the input impedance and insertion loss function obtained from this matrix product, with the corresponding functions obtained with $\bar{p}$ put equal to zero, will indicate the error in the approximate solution. Now the coefficient of every power of $p$ in $A$, $B$, $C$, and $D$ will contain terms contributed by $p$ and by $\bar{p}$ since $\bar{p}$ must be replaced by $p$ in an exact calculation. Although the $n$th degree term contains only $p^n$ and $\bar{p}^n$, in general, terms of the form $p^r\bar{p}^s$ appear. Now the theorem states that in each coefficient, the contribution of $p^r$ is of the order of $t^r$ while the corresponding contribution of $\bar{p}^r$ is of the order of $t^{-r}$. In general then, the error in neglecting $\bar{p}$ terms is of the order of $1/t^2$, and for the coefficient of $p^n$, the error is of the order of $1/t^{2n}$. The limit for large $t$, with $tp$ fixed, can be attained then by putting $\bar{p}=0$ and cos $\theta=1$.

Since the determinant of (34) is unity, the insertion loss function is given, in the limit, by

$$1/4\cos^{2n}(\theta)\,\big|\,A(pt)+B(pt)+C(pt)+D(pt)\,\big|^2. \tag{36}$$

This is an even polynomial in tan $\theta$ of the form,

$$a_{2n}t^{2n}\tan^{2n}\theta + a_{2n-2}t^{n-2}\tan^{2n-2}\theta + \cdots.$$

Multiplication by $\cos^{2n}(\theta)$ gives the expression,

$$a_{2n}t^{2n}\sin^{2n}\theta + a_{2n-2}t^{2n-2}\sin^{2n-2}(\theta)\cos^2(\theta) + \cdots.$$

Now the resulting terms in $\cos^2\theta$ can be replaced by $\sin^2\theta$ but the error in replacing $\cos^2\theta$ by 1 is always of the order of $1/t^2$. Thus in the exact admittance transformation (24) approaches, as $t\to\infty$, the limit obtained from it by replacing $\bar{p}$ by zero and $p$ by $j\sin\theta$. Assumption 2 is thus rigorously justified.

It may be of interest to observe that assumption 2 is not essential for a synthesis based on a prescribed insertion loss function. The exact transmission line synthesis procedure for filters consisting only of equal length impedance transformers mentioned by Riblet[15] and discussed in detail by Seidel[16] is immediately applicable so long as assumption 1 is valid. Seidel has arrived at the same conclusion and has applied this theory to the design of direct-coupled filters. He is concerned, however, with transmission line elements which are nominally a quarter wavelength long so that his results do not appear to be directly applicable to the narrow band problem. This paper is the direct consequence of early efforts to carry through the exact synthesis of a narrow band filter on the basis of the exact procedure. When it was discovered that the $p$ roots[15] had to be calculated with extreme accuracy, in order to satisfy (2) for physical realizability, the present analysis of the approximate solution was forced on the writer.

### Conclusions

Formulas previously given[1,2,4] are rederived on the basis of two approximations which are shown, under general conditions, to be necessary and sufficient for a general synthesis of direct-coupled filters having the frequency behavior associated with ladder network prototypes. Differences in the formulas, not to due to typographical errors, are traced primarily to an approximation used to express the susceptance of a reflecting element in terms of its VSWR, and secondarily to small angle approximations and the use of differentials in place of differences. Formulas[3] for the design of quarter-wave-coupled filters are rederived on the basis of an exact equivalence which is given for a direct-coupled filter and a "Mumford" quarter-wave-coupled filter.

The usefulness of the formulas is extended by showing how the VSWR's of the reflecting elements are altered when the interconnecting lines are lengthened in multiples of half of a guide wavelength. It is shown how other approximate solutions[1,2,4] are a rigorous limit of an exact solution and that the error in each coefficient of the insertion loss function, made by replacing each half

[15] H. J. Riblet, "General synthesis of quarter-wave impedance transformers," IRE Trans. on Microwave Theory and Techniques, vol. MTT-5, pp. 36–43; January, 1957. See p. 38.

[16] H. Seidel, "Synthesis of a class of microwave filters," IRE Trans. on Microwave Theory and Techniques, vol. MTT-5, pp. 107–114; April, 1957.

wavelength of transmission line by a series resonant element, is of the order of one half the square of the percentage bandwidth measured in guide wavelengths.

## Appendix I

We are concerned here with the conditions satisfied by general reflecting elements if it is required that they are to be used in a general synthesis of direct-coupled filters[17] based on a ladder network prototype. The proofs assume that the primary frequency sensitive elements of the direct-coupled filters consist of *equal* lengths of transmission line which separate them or, as we shall see, series resonant elements which approximate transmission lines in their frequency behavior. Although the assumption of equal line lengths may not be a physical necessity, it is difficult to imagine any general synthesis theory based on a ladder network prototype which does not require this simplifying assumption.

Consider the admittance transformation, $(R)$, ($D$, $C$, $B$, $A$ matrix), of a symmetric, nonresonant, reflecting element, written,

$$(R) = \begin{pmatrix} a_1\theta + a_2\theta^2 + a_3\theta^3 + \cdots & j(c_0 + c_1\theta + c_2\theta^2 + c_3\theta^3 + \cdots) \\ j(b_0 + b_1\theta + b_2\theta^2 + b_3\theta^3 + \cdots) & a_1\theta + a_2\theta^2 + a_3\theta^3 + \cdots \end{pmatrix}$$

$$(R) = \begin{pmatrix} A(\theta) & C(\theta) \\ B(\theta) & A(\theta) \end{pmatrix},$$

where $A$, $B$, $C$ satisfy the following conditions:

1) $A$, $B$, and $C$ are analytic functions of the complex variable $\theta$ in the vicinity of $\theta = 0$.
2) $A^2 - BC = 1$

It should be observed that the implied assumption has been made that resonance, $\omega = 0$, occurs when the connecting lines are all one half-wavelength long. This assumption is no restriction, since identical line lengths can be added to or subtracted from each $(R_i)$ without changing the conditions of the theorem or essentially altering the input admittance function of the cascade. Moreover, it is the assumption previously made.[1,2,4,5]

*Proof*

We require that for arbitrary $(R)$ satisfying conditions 1 and 2 that

$$(R)(T)(R) = \begin{pmatrix} 1 & 4Q\omega \\ 0 & 1 \end{pmatrix},$$

since the right-hand matrix represents the ladder network element consisting of a single resonant element of given $Q$. This requirement is certainly satisfied by the reflecting elements mentioned previously.[1-5]

If

$$(T) = \begin{pmatrix} -(1 - \theta^2/2 \cdots) & -j(\theta - \theta^3/6 \cdots) \\ -j(\theta - \theta^3/6 \cdots) & -(1 - \theta^2/2 \cdots) \end{pmatrix}$$

and put $\omega = \theta - \omega_3\theta^3$, the following conditions on the coefficients of $(R)$ are found.

$$\begin{array}{lll} a_1 = \phi/2 & b_0 = \phi & c_0 = 1/\phi \\ a_2 = 0 & b_1 = 0 & c_1 = 0 \\ a_3 = -\phi^3/48 + (\phi - \phi^3)\omega_3 & b_2 = -\phi^3/24 - \phi/12 + 2(\phi - \phi^3)\omega_3 & c_2 = -\dfrac{5\phi}{24} + \dfrac{1}{12\phi} - 2\left(\dfrac{1}{\phi} - \phi\right)\omega_3, \end{array} \quad (37)$$

If we denote by $(T)$, the admittance transformation of a uniform transmission line so that

$$(T) = \begin{pmatrix} \cos(\theta + \pi) & j\sin(\theta + \pi) \\ j\sin(\theta + \pi) & \cos(\theta + \pi) \end{pmatrix},$$

then we may prove the following theorem.

*Theorem A*

If $\omega$ is a frequency variable assumed to be an odd function of $\theta$ then matrix products of the form,

$$(R_1)(T)(R_2)(T)\cdots(T)(R_{n+1}),$$

cannot yield a general representation of the input impedance functions in $\omega$ of ladder network prototypes.

where $\phi$ is determined by

$$4Q = 1/\phi^2 - 1.$$

It is interesting that for a suitable choice of the frequency behavior of the reflecting elements, a shunt resonant element can be exactly obtained with a half wavelength of transmission line. It should be recalled, of course, that the $Q$ previously used[3,5,14] is only approximate and assumes that the resonant element is terminated in a match.

The theorem follows, however, when an attempt is made to combine three reflecting elements satisfying (37). In this case, it is readily shown that a product of the form $(R_1)(T)(R_2)(T)(R_3)$ will be, in general, of second degree in $\omega$ in both the numerator and the denominator of the input admittance function. This, of course, makes it impossible to represent the general two-element ladder network in the required form.

[17] This term is defined by Fig. 2 and has also been previously illustrated.[1,2,4,5]

We may now replace $(T)$ by

$$(T) = \begin{pmatrix} -1 & 0 \\ j \sin(\theta + \pi) & -1 \end{pmatrix},$$

which is an approximation justified in Appendix II and prove the following theorem.

*Theorem B*

If $\omega$, the frequency variable, vanishes for $\theta = 0$ (half wavelength spacing) and $\sin\theta$ is an analytic function of $\omega$, then matrix products of the form,

$$(R_1)(\tilde{T})(R_2)(\tilde{T}) \cdots (\tilde{T})(R_{n+1}),$$

can define the general input admittance function of all ladder network prototypes only if

$$(R_i) = \begin{pmatrix} 0 & j\sqrt{\rho_i} \\ \dfrac{j}{\sqrt{\rho_i}} & 0 \end{pmatrix},$$

where $\rho_i$ is a positive real constant.

*Proof*

We consider consequences of the assumption that

$$\begin{pmatrix} A & C \\ B & A \end{pmatrix}\begin{pmatrix} -1 & 0 \\ -j\sin\theta & -1 \end{pmatrix}\begin{pmatrix} A & C \\ B & A \end{pmatrix} = \begin{pmatrix} 1 & jf\omega \\ 0 & 0 \end{pmatrix},$$

where $f$ is a constant. If we put $\omega = 0$, it is readily shown that $A(0) = 0$, while $B(0) \cdot C(0) = -1$. Moreover, since

$$\begin{pmatrix} c_1 p\sqrt{t} & c_1\sqrt{t} \\ \dfrac{1}{c_1\sqrt{t}} & \dfrac{\bar{p}}{c_1\sqrt{t}} \end{pmatrix}\begin{pmatrix} D(pt, \bar{p}/t) & tC(pt, \bar{p}/t) \\ 1/tB\ pt, \bar{p}/t) & A(pt, p/t) \end{pmatrix}\begin{pmatrix} 0 & c_{n+1}\sqrt{t} \\ \dfrac{1}{c_{n+1}\sqrt{t}} & 0 \end{pmatrix}. \tag{39}$$

$2AB + jA^2 \sin\theta \equiv 0$, from the lower left-hand element of the product, we conclude that $A \equiv 0$ or $jA\sin\theta = -2B$. The latter case is excluded by the fact that $B(0) \neq 0$. From the upper left-hand element of the product, we conclude that $CB \equiv -1$ and from the upper right-hand element that $-C^2 \sin\theta = f\omega$. Therefore, the permitted form for $(R_i)$ is

$$(R_i) = \begin{pmatrix} 0 & j\sqrt{\dfrac{f\omega}{\sin\theta}} \\ \sqrt{\dfrac{\sin\theta}{f\omega}} & 0 \end{pmatrix},$$

showing that some frequency variations in $(R_i)$ is permitted. However, if one considers a cascade containing three of these reflecting elements, then the condition $\omega = \sin\theta$ can be shown to be necessary in order that the frequency behavior of two element ladder network prototypes be representable in the given frequency variable, $\omega$.

## Appendix II

The proof of the theorem underlying assumption 2 follows by mathematical induction.

Consider

$$\begin{pmatrix} 0 & c_n t \\ \dfrac{1}{c_n t} & 0 \end{pmatrix}\begin{pmatrix} 1 & \bar{p} \\ p & 1 \end{pmatrix} = \begin{pmatrix} c_n pt & c_n t \\ \dfrac{1}{c_n t} & 1/c_n\bar{p}/t \end{pmatrix}. \tag{38}$$

It has the general form,

$$\begin{pmatrix} D(pt, \bar{p}/t) & tC(pt, \bar{p}/t) \\ \dfrac{1}{t} B(pt, \bar{p}/t) & A(pt, \bar{p}/t) \end{pmatrix}, \tag{39}$$

in which the highest power of $p$ occurs in $D$, and the highest power of $\bar{p}$ occurs in $A$. Furthermore the form of (39) is not changed by multiplication by matrices of the form of (38), while the highest power of $p$ still occurs in $D$ and the highest power of $\bar{p}$ occurs in $A$. Thus the original product (34) can be written

When this multiplication is carried through, one obtains

$$\begin{pmatrix} \dfrac{c_1}{c_{n+1}}(ptC + A) & c_1 c_{n+1}(ptD + B) \\ \dfrac{1}{c_1 c_{n+1}}(C + \bar{p}/tA) & \dfrac{c_{n+1}}{c_1}(D + \bar{p}/tB) \end{pmatrix}.$$

This is the result claimed in the theorem. The $C$ term in this matrix contains $(pt)^n$ and the $B$ term contains $(\bar{p}/t)^n$. No cross product terms having a total degree of $n$ can occur.

# An Analysis of a Broad-Band Coaxial Hybrid Ring*

V. J. ALBANESE† AND W. P. PEYSER‡

*Summary*—This paper describes a broad-band coaxial hybrid ring which has excellent isolation and balance characteristics. The ring differs from the conventional hybrid in that the fourth arm has a series-type balun feed and is positioned so that a plane of symmetry exists through two of the arms. Isolation between these arms and balance between the output arms are theoretically independent of frequency. The admittance and VSWR of the input arms are computed by bisecting the ring about the plane of symmetry and employing standard Smith Chart techniques. Corresponding experimental data are included. A comparison is made with the conventional coaxial hybrid ring.

## Coaxial Hybrid Symmetric About Arms 1 and 4

THE symmetric coaxial hybrid ring (Fig. 1) was first presented schematically by Tyrell as one of the six fundamental forms.[1] It differs from the conventional hybrid (Fig. 2) in the positioning and type of feed at arm 4. In the conventional coaxial hybrid all arms are shunt fed. If arm 4 is moved a quarter wavelength at the design frequency and changed from a shunt to a series feed, the hybrid action will be maintained, although arm 4 no longer will be matched to the same $Y_0$. The series feed is achieved by an unbalanced-to-balanced-line transformer (*i.e.*, a balun).

A practical broad-band hybrid, shown in Fig. 3, has been designed for $S$ band. It performs satisfactorily in a number of applications over a $\pm 25$ per cent bandwidth centered about 3000 mc. It should be noted that this design is symmetrical about axis $A$–$A'$ (Fig. 4), so that power from arms 1 or 4 will divide evenly between arms 2 and 3. It also can be seen that any power from arm 1 will arrive at the balanced-line inputs to arm 4 in phase; hence, there is isolation between arms 1 and 4. The half-wavelength sections between arms 2 or 3 and arm 4 are each divided into two quarter-wave sections having admittances $Y_0$ and $Y_1$, so that arm 4 may remain matched to $Y_0$. In moving arm 4 a quarter wavelength, it would become matched to $Y_0/Y_1^2$ if the characteristic admittance of this section of the ring were not altered.

These effects now are shown mathematically. The equivalent circuit of the hybrid is shown in Fig. 5. The admittances of the $\pi$ equivalents for the transmission line sections are shown in generalized form and include the admittance of the balun to ground. This admittance is zero at the center frequency. Arm 4 is treated by introducing two nodes, 4 and 5, since it is a series feed. Power fed into arm 1 is represented by a current $I_N$ fed to node 1. Power fed to arm 4, however, is represented schematically by a current $I_N$ into node 4 and out of node 5, to account for the balanced push-pull feed. Assuming power is fed only to arm 1, a fifth-order system of equations is obtained:

$$\begin{bmatrix} I_N \\ 0 \\ 0 \\ 0 \\ 0 \end{bmatrix} = \begin{bmatrix} Y_{11} & Y_{12} & Y_{13} & Y_{14} & Y_{15} \\ Y_{21} & Y_{22} & Y_{23} & Y_{24} & Y_{25} \\ Y_{31} & Y_{32} & Y_{33} & Y_{34} & Y_{35} \\ Y_{41} & Y_{42} & Y_{43} & Y_{44} & Y_{45} \\ Y_{51} & Y_{52} & Y_{53} & Y_{54} & Y_{55} \end{bmatrix} \times \begin{bmatrix} V_1 \\ V_2 \\ V_3 \\ V_4 \\ V_5 \end{bmatrix}.$$

Now the following quantities can be defined:

$$Y_A = Y_{11} \qquad Y_E = Y_{35} = Y_{24} = Y_{53} = Y_{42}$$

$$Y_B = Y_{22} = Y_{33} \qquad Y_F = Y_{45} = Y_{54}$$

$$Y_C = Y_{44} = Y_{55} \qquad 0 = Y_{15} = Y_{14} = Y_{25} = Y_{34} = Y_{23}$$

$$Y_D = Y_{12} = Y_{13} = Y_{21} = Y_{31} \qquad = Y_{51} = Y_{41} = Y_{52} = Y_{43} = Y_{32}$$

(independent of frequency)

Rewriting our system of equations,

$$\begin{bmatrix} I_N \\ 0 \\ 0 \\ 0 \\ 0 \end{bmatrix} = \begin{bmatrix} Y_A & Y_D & Y_D & 0 & 0 \\ Y_D & Y_B & 0 & Y_E & 0 \\ Y_D & 0 & Y_B & 0 & Y_E \\ 0 & Y_E & 0 & Y_C & Y_F \\ 0 & 0 & Y_E & Y_F & Y_C \end{bmatrix} \times \begin{bmatrix} V_1 \\ V_2 \\ V_3 \\ V_4 \\ V_5 \end{bmatrix}. \quad (1)$$

Expanding and solving in general form,

$$V_4 = V_5 = \frac{-I_N}{D} Y_D Y_E [Y_E^2 + Y_B(Y_F - Y_C)]. \quad (2)$$

Since $V_4$ and $V_5$ are identical voltages, it can be seen that no potential difference is developed across nodes 4 and 5; hence, no power can be dissipated in arm 4. The isolation between arms 1 and 4 therefore is infinite and, since the solution is in generalized terms, independent of frequency. Solving for $V_2$ and $V_3$,

$$V_2 = V_3 = \frac{I_N Y_D}{D} [Y_F + Y_C][Y_E^2 - Y_B(Y_C - Y_F)]. \quad (3)$$

$V_2$ and $V_3$ then are equal. Arms 2 and 3, therefore, receive equal power at all frequencies. If $V_1$, $V_2$, and $V_3$ are specifically solved for at the center frequency, the solutions take on indeterminate forms because of the half wavelength sections of line. When evaluated, the re-

* Manuscript received by the PGMTT, December 9, 1957; revised manuscript received, May 1, 1958.

† Bogart Manufacturing Corp., Brooklyn, N. Y.

‡ Airborne Instruments Lab., Mineola, N. Y. Formerly with Bogart Manufacturing Corp., Brooklyn, N. Y.

[1] W. A. Tyrell, "Hybrid circuits for microwaves," PROC. IRE, vol. 35, pp. 1294–1306; November, 1947.

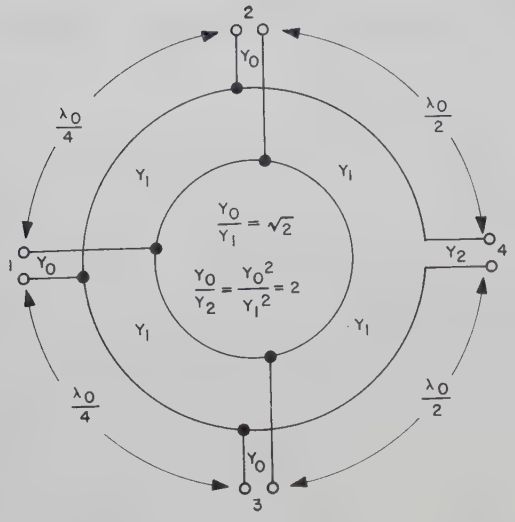


Fig. 1—Schematic representation of symmetric coaxial hybrid ring.

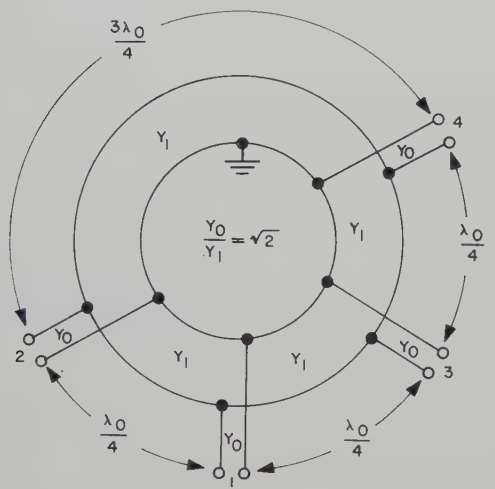


Fig. 2—Schematic representation of conventional 6/4λ hybrid ring.

sults are identical with those for the conventional hybrid,

$$V_1 = -\frac{I_N}{2\sqrt{2}}, \qquad V_2 = V_3 = -j\frac{I_N}{4}. \tag{4}$$

Consider now the hybrid behavior if power is fed to arm 4 instead of to arm 1. The current matrix becomes

$$\begin{bmatrix} 0 \\ 0 \\ 0 \\ I_N \\ -I_N \end{bmatrix}.$$

Although infinite isolation has been proved, it can be shown that, for this case, $V_1 = 0$. $V_2$ and $V_3$ may be solved for

$$V_2 = -V_3 = \frac{I_N Y_E}{D}\left[Y_A Y_E^2 + (Y_C + Y_F)(2Y_D^2 - Y_A Y_B)\right]. \tag{5}$$

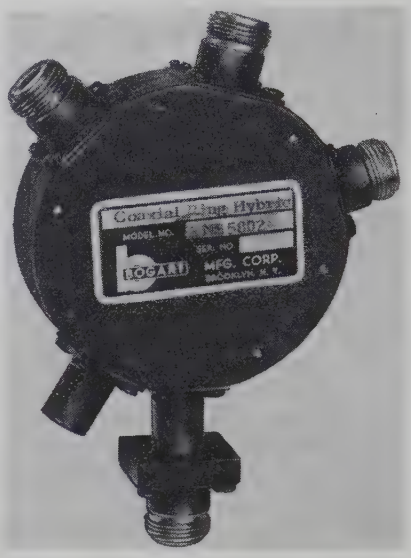


Fig. 3—Symmetric coaxial hybrid ring

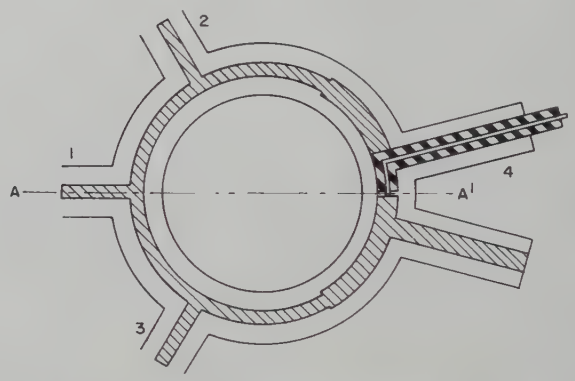


Fig. 4—Cross section of symmetric coaxial hybrid ring.

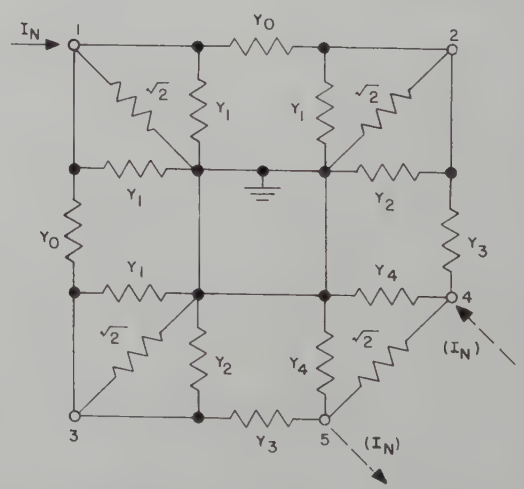


Fig. 5—Equivalent circuit of symmetric coaxial hybrid ring.

For the case of power being fed to arm 4, arms 2 and 3 will receive signals which are equal but out of phase, and again independent of frequency.

It is of interest to determine the isolation between arms 2 and 3. If a current $I_N$ was fed to node 2, for example, $V_2$ and $V_3$ could be solved for, and their

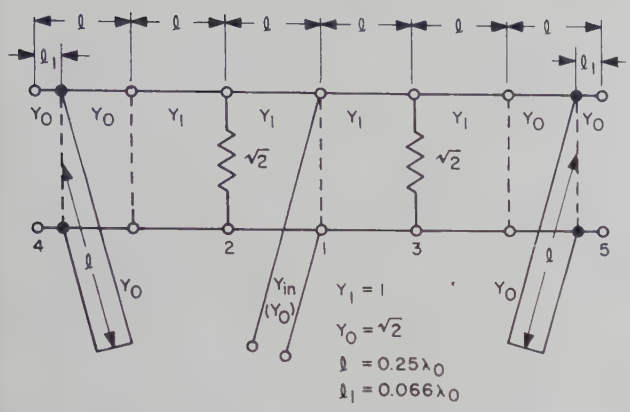


Fig. 6—Equivalent circuit of symmetric coaxial hybrid ring, bisected at arm 1.

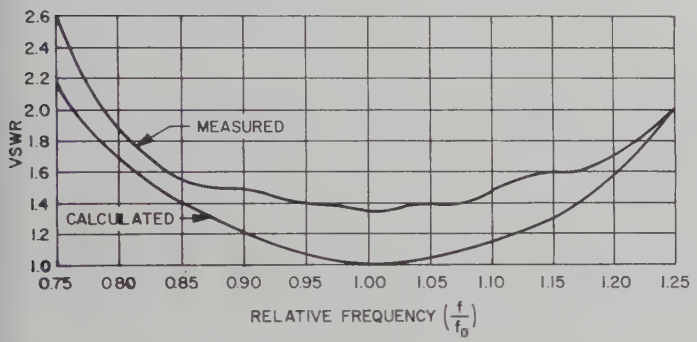


Fig. 7—VSWR vs frequency at arm 1 of symmetric hybrid ring.

ratio evaluated as isolation. At the center frequency, $V_3 = 0$, so that the isolation is infinite. Since there is a lack of symmetry about arms 2 and 3, the isolation is not independent of frequency. At the ends of a $\pm 25$ per cent band, it has been evaluated at approximately 13.5 db.

The VSWR at arms 1 and 4 can be calculated by evaluating $V_1$ and $V_4 - V_5$, respectively, with power fed into these arms. The calculations, however, may be greatly simplified by employing the symmetry conditions. To find input admittance and VSWR at arm 1, bisect the hybrid through axis $A-A'$ (Fig. 4) and unfold it into the form seen in Fig. 6. Admittances looking left and right are identical; it is necessary to compute only the admittance looking in one direction, and then double it to obtain total admittance. The use of a Smith Chart greatly facilitates the calculations. $Y_{in}$ (normalized to $Y_0$) equals unity at the design frequency, $f_0$, assuming all other arms are terminated in $Y_0$. Therefore, VSWR is also unity. VSWR values, computed by this technique, are plotted as a function of fractional bandwidth in Fig. 7.

To find input admittance or VSWR at arm 4, the ring may be bisected again through axis $A-A'$ and unfolded into the form shown in Fig. 8. Using the Smith Chart, the input VSWR values at arm 4 have been computed and are shown in Fig. 9.

The characteristics of the symmetric hybrid have been measured at $S$ band and, for comparison, have

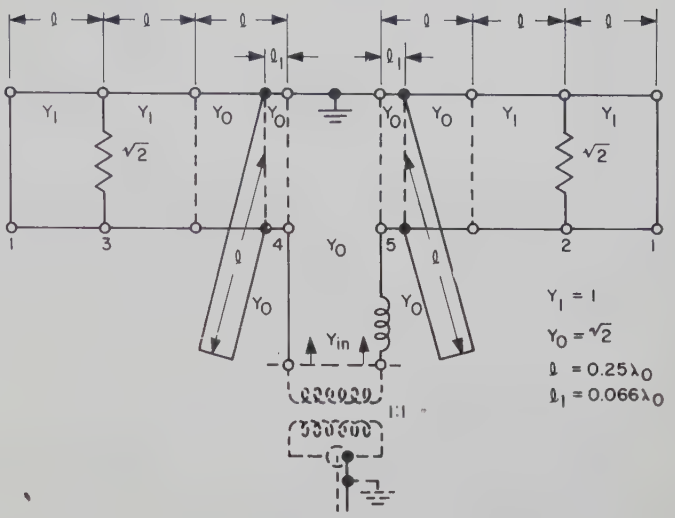


Fig. 8—Equivalent circuit of symmetric coaxial hybrid ring, bisected at arm 4.

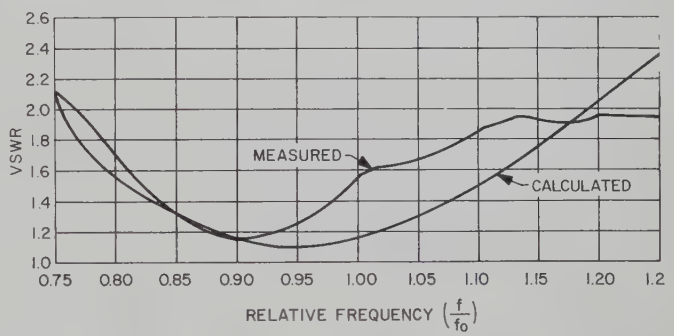


Fig. 9—VSWR vs frequency at arm 4 of symmetric hybrid ring.

been plotted in terms of fractional bandwidth. The results represent average data measured on 15 production units. Input VSWR's at arms 1 and 4 have been plotted on Figs. 7 and 9, respectively. The measured isolations between arms 1 and 4 and between arms 2 and 3 are shown in Figs. 10 and 11, respectively. Minimum measured isolation between arms 1 and 4 was in excess of 38 db. The jagged nature of the curve is caused by the imperfections in the matched loads terminating the output arms during measurement, and also by the residual unbalances in the reflections created in the tee junctions and connectors of these arms. When dealing with isolations of the magnitude measured here, even a very small reflection at one of the output arms has a marked effect on the isolation reading.

The power unbalance at the various arms also has been measured and is shown in Figs. 12 and 13. In no case does the unbalance in output power at arms 2 and 3 exceed 0.1 db, with signal input at either arm 1 or arm 4.

## Additional Considerations

The sections of transmission line between arm 4 and arms 2 and 3 are not absolutely necessary for the electrical operation of the hybrid. If another method, such

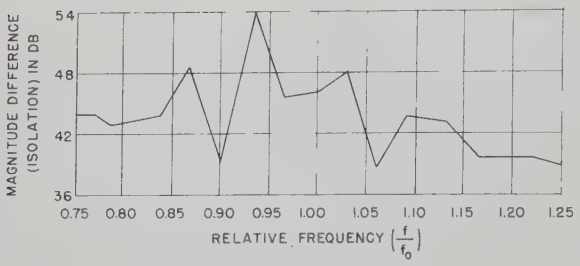


Fig. 10—Measured isolation between arms 1 and 4 of symmetric hybrid ring.

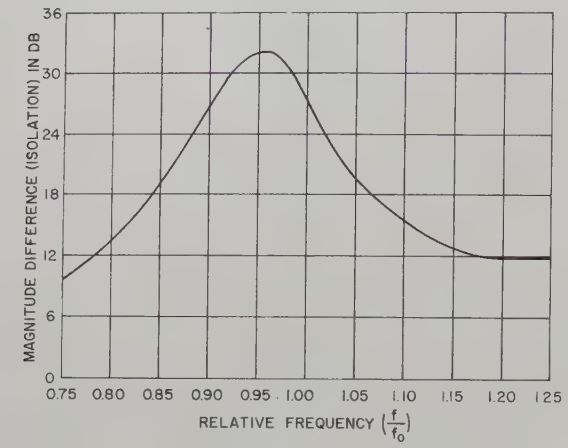


Fig. 11—Measured isolation between arms 2 and 3 of symmetric hybrid ring.

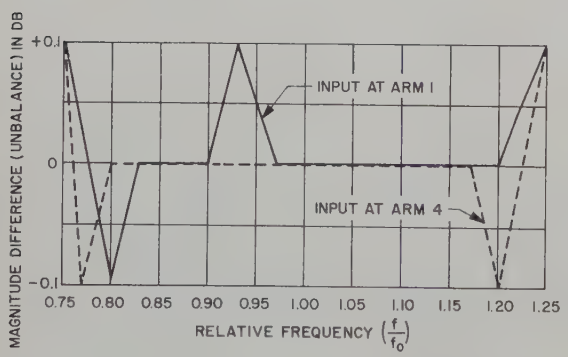


Fig. 12—Measured relative magnitude (unbalance) of output at arms 2 and 3 of symmetric hybrid ring, with signal input at arm 1 and at arm 4.

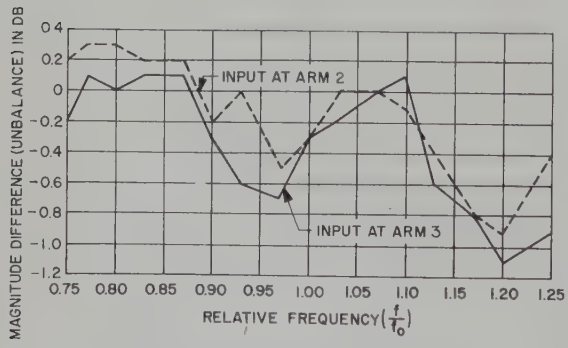


Fig. 13—Measured relative magnitude (unbalance) of output at arms 1 and 4 of symmetric hybrid ring, with signal input at arm 2 and at arm 3.

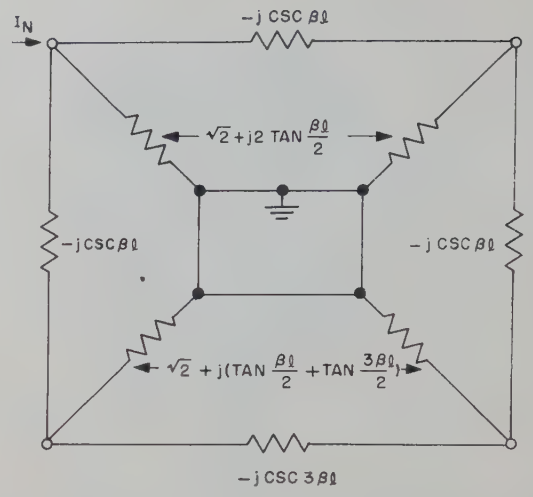


Fig. 14—Equivalent circuit of conventional 6/4λ hybrid ring; admittances normalized to $Y_1$.

as a quarter-wave transformer within the arm itself, is employed for matching arm 4, and the mechanical arrangement of coaxial inputs is altered, these two sections of line may be eliminated. The broad-band performance will be somewhat improved. Such a design is particularly adaptable to the lower frequency bands, but fabrication is extremely difficult at frequencies above *S* band.

## Conventional Coaxial Hybrid Ring

A conventional coaxial hybrid ring (Fig. 2) suffers from several shortcomings in broad-band applications. For example, ifthe hybrid is to be used with a balanced mixer, the isolation between the signal and local oscillator arms (1 and 4, respectively) will fall off sharply as the frequency is varied from design center. The balance between the signals reaching the two output arms (2 and 3) also will deteriorate with frequency change.

The conventional hybrid is shown in Fig. 14 as an equivalent lumped-parameter network. Assuming a constant current $I_N$ applied to node 1, the matrix equation may be written

$$\begin{bmatrix} I_N \\ 0 \\ 0 \\ 0 \end{bmatrix} = \begin{bmatrix} Y_{11} & Y_{12} & Y_{13} & Y_{14} \\ Y_{21} & Y_{22} & Y_{23} & Y_{24} \\ Y_{31} & Y_{32} & Y_{33} & Y_{34} \\ Y_{41} & Y_{42} & Y_{43} & Y_{44} \end{bmatrix} \times \begin{bmatrix} V_1 \\ V_2 \\ V_3 \\ V_4 \end{bmatrix}.$$

The nodal voltages are evaluated at $f_0$ as

$$V_1 = \frac{I_N}{2\sqrt{2}}; \quad V_2 = V_3 = -j\frac{I_N}{4}; \quad V_4 = 0. \qquad (6)$$

If we assume a constant current applied to node 4, the current matrix becomes

$$\begin{bmatrix} 0 \\ 0 \\ 0 \\ I_N \end{bmatrix}.$$

The nodal voltages at $f_0$ are evaluated again.

$$V_2 = -j\frac{I_N}{4}; \quad V_3 = +j\frac{I_N}{4}; \quad V_4 = \frac{I_N}{2\sqrt{2}}; \quad V_1 = 0. \quad (7)$$

The voltages have the same form as in (6) with the exception that $V_2$ and $V_3$ are 180 degrees out of phase. Then, it may be concluded that, at $f_0$, there is infinite isolation between arms 1 and 4, and power is divided equally between arms 2 and 3.

This technique can be used to calculate the behavior of the hybrid over a frequency band. The results have been computed over a large bandwidth and are compared with available measured data in Figs. 15–17.[2] It is seen that isolation and balance deteriorate rapidly when the frequency departs from $f_0$.

## Conclusion

In the case of the symmetric hybrid, correlation between the calculated and experimental data is close. Deviations in VSWR can be attributed to the inherent mismatch of the Type *N* connectors and the tee junctions.

It has been mentioned that even slight residual reflections from the output arms might cause radical changes in the apparent isolation between arms 1 and 4. This is largely dependent on the relative phase of the reflections and, for lower values of isolation (less than 30 db), the effect is much less noticeable. This explains the jagged nature of the curve in Fig. 10, whereas Fig. 11 shows a smooth curve.

Maximum measured isolation between arms 2 and 3 of the symmetric hybrid is lower than that of the conventional design. This might be attributed to the disturbing effects of the baluns and the physical structure of arm 4. In many applications, however, the isolation between arms 2 and 3 is relatively unimportant.

## Bibliography

[1] W. V. Tyminski and A. E. Hylas, "A wide-band hybrid ring for UHF," Proc. IRE, vol. 41, pp. 81–87; January, 1953.
[2] T. Morita and L. S. Sheingold, "A coaxial magic T," IRE Trans. on Microwave Theory and Techniques, vol. MTT-1, pp. 17–23; November, 1953.
[3] J. Reed and G. J. Wheeler, "A method of analysis of symmetrical four-port networks," IRE Trans. on Microwave Theory and Techniques, vol. MTT-4, pp. 246–252; October, 1956.
[4] R. V. Pound, "Microwave-Mixers," M.I.T. Rad. Lab. Ser., McGraw-Hill Book Co., Inc., New York, N. Y., vol. 16, p. 268; 1948.

[2] J. E. Butler, "Design of strip transmission line systems and antennas," thesis submitted in partial fulfillment of requirements for the M.S.E.E. degree, U. S. Naval Postgraduate School, Monterey, Calif.; June, 1955. Experimental work performed at Airborne Instruments Lab., Inc., Mineola, N. Y.

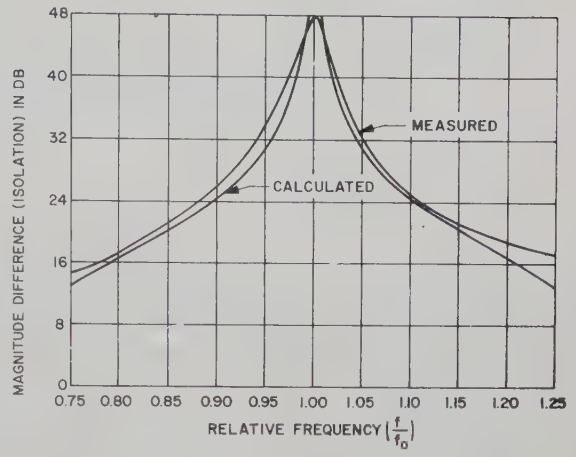


Fig. 15—Isolation between arms 1 and 4 or between arms 2 and 3 of conventional hybrid ring.

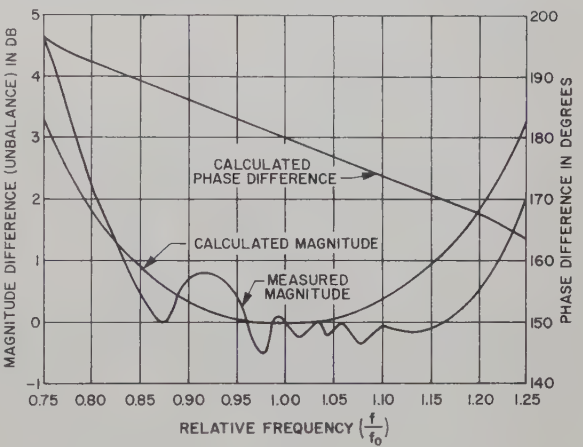


Fig. 16—Relative phase and magnitude (unbalance) of output at arms 2 and 3 of conventional hybrid ring, with signal input at arm 4.

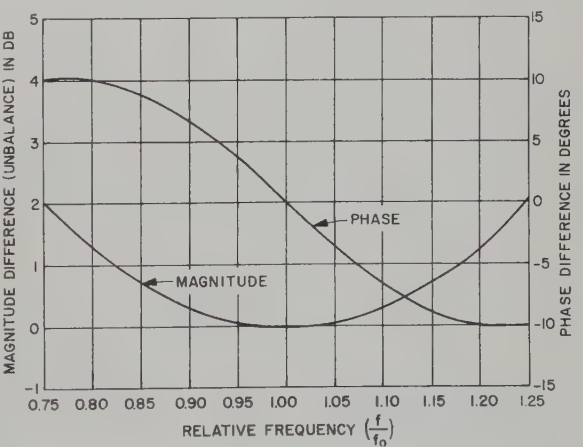


Fig. 17—Calculated relative phase and magnitude (unbalance) of output at arms 2 and 3 of conventional hybrid ring, with signal input at arm 1.

# Some Notes on the Optimum Design of Stepped Transmission-Line Transformers*

L. SOLYMAR†

*Summary*—**This paper describes an optimum design of monotonic stepped transmission-line transformers when the reflection coefficient and the bandwidth ratio are prescribed. For the analysis, discontinuity capacitances and reflection interactions are neglected and the validity of the conclusions is therefore restricted to small steps. The analysis is applicable to a multistep transmission line of which the quarter-wave transformer is a special case. In particular, it is shown that if the number of steps is increased from three to five a larger bandwidth may be obtained, but it is not possible to reduce the over-all length in this manner. For a given bandwidth, the shortest taper is always a stepped transmission line and never a continuous one.**

## Introduction

THE optimum design of stepped transmission-line transformers (hence called step-lines) has been a subject of interest for the past few years.

At first Burkhardtmaier[1] gave an optimum design method for step-lines using the Tchebycheff polynomials. Bolinder,[2] solving approximately the synthesis of continuous lines, suggested the use of Dolph's method for optimizing the properties of the step-lines. Collin,[3] independently of Burkhardtmaier, solved the same problem and got the same results. Riblet[4] gave the general synthesis of step-lines and proved the physical realizability of the optimum step-line. Cohn,[5] supposing small steps, derived simple expressions for the design of the optimum step-line.

The problem solved in these papers is the following: For a specified number of steps the design method provides the maximum possible bandwidth for a specified reflection coefficient, or conversely, the minimum possible reflection coefficient for a given bandwidth. The length of the steps (at center frequency) is in each case a quarter-wavelength.

By increasing the number of steps, wider bandwidth is attainable, but the over-all length of the step-line increases. The question obviously arises: Is it possible to realize the same specified reflection coefficient with a shorter over-all length (using, where necessary, steps shorter than the quarter-wavelength) if we allow a certain reduction in the bandwidth?

Because of the validity of the different approximations, some restrictions upon the form of the step-line are necessary. (For the design, all the solutions neglect the higher order modes and the junction discontinuities.) Therefore we use the requirement that the taper has to be monotonic. In our calculations we shall apply the same approximations as Cohn; *i.e.*, we assume small steps.

## Design of a General (Not-Quarter-Wave) Step-Line

Assuming that the steps are small, we may neglect reflection interactions and express the reflection coefficient of the step-line (see Fig. 1) referred to the center as follows:

$$\rho = A_1 e^{j(n-1)\phi} + A_2 e^{j(n-3)\phi} + \cdots + A_n e^{-j(n-1)\phi} \quad (1)$$

where

$$A_m = \frac{Z_{m+1} - Z_m}{Z_{m+1} + Z_m} \simeq \frac{1}{2} \ln \frac{Z_{m+1}}{Z_m},$$

$Z_m$ = the characteristic impedance of the $m$th step,
$\phi = \beta l$,
$\beta$ = phase-change coefficient,
$l$ = the length of a step.

Supposing the step reflections to be symmetrical, *i.e.*, $A_1 = A_n$, $A_2 = A_{n-1}$, etc., and $n$ to be odd (as will be clear later, this by no means restricts generality), we get

$$\rho = A_{(n+1)/2} + 2A_{(n-1)/2} \cos 2\phi + 2A_{(n-3)/2} \cos 4\phi + \cdots + 2A_1 \cos (n-1)\phi. \quad (2)$$

To get an optimum performance, we let the reflection coefficient be proportional to a Tchebycheff polynomial, *i.e.*,

$$\rho = \alpha T_{(n-1)/2}(\mu \cos 2\phi + \nu) \quad (3)$$

where[6]

* Manuscript received by the PGMTT, February 7, 1958; revised manuscript received, May 2, 1958.

† Standard Telecommun. Labs. Ltd., Enfield Labs., Enfield, Middlesex, Eng.

[1] W. Burkhardtmaier, "Widerstandstransformation mit Leitungen," *Funk und Ton*, vol. 3, pp. 151–167, 202–213; March, 1949.

[2] F. Bolinder, "Fourier transforms in the theory of inhomogeneous transmission lines," in "Kungliga Tekniska Hogskolans Handlingar," Stockholm, Sweden, no. 48; 1951.

[3] R. E. Collin, "Theory and design of wide-band multi-section quarter wave transformers," Proc. IRE, vol. 43, pp. 179–185; February, 1955.

[4] H. J. Riblet, "General synthesis of quarter-wave impedance transformers," IRE Trans. on Microwave Theory and Techniques, vol. MTT-5, pp. 36–37; January, 1957.

[5] S. B. Cohn, "Optimum design of stepped transmission-line transformers," IRE Trans. on Microwave Theory and Techniques, vol. MTT-3, pp. 16–21; April, 1955.

[6] We use the same method by which Riblet generalized Dolph's paper. See H. J. Riblet, "Discussion on 'A current distribution for broadside arrays which optimizes the relationships between beam-width and side-lobe level,'" Proc. IRE, vol. 35, pp. 489–492; May, 1947.

C. L. Dolph, "A current distribution for broadside arrays which optimizes the relationship between beam-width and side-lobe level," Proc. IRE, vol. 34, pp. 335–348; June, 1946.

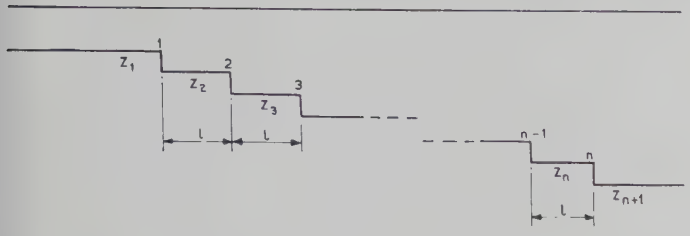


Fig. 1—The stepped transmission line.

$$T_m(x) = \cos\ (m \cos^{-1} x) \qquad |x| \leq 1$$
$$T_m(x) = \cosh\ (m \cosh^{-1} x) \qquad |x| \geq 1. \quad (4)$$

Now, having two free parameters $\mu$ and $\nu$, we may prescribe the value of the reflection coefficient at zero frequency and at the highest frequency of the pass band as well. Hence the two unknowns in the argument may be determined by the conditions

$$\frac{\rho}{\rho_m} = p \quad \text{if} \quad \phi = 0 \qquad (5)$$

and

$$\left|\frac{\rho}{\rho_m}\right| = 1 \quad \text{if} \quad \phi = \phi_2,$$

where $\rho_m$ is the specified value of the reflection coefficient in the pass band and $p$ is defined by (5); *i.e.*, it is the ratio of the reflection coefficient at zero frequency and the maximum reflection coefficient in the pass band. Choosing $\alpha = \rho_m$, the equations for the unknowns are

$$\mu + \nu = z_0$$
$$\mu \cos 2\phi_2 + \nu = -1 \qquad (6)$$

where $z_0$ is to be determined by

$$T_{(n-1)/2}(z_0) = p. \qquad (7)$$

Solving (6) for $\mu$ and $\nu$, we get

$$\mu = \frac{z_0 + 1}{1 - \cos 2\phi_2}, \qquad \nu = -\frac{1 + z_0 \cos 2\phi_2}{1 - \cos 2\phi_2}. \qquad (8)$$

In Fig. 2 we see the transformation

$$z = \mu \cos 2\phi + \nu. \qquad (9)$$

When $\phi$ changes from 0 to $\phi_2 (\phi_2 \leq 90°)$, $z$ runs from $z_0$ to $-1$. At $\phi = \phi_1$ (where $\phi_1$ fulfills $\mu \cos 2\phi_1 + \nu = 1$) $z = 1$. So between $\phi_1$ and $\phi_2$, $|z| \leq 1$.

Because of the properties of the Tchebycheff polynomials, if $|z| \leq 1$, then $|T_{1/2(n-1)}(z)| \leq 1$. So between $\lambda_2 = 2\pi l/\phi_2$ and $\lambda_1 = 2\pi l/\phi_1$ the reflection coefficient fulfills the requirements. The design is optimum in the sense that for a given $p$, and for a given $\phi_2$ (*i.e.*, lower edge of the band is given), it results in the greatest bandwidth.

It may be shown that our design contains, as a special case, the design of Cohn. If $\phi_2 = 90$ degrees our design agrees with that of Cohn for $n$ steps. If

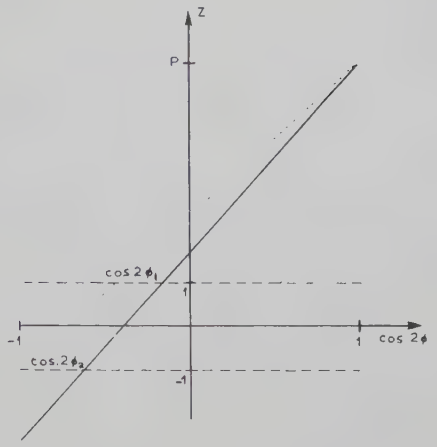


Fig. 2—The transformation $z = \mu \cos 2\phi + \nu$.

$$\phi_2 = \tfrac{1}{2} \cos^{-1}\left(-\frac{1}{z_0}\right),$$

*i.e.*, $\nu = 0$, we get the step-line of Cohn for $(n+1)/2$ steps. So it also includes all the cases when the number of steps is even.

Further, we must compute the coefficients

$$A_k \left(\text{or the coefficient } a_k = \frac{A_k}{\rho_m}.\right)$$

and with their help, determine the characteristic impedances. Performing the necessary calculations, we get for the ratio of consecutive characteristic impedances

$$\frac{Z_{m+1}}{Z_m} = \left(\frac{Z_{n+1}}{Z_1}\right)^{a_m/(a_1 + a_2 \cdots + a_n).} \qquad (10)$$

It may be immediately seen from (10) that the requirement for a monotonic step-line is equivalent to the mathematical condition that $a_m \geq 0$.

*Examples*

If $n = 3$, $T_{(n-1)/2}(z) = T_1(z) = z = \mu \cos 2\phi + \nu$.

Equating the coefficients

$$a_2 + 2a_1 \cos 2\phi = \mu \cos 2\phi + \nu \qquad (11)$$

we get

$$a_2 = \nu; \quad a_1 = \tfrac{1}{2}\mu. \qquad (12)$$

For the particular case of $p = 10$, Fig. 3(a) shows the value $L/\lambda_c [(L = (n-1))$ is the over-all length, $\lambda_c$ is the wavelength at center frequency], and Fig. 3(d) the bandwidth ratio $(q = \lambda_1/\lambda_2)$ as a function of $\phi_2$. It is seen that although the bandwidth is nearly constant, the over-all length can be made arbitrarily small. However the shortening of the taper will have a considerable influence on the characteristic impedances. $Z_2$ and $Z_3$ depend on $\mu$ and $\nu$, which are plotted on Fig. 3(b) against $\phi_2$. As $\phi_2$ decreases, $\nu$ decreases also, becoming zero at $\phi_2 \cong 47.8$ degrees. This means that one step vanishes. The over-all length is just a quarter wavelength; *i.e.*, we have the ordinary quarter-wave transformer. If $\phi_2 < 47.8$ degrees, the over-all length will

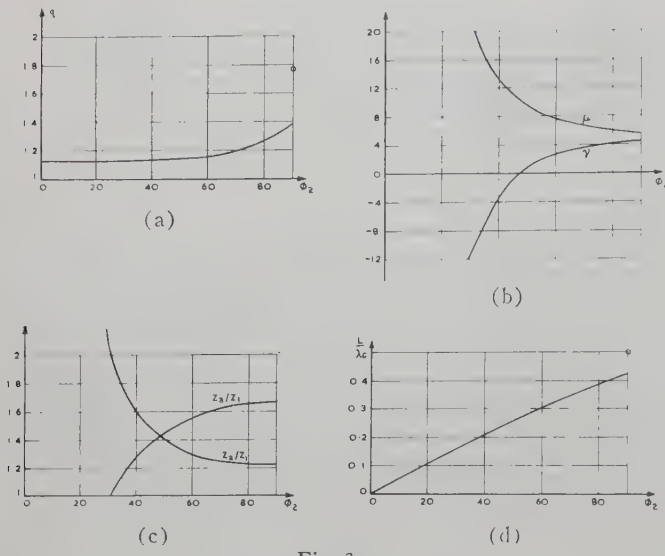


Fig. 3.

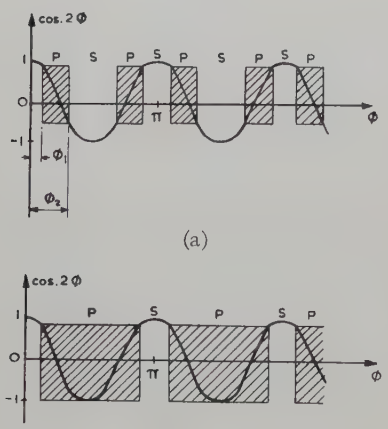


Fig. 4—The pass ($p$) and stop ($s$) bands, for (a) $\phi_2<90$ degrees, (b) $\phi_2=90$ degrees.

be shorter than a quarter-wavelength, but $\nu$ at the same time will become negative and the step-line is no longer monotonic. Supposing $Z_4/Z_1=2$, Fig. 3(c) shows $Z_2/Z_1$ and $Z_3/Z_1$ as functions of $\phi_2$. At $\phi_2\cong 47.8$ degrees, $Z_2=Z_3=\sqrt{2}Z_1$. If $\phi_2$ decreases further, $Z_3/Z_1$ rapidly decreases and $Z_2/Z_1$ rapidly increases.

We must remark that the curves $L/\lambda_c$ and $q$ are discontinuous at $\phi_2=90$ degrees. The reason for this is shown in Fig. 4(a) and 4(b). Since the requirement for the pass band is $\cos 2\phi_2\leq\cos 2\phi\leq\cos 2\phi_1$, we have an infinite number of pass and stop bands as shown on Fig. 4(a). If $\phi_2=90$ degrees, $\cos 2\phi_2=-1$, and the first, second, third, and fourth, etc., pass bands merge into each other [Fig. 4(b)]. Consequently, the bandwidth, and the over-all length at the central frequency, suddenly increase.

If $n=5$, $T_2(z)=2z^2-1=2(\mu\cos 2\phi+\nu)^2-1$.

Equating the coefficients,

$$a_3+2a_2\cos 2\phi+2a_1\cos 4\phi=\mu^2\cos 4\phi+4\mu\cos 2\phi+\mu^2+2\nu^2-1 \quad (13)$$

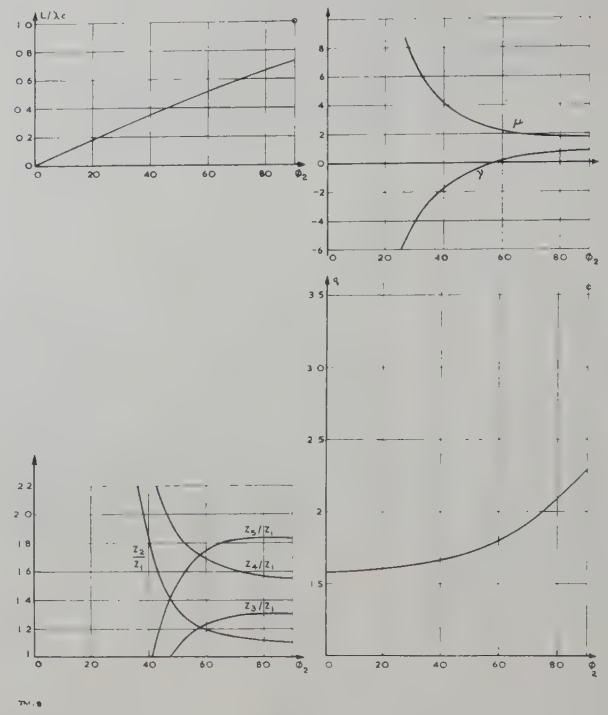

Fig. 5.

we get

$$a_3=\mu^2+2\nu^2-1;\quad a_2=2\mu;\quad a_1=\tfrac{1}{2}\mu^2. \quad (14)$$

The situation is similar again. If $\nu<0$, the step-line is not monotonic. Fig. 5 shows the same quantities for $n=5$, which we have drawn previously for $n=3$. The consequences are also the same. If $\phi_2\simeq 57.5$ degrees we get the same step-line as at $\phi_2=90$ degrees for $n=3$.

Let us see now what is the connection between $L/\lambda_c$ and $q$. Fig. 6 shows this curve for $p=10$ and $n=3, 5, 7, 9$. For any $n$ the shortening of the step-line means a reduction of the bandwidth. At the points where $L$ is an integral multiple of $\lambda_c/4$ (marked with small circles in Fig. 6), the number of steps in the step-line changes from $n$ to $(n+1)/2$. The further shortening will result in a nonmonotonic step-line represented by the broken lines.

For the comparison of the actual lengths of the step-line for different values of $n$, the bandwidth ratio is plotted in Fig. 7 against $L/\lambda_1$. It may be seen that for a given $p$ and $q$ the length of this type step-line might be shorter than that of a quarter-wave type. If, for example, $p=10$, $q=1.85$, we get $n=5$ and $L/\lambda_1=0.391$, while the usual (quarter-wave) design would result in $n=4$ and $L/\lambda_1=0.412$.

## The Shortening of the Step-Line by the Application of More Steps

We have seen that increasing the number of steps results in a larger bandwidth. Let us investigate the relation between the number of steps and over-all length for a given bandwidth and see if it is possible to

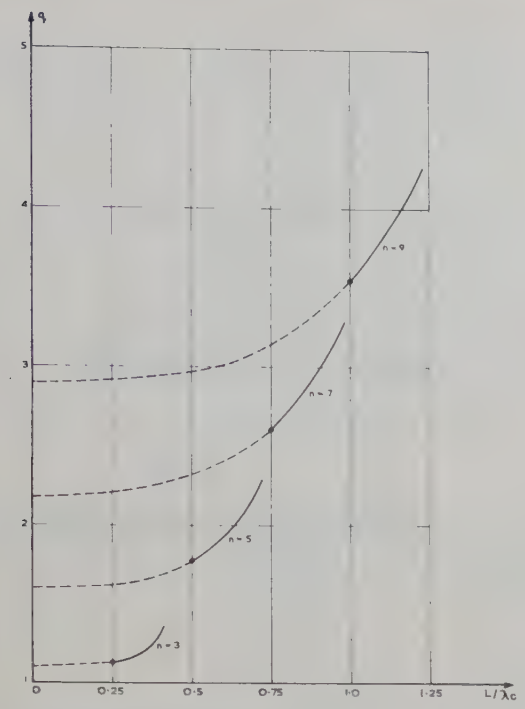


Fig. 6—The bandwidth ratio as a function of $L/\lambda_1$. The broken lines represent the nonmonotonic solutions.

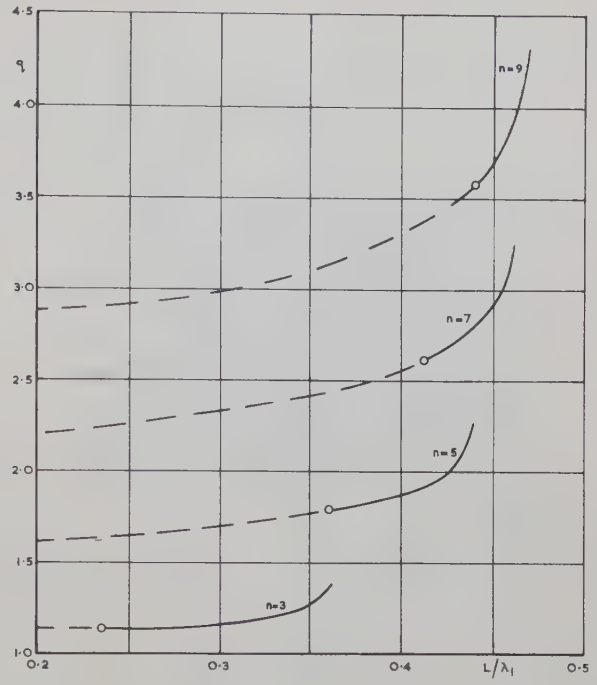


Fig. 7—The bandwidth ratio as a function of $L/\lambda_1$. The broken lines represent the nonmonotonic solutions.

shorten the monotonic step-line by using more steps. If this is possible, the problem can now be redefined: For a given reflection coefficient and bandwidth ratio, what is the optimum number of steps that will result in a minimum over-all length? Generally, to solve this problem is very difficult because of the complicated mathematical treatment involved. However a special case can be solved easily.

The normalized reflection coefficient for $n=5$ has the form

$$\frac{\rho}{\rho_m} = a_3 + 2a_2 \cos 2\phi + 2a_1 \cos 4\phi. \tag{15}$$

Let us introduce the notation $x=\cos 2\phi=\cos \beta L/2$, and arrange (15) in powers of $x$. Then

$$\frac{\rho}{\rho_m} = C_2x^2 + C_1x + C_0 \tag{16}$$

where

$$a_1 = \frac{C_2}{4}; \quad a_2 = \tfrac{1}{2}C_1; \quad a_3 = C_0 + \tfrac{1}{2}C_2. \tag{17}$$

If (16) has no linear term, *i.e.*, $a_2=0$, we get the special case of the step-line with three steps. When the linear term is not zero we get the step-line with five steps.

Let us first design a monotonic step-line for a given $p$ and $\phi_2$ whith three steps; and later, by adding the linear term, let us construct a shorter step-line with the same bandwidth but having five steps.

Prescribing $x_2=\cos 2\phi_2$ the curve of the normalized reflection coefficient is shown in Fig. 8. It cuts the $\rho/\rho_m=1$ line at the point $x=x_1$. These two points determine the bandwidth ratio and the length of the step-line. The nearer $x_1$ is to unity, the shorter is the step-line.

Thus, if we want to construct a shorter step-line having the same bandwidth, we have to construct a parabola through the points $p$, $x_1+\epsilon$, $x_2+\delta$ where $\epsilon$ and $\delta$ must satisfy

$$q = \frac{\cos^{-1} x_2}{\cos^{-1} x_1} = \frac{\cos^{-1} (x_2 + \delta)}{\cos^{-1} (x_1 + \epsilon)}. \tag{18}$$

It may be shown (see the Appendix), that $C_1$ is always negative; *i.e.*, these requirements cannot be fulfilled with a monotonic step-line of five steps. It is proved, therefore, that the application of two further steps cannot result in a shorter step-line.

Because of the mathematical difficulty of the general proof, we cannot generalize this result. From the physical point of view, however, it is very likely that if the application of two further steps does not result in a shorter step-line, then the application of any number of steps will not shorten it. Similarly, if the length of a three steps step-line cannot be shortened, then very likely the length of any properly designed step-line consisting of any number of steps cannot be reduced. Hence, if the bandwidth ratio and the reflection coefficient are specified, by drawing the diagrams similar to Fig. 7 we get the optimum number of steps.

Since in practice a finite bandwidth is always required, a finite number of steps always gives the shortest line. This statement does not mean that a continuous

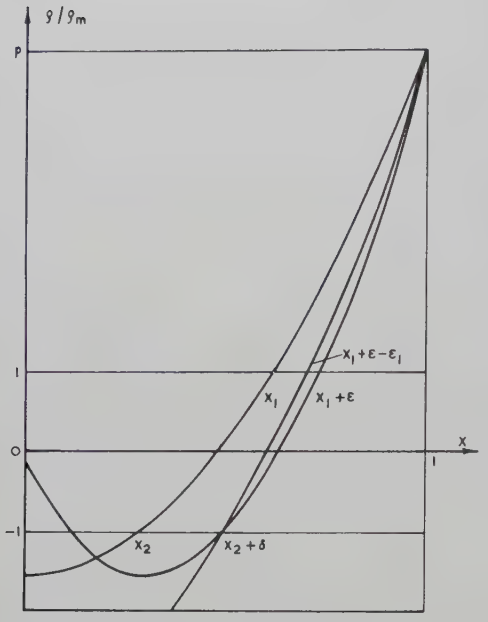


Fig. 8—The normalized reflection coefficient as a function of $x=\cos 2\phi$ for $n=3$ and $n=5$.

line (a step-line consisting of an infinite number of steps) cannot be useful. The application of a continuous taper may be recommended for microwaves if the resulting steps, and the discontinuity capacitances, are large, because the compensation of them will generally result in a narrower bandwidth.

There is always another application where the continuous line is preferable. This is the case when two or more pass bands are required. Because of the periodic structure of the reflection coefficient of step-lines, these requirements may be fulfilled with them only in special cases.

## Appendix

The parabola for five steps through the points $p$, $x_1+\epsilon$, $x_2+\delta$ is shown in Fig. 8. The coefficient of the linear term is given by

$$C_1 = \frac{2-(p+1)(x_1+\epsilon)^2+(p-1)(x_2+\delta)^2}{[(x_1+\epsilon)-(x_2+\delta)][1-(x_1+\epsilon)][1-(x_2+\delta)]}. \quad (19)$$

Let us draw now a curve for three steps through the points $x_2+\delta$ and $p$. This curve cuts the $\rho/\rho_m=1$ line at the point $x_1+\epsilon-\epsilon_1$, where $\epsilon_1>0$[7] and the equation connecting $(x_2+\delta)$ and $x_1+\epsilon-\epsilon_1$ is as follows:

$$2-(p+1)(x_1+\epsilon)^2+(p-1)(x_2+\delta)^2 = -(p+1)\epsilon_1(2x_1+\epsilon-\epsilon_1). \quad (20)$$

We now prove that under the above conditions $C_1$ is negative. Since the denominator is positive it is sufficient to investigate the sign of the numerator.

Substituting (20) in the numerator of (19) we obtain

$$-(p+1)\epsilon_1[2(x_1+\epsilon)-\epsilon_1] \quad (21)$$

which is negative as far as

$$2(x_1+\epsilon) > \epsilon_1 > 0. \quad (22)$$

Hence $C_1$ is negative.

## Acknowledgment

The author wishes to thank L. Lewin for reading the manuscript, and for a number of interesting and stimulating discussions. Acknowledgment is also made to Standard Telecommunication Laboratories for facilities granted in the preparation of the manuscript and permission to publish the paper.

[7] $\epsilon_1$ must be positive, because the bandwidth ratio is decreasing as $\phi_2$ decreases.

# Microwave Semiconductor Switching Techniques*

R. V. GARVER†, E. G. SPENCER‡, AND M. A. HARPER†

*Summary*—**This paper describes new microwave techniques employing the properties of *N*-type germanium diode switches. For applications requiring very high isolations, multiple switches are added in tandem. With proper spacing, they form antiresonant cavity circuits. In this case the isolations and insertion losses in db are directly additive. A switch is described which is normally ON and is pulsed OFF. Finally, details are given of a switch in a hybrid-tee configuration in which switching isolations of 50 db are obtained with an insertion loss of 0.7 db.**

* Manuscript received by the PGMTT, February 7, 1958; revised manuscript received, April 18, 1958.

† Diamond Ordnance Fuze Labs., Washington, D. C.
‡ Bell Telephone Labs., Murray Hill, N. J. Formerly at Diamond Ordnance Fuze Labs., Washington, D. C.

## Introduction

In a previous publication,[1] a description is given of the low-power microwave semiconductor switch using *N*-type germanium. The switch consists of a germanium, point contact, diode placed across a section of standard *X*-band waveguide. Isolations of 25 to 35 db, with insertion losses of 1 db, are obtained over a 1000-mc bandwidth. The switching characteristics are

[1] M. A. Armistead, E. G. Spencer, and R. D. Hatcher, "Microwave semiconductor switch," PROC. IRE, vol. 44, p. 1875; December, 1956.

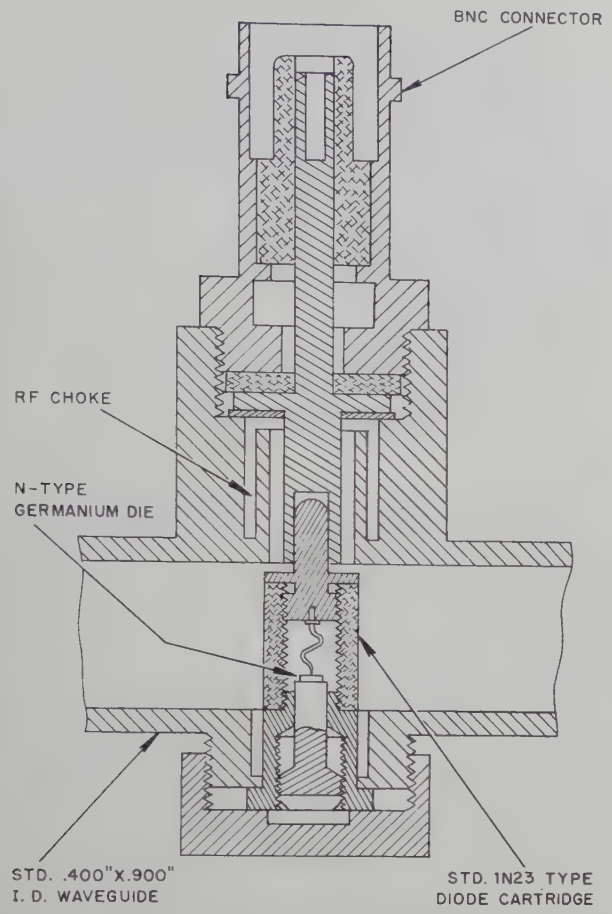


Fig. 1—Microwave semiconductor switch with germanium diode mounted in ceramic cartridge.

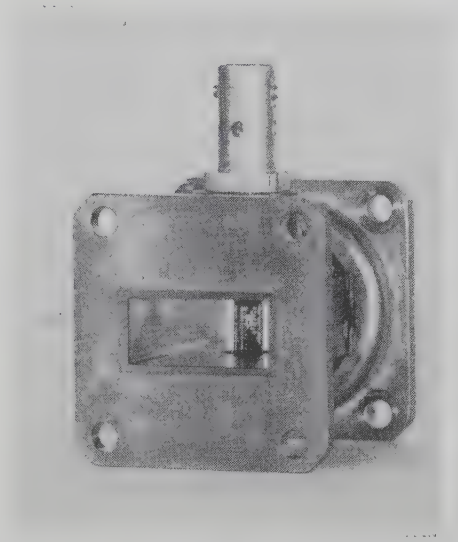

Fig. 2—External view of microwave semiconductor switch employing 1N263 germanium diode showing its small size. The switch can be made as thin as the RF choke permits.

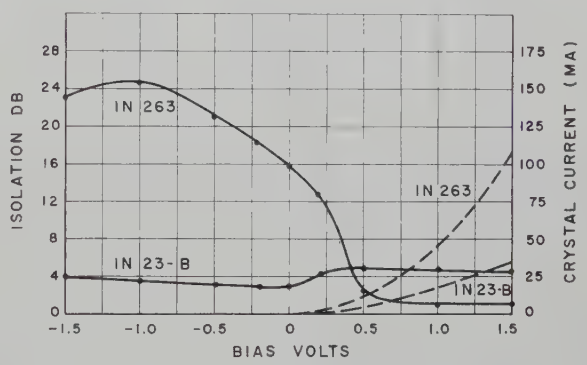


Fig. 3—At a frequency of 9200 mc and incident power of 0.1 milliwatt, the solid lines show switching function of *N*-type germanium (1N263) and *P*-type silicon (1N23-B) crystal diodes. Dashed lines show crystal current. The voltage for 1N23-B is shown inverted for purposes of comparison.

deteriorated but little by temperatures of 150°C. Another paper[2] presents data on the switching speeds. Rise times and decay times as fast as 3 millimicroseconds (m$\mu$sec) are obtained and there is no measurable dead time between switching events. Further data are given to demonstrate the increase in microwave power-handling capabilities obtained by reducing the number of impurity donors. One watt of RF power has been successfully switched without deterioration of the semiconductor contact.

The purpose of this paper is to describe some new microwave techniques employing the particular properties of the semiconductor switches.

## Normal Switch

Fig. 1 shows a diagram of the *X*-band semiconductor diode with the mounted germanium wafer and the point contact. The diode is shown mounted as a switch in standard *X*-band waveguide. A photograph of the complete switch showing its small size is seen in Fig. 2. The isolation as a function of applied voltage is given in Fig. 3. The 1N263 curve is characteristic of *N*-type germanium microwave diodes while the 1N23-B curve is characteristic of *P*-type silicon microwave diodes. It was found early that the semiconductor material and not the form of the diode cartridge determines the switching action. Therefore, all higher power diode switches were *N*-type germanium in 1N23-type cartridges, since this cartridge is more easily assembled. The minimum isolation in all cases defines the insertion loss. This curve is necessary for the discussions of this paper. The other data mentioned in the Introduction are not repeated here.

## Multiple Switches in Cavity Form

In many applications it is necessary to switch with considerably more isolation than the 25 to 35 db of a single crystal switch.

For example, in the measurement of pulse radar receiver sensitivity, switching of two to three times this value is required. This can be attained by use of a multiple switch arrangement.

In adding switches in tandem, the total isolation depends strongly on the spacing between switching diodes.

[2] R. V. Garver, E. G. Spencer, and R. C. LeCraw, "High speed microwave switching of semiconductors," *J. Appl. Phys.*, vol. 28, pp. 1336–1338; November, 1957.

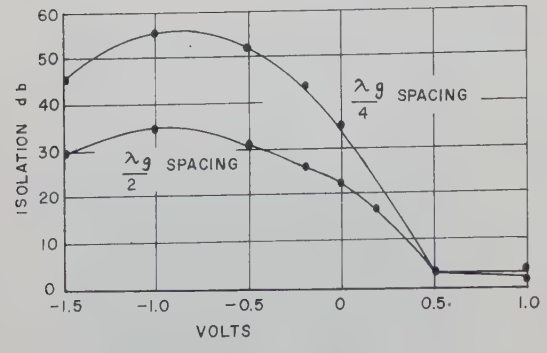


(a)

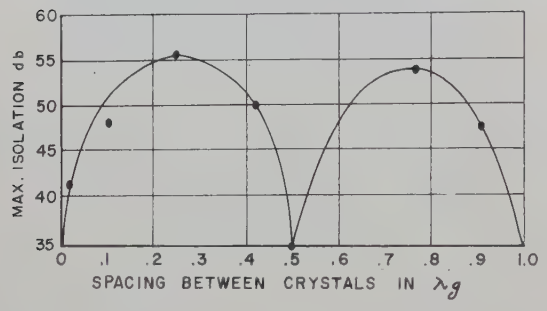


(b)

Fig. 4—(a) Isolation in db for two switches in series spaced $\lambda_g/2$ and $\lambda_g/4$ apart. The individual switches have a maximum isolation of 30 db and an insertion loss of 1 db. In this form the switches in tandem have characteristics of a microwave cavity. (b) Maximum isolation as a function of spacing.

Results are shown in Fig. 4. The upper curves show switching as functions of voltages applied to the switch for $\lambda_g/2$ and $\lambda_g/4$ spacing, where $\lambda_g$ is the guide wavelength. Results for all other spacings lie between these limits. The lower curve, showing the maximum isolation as a function of spacing, indicates that the two crystal switches form a cavity arrangement. The maximum isolation occurs for antiresonant spacing or odd numbers of quarter wavelengths in the guide. For half-wavelength spacing, the isolation is a minimum, corresponding to insertion losses in a resonant transmission type cavity. The isolations and insertion losses are straightforwardly additive in db for the antiresonant cavity spacing.

## Reversed Switch

The microwave semiconductor switch, consisting of a germanium diode placed in the center of a waveguide, is normally OFF for a negative voltage applied to the point contact and normally ON for a positive voltage. There is a current flow for the positive applied voltage (ON) and a negligible amount for the negative applied voltage (OFF). Thus, if it is necessary to hold the switch ON, and pulse OFF, a heat dissipation problem might arise. The heating problem is more serious at the higher switching powers.

This problem has been circumvented by the design of a *reversed* switch, by which is meant that the ON and OFF conditions are reversed. The basic idea behind the reversed switch is as follows. A vertical post is extended down from the top wall of an $X$-band waveguide and a shorting or switching post is extended horizontally in from the side wall. When the posts are in contact the length of the vertical post is varied to obtain a series resonant structure, and the transmitted microwave power is reduced by 20 db. With the posts almost touching the structure is detuned, and the power reduction is 0.2 db. These values are called the isolation and insertion loss, respectively. The length of the vertical post has to be tuned for maximum isolation and its diameter determines bandwidth and isolation. One is allowed to increase at the expense of the other.

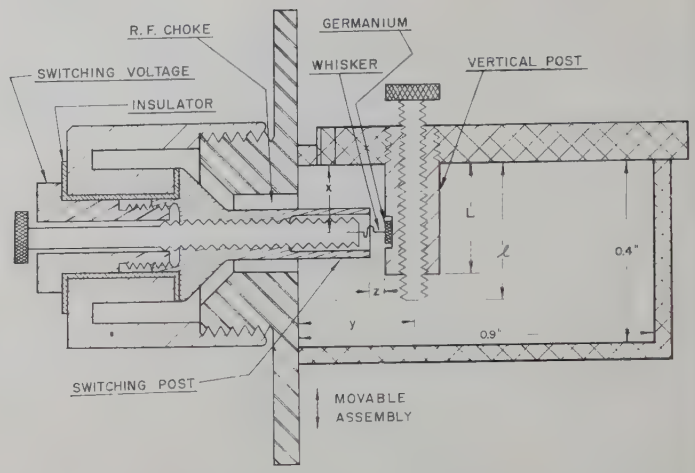


Fig. 5—Semiconductor reversed switch mounted in $X$-band waveguide. For a negative applied voltage the switch is ON and for a positive voltage the switch is OFF. This function is reversed from that of the switch of Fig. 1.

A schematic drawing of the reversed switch assembly is shown in Fig. 5. The germanium wafer ($10^{16}$ impurity donors per $cm^3$) is soldered to the vertical post, which is tunable. The contact whisker is 0.003 inch in diameter and is mounted on the switching post, to which the switching voltage pulses are applied. An RF choke also is shown in the mount. The switching post assembly is movable to allow for small adjustments. The diameter of the vertical post is 0.125 inch and the diameter of the switching post is 0.100 inch.

A block diagram of the measurements technique is shown in Fig. 6. A CW klystron furnishes 40 milliwatts at 9300 mc to the semiconductor switch. The switch is biased negatively ON and is pulsed OFF. The resulting pulse is displayed on a high-speed cathode-ray oscilloscope. The insertion loss and isolation are read with the calibrated variable attenuator.

Referring to Fig. 5, the design parameters are the vertical post length $L$, the tuning length $l$, the distance between the top waveguide wall and the point contact $X$, the distance between the side waveguide wall and the center of the vertical post $y$, and the length of projection of the diode whisker $z$. Many variations of these parameters were tried but no simple relation was found between these and the switching characteristics. Several regions of good switching were found and the best one

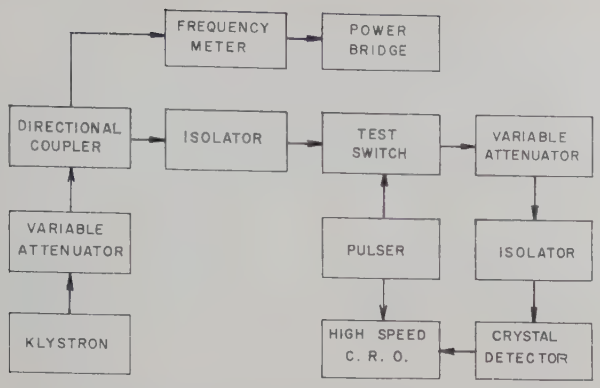


Fig. 6—Microwave equipment used in measurements of the reverse switch.

is shown in Fig. 7. It is felt that a more detailed study of these parameters could lead to much better switching characteristics.

The frequency response of the normal semiconductor switch is more than 1000 mc at *X* band and is limited largely by the bandwidth of the rectangular waveguide. Since the reversed switch is a resonant microwave structure, the frequency response might be expected to be somewhat less. However, by proper design an optimum in bandwidth is achieved. Measured data of frequency response are given in Fig. 7. This shows that better than 12-db isolation with less than 1.1-db insertion loss is obtained over a frequency range of 200 mc.

To summarize, the reversed semiconductor switch is a small microwave unit in which the ON and OFF functions are reversed. It has low insertion loss and good isolation. Several may be added in tandem for higher switching values. It has the properties of the normal switch such as fast pulse rise times and decay times, and power-handling capabilities depending on the number of donor impurities in the germanium.

### Hybrid Tee Semiconductor Switch

The properties of a balanced hybrid-tee modulator are described in the literature.[3] Silicon diodes are placed in two appropriate arms of a hybrid tee and are backed by tunable waveguide shorts. An RF signal is applied to the two diodes and thus modulates a microwave signal passing through the hybrid tee. By proper adjustment of the diode position and the phase of the modulating voltage, the phase or amplitude of the modulated microwave signals is controlled. Carrier suppression of 40 db can be obtained over a narrow frequency band.

By applying either dc or pulse voltages to two germanium diodes in a similar arrangement, an interesting form of *reversed* switch is obtained. A drawing of the assembly is seen in Fig. 8 with dimensions indicated for an operating frequency of 9375 mc. Standard JAN-1N263 diodes are used.

[3] C. G. Montgomery, "Technique of Microwave Measurements," M.I.T. Rad. Lab. Ser., McGraw-Hill Book Co., Inc., New York, N. Y., vol. 11, p. 331; 1947.

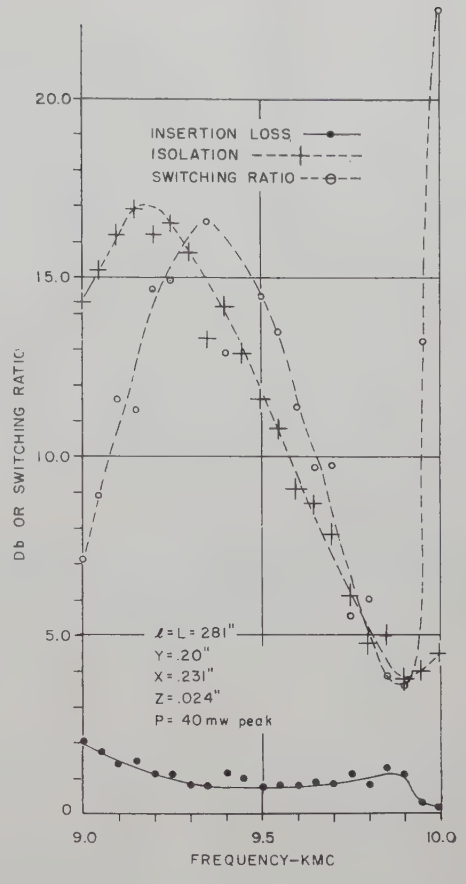


Fig. 7—Frequency dependence of the reverse switch.

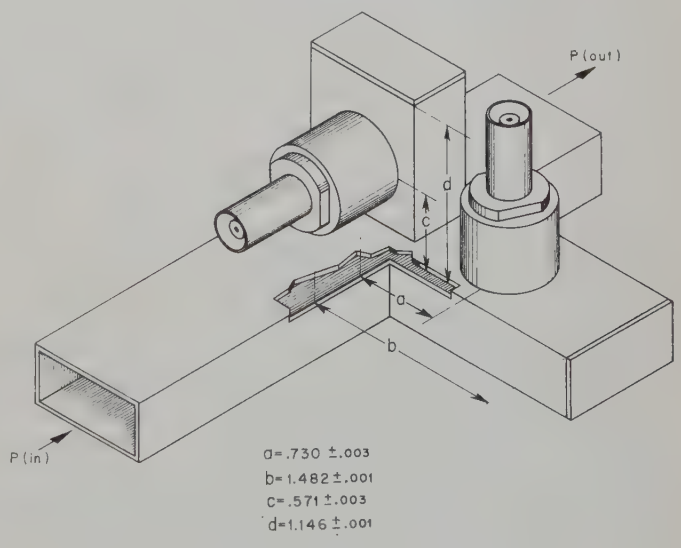


Fig. 8—Design data of hybrid-tee switch for 9375 mc using two 1N263 diodes.

The switching action is shown in Fig. 9. Insertion losses of 0.7 db and isolations of 50 db are obtained at 1 milliwatt incident microwave peak power. It should be noted that since two diodes are used, the characteristics of this switch are to be compared with those of two of the other reversed switches operating in tandem. It might also be noted that if the hybrid tee is replaced by a Riblet hybrid, only the physical form of this switch is altered.

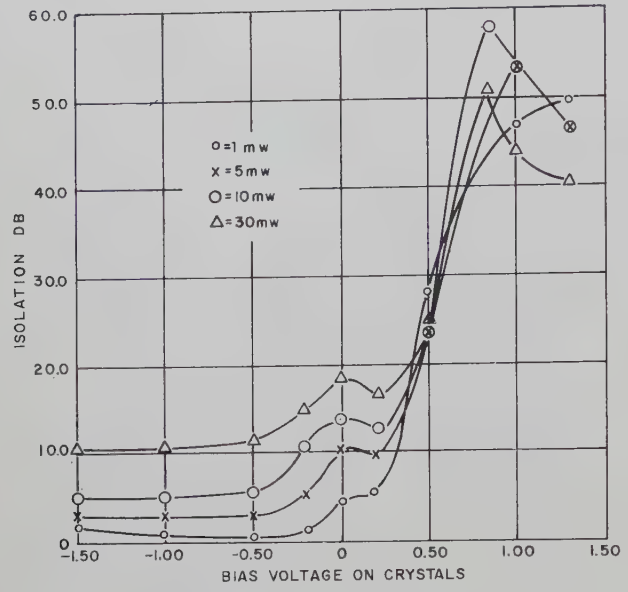


Fig. 9—Switching function of hybrid-tee switch using germanium diodes at different power levels.

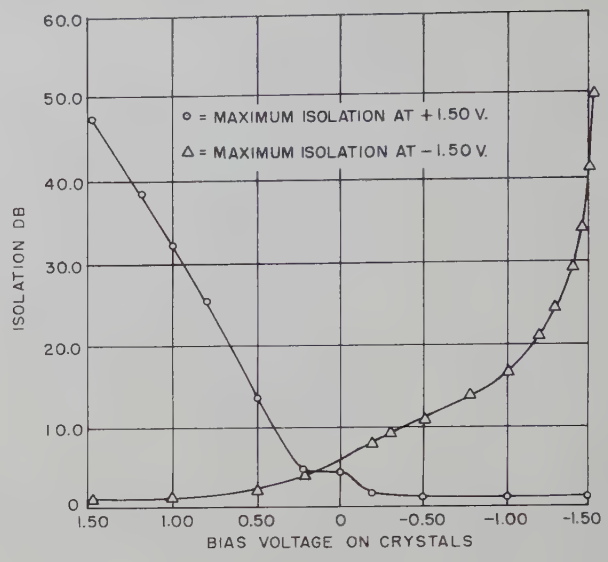


Fig. 10—Switching function of hybrid-tee switch using silicon diodes. Spacing can be optimized to obtain maximum isolation at either plus or minus bias voltage.

The hybrid junction is a symmetrical four terminal-pair network and may be considered from the viewpoint of the equivalent circuit for such a network. See, for instance, Marcuvitz.[4] By proper choice of terminal planes the equivalent reactances representing the open hybrid tee may be evaluated. It then becomes possible, through the application of network theory, to calculate the reactive loads that must be placed on the shunt and series arms, with a matched resistive load on the fourth arm, to convert the equivalent impedance of the network into a pure reactance. This calculation, however, is extremely tedious and it is convenient to determine the most satisfactory position for the short circuit behind the crystal diode experimentally. This is also true because of the imperfect conductivity of the waveguide walls which introduces an error in computations.

It has been observed experimentally that if a curve is plotted showing the position of one short circuit as a function of the other short circuit as the microwave null is maintained, that the sharpest nulls occur at positions coinciding with the knees of the curve. The use of such a curve therefore permits a quick selection of the waveguide lengths in designing the basic switch structure.

In Fig. 3 (see also Armistead, *et al.*[1]), a comparison is made of the switching properties of *P*-type silicon and *N*-type germanium for switching. The germanium diode changes microwave resistance with applied voltage while the silicon diode changes microwave reactance. This reactance change is not effective in a normal waveguide switch. In the hybrid-tee switch, however, the changes in reactances cause microwave phase changes which can cause a switching action. Fig. 10 shows the properties of this switch using standard 1N23-B *P*-type silicon diodes. An insertion loss of 1.5 db and an isolation of 45 db are obtained.

The effect of increasing microwave power incident to the silicon hybrid tee switch is the same as for germanium which is to increase minimum insertion loss (Fig. 9). Also, either hybrid switch can be made to have maximum isolation for plus or minus applied voltages by changing the dimensions shown in Fig. 8. See Fig. 10.

Isolation decreases rapidly as the frequency is changed from the design value (Fig. 11) on either hybrid switch. Isolation greater than 30 db is available over a 20-mc bandwidth. The insertion loss remains flat.

## Conclusions

The microwave semiconductor switch using germanium diodes may take the form of the *normal* switch, the *reversed* switch, the tandem cavity-type switch, or the hybrid-tee switch. In various forms, it has become an important microwave device in this laboratory. It is being used in radar receiver circuits, in conjunction with precise microwave measurements, and for bench testing of pulse radar systems. In some applications it is used to sample and measure RF signals at accurately specified time intervals.

Because of the similarity of functions, the crystal switch might be compared with ferrite high-speed switches.[5–7] At the present time the semiconductor

[4] N. Marcuvitz, "Waveguide Handbook," M.I.T. Rad. Lab. Ser. McGraw-Hill Book Co., Inc., New York, N. Y., vol. 10, pp. 117, 386; 1951.

[5] R. C. LeCraw, "High speed pulsing of ferrites," *J. Appl. Phys.*, vol. 25, pp. 678–679; May, 1954.

[6] R. C. LeCraw and H. B. Bruns, "Time delay in high-speed ferrite microwave switches," *J. Appl. Phys.*, vol. 26, p. 124; January, 1955.

[7] R. F. Sullivan and R. C. LeCraw, "New type ferrite microwave switch," *J. Appl. Phys.*, vol. 26, pp. 1282–1283; October, 1955.

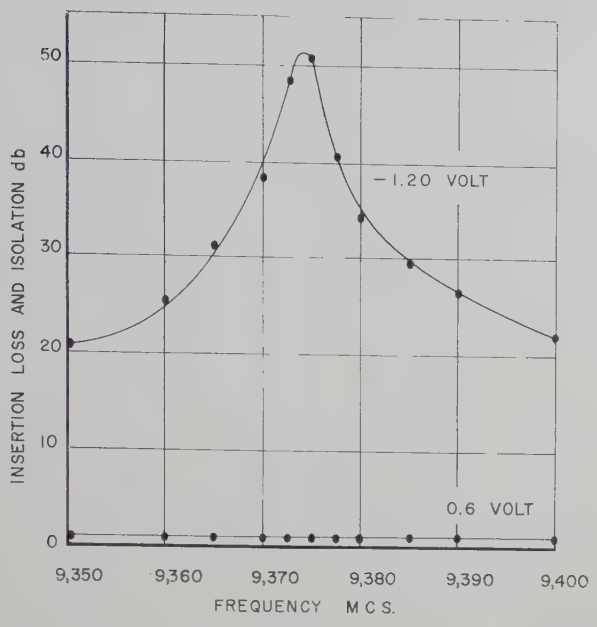


Fig. 11—Frequency dependence of hybrid-tee switch characteristic of both silicon and germanium diodes.

switch has proved to be faster than the ferrite switch. As far as the solid-state material is concerned, both germanium and ferrite have relaxation times less than 1 mμsec. It is considerably more difficult to develop fast rise time magnetic pulses (20 to 30 oersteds) for ferrite switching than it is to develop fast rise time voltage pulses for semiconductor switching. Ferrite switches are indicated for high-power high-speed microwave switching and semiconductor switches are indicated for low-power high-speed microwave switching.[8]

### Acknowledgment

The authors thank R. D. Hatcher, R. C. LeCraw, R. F. Sullivan and H. B. Bruns for many helpful discussions and suggestions.

[8] Since the writing of this article, another microwave diode switch has been proposed by A. Uhlir, Jr., "The potential of semiconductor diodes in high-frequency communications," Proc. IRE, vol. 46, pp. 1099–1115; June, 1958. If his theory results in another practical switch, the techniques reported here should be equally useful with either switch.

# Microwave *Q* Measurements in the Presence of Coupling Losses*

E. L. GINZTON†

*Summary*—In the use of the impedance (*Q*-circle) method of measuring the cavity *Q* values, the presence of losses in the coupling network (between the cavity and the available external terminals) is usually neglected. If appreciable losses are present this simplification is not justified, and its use can lead to significant errors.

The losses in any coupling network can be described by means of an equivalent canonical circuit containing a series and a shunt resistor. The losses due to the series element are immediately apparent from the character of the impedance locus when plotted on a Smith Chart and can be corrected for an "apparent" *Q* value. However, unless the shunt loss can be determined by a separate calibration of the coupling network, the apparent *Q* value will be ambiguous because the shunt losses occurring in the coupling network are not distinguishable from those in the cavity proper.

Methods for using the impedance data for determining the *Q* values are given on the assumption that the coupling network parameters can be found. It is also pointed out that due to the presence of coupling losses the loaded and external *Q* values are no longer uniquely defined, but their meaning depends upon the application of interest. Formulas relating these to the coupling network parameters are given.

* Manuscript received by the PGMTT, February 12, 1958; revised manuscript received, May 26, 1958.

† Microwave Lab., W. W. Hansen Phys. Labs., Stanford University, Stanford, Calif.

## Introduction

A COMMON useful method of measuring the *Q* values of a microwave cavity consists of measuring the self-impedance of the cavity as a function of frequency. The equivalent circuit of the main elements of apparatus needed for this measurement is shown schematically in Fig. 1, where the cavity is shown as if it were a lumped-constant resonant circuit inductively coupled to the uniform transmission line (which contains a slotted section for impedance measurements). This special form of the equivalent circuit has been shown to be sufficiently general and accurate for most practical cases: the resonance phenomenon occurs within the cavity so that the losses within it can be represented by the resistor in series with $L_2$ and $C_2$.

The losses in the *coupling network*, *i.e.*, in the elements which transfer energy from the transmission line into the cavity, are generally very small and usually their presence can be neglected. The theory of the experiment required to determine the *Q* values, details of

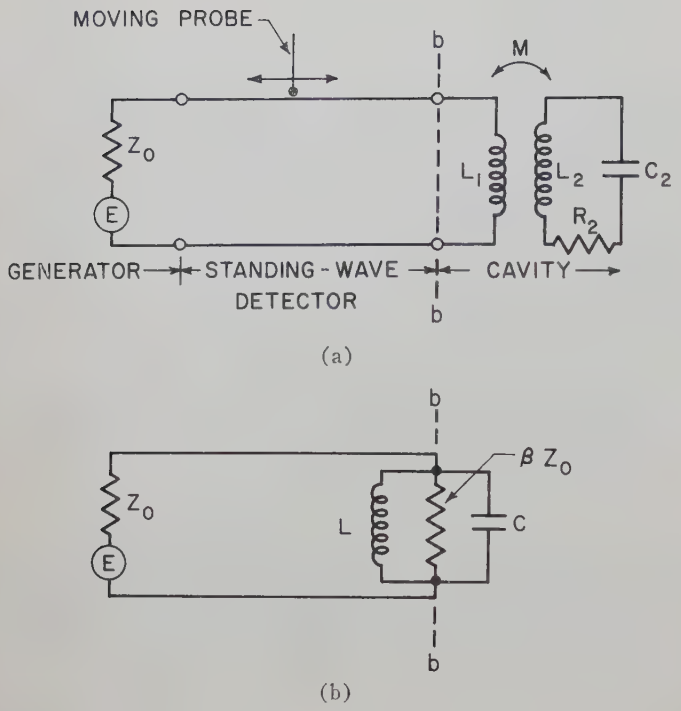


Fig. 1—(a) Schematic representation of the apparatus used in impedance method of cavity-$Q$ measurement. (b) The equivalent circuit at the detuned short position for the negligible coupling-loss case.

measurement, and interpretation of the impedance data, sources of error, helpful techniques, etc., are discussed in numerous sources.[1,2]

The assumption that the coupling network is *lossless* is not always accurate. If sufficient losses are present, the available methods for determination of $Q$ are not valid in general and their use can lead to significant errors. This fact has been recognized previously, and a special case in which the coupling loss can be represented by a simple resistance in series with the coupling element has been described.[2–4]

The purpose of this paper is to discuss the more general case in which the losses in the coupling network need not be presumed to be of the series type but can be of the series, shunt, or distributed form.

## The Equivalent Circuit

The general form of the equivalent circuit representing the cavity and its coupling network is shown in Fig. 2. The terminals of the *coupling network* 1-1 and 2-2 are presumed to be selected so that all sources of loss within the network are included between these terminals. Further, the terminals 1-1 are to be located within the uniform transmission line of the standing-wave detector and are to be selected in a manner which

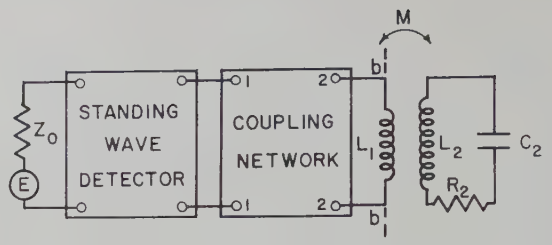


Fig. 2—The general form of the equivalent circuit representing the apparatus shown in Fig. 1(a).

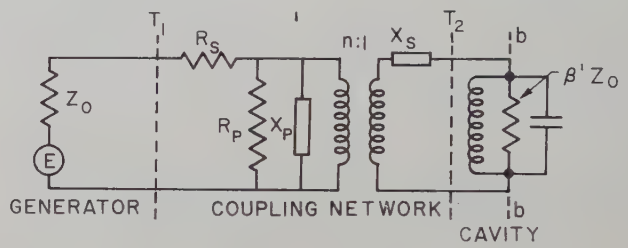


(a)

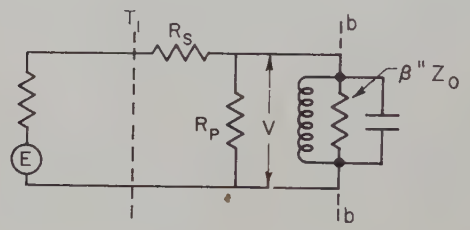


(b)

Fig. 3—(a) Representation of the coupling network in the canonical form. (b) Simplification of (a) transforming the elements on the secondary side to the primary.

will simplify the interpretation and manipulation of the laboratory data. Specifically, terminals 1-1 will be located at the position which is called the *detuned-short* (DS) position, in analogy with the unambiguous location of such terminals in the absence of losses in the coupling network; the actual location of these terminals will be discussed below.

There are several forms of an equivalent circuit which can be used to describe the coupling network: the $L$, $T$, $\pi$, lattice, etc. In this case, it is convenient to use the canonical network shown in Fig. 3(a).[5–7] In this network, the resistances $R_s$ and $R_p$ represent the dissipative losses of the network; the reactances $X_p$ and $X_s$, together with the location of the input reference plane $T_1$, represent the reactive elements. The equivalent circuit of Fig. 3(a) can be simplified as shown in Fig. 3(b), where the new resonant circuit has a resonant impedance $\beta'' Z_0$ after transformation through the transformer. Due to the presence of various coupling reactances, which are assumed to be small, the resonant

[1] For example, E. L. Ginzton, "Microwave Measurements," McGraw-Hill Book Co., Inc., New York, N. Y., ch. 9; 1957.

[2] A. Singh, "An improved method for the determination of $Q$ of cavity resonators," IRE Trans. on Microwave Theory and Techniques, vol. MTT-6, pp. 155–160; April, 1958.

[3] L. Malter and G. R. Brewer, "Microwave $Q$ measurements in the presence of series losses," *J. Appl. Phys.*, vol. 20, pp. 918–925; October, 1949.

[4] Ginzton, *op. cit.*, pp. 424–428.

[5] A. Weissfloch, "Circle geometric four-terminal network theory; its significance as a circuit theory at microwaves," *Hochfrequenz. Elektr* , pp. 100–123; April, 1943.

[6] L. B. Felsen and A. A. Oliner, "Determination of equivalent circuit parameters for dissipative microwave structures," Proc. IRE, vol. 42, pp. 477–483; February, 1954.

[7] Ginzton, *op. cit.*, pp. 323–326, 328–329.

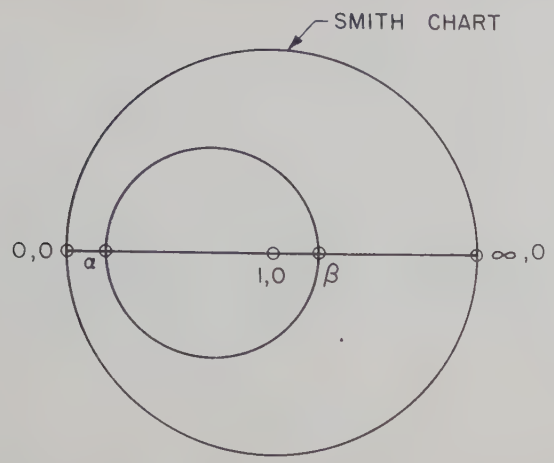


Fig. 4—Variation of the cavity impedance with frequency in the presence of coupling loss (plotted on a Smith Chart).

frequency of the circuit shown in Fig. 3(b) is no longer equal to the resonant frequency of the cavity itself; however, this is of no particular importance, just as the presence of the small coupling reactances in the case of negligible losses is immaterial.

The variation of impedance with frequency of the circuit shown in Fig. 3(b) at terminals 1-1 is indicated in Fig. 4 for a typical case. This locus must be a circle, since the transformation of the circular impedance locus of the impedance at terminals b-b in Fig. 3 through the coupling network is conformal.

For simplicity, the terminals 1-1, henceforth called the reference plane $T_1$ or merely $T_1$, are chosen such that the impedance locus in Fig. 4 is symmetrical about the resistive axis. (Actually, there are two such planes $\lambda_t/4$ apart; the one that makes $\alpha<1$ is selected, as indicated in Fig. 4.) If the series resistance in Fig. 3(b) were zero, the impedance locus would pass through the origin ($R=0$, $X=0$); hence, the location of $T_1$ in the manner stated corresponds to the location of the "detuned-short position" in the no-loss case.

Referring to Fig. 4, let the intercepts of the impedance locus with the normalized resistive axis of the Smith Chart be called $\alpha$ and $\beta$ which, by comparison with Fig. 3(b), are:

$$\alpha = \frac{R_s}{Z_0} \tag{1}$$

$$\beta = \alpha + \beta' \tag{2a}$$

where

$$\beta' = \frac{R_p\beta''}{R_p + \beta''Z_0},$$

or

$$\beta' = \beta''\frac{\gamma}{\gamma+1} \tag{2b}$$

where

$$\gamma = R_p/\beta''Z_0.$$

The intercepts described by $\alpha$ and $\beta$ result, respectively, when the cavity is tuned far off resonance and when it is tuned to the angular frequency $\omega_0$ (at which the impedance across $R_p$ becomes a maximum and purely resistive). For descriptive purposes, quite arbitrarily, the angular frequency $\omega_0$ may be called the *resonant frequency*.

Referring to Fig. 3(b), the impedance $Z_{11}$ at $T_1$ can be represented by

$$Z_{11} = R_s + \frac{R_pZ_{bb}}{R_p + Z_{bb}}, \tag{3}$$

but

$$\frac{Z_{bb}}{Z_0} = \frac{\beta''}{1 + j2Q_0\delta} \tag{4}$$

where $Z_0$ = characteristic impedance of the input transmission line. $Q_0$ is the unloaded $Q$ value of the resonant cavity, and

$\delta = (\omega - \omega_0)/\omega$ = frequency tuning parameter
$\omega$ = angular frequency = $2\pi f$
$\omega_0$ = angular frequency at which the input impedance is maximum and real.

Combining (3) and (4) and rearranging,

$$\frac{Z_{11}}{Z_0} = \alpha + \frac{\beta - \alpha}{1 + j2Q_0'\delta}, \tag{5}$$

where

$$Q_0' = Q_0\left(\frac{1}{1 + \dfrac{\beta''Z_0}{R_p}}\right) \tag{6a}$$

$$= Q_0\frac{\gamma}{\gamma+1}. \tag{6b}$$

Thus, the Smith Chart impedance locus as seen at $T_1$ is modified by the presence of loss in the two ways indicated in Fig. 5. The dashed circle shows the locus that would be obtained if there were no coupling losses. If the series losses alone were present ($R_p=\infty$), the impedance locus would pass through the point ($\alpha$, 0) instead of (0, 0). If the shunt losses alone were present ($R_s=0$), the circle would pass through (0, 0) but would correspond to a cavity with a lowered $Q_0$. The solid circle shown is one that would be obtained if both losses were present simultaneously.

### General Discussion and Determination of $Q_0$

It is apparent from the above discussion that it is necessary to know the coupling network parameters $R_s$ and $R_p$ to permit the interpretation of the impedance information available at terminals 1-1. The constants $R_s$ and $R_p$ could be found experimentally if the coupling network at its output terminals could be replaced by a moving short circuit to permit separate experimental determination of the parameters of the canoni-

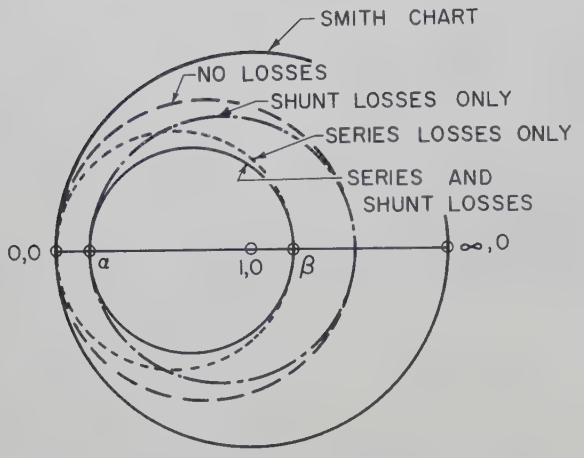


Fig. 5—The effect of coupling network losses upon the impedance locus.

cal circuit.[8] If these parameters were experimentally determined, there would be two possible approaches to the determination of cavity $Q$: the measured values of impedance $Z_{11}$ could be converted to the values of impedance $Z_{bb}$ at the cavity terminals, and the usual well-known procedures to analyze the resultant *ideal* impedance locus could be used; or, the measured impedance locus could be analyzed directly using the approach which is described below.

In many cases, however, the separation of the cavity from its coupling network is impractical or impossible; this leads to difficulties which are discussed more fully further on. It should be obvious that the value of parameter $R_s$ (*i.e.*, $\alpha$) can be determined immediately from the experimentally determined impedance locus at terminals 1-1.

Consider for the moment that the parameters $\alpha$, $\beta$, and $\gamma$ are all known. Since in many practical cases the coupling network losses are small and are due to *either* series or shunt elements, it is convenient at first to consider these two cases separately from the more general case.

*Case 1) Shunt Losses Only*

In this case, $\alpha = 0$, and (5) becomes

$$Z_{11} = \frac{\beta}{1 + j2Q_0'\delta} . \tag{7}$$

The apparent value $Q_0'$ can be found using the measured impedance locus.[9] The true value of $Q_0$ can be found from (6) which is repeated below.

$$Q_0 = Q_0' \frac{\gamma + 1}{\gamma} . \tag{8}$$

The evaluation of the true value of $Q_0$ *requires* the knowledge of the parameter $\gamma$.

[8] The parameters of the canonical network can be found as described in Felsen and Oliner, *op. cit.*, or Ginzton, *op. cit.*, pp. 343–345.
[9] See, for instance, Ginzton, *op. cit.*, pp. 406–424.

*Case 2) Series Losses Only*

In this case, $R_p = \infty$, and (5) becomes:

$$\frac{Z_{11}}{Z_0} = \alpha + \frac{\beta - \alpha}{1 + j2Q_0\delta} . \tag{9}$$

Assuming that an experimental impedance locus such as is shown in Fig. 4 has been obtained by measuring the impedance at a number of frequencies which are also measured, the $Q_0$ value can be found as follows.

Let $2Q_0\delta = \pm 1$. Substituting this into (9) and simplifying:

$$\frac{Z_{11}}{Z_0} = \frac{\beta + \alpha \pm j(\beta - \alpha)}{2} . \tag{10}$$

Using the values of $\alpha$ and $\beta$ obtained from the experimental plot for the given locus, the real and imaginary parts of (10) can be computed and located on the locus. This determines the two points on the locus for which $2Q_0\delta = \pm 1$. If the frequencies at which they occur are found to be $f_1$ and $f_2$, then

$$Q_0 = \delta_1 - \delta_2 = \frac{f_1 - f_2}{f_0} . \tag{11}$$

If the two points on the locus so determined do not correspond to the points for which the frequencies have been measured, the desired frequencies $f_1$ and $f_2$ can be found by means of an *auxiliary linear frequency scale* which can be constructed as indicated in Fig. 6, the geometrical construction for which is justified in the Appendix. Let points $a$, $b$, $c$, $d$, $e$, and $f$ represent a set of impedances measured at frequencies $f_a$, $f_b$, $f_c$, $f_d$, $f_e$, and $f_f$, respectively. A line $\overline{AB}$ is drawn perpendicularly to the resistive axis and radial lines are drawn from ($\alpha$, 0) through the known impedance points. The intercepts along line $AB$ are labeled with the known frequency $f_a \cdots f_e$ and are linear in frequency, thus permitting the determination of the frequency of any point along the impedance locus.

*Case 3) Series and Shunt Losses*

If both the series and shunt losses are present, and each is small, the $Q_0'$ value can be found, first using (11) which takes into account the presence of the series losses alone; the effect of the presence of the shunt losses can then be taken into account by multiplying this value by the correction factor given by (8).

If the losses are not small, the known parameters of the coupling network permit the calculation of the impedance at the reference plane $T_1$ for the half-power points (*i.e.*, $2Q_0\delta = \pm 1$). The two frequencies at which these impedances are actually found define the half-power bandwidth from which the $Q_0$ value can be computed. Alternatively, the impedance at $T_1$ can be measured as a function of frequency and each of the measured values converted by computation, resulting in the ideal impedance locus which can be analyzed by conventional means.

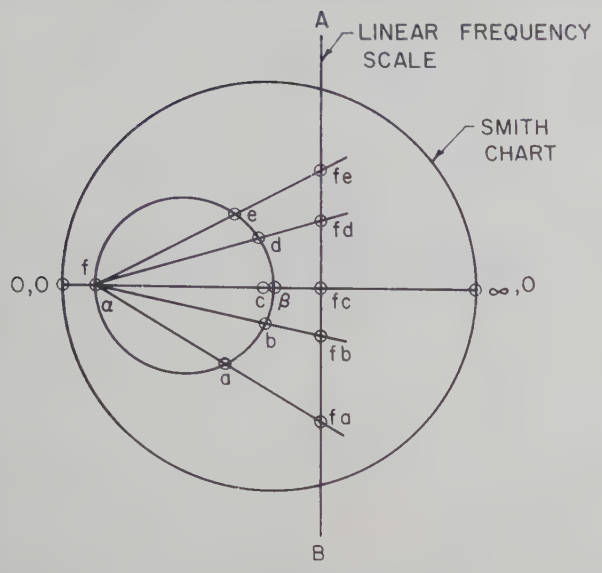


Fig. 6—Geometrical construction used to establish a linear frequency scale for interpolation between measured impedance points.

In some cases, the coupling network may happen to be an integral part of the cavity, making it impossible or impractical to determine the network constants. In this case, the observation of the impedance locus at the input of the coupling network allows the evaluation of the series losses $\alpha$ and the apparent value $Q_0'$. The separation of losses occurring within the resonant cavity and the coupling network becomes *impossible;* if this distinction happens to be important, some expedient must be found to separate the losses in the two parts of the structure. Sometimes this can be done by constructing an auxiliary structure susceptible to physical dismounting to permit a more complete experimental study of its parts.

## Determination of Loaded and External $Q$ Values

In addition to the natural or unloaded $Q$ values of the cavity, $Q_0$, other $Q$ values are important in the usual practice. These normally are $Q_L$ and $Q_{ext}$, the loaded and external $Q$ values, respectively. In the presence of losses, still other $Q$ values become relevant, as defined below. Using the conventional definition for $Q$, the following descriptive statements can be made:

$$Q_0 = 2\pi f \frac{\text{energy stored}}{\text{energy lost in the cavity proper}} \tag{12}$$

$$Q_0' = 2\pi f \frac{\text{energy stored}}{\text{energy lost in cavity and shunt element of coupling network}} \tag{13}$$

$$Q_0'' = 2\pi f \frac{\text{energy stored}}{\text{energy lost in cavity and coupling network}^9} \tag{14}$$

$$Q_L = 2\pi f \frac{\text{energy stored}}{\text{energy lost in cavity, coupling network, and load}} \tag{15}$$

$$Q_{ext} = 2\pi f \frac{\text{energy stored}}{\text{energy lost in the load}} . \tag{16}$$

For reference, in the absence of coupling network losses, these can be written as follows, using the notation shown in Fig. 1(b) (with the cavity coupled through the coupling network to a source with impedance equal to $Z_0$).[10]

$$Q_0 = \frac{\beta Z_0}{\omega L} = \omega C \beta Z_0 \tag{17}$$

$$Q_L = \omega C \frac{\beta Z_0^2}{\beta Z_0 + Z_0} \tag{18}$$

$$Q_{ext} = \omega C Z_0 \tag{19}$$

$$Q_0 = Q_0' = Q_0'' \tag{20}$$

and

$$\frac{1}{Q_L} = \frac{1}{Q_0} + \frac{1}{Q_{ext}} . \tag{21}$$

In the presence of coupling losses, the meaning of $Q_0$, $Q_0'$, $Q_0''$, and $Q_L$ remains clear and unambiguous. In the case of $Q_{ext}$, it is necessary to be specific about the meaning of the *load.* Referring to Fig. 3(b), it is natural to regard the source impedance $Z_0$ as the "load" upon the network and the cavity. However, in the design of certain electron devices, it is convenient to include part or all of the loss in the coupling network with the load. This leads to the following three cases.

*Case 1)*

Consider $Z_0$ alone as the load. In this case, the expression corresponding to (21) becomes:

$$\frac{1}{Q_L} = \frac{1}{Q_0''} + \frac{1}{Q_{ext}} . \tag{22}$$

*Case 2)*

Consider $Z_0$ and $R_s$ as the load, and

$$\frac{1}{Q_L} = \frac{1}{Q_0'} + \frac{1}{Q_{ext}} . \tag{23}$$

*Case 3)*

Consider $Z_0$, $R_s$, and $R_p$ as the load and

$$\frac{1}{Q_L} = \frac{1}{Q_0} + \frac{1}{Q_{ext}} . \tag{24}$$

Assuming that the values of $Q_0'$ and/or $Q_0$ have been experimentally obtained as described above, and assuming that the parameters $\alpha$, $\beta$, and $\gamma$ are known, the expressions for $Q_L$ and $Q_{ext}$ for the three cases can be written as follows.

Referring to Fig. 3(b), if $V$ is the voltage across $C$, then, from (12),

[10] *Ibid.*, pp. 393–397.

$$Q_0 = 2\pi f \frac{\frac{1}{2} CV^2}{\frac{1}{2}\left(\frac{V^2}{\beta'' Z_0}\right)} \tag{25}$$

$$Q_0 = \omega C \beta'' Z_0. \tag{26}$$

Similarly,

$$Q_0' = \omega C \beta'' Z_0 \frac{1}{1 + \beta'' Z_0 / R_p} \tag{27}$$

$$= \frac{\gamma}{\gamma + 1} \tag{28}$$

and,

$$Q_0'' = Q_0' \frac{(1+\alpha)^2}{1 + \alpha(2+\beta)} \tag{29}$$

$$= Q_0 \frac{\gamma}{1+\gamma} \cdot \frac{(1+\alpha)^2}{1+\alpha(2+\beta)} \tag{30}$$

$$Q_L = Q_0' \left(\frac{1+\alpha}{1+\beta}\right) \tag{31}$$

$$= Q_0 \frac{\gamma}{1+\gamma} \cdot \frac{1+\alpha}{1+\beta}. \tag{32}$$

The $Q$ external values can be found from (16) for the three conditions stated above or by combining (22), (23), and (24), with (29), (28), and (26), respectively. These lead to:

*Case 1*)

$$Q_{\text{ext}} = Q_0' \frac{(\alpha+1)^2}{\beta - \alpha} \tag{33}$$

*Case 2*)

$$Q_{\text{ext}} = Q_0' \frac{1+\alpha}{\beta - \alpha} \tag{34}$$

*Case 3*)

$$Q_{\text{ext}} = Q_0 \frac{1+\alpha}{\beta - \alpha + (\beta+1)/\gamma}. \tag{35}$$

Thus, if $\alpha$, $\beta$, and $\gamma$ are all known, it is possible to determine the various $Q$ values by using the appropriate relations. If $\gamma$ is not known, the remaining $Q$ values can still be computed, but only in terms of the *apparent* $Q$ value, $Q_0'$, a value which does not distinguish between the losses in the cavity and the shunt element of the coupling network.

## Conclusion

It has been shown that an arbitrary coupling network between a uniform transmission line and a cavity can be represented by means of an equivalent network consisting of series and shunt resistors which, qualitatively, represent the series and the shunt losses in the coupling network. If both of these can be measured by an independent calibration experiment, the $Q_0$ of the cavity can be determined unambiguously from the measurements of input impedance in the uniform transmission line as a function of frequency. If separate measurements cannot be made, the measurement of input impedance as a function of frequency permits the determination only of the apparent $Q$ value of the cavity, $Q_0'$. Unless the shunt losses in the coupling network are separately evaluated, this apparent $Q$ value does not distinguish between the losses in the coupling network and the cavity proper.

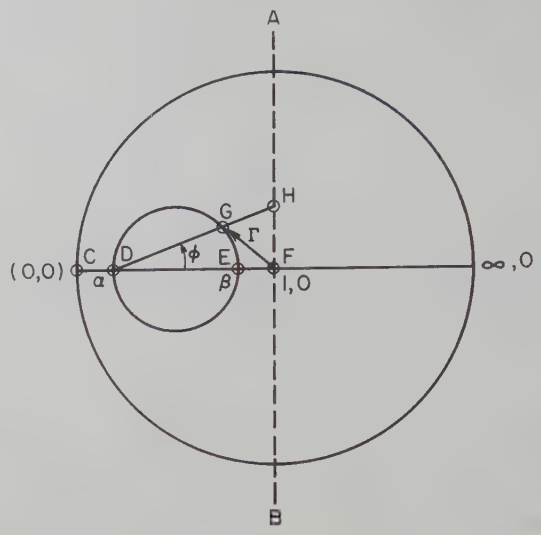


Fig. 7—Geometrical construction used to prove the linearity of the frequency scale.

## Appendix

### Construction of a Linear Frequency Scale

Fig. 6 shows the geometrical construction which may be used to establish a linear frequency scale in order to obtain frequencies for points along an impedance locus for which experimental frequency values are not available.

Referring to Fig. 7, draw a straight line perpendicular to the resistive axis; although the location of this line is immaterial, for the sake of simplicity in the proof, assume that it passes through the point ($R=1$, $X=0$). Radial lines originating from the point $(\alpha, 0)$ and passing through the point on the impedance locus for which the frequencies are known provide intercepts along the lines $A$-$B$ in frequency units. It will be shown below that the frequency along the axis $A$-$B$ is linear so that the frequency of any point on the locus can be determined by projecting a radial line from $(\alpha, 0)$ to $A$-$B$ and reading the distance along $A$-$B$ in frequency units (as established from the known frequency points). The proof of the construction is as follows.

Using the large circle in Fig. 7 to represent the *reflection coefficient* plane, the vector $\overline{FG}$ is the reflection coefficient $\Gamma$. The impedance value along the impedance locus is given by (5). The corresponding values of the

reflection coefficient can be computed from

$$\Gamma = \frac{Z_{11} - 1}{Z_{11} + 1} \tag{36}$$

or, combining with (5),

$$\Gamma = \frac{(\beta - 1) + j2Q_0\delta(\alpha - 1)}{(\beta + 1) + j2Q_0\delta(\alpha + 1)} . \tag{37}$$

Thus, when $2Q_0\delta = \pm \infty$,

$$\overline{DF} = |\Gamma_\infty|$$

$$\overline{DF} = \frac{1 - \alpha}{1 + \alpha} . \tag{38}$$

The distance

$$\overline{DG} = \overline{DF} + \Gamma$$

$$\overline{DG} = \frac{1 - \alpha}{1 + \alpha} + \frac{(\beta - 1) + j2Q_0\delta(\alpha - 1)}{(\beta + 1) + j2Q_0\delta(\alpha + 1)} \tag{39}$$

$$= \frac{2(\beta - \alpha)}{(\alpha + 1)(\beta + 1) + j(\alpha + 1)^2 2Q_0\delta} . \tag{40}$$

The phase angle $\Phi$, shown in Fig. 7, is equal to argument $\overline{DG}$ and is found from the ratio of imaginary to real parts of (40):

$$\Phi = \tan^{-1} \frac{2Q_0\delta(\alpha + 1)}{\beta + 1} . \tag{41}$$

The distance $\overline{FH}$, being proportional to tan $\Phi$, is proportional to $\delta$, *i.e.*, the frequency. Thus, the points projected from the locus onto the straight line $A$-$B$ produce intercepts whose lengths are proportional to frequency (*Q.E.D.*).

# The Excitation of a Dielectric Rod by a Cylindrical Waveguide*

C. M. ANGULO† AND W. S. C. CHANG‡

*Summary*—**This paper is a theoretical analysis of the excitation of the lowest circular symmetric TM surface wave along an infinite circular dielectric rod by a metallic cylindrical waveguide coaxial with the rod. The asymptotic expressions for all the fields are obtained by means of the Wiener-Hopf method. The expressions for the total average power transmitted to the surface wave, the total average power reflected, and the total power radiated, per unit incident power, are derived and computed for $\epsilon = 2.49$ for various radii of the dielectric rod.**

## Introduction

It is well known that a TM circular symmetric surface wave can be easily launched along a circular dielectric rod by a metallic cylindrical waveguide. A condensed theoretical analysis of an idealized version of this problem is given here. For the detailed analysis, the reader is referred to a previous report by the authors.[1]

The structure under consideration is represented in Fig. 1. It consists of an infinite circular dielectric rod of relative permittivity $\epsilon$ and radius $a$ fitted tight into a semi-infinite cylindrical waveguide of infinitely thin metallic wall which extends from $z = -\infty$ to $z = 0$.

The incident energy is carried by the $TM_{0,1}$ mode of the cylindrical metallic waveguide. It excites a TM surface wave along the rod, a reflected wave in the waveguide, and a scattered radiation at the end of the metallic waveguide. It is assumed here that along the dielectric rod only the lowest circular symmetric surface wave can exist and that the $TM_{0,1}$ mode is the only mode propagating inside the waveguide. This is true if $2.405(\epsilon - 1)^{-1/2} < Ka < 5.52\epsilon^{-1/2}$, where $K = 2\pi/\lambda_0$.

Since the structure considered (see Fig. 1) is independent of $\phi$ and the incident wave is the $TM_{0,1}$ mode, only the circular symmetric TM proper and improper modes are excited. Therefore, $\partial/\partial\phi = 0$ and $H_\rho = E_\phi = H_z = 0$. Furthermore, all the higher TM modes excited inside the cylindrical guide attenuate exponentially in the negative $z$ direction. It follows immediately that the far zone fields of our problem must be of the forms:

$$E_z = AJ_0(K_c\rho) \exp\left[-j(K^2\epsilon - K_c^2)^{1/2}z\right] + BJ_0(K_c\rho) \exp\left[j(K^2\epsilon - K_c^2)^{1/2}z\right] \tag{1}$$

$$H_\phi = \frac{jA\omega\epsilon\epsilon_0}{K_c} J_1(K_c\rho) \exp\left[-j(K^2\epsilon - K_c^2)^{1/2}z\right] + j\frac{B\omega\epsilon\epsilon_0}{K_c} J_1(K_c\rho) \exp\left[j(K^2\epsilon - K_c^2)^{1/2}z\right] \tag{2}$$

* Manuscript received by the PGMTT, February 14, 1958; revised manuscript received, June 2, 1958. The research described in this paper has been sponsored by the Cambridge AF Res. Ctr. under Contract AF 19(604)-1391 with Brown University.

† Brown University, Providence, R. I.

‡ Electronics Res. Lab., Stanford University, Stanford, Calif. Formerly at Brown University, Providence, R. I.

[1] C. M. Angulo and W. S. Chang, "Excitation of a Dielectric Rod by a Cylindrical Waveguide," Div. of Eng., Brown University, Providence, R. I., Scientific Rep. AF 1391/7; July, 1957.

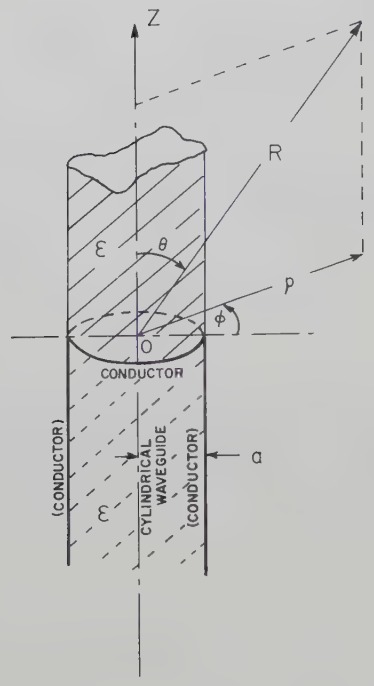


Fig. 1—The dielectric rod excited by a cylindrical waveguide.

for $Kz \ll -1$, inside the metallic waveguide

$$E_z = \frac{-g(\theta)\sin\theta e^{-jKR}}{R} + C\left[K_0(K\rho q)U(\rho-a) + \frac{K_0(Kaq)J_0(K\rho p)}{J_0(Kap)}U(a-\rho)\right] \cdot U(z)\exp\left[-jK(1+q^2)^{1/2}z\right] \quad (3)$$

$$H_\phi = \frac{\epsilon_0^{1/2}g(\theta)e^{-jKR}}{\mu_0^{1/2}R} - j\frac{\epsilon_0^{1/2}C}{\mu_0^{1/2}q}\left[K_1(K\rho q)U(\rho-a) + \frac{K_1(Kaq)J_1(K\rho p)}{J_1(Kap)} \cdot U(a-\rho)\right]U(z)\exp\left[-jK(1+q^2)^{1/2}z\right] \quad (4)$$

for $KR \gg 1$, outside the metallic waveguide, where $U$ stands for the Heaviside unit step function [$U(x)=0$ for $x<0$; $U(x)=1$ for $x>0$]. $A$ is the amplitude of the incident $TM_{0,1}$ mode inside the metallic cylindrical waveguide. $B$ is the amplitude of the reflected $TM_{0,1}$ mode inside the metallic waveguide. $C$ is the amplitude of the transmitted surface wave along the dielectric rod. $g(\theta)$ is the angular distribution function of the radiation field. $K_c$ is the cutoff wave number of the $TM_{0,1}$ mode inside the metallic guide ($K_c a$ = first zero of $J_0$).

$p$ and $q$ are the propagation wave numbers of the lowest TM circular symmetric surface wave.[2]

$$p^2 + q^2 = \epsilon - 1 \quad (5)$$

$$\epsilon q J_1(Kpa)K_0(Kqa) + pJ_0(Kpa)K_1(Kqa) = 0. \quad (6)$$

[2] S. A. Schelkunoff, "Electro-magnetic Waves," D. Van Nostrand Co., Inc., New York, N. Y., pp. 425–428; 1943.

## The Representation of the Fields

Mathematically, we separate the total fields into two parts,

$$E_z = E_{0z} + \mathcal{E}_z, \qquad H_\phi = H_{0\phi} + \mathcal{H}_\phi, \quad (7)$$

where

$$H_{0\phi} = A\frac{j\omega\epsilon_0\epsilon}{K_c}J_1(K_c\rho)U(a-\rho)\exp\left[-j(K^2\epsilon - K_c^2)z\right] \quad (8)$$

$$E_{0z} = AJ_0(K_c\rho)U(a-\rho)\exp\left[-j(K^2\epsilon - K_c^2)z\right]. \quad (9)$$

$H_{0\phi}$ and $E_{0z}$ obviously have the meaning of the incident wave. Whereas, $\mathcal{H}_\phi$ and $\mathcal{E}_z$ are the incomplete scattered fields. We represent these two incomplete scattered fields $\mathcal{H}_\phi$ and $\mathcal{E}_z$ by their Fourier transforms,

$$\mathcal{H}_\phi = \frac{1}{(2\pi)^{1/2}}\int_{-\infty}^{+\infty}\left[\frac{I(\eta,\rho)}{\rho}\right]e^{-j\eta z}d\eta, \quad (10)$$

$$\mathcal{E}_z = \frac{-1}{(2\pi)^{1/2}}\int_{-\infty}^{+\infty}[V(\eta,\rho)]e^{-j\eta z}d\eta. \quad (11)$$

## The Equation of the Fourier Transforms at $\rho = a$

Since $E_{0z}$ and $H_{0\phi}$ satisfy the steady-state Maxwell's equations with time dependence $e^{+j\omega t}$ for $\rho \lessgtr a$, $\mathcal{E}_z$ and $\mathcal{H}_\phi$ must satisfy them also in the same regions. This means that $V(\eta,\rho)$ and $I(\eta,\rho)$ for $\rho \lessgtr a$ are[1]

$$V = V(\eta, a_-)\frac{J_0(\Lambda_d\rho)}{J_0(\Lambda_d a)}U(a_- - \rho) + V(\eta, a_+)\frac{H_0^{(2)}(\Lambda_a\rho)}{H_0^{(2)}(\Lambda_a a)}U(\rho - a_+), \quad (12)$$

$$I = -jY_dV(\eta, a_-)\frac{J_1(\Lambda_d\rho)}{J_0(\Lambda_d a)}U(a_- - \rho) - jY_aV(\eta, a_+)\frac{H_1^{(2)}(\Lambda_a\rho)}{H_0^{(2)}(\Lambda_a a)}U(\rho - a_+), \quad (13)$$

$$\Lambda_a = (K^2 - \eta^2)^{1/2}, \quad (14a)$$

$$\Lambda_d = (K^2\epsilon - \eta^2)^{1/2} \quad (14b)$$

$$Z_a = \frac{1}{Y_a} = \frac{(K^2 - \eta^2)^{1/2}}{\omega\epsilon_0\rho}, \quad (15a)$$

$$Z_d = \frac{1}{Y_d} = \frac{(K^2\epsilon - \eta^2)^{1/2}}{\omega\epsilon_0\epsilon\rho} \quad (15b)$$

where the subscript plus means $\lim_{\rho\to a}$ from $\rho > a$ and the subscript minus means $\lim_{\rho\to a}$ from $\rho < a$.

At $\rho = a$, $V(\eta,\rho)$ and $I(\eta,\rho)$ must satisfy the boundary conditions determined by $E_z$ and $H_\phi$, *i.e.*,

1) $\mathcal{E}_z = 0$ for $z<0$.
2) $\mathcal{E}_z(z, a_+) = \mathcal{E}_z(z, a_-) = \mathcal{E}_z(z, a)$ for all $z$.
3) $\mathcal{H}_\phi(z, a_+) - \mathcal{H}_\phi(z, a_-) = H_{0\phi}(z, a_-)$ for $z>0$.

Let

$$g^+(\eta, a) = \frac{1}{(2\pi)^{1/2}}\int_0^{+\infty}[\mathcal{H}_\phi(z, a_+) - \mathcal{H}_\phi(z, a_-)]e^{j\eta z}dz, \quad (16)$$

$$\mathcal{G}^-(\eta, a) = \frac{1}{(2\pi)^{1/2}} \int_{-\infty}^{0} [\mathcal{H}_\phi(z, a_+) - \mathcal{H}_\phi(z, a_-)] e^{j\eta z} dz, \quad (17)$$

$$V^+(\eta, a) = \frac{-1}{(2\pi)^{1/2}} \int_{0}^{+\infty} \mathcal{E}_z(z, a) e^{j\eta z} dz, \quad (18)$$

$$V^-(\eta, a) = \frac{-1}{(2\pi)^{1/2}} \int_{-\infty}^{0} \mathcal{E}_z(z, a) e^{j\eta z} dz. \quad (19)$$

$\mathcal{G}_m(\eta) > -W_d$, where $W_d > 0$, $W_d < |\mathcal{G}_m(K)|$, $W_d < |\mathcal{G}_m[(K^2\epsilon - K_c^2)^{1/2}]|$, and $W_d < |\mathcal{G}_m[K(1+q^2)^{1/2}]|$.[3] On the other hand, $F(\eta)$ is analytic and free of zeros inside a narrow strip $2W_d$ about the real axis of the $\eta$ plane. Therefore, we can rearrange (20) into a new equation where the left-hand side is analytic for $\mathcal{G}_m(\eta) < W_d$ and the right-hand side is analytic for $\mathcal{G}_m(\eta) > -W_d$ as follows:[1]

$$\frac{\mathcal{G}^-(\eta, a)(K+\eta)^{1/2}[\eta + (K^2\epsilon - K_c^2)^{1/2}]}{[\eta + K(1+q^2)^{1/2}] \exp[\xi^-(\eta)]} - \frac{\omega\epsilon\epsilon_0 a A J_1(K_c a)}{(2\pi)^{1/2} K_c [\eta - (K^2\epsilon - K_c^2)^{1/2}}$$
$$\cdot \left\{ \frac{[\eta + (K^2\epsilon - K_c^2)^{1/2}](K+\eta)^{1/2}}{[\eta + K(1+q^2)^{1/2}] \exp[\xi^-(\eta)]} - \frac{2(K^2\epsilon - K_c^2)^{1/2}[K + (K^2\epsilon - K_c^2)^{1/2}]^{1/2}}{[(K^2\epsilon - K_c^2)^{1/2} + K(1+q^2)^{1/2}] \exp[\xi^-\{(K^2\epsilon - K_c^2)^{1/2}\}]} \right\}$$
$$= \frac{\omega\epsilon_0(\epsilon+1) a [\eta - K(1+q^2)^{1/2}] V^+(\eta, a)}{[\eta - (K^2\epsilon - K_c^2)^{1/2}](K-\eta)^{1/2} \exp[\xi^+(\eta)]}$$
$$+ \frac{2\omega\epsilon\epsilon_0 a J_1(K_c a)(K^2\epsilon - K_c^2)^{1/2}[K + (K^2\epsilon - K_c^2)^{1/2}]^{1/2}}{(2\pi)^{1/2} K_c [\eta - (K^2\epsilon - K_c^2)^{1/2}][(K^2\epsilon - K_c^2)^{1/2} + K(1+q^2)^{1/2}] \exp[\xi^-\{K^2\epsilon - K_c^2)^{1/2}\}]} \quad (22)$$

Then the boundary conditions 1), 2), and 3) give[1]

$$\mathcal{G}^-(\eta, a) = \frac{\omega\epsilon_0(\epsilon+1) a [\eta^2 - K^2(1+q^2)]}{\Lambda_a [\eta^2 - (K^2\epsilon - K_c^2)]} F_{(\eta)} V^+(\eta, a)$$
$$+ \frac{\omega\epsilon_0 a A J_1(K_c a)}{(2\pi)^{1/2} K_c [\eta - (K^2\epsilon - K_c^2)^{1/2}]} \quad (20)$$

where

$$F_{(\eta)} = \frac{j\Lambda_a [\eta^2 - (K^2\epsilon - K_c^2)]}{\left(1 + \frac{1}{\epsilon}\right)[\eta^2 + K^2(1+q^2)]}$$
$$\cdot \frac{J_1(\Lambda_d a) - \frac{\Lambda_d}{\epsilon\Lambda_a} \frac{H_1^{(2)}(\Lambda_a a)}{H_0^2(\Lambda_a a)} J_0(\Lambda_d a)}{\Lambda_d J_0(\Lambda_d a)}. \quad (21)$$

where

$$\xi^-(\eta) = \frac{-1}{2\pi j} \int_{-\infty+jW^d}^{+\infty+jW_d} \frac{\ln F(\xi)}{\xi - \eta} d\xi, \quad (23)$$

$$\xi^+(\eta) = \frac{-1}{2\pi j} \int_{-\infty-jW^d}^{+\infty-jW_d} \frac{\ln F(\zeta)}{\zeta - \eta} d\zeta. \quad (24)$$

$\xi^-(\eta)$ is analytic for $\mathcal{G}_m(\eta) < W_d$. $\xi^+(\eta)$ is analytic for $\mathcal{G}_m(\eta) > -W_d$.

Both sides of (22) are analytic for $|\mathcal{G}_m(\eta)| < W_d$. Thus, they are the analytic continuation of each other. We can show from their asymptotic behaviors that they must both be identically equal to the constant zero.[1]

Hence,

$$V^+(\eta, a) = -\frac{2\epsilon A J_1(K_c a)(K^2\epsilon - K_c^2)^{1/2}[K + (K^2\epsilon - K_c^2)^{1/2}]^{1/2}(K-\eta)^{1/2} \exp[\xi^+(\eta) - \xi^-\{(K^2\epsilon - K_c^2)^{1/2}\}]}{(2\pi)^{1/2} K_c [(K^2\epsilon - K_c^2)^{1/2} + K(1+q^2)^{1/2}](\epsilon+1)[\eta - K(1+q^2)^{1/2}]}, \quad (25)$$

$$\mathcal{G}^-(\eta, a) = \frac{A\omega\epsilon_0\epsilon a J_1(K_c a)[\eta + K(1+q^2)^{1/2}] \exp[\xi^-(\eta)]}{K_c [\eta^2 - (K^2\epsilon - K_c^2)](2\pi)^{1/2} [\eta - K(1+q^2)^{1/2}]}$$
$$\cdot \left[ \frac{(K+\eta)^{1/2}[\eta + (K^2\epsilon - K_c^2)^{1/2}]}{[\eta + K(1+q^2)^{1/2}] \exp[\xi^-(\eta)]} - \frac{2(K^2\epsilon - K_c^2)^{1/2}[K - (K^2\epsilon - K_c^2)^{1/2}]^{1/2}}{[(K^2\epsilon - K_c^2)^{1/2} + K(1+q^2)^{1/2}] \exp[\xi^-\{(K^2\epsilon - K_c^2)^{1/2}\}]} \right]. \quad (26)$$

## The Solutions of the Far Zone Fields

In slightly dissipative media, $K$, $(K^2\epsilon - K_c^2)^{1/2}$, and $K(1+q^2)^{1/2}$ must have a small negative imaginary part to comply with the law of conservation of energy. It follows that $\mathcal{G}^-(\eta, a)$ must be analytic for $\mathcal{G}_m(\eta) < W_d$ and that $\mathcal{G}^+(\eta, a)$ and $V^+(\eta, a)$ must be analytic for

In this section, we have regarded (22) valid for all $\eta$. Thus the solutions expressed in (25) and (26) are equal to the solutions of $\mathcal{G}^-(\eta, a)$ and $V^+(\eta, a)$ associated with the physical fields only for $|\mathcal{G}_m(\eta)| < W_d$. Never-

[3] P. M. Morse and H. Feshbach, "Methods of Theoretical Physics," McGraw-Hill Book Co., Inc., New York, N. Y., pp. 453–471; 1953.

theless, these $g^-(\eta, a)$ and $V^+(\eta, a)$ will yield the correct far zone fields through the inverse Fourier transform, since the inverse transform is performed on the real $\eta$ axis.

Carrying out the inverse transforms of $\mathcal{E}_z$ and $\mathcal{H}_\phi(z,a_+) - \mathcal{H}_\phi(z, a_-)$ by means of the method of steepest descent and then comparing them with (1) to (4), we obtain:[1]

$$CK_0(Kqa) = (2\pi j)^{1/2} \lim_{\eta \to K(1+q)^{1/2}} [\{\eta - K(1+q^2)^{1/2}\} V^+(\eta, a)] \cdot U\left[\frac{\pi}{4} - \frac{\theta}{2} - \arctan\{(1+q^2)^{1/2} - q\}\right], \quad (27)$$

$$g(\theta) = j\left(\frac{2}{\pi}\right)^{1/2} \csc\theta \frac{V^+(K\cos\theta, a)}{H_0^{(2)}(Ka\sin\theta)}, \quad (28)$$

and

$$BJ_1(K_c a) = \frac{-(2\pi)^{1/2} K_c}{\omega\epsilon_0\epsilon a} \lim_{\eta \to -(K^2\epsilon - K_c^2)^{1/2}} \cdot \{[\eta + (K^2\epsilon - K_c^2)^{1/2}] g^-(\eta, a)\}. \quad (29)$$

The answers here to the reflected coefficient $B$ and transmitted coefficient $C$ are exact. The answer of $g(\theta)$ is only evaluated to the first term of the asymptotic series, but accuracy of $g(\theta)$ obviously can be readily improved by evaluating more terms of the asymptotic series.

## The Excitation Efficiency and the Calculation of Power Reflected, Transmitted, and Radiated

Due to the orthogonality of the proper and improper modes, the average power radiated, reflected, and transmitted, can be derived by Poynting's theorem from $g(\theta)$, $B$, and $C$, alone. After some tedious manipulations, we obtained the following expression for the reflected power $R$, transmitted power $T$ (excitation efficiency), and radiation loss $L$, per unit incident power.[1]

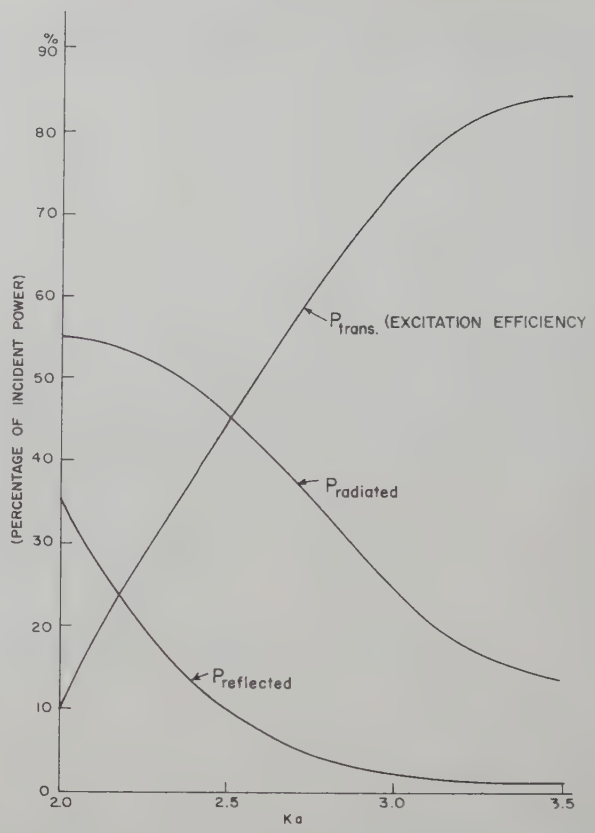


Fig. 2—Plot of the powers radiated, transmitted, and reflected.

for $0 < \theta < \pi$ per unit angle. Where

$$E(\alpha) = \frac{-2\alpha^{1/2}}{\pi K^2 a^2} \cdot \int_0^{Ka} \left[\frac{\arctan[W_{(x)}]}{1 - \frac{x^2}{K^2a^2} - \alpha}\right] \frac{x\,dx}{\left(1 - \frac{x^2}{K^2a^2}\right)^{1/2}}. \quad (33)$$

$$T = \frac{4(1+q^2)^{1/2}\left(\epsilon - \frac{K_c^2}{K^2}\right)^{1/2}\left[\left(\epsilon - \frac{K_c^2}{K^2}\right)^{1/2} + 1\right][(1+q^2)^{1/2} - 1]}{q\left[\left(\epsilon - \frac{K_c^2}{K^2}\right)^{1/2} + (1+q^2)^{1/2}\right]^2\left(\epsilon - 1 - \frac{K_c^2}{K^2}\right)^{1/2}} \exp\left[E(1+q^2) - E\left(\epsilon - \frac{K_c^2}{K^2}\right)\right], \quad (30)$$

$$R = \frac{\left[(1+q^2)^{1/2} - \left(\epsilon - \frac{K_c^2}{K^2}\right)^{1/2}\right]^2\left[\left(\epsilon - \frac{K_c^2}{K^2}\right)^{1/2} + 1\right]}{\left[(1+q^2)^{1/2} + \left(\epsilon - \frac{K_c^2}{K^2}\right)^{1/2}\right]^2\left[\left(\epsilon - \frac{K_c^2}{K^2}\right)^{1/2} - 1\right]} \exp\left\{-2E\left(\epsilon - \frac{K_c^2}{K^2}\right)\right\}, \quad (31)$$

$$L = \frac{4\left(\epsilon - \frac{K_c^2}{K^2}\right)^{1/2}\left[\left(\epsilon - \frac{K_c^2}{K^2}\right)^{1/2} + 1\right]\left(p^2 - \frac{K_c^2}{K^2}\right)(1 - \cos\theta)(q^2 + \sin^2\theta)}{\epsilon\pi\left[\left(\epsilon - \frac{K_c^2}{K^2}\right)^{1/2} + (1+q^2)^{1/2}\right]^2\left(\epsilon - 1 - \frac{K_c^2}{K^2}\right)^{1/2}[(1+q^2)^{1/2} - \cos\theta]^2\left(\epsilon - \frac{K_c^2}{K^2} - \cos^2\theta\right)} \cdot \frac{(\epsilon - \cos^2\theta)^{1/2} J_0[Ka(\epsilon - \cos^2\theta)^{1/2}] \exp\left[E(\cos^2\theta) - E\left(\epsilon - \frac{K_c^2}{K^2}\right)\right]}{\{4(\epsilon - \cos^2\theta) J_0^2[Ka(\epsilon - \cos^2\theta)^{1/2}] + \pi^2 K^2 a^2 \sin^2\theta M^2(\theta)\}^{1/2}}. \quad (32)$$

$$W_{(x)} = -\frac{\pi\epsilon x^2 J_1\{[K^2a^2(\epsilon-1)+x^2]^{1/2}\}[J_0^2(x)+N_0^2(x)]}{2[K^2a^2(\epsilon-1)+x^2]^{1/2}J_0\{[K^2a^2(\epsilon-1)+x^2]^{1/2}\}} - \frac{\pi x}{2}[J_1(x)J_0(x) - N_1(x)N_0(x)], \quad (34)$$

$$M(\theta) = J_1[Ka(\epsilon-\cos^2\theta)^{1/2}]\epsilon\sin\theta[J_0^2(\beta)+N_0^2(\beta)] - (\epsilon-\cos^2\theta)^{1/2}J_0[Ka(\epsilon-\cos^2\theta)^{1/2}] \cdot [J_1(\beta)J_0(\beta)+N_1(\beta)N_0(\beta)], \quad (35)$$

$$\beta = Ka\sin\theta. \quad (36)$$

$$\text{Total power radiated} = \int_0^{\pi} L(\theta)d\theta. \quad (37)$$

Eqs. (30) and (31) are computed numerically on the computer for $\epsilon=2.49$ for various values of $Ka$. These numerical results are plotted in Fig. 2. From these results it is clear that

1) The excitation efficiency for $Ka>3$ is quite high (above 70 per cent). Hence it is an efficient way of excitation. The excitation efficiency does not depend critically upon the precise values of $Ka$.
2) The larger the normalized cross section of the dielectric rod ($Ka$) is, the higher is the excitation efficiency.
3) The excitation efficiency curve resembles very closely the efficiency curves obtained in exciting a corrugated surface[4] or a dielectric slab.[5]
4) The excitation efficiency can be improved by flaring out the edge of the metallic waveguide at $z=0$ to accommodate a larger dielectric rod without causing a second mode to propagate inside the metallic waveguide.

[4] A. L. Cullen, "The excitation of plane surface waves," *Proc. IEE*, Monograph No. 93, vol. 101, pt. 4; 1954.
[5] C. M. Angulo and W. S. C. Chang, "On the Excitation of Surface Waves, Part I, II, and III," Div. of Eng., Brown University, Providence, R. I., Scientific Reps. No. AF 1391/3 to AF 1391/5, pp. 67–72; 1956.

# An Investigation of the Properties of Germanium Mixer Crystals at Low Temperatures*

L. K. ANDERSON† AND A. HENDRY‡

*Summary*—**Experimental determinations of the noise temperature ratio, IF resistance, and conversion loss of 1N263 germanium mixer diodes operated in an *X*-band receiver are presented as a function of mixer temperature for the range −196°C to 27°C. No improvement in receiver noise factor was obtained by cooling the mixer to −196°C; however an improvement of 0.3 to 0.6 db was observed by cooling to a temperature in the region −100°C to −50°C. The exact value of the improvement and the optimum temperature depends on the individual crystal, as well as on dc bias and local oscillator drive.**

## I. Introduction

It has been suggested,[1] largely on theoretical grounds, that the over-all noise factor of a superheterodyne receiver, employing a germanium crystal mixer, may be improved by cooling the crystal to a temperature substantially below the ambient temperature. The work discussed in this paper was carried out in an effort to verify this prediction, and also to determine how the various crystal parameters, such as IF resistance and noise temperature ratio, vary with temperature in the range from room temperature to the boiling point of nitrogen (about −196°C). The work was carried out at 9375 mc, using type 1N263 germanium diodes.

## II. Measurement of Crystal and System Parameters

Fig. 1 is a block diagram of the apparatus, with which the following parameters may be determined: over-all receiver noise factor, IF amplifier noise factor, and the noise temperature ratio, IF resistance, and conversion loss of the crystal mixer. The over-all receiver noise factor and the IF amplifier noise factor are determined by standard methods, *e.g.*, fluorescent lamp waveguide noise source followed by a precision waveguide attenuator for the over-all noise factor, and a temperature limited noise diode with 3-db attenuator in the IF amplifier for the IF noise factor.

The methods used for the measurement of the crystal parameters are largely those described by Torrey and Whitmer.[2]

* Manuscript received by the PGMTT, February 25, 1958; revised manuscript received, June 25, 1958.
† Microwave Lab., Stanford University, Stanford, Calif.; formerly at Natl. Res. Council, Ottawa 2, Ont., Can.
‡ Natl. Res. Council, Ottawa 2, Ont., Can.
[1] G. C. Messenger, "Cooling of microwave crystal mixers and antennas," IRE Trans. on Microwave Theory and Techniques, vol. MTT-5, pp. 62–63; January, 1957.

[2] H. C. Torrey and C. A. Whitmer, "Crystal Rectifiers," M.I.T. Rad. Lab. Ser., McGraw-Hill Book, Co., Inc., New York, N. Y., vol. 15, pp. 223–226; 1948.

### A. Noise Temperature Ratio

For the measurement of the noise temperature ratio of the crystal, the output meter of the receiver was calibrated by means of a resistance cartridge in place of the crystal. For calibration, the resistance cartridge was made noisy by means of a current $I$ passing through the noise diode. Such a resistor has a noise temperature ratio given by:[3]

$$t = \frac{T}{T_0} + 20IR \tag{1}$$

where

$t$ = noise temperature ratio,
$T$ = absolute temperature of resistance cartridge,
$T_0$ = 290°K, the standard temperature,
$R$ = resistance of cartridge, which serves as the noise diode plate load.

The use of a Roberts coupling circuit[4] allowed calibration of the output meter directly in terms of crystal noise temperature ratio without knowledge of the IF resistance. Provided that the resistance was in the range 100–200 ohms, and that the noise temperature ratio did not exceed 2, $t$ could be determined within about 5 per cent by this method.

### B. Crystal IF Resistance

The IF resistance was determined from the change in noise power output of the amplifier occasioned by a specified change in diode plate current, using the crystal as a diode load. A calibration was made using resistor cartridges of known resistance.

### C. Conversion Loss

The conversion loss may be calculated from the expression for over-all noise factor

$$L = \frac{F_{\text{rec}}}{F_{\text{IF}} + (t - 1)} . \tag{2}$$

However, the need for separate knowledge of $F_{\text{IF}}$ and $t$ may be circumvented by a measurement using the crystal as a plate load for the noise diode in place of the usual load resistor in the standard measurement of $F_{\text{IF}}$. With this change, the quantity measured is essentially the denominator of (2), and it may then be shown[5] that the conversion loss is given by:

$$L = \frac{F_{\text{rec}}}{20I_D R_{\text{IF}}} \tag{3}$$

where $I_D$ is the diode plate current to double the noise power output of the IF amplifier.

*Note:* The accuracy of the value of $R_{\text{IF}}$ determined in Part B above is limited by uncertainties in the measurement of the change of output power. A more accurate value may be obtained by combining (2) and (3) to obtain:

$$R_{\text{IF}} = \frac{F_{\text{IF}} + t - 1}{20I_D} . \tag{4}$$

Since $F_{\text{IF}}$ is a slowly varying function of $R_{\text{IF}}$, the less accurate value of $R_{\text{IF}}$ determined in Part B may be used to obtain $F_{\text{IF}}$ for insertion in (4).

## III. Apparatus and Experimental Techniques

A block diagram of the entire setup is shown in Fig. 1. Fig. 2 is a photograph of the crystal mount and cooling bath.

### A. RF Section

All of the RF components, with the exception of the crystal mount, are completely conventional. The TR tube in the local oscillator line was used as a noise filter, and was tuned to the local oscillator frequency. At the signal frequency the attenuation of the filter was sufficient to reduce the LO noise to insignificance.

The crystal mount used was a simple broad-band type, primarily designed for detector use. The VSWR of the mount itself, which was never more than 2 for any of the crystals tested, was reduced to better than 1.1 for every determination by means of a slide-screw tuner ahead of the crystal mount. The use of this type of holder was established by two requirements: 1) The mount had to be easily cooled and so had to be small, and 2) it had to be capable of being sealed against the entry of the coolant (liquid nitrogen) and circulating air; thus no internal tuning adjustments could be used.

Fig. 3 is a sketch of the crystal mount assembly. The crystal mount was cooled by immersion in liquid nitrogen (boiling point: −195.8°C) to the level indicated. In order to prevent condensation of oxygen in the crystal mount it was necessary to seal it off from the rest of the waveguide by means of a thin celluloid window.

A one-foot section of "Glas-guide" was placed between the crystal mount and the rest of the waveguide system. This waveguide, with a thermal conductivity only one-hundredth that of equivalent brass waveguide, provided the necessary thermal isolation. In addition, the long vertical section of "Glas-guide" provided a column of stagnant air which, except on very humid days, prevented the appearance of any significant amounts of frost inside the waveguide despite a considerable accumulation on the outside.

With the crystal mount at the desired temperature, the dc bias was set to the desired value with no RF excitation, and then the local oscillator drive was adjusted to give the desired total crystal current. The crystal mount VSWR, measured at the local oscillator frequency (9375 mc), was then reduced to less than 1.05 by means of the slide-screw tuner.

Details of the crystal bias supply are given in Fig. 4.

[3] *Ibid.*, p. 230.
[4] *Ibid.*, p. 231.
[5] T. Nicoll, "Noise in silicon microwave diodes," *Proc. IEE*, pt. 3, vol. 101, pp. 317–324; September, 1954.

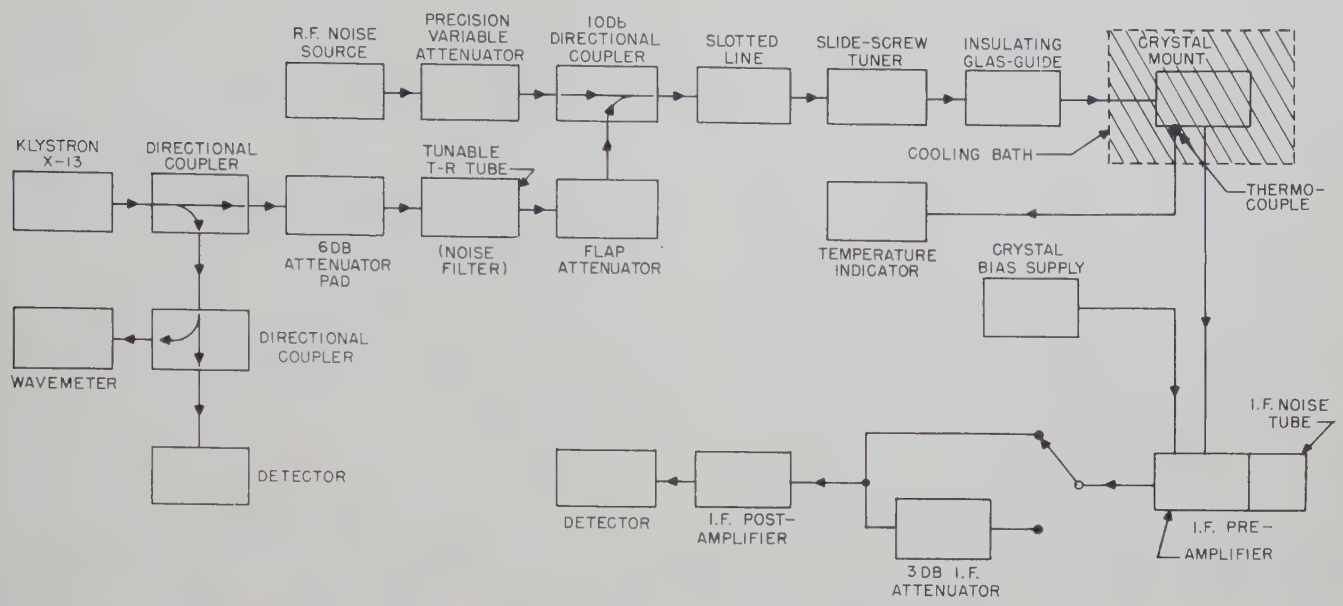


Fig. 1—Block diagram of test set-up.

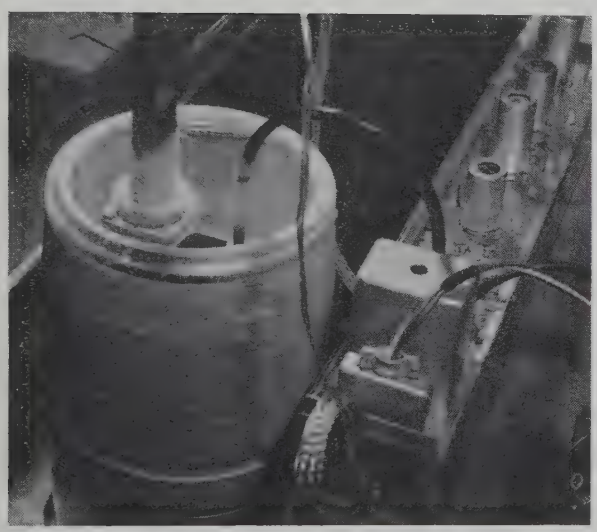

Fig. 2—Crystal mount and cooling bath.

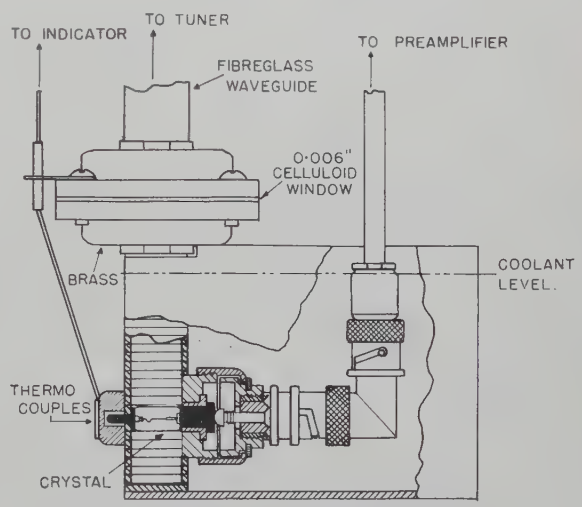


Fig. 3 Crystal holder assembly.

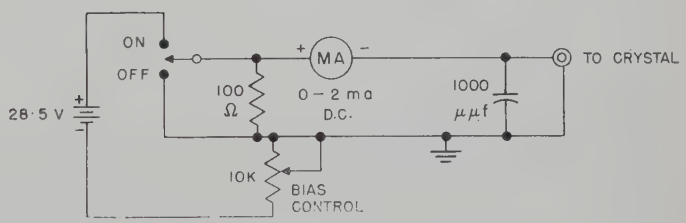


Fig. 4—Crystal bias supply.

### B. IF Section

The IF amplifiers constructed were of conventional design except for the Roberts coupling circuit used at the input to the preamplifier.

The IF amplifier bandwidth is 1 mc, while the center frequency is 30 mc.

The detector circuit employed is approximately square law, but for accurate determination of relative output power levels, as required in the determination of $R_{IF}$, the IF power was measured directly at 30 mc by a barretter bridge at the output of the post-amplifier.

## IV. Experimental Results

### A. Comparison of Over-all Receiver Noise Factor at Room Temperature and at −196°C

Using the gas discharge RF noise source, the over-all receiver noise factor $F_{rec}$ was measured: 1) at room temperature, 2) at −196°C, and 3) at room temperature again. This was done for twelve 1N263 crystals. The results of the measurements are given in Table I.

For the above determinations, the crystals were biased as follows:

At 27°C: dc bias current 0.9 ma, with local oscillator drive adjusted to give 1.8-ma total crystal current.

At −196°C: dc bias current 0.3 ma, with local oscillator drive adjusted to give 1.8-ma total crystal current.

TABLE I
COMPARISON OF NOISE FACTORS AT 27°C AND −196°C

| Crystal No. | $F_{rec}$ db | | |
|---|---|---|---|
| | 27°C | −196°C | 27°C |
| 1 | 10.9 | 11.1 | 10.9 |
| 2 | 11.7 | 12.9 | 11.7 |
| 3 | 11.4 | 11.6 | 11.5 |
| 4 | 10.4 | 11.1 | 10.5 |
| 5 | 10.3 | 9.9 | 10.4 |
| 6 | 11.1 | 11.0 | 11.1 |
| 7 | 11.4 | 15.4 | 11.9 |
| 8 | 11.3 | 11.6 | 10.4 |
| 9 | 11.2 | 11.4 | 10.4 |
| 10 | 10.5 | 10.6 | 11.0 |
| 11 | 11.5 | 12.3 | 10.4 |
| 12 | 11.4 | 10.8 | 10.7 |

TABLE II
CRYSTAL PARAMETERS AT 27°C AND −196°C

| Crystal No. | Temp. °C | $t$ (ratio) | $R_{IF}$ (ohms) | $L$ (ratio) | $F_x = Lt$ (ratio) |
|---|---|---|---|---|---|
| 1 | 27 | 1.35 | 118 | 4.41 | 5.95 |
| | −196 | 1.99 | 169 | 3.70 | 7.36 |
| | 27 | 1.35 | 117 | 4.72 | 6.38 |
| 2 | 27 | 1.33 | 124 | 4.02 | 5.35 |
| | −196 | 1.86 | 177 | 2.97 | 5.52 |
| | 27 | 1.33 | 126 | 3.92 | 5.22 |

The room temperature bias is that recommended by the crystal manufacturer, while the dc bias used at −196°C is that value which was found by experiment to produce the minimum average value of $F_{rec}$ for the twelve crystals in the group, when the local oscillator excitation was fixed at a value sufficient to provide 1.8-ma total current.

With the exception of crystal no. 7, these results indicate no consistent trend of either improvement or deterioration, although it is of interest to note that the worst crystal at room temperature suffered a deterioration, while the best showed an improvement upon cooling. Most of the others showed little change.

*B. Comparison of Crystal Parameters at Room Temperature and at −196°C*

Using the method outlined in Part A above, extensive measurements were made on three 1N263 crystals. One of these showed an excessive change in room temperature parameters after the cooling cycle, and therefore the results for this crystal were discarded. Data obtained on the remaining two are presented in Table II.

The bias conditions were as follows:

At 27°C: dc bias current 0.9 ma, with local oscillator drive adjusted to give 1.8-ma total crystal current;
At −196°C: dc bias current 0.3 ma, with local oscillator drive adjusted to give 2.0-ma total crystal current.

(Considering only the two crystals for which data are given in Table II, a total bias current of 2.0 ma rather than 1.8 ma yielded the minimum average value of $F_{rec}$.)

In both cases, although there was a slight reduction in the conversion loss at −196°C, the increase in the noise temperature ratio resulted in a net deterioration of the crystal noise factor.

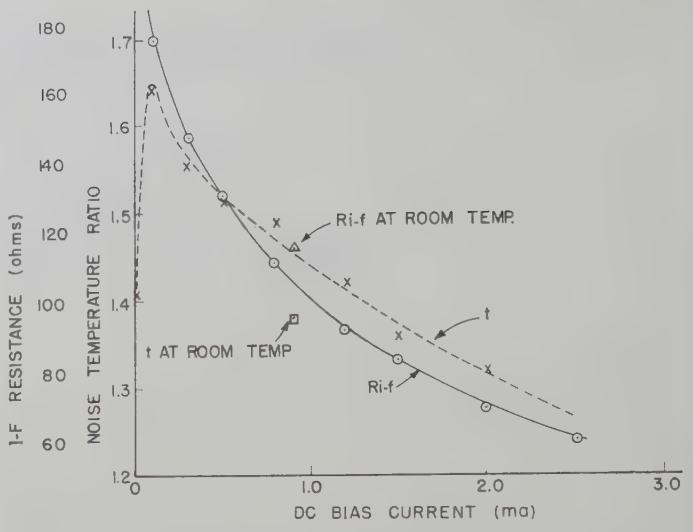


Fig. 5—Crystal IF resistance and noise temperature ratio as a function of bias at −196°C.

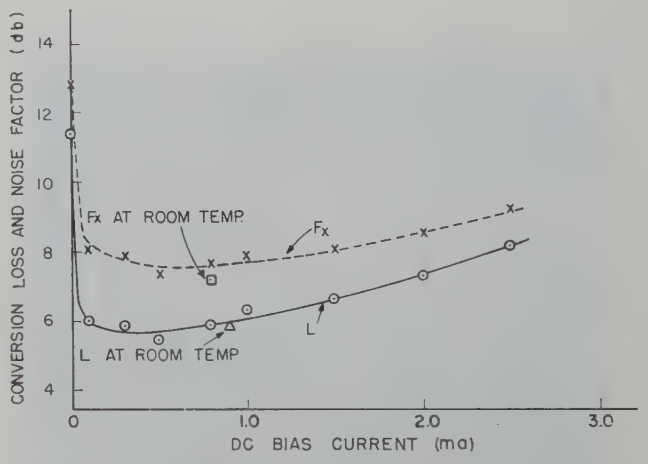


Fig. 6–Crystal conversion loss and noise factor as a function of bias at −196°C.

*C. Variation of Crystal Parameters at −196°C with DC Forward Bias*

It was felt that a combination of bias and local oscillator drive differing from the values used in obtaining the preceding data might result in some net improvement of crystal noise factor. The effect of the variation of dc forward bias was investigated for a single crystal. The local oscillator level used was about 0.5 milliwatt, a value which had been found to be sufficiently close to optimum on the basis of some rough preliminary measurements. The results of these measurements are shown in Figs. 5 and 6. Room temperature values for these parameters, with 0.9-ma current bias, are also indicated.

These curves indicate that the optimum value of dc

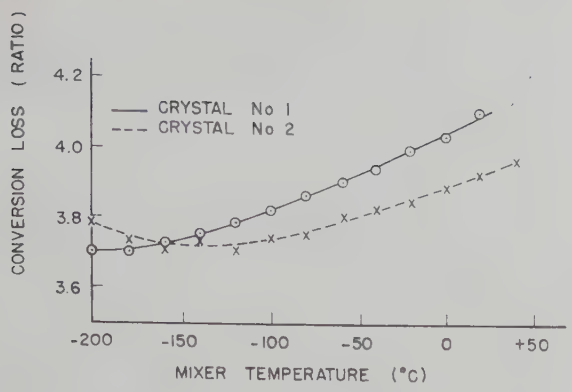


Fig. 7—Crystal conversion loss as a function of temperature.

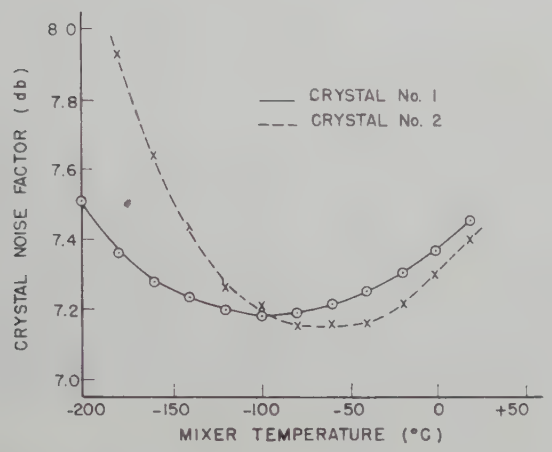


Fig. 8—Crystal noise factor as a function of temperature.

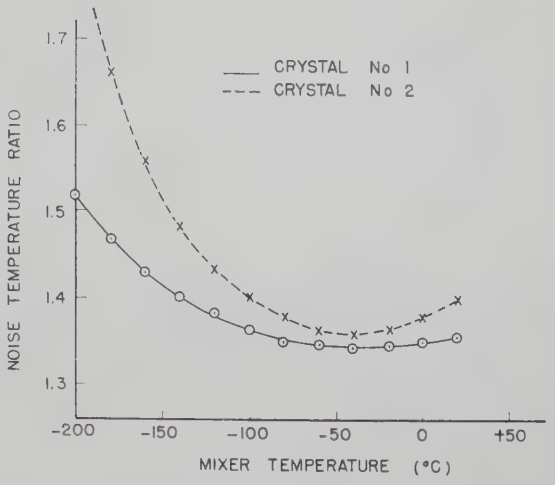


Fig. 9—Crystal noise temperature ratio as a function of temperature.

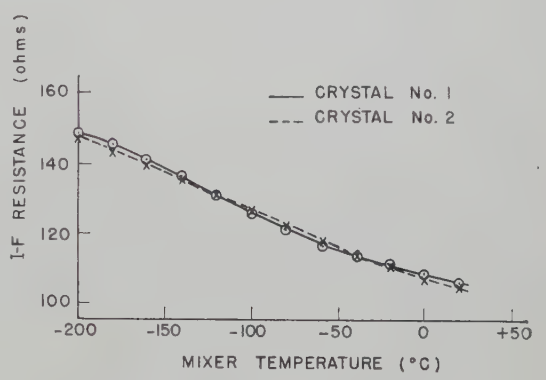


Fig. 10—Crystal IF resistance as a function of temperature.

bias current is between 0.5 and 0.6 ma, with the exact value being relatively uncritical. However, the best noise factor that can be obtained at −196°C is still inferior to that obtained at room temperature with the recommended values of bias and local oscillator drive.

### *D. Variation of Crystal Parameters with Temperature*

Although on the basis of simple theoretical considerations[1] the crystal noise factor should decrease steadily with decreasing temperature, it was felt that in practice some optimum intermediate temperature might exist. Accordingly, the various crystal parameters as a function of temperature were measured, for two different crystals, over the range from room temperature down to −196°C.

Although the dc bias required for optimum receiver noise figure is a function of temperature, this function was not known, and so it was decided to hold the dc bias constant at some compromise value. The value selected was such as to cause 0.4 ma of crystal current to flow at −1.96°C. The local oscillator level remained at 0.5 milliwatt.

The results are shown in Figs. 7–10. In Fig. 8 the crystal noise factor, $F_x = Lt$, is shown as a function of temperature. This quantity represents the noise factor of a receiver having a noise free IF amplifier ($F_{IF} = 1$ time). Both curves are seen to have minima which occur between −100 and −50°C, but the best value of $F_x$ is, in both cases, only 0.25 db below the corresponding room temperature value.

In the determination of crystal parameters as a function of temperature, the conversion loss $L$ and IF resistance $R_{IF}$ varied somewhat erratically with temperature. Figs. 7 and 8 thus represent smoothed-out versions of the original curves. The cause of this erratic behavior is not known, but may be associated with discontinuous changes in the mechanical configuration of the crystal package, brought about by the steady drift in the temperature of the crystal mount as it was allowed to warm up.

In order to determine whether or not further improvements in the crystal noise factor could be made at intermediate temperatures, the parameters of two 1N263 crystals were determined as a function of local oscillator drive and dc bias at a mixer temperature of approximately −75°C. At that temperature, the crystal noise factors, $F_x = Lt$, exhibit very broad minima with best performance in the region of 0.8-ma dc bias current, and 1.8-ma total crystal current. Crystal noise factors 0.3 to 0.6 db lower than room temperature values were observed; however, the crystal parameters varied erratically at this temperature.

Some measurements were made at a mixer temperature of approximately −125°C, where the optimum operating conditions were determined to be: dc bias current 0.4 ma, total current 1.8 ma, at which improvements of 0.4 db in $F_x$ compared to room temperature values were observed.

### *E. Dependence of Crystal Parameters on RF Circuitry*

Using a mixer crystal mount of different design, some of the measurements made previously were repeated. These measurements, which were made first at room temperature, and later at −196°C, showed that the over-all receiver noise factor was approximately 0.7 db lower at all temperatures than the values obtained with first crystal mount, owing, apparently, to superior performance of the new crystal mount. There was, however, no change in the previously determined variations of crystal parameters with temperature. Thus it may be concluded that the failure to observe significant improvements in crystal sensitivity was not due to the performance of the particular crystal mount used.

## V. Effect of Temperature Cycling on the Crystal Package

Seventeen 1N263 crystals were used in the tests, not all of them continuously. Of this number, two were ruined by the temperature cycling; *i.e.*, the noise factors became unusably high. The remainder exhibited little change in electrical properties, although small cracks appeared in the glass at the glass-to-metal seal on two of the crystals. This may cause eventual failure of these units.

## VI. Conclusions

The following conclusions have been reached concerning the operation of 1N263 crystals in an $X$-band mixer:

1) No improvement can be made in crystal noise factor by operating the mixer at liquid nitrogen temperatures.

2) A small improvement in crystal noise factor may be possible by operating the mixer at some temperature intermediate between −196°C and room temperature. The improvement is of the order of 0.3 to 0.6 db, with the minimum value of the crystal noise factor occurring in the region between −100°C and −50°C, the exact value depending on the individual crystal, as well as on bias and local oscillator drive.

The failure to obtain significant improvement by mixer cooling is due to an increase in the noise temperature ratio of the crystal as the temperature is lowered. This suggests that flicker noise may be appreciable at 30 mc for germanium as well as for silicon mixer crystals[5] and furthermore that this excess noise is temperature dependent.

# The Multiple Branch Waveguide Coupler*

JOHN REED†

***Summary*—A multiple branch directional coupler is discussed for rectangular waveguide applications for series junctions. A design method is developed which is valid for any coupling ratio and any number of branch lines with perfect match and directivity. The frequency response of this type coupler is calculated with the aid of a digital computer.**

## Introduction

THE multiple branch waveguide directional coupler has been found to be a useful type of coupler, especially for rather tight ratios such as from zero to fifteen decibels. This paper describes the design of such a coupler and the calculation of its frequency response. The coupler is particularly desirable since the design constants are readily found and its frequency response can be calculated.

Fig. 1 shows a typical coupler with five branches. The three center connecting branch lines are made of waveguide of the same width as the main line but of reduced height $c$. The height of the two end branches is a different value $a$ but the width is the same as the main line. The $a$ and $c$ values are normalized to the height of the main line as unity. The spacing between the center lines of adjacent branch lines is assumed to be identical and the length of all these branch lines is assumed to be the same. At first, each of these two distances will be considered to be a quarter wavelength, but for considering the frequency dependence of the coupler this restriction will be dropped. The junction effects will be disregarded, that is to say, the junctions will be regarded as pure series junctions.[1] This is strictly valid only for the case that $a$ and $c$ are very small, but for a first approximation it is quite valuable.

* Manuscript received by the PGMTT, March 3, 1958; revised manuscript received, July 7, 1958.

† Raytheon Mfg. Co., Wayland, Mass

[1] C. G. Montgomery, R. H. Dicke, and E. M. Purcell, "Principles of Microwave Circuits," McGraw-Hill Book Co., Inc., New York, N. Y., p. 288; 1948.

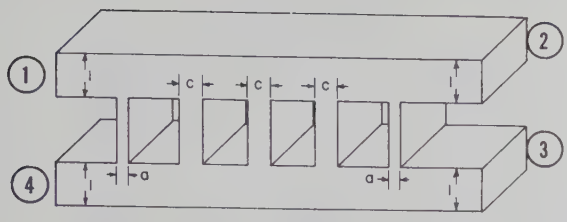


Fig. 1—Typical coupler with five branches.

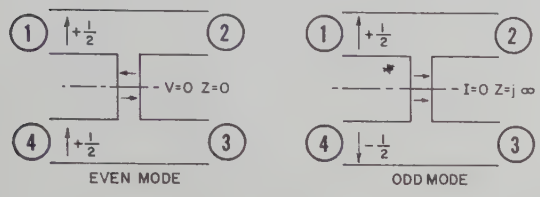


Fig. 2—Even and odd modes.

## Symmetry Analysis

A signal of amplitude equal to one is applied to arm (1) of the network of Fig. 2. This figure represents a cross section of one branch of the coupler in Fig. 1. To determine the vector amplitudes out the other arms assuming matched terminations, use is made of the even and odd mode concept.[2–4] In Fig. 2, if two coherent signals, each of amplitude $\frac{1}{2}$ and in phase, are applied at arms (1) and (4) a voltage null will occur at every point on the plane of symmetry. This will be denoted as an even mode. Likewise, if two coherent waves, each of amplitude $\frac{1}{2}$ and out of phase with each other, are applied at arms (1) and (4) there will be a voltage maximum and current null at every point on the plane of symmetry. This will be denoted as an odd mode. In each case the symmetry of the modes will not be disturbed on passing through the network. It will be assumed that the transmitted amplitudes $T_e/2$ and $T_o/2$, and the reflected amplitudes $\Gamma_e/2$ and $\Gamma_o/2$ for the even and odd modes, can be calculated. The sum of these two modes properly phased is equal to a wave of amplitude 1 in arm (1) and 0 in arm (4) incident on the system. The amplitude out arm (2) will be the sum of the transmitted amplitudes for the even and odd modes, and the amplitude out arm (3) will be the difference of these transmitted amplitudes. Likewise, the amplitudes out arms (1) and (4) are the sum and difference of the reflected amplitudes. Putting this in symbols we have

$$A_1 = \Gamma_e/2 + \Gamma_o/2 \qquad A_2 = T_e/2 + T_o/2$$
$$A_4 = \Gamma_e/2 - \Gamma_o/2 \qquad A_3 = T_e/2 - T_o/2. \qquad (1)$$

Thus the analysis of the directional coupler of the type shown in Fig. 1 can be performed in terms of the results for two two-terminal-pair networks. The $ABCD$ matrices of the network are determined for both the even and odd mode, and from these matrices the reflected and transmitted amplitudes can be found. In this paper the networks, such as Fig. 1, give rise to matrices of lossless two-terminal-pair circuits so that the $A$ and $D$ terms are pure real quantities while the $B$ and $C$ are pure imaginary quantities. The values of the reflected and transmitted amplitudes of each mode are given in terms of the elements of the $ABCD$ matrix by

$$\Gamma/2 = \frac{A + B - C - D}{2(A + B + C + D)} \qquad T/2 = \frac{1}{A + B + C + D}. \qquad (2)$$

The quantities $T$ and $\Gamma$ are the elements $S_{12}$ and $S_{11}$ of the scattering matrix for a two-port network.[5]

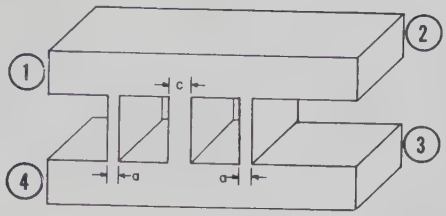


Fig. 3—Three branch coupler.

## Design at Band Center

For the first application of the above method, consider a three branch coupler shown in Fig. 3. The three connecting branch lines are assumed to be a quarter wavelength long, the center line is of height $c$ relative to the main line, and the two end branch lines are of height $a$. The branch lines are spaced a quarter wavelength apart on uniform height lines. The matrix for the even mode is

$$M_{e3} = \begin{bmatrix} 1 & ja \\ 0 & 1 \end{bmatrix}\begin{bmatrix} 0 & j \\ j & 0 \end{bmatrix}\begin{bmatrix} 1 & jc \\ 0 & 1 \end{bmatrix}\begin{bmatrix} 0 & j \\ j & 0 \end{bmatrix}\begin{bmatrix} 1 & ja \\ 0 & 1 \end{bmatrix}$$
$$= \begin{bmatrix} -a(-c) - 1 & -j(a^2(-c) + 2a) \\ +j(-c) & -a(-c) - 1 \end{bmatrix}.$$

This matrix is the product of five matrices; the first, third, and fifth being those of short circuited waveguide stubs an eighth wavelength long and of characteristic impedances $a$, $c$, and $a$ respectively. The second and fourth are of quarter wavelength lines of characteristic impedance unity. The matrix for the odd mode will be similar except that open circuited eighth wavelength stubs are imagined. The matrix product is found quickly by replacing $a$ and $c$ by $-a$ and $-c$.

$$M_{o3} = \begin{bmatrix} ac - 1 & -j(a^2c - 2a) \\ +jc & ac - 1 \end{bmatrix}$$

For perfect match and directivity, there must be no reflection of either the even or odd mode. For these

[2] B. A. Lippmann, "Theory of Directional Couplers," Mass. Inst. Tech., Cambridge, Mass., Rad. Lab. Rep. No. 860; December 28, 1945.

[3] J. Reed and G. J. Wheeler, "A method of analysis of symmetrical four-port networks," IRE Trans. on Microwave Theory and Techniques, vol. MTT-4, pp. 246–252; October, 1956.

[4] L. Young, "Branch guide couplers," *Proc. Natl. Electronics Conf.*, vol. 12, pp. 723–732; 1956.

[5] H. M. Altschuler and W. K. Kahn, "Nonreciprocal two-ports represented by modified Wheeler networks," IRE Trans. on Microwave Theory and Techniques, vol. MTT-4, pp. 228–233; October, 1956.

matrices this condition is achieved by setting the $B$ term equal to the $C$ term since the $A$ term is already equal to the $D$ term. Once the value of $c$ is chosen, there are two possible values of $a$ to be found from equating the $B$ and $C$ terms of the matrices. The smaller of these should be chosen to reduce junction effects and increase bandwidth.

$$a = \frac{1 - \sqrt{1 - c^2}}{c}$$

The matrices for the three branch couplers, when this relationship of $a$ to $c$ is chosen, can be written in terms of an angle $\theta$ as

$$M_{e3} = \begin{bmatrix} \cos\theta & j\sin\theta \\ j\sin\theta & \cos\theta \end{bmatrix} \text{ ayd } M_{o3} = \begin{bmatrix} \cos\theta & -j\sin\theta \\ -j\sin\theta & \cos\theta \end{bmatrix}$$

and so $A_2 = \cos\theta$ and $A_3 = j\sin\theta$. Thus when this coupler is matched and perfectly directive, the voltage amplitude out arm (2) is equal to the magnitude of the $A$ term of the $M_{e3}$ matrix, while the amplitude out arm (3) is equal to the magnitude of the $C$ term.

For a four element coupler (see Fig. 4) a similar procedure may be followed.

$$M_{c4} = \begin{bmatrix} -a(c^2-1)-(-c) & -j(a^2(c^2-1)+2a(-c)+1) \\ j(c^2-1) & -a(c^2-1)-(-c) \end{bmatrix}$$

As before, the matrix for the odd mode may be found by putting $-a$ and $-c$ for $a$ and $c$. The amplitude out arm (3), when the proper relationship of $a$ to $c$ is chosen, is now equal to the $A$ term in the matrix, and the amplitude out arm (2) is equal to the $C$ term. This is true for all of this class of couplers with an even number of branches while the former case of power division is true for all couplers with an odd number of branch arms.

For a five branch coupler such as shown in Fig. 1 the matrix is

$$M_{c5} = \begin{bmatrix} -a(-c^3+2c)-(c^2-1) & -j(a^2(-c^3+2c)+2a(c^2-1)-c) \\ j(-c^3+2c) & -a(-c^3+2c)-(c^2-1) \end{bmatrix}.$$

For the general case of $n+2$ branches, with each branch a quarter wavelength long and spaced a quarter wavelength away from adjacent branches on uniform height waveguide, the matrix can be found. If the center $n$ branches all have the same impedance $c$, and the two end branches have the impedance $a$, the even mode matrix is

$$M_{e(n+2)} = \begin{bmatrix} -aS_n(-c) - S_{n-1}(-c) & -j(a^2S_n(-c) + 2aS_{n-1}(-c) + S_{n-2}(-c)) \\ +jS_n(-c) & -aS_n(-c) - S_{n-1}(-c) \end{bmatrix}. \quad (3)$$

The elements $S_n(-c)$ are Chebyshev polynomials in $c$ and the first few have the following values.

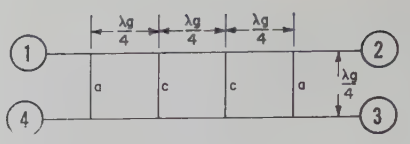


Fig. 4—Four branch coupler schematic.

$$\begin{aligned} S_0(-c) &= +1 \\ S_1(-c) &= -c \\ S_2(-c) &= c^2 - 1 \\ S_3(-c) &= -c^3 + 2c \\ S_4(-c) &= c^4 - 3c^2 + 1 \\ S_5(-c) &= -c^5 + 4c^3 - 3c \\ S_6(-c) &= c^6 - 5c^4 + 6c^2 - 1 \\ S_{n+1}(-c) &= -cS_n(-c) - S_{n-1}(-c) \\ S_n(2x) &= U_n(x) \end{aligned}$$

The values of $S_n(x)$ are available[6] to twelve decimal places for $x$ ranging from 0 to 2 in steps of 0.001 and for integral values of $n$ from 2 to 12.

In order to design a matched and perfectly directive coupler of given coupling ratio the value of $c$, the relative height of the center $n$ waveguide branches, is to be calculated. To do this the number of branches $n+2$ is chosen and the voltage amplitudes out arms (2) and (3) for unity amplitude into arm (1) determined. For an even number of branches $S_n(-c)$, the magnitude of the $C$ term in the $Me_{n+2}$ matrix, is set equal to $A_2$ and the value of $c$ computed. If the number of branches is odd, the value of $S_n(-c)$ is set equal to $A_3$, and $c$ is calculated. The value of $a$ which will then give a matched and perfectly directive coupler is

$$a = \left| \frac{|\sqrt{1 - S_n^2(-c)}| - |S_{n-1}(-c)|}{S_n(-c)} \right|. \quad (4)$$

This equation is found from the general matrix above by equating the sum of the squares of the $A$ term and the $C$ term in the matrix to unity. The magnitude signs are used in this equation to make sure that the smaller of the two possible values of $a$ is used.

For example an 8.5 decibel coupler was desired with six branches. The amplitudes $A_2$ and $A_3$ are therefore

[6] Tables of Chebyshev Polynomials $S_n(x)$ and $C_n(x)$, National Bureau of Standards Applied Mathematics Series No. 9, United States Government Printing Office, Washington 25, D. C., 1952.

TABLE I

EXAMPLES OF 0, 3, AND 10-DB COUPLERS

| Number of Branches $(n+2)$ | 0-db Coupler | | 3-db Hybrid Even Split | | 10-db Coupler | |
|---|---|---|---|---|---|---|
| | $a$ | $c$ | $a$ | $c$ | $a$ | $c$ |
| 3 | 1.000* | 1.000* | 0.4141 | 0.7071 | 0.162 | 0.3162 |
| 4 | 0.500* | 1.000* | 0.2346* | 0.5412* | 0.0945 | 0.2265 |
| 5 | 0.618 | 0.618 | 0.2088 | 0.3810 | 0.0811 | 0.1602 |
| 6 | 0.309 | 0.618 | 0.1464* | 0.3179* | 0.0592 | 0.1312 |
| 7 | 0.445 | 0.445 | 0.1374 | 0.2583 | | |
| 8 | 0.2225 | 0.445 | 0.1064 | 0.2257 | | |
| 9 | 0.3473 | 0.3473 | 0.1022 | 0.1948 | | |
| 10 | 0.1736 | 0.3743 | 0.0837 | 0.1752 | | |
| 11 | 0.2846* | 0.2846* | | | | |
| 12 | 0.1423* | 0.2846* | | | | |
| 13 | 0.2410 | 0.2410 | | | | |
| 14 | 0.1205 | 0.2410 | 0.0587* | 0.12104* | | |
| 23 | 0.1365 | 0.1365 | | | | |
| 24 | 0.0682* | 0.1365* | | | | |

* Frequency response curves given.

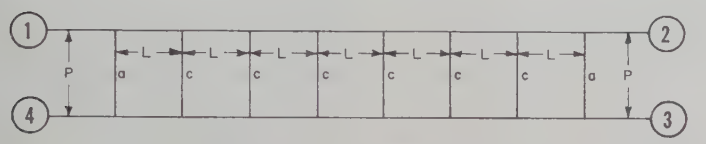


Fig. 5—General coupler schematic.

respectively in magnitude 0.926686 and 0.375837. On setting $S_4(-c)$ equal to 0.926686 the value of $c$ is found to be 0.156972. Then the value of $a$ is found to be 0.070964. The values of $a$ and $c$ are made to be the heights of the branches with respect to that of the main and auxiliary waveguides. A tabulation of values of $a$ and $c$ for couplers of 0 decibels coupling [complete transfer of power from arm (1) to arm (3)], 3 decibels [even split of power between arms (2) and (3)], and 10 decibels [power out arm (3) is 10 decibels below the incident], is given in Table I.

## Frequency Sensitivity

To determine the frequency response of this type of coupler, we assume that the junction effects do not change with frequency. That is to say, the junctions are regarded as series junctions with reference planes chosen so that the phase between them varies as does the phase in an equivalent piece of uniform waveguide. A schematic diagram of the coupler is shown in Fig. 5.

The coupler is considered as a cascade of series branches each of a length $P$ and spaced along a uniform waveguide a distance $L$ from the next. The impedances of the branches are chosen to be $c$ for the center $n$ branches and $a$ for the two end branches. The basic matrices for the components of this array are as follows.

Even mode stub at ends

$$\begin{bmatrix} 1 & jag \\ 0 & 1 \end{bmatrix}$$

Even mode stub at center

$$\begin{bmatrix} 1 & jcg \\ 0 & 1 \end{bmatrix}$$

$$g = \tan\frac{\pi P}{\lambda_g} \qquad \lambda_g = \text{guide wavelength.}$$

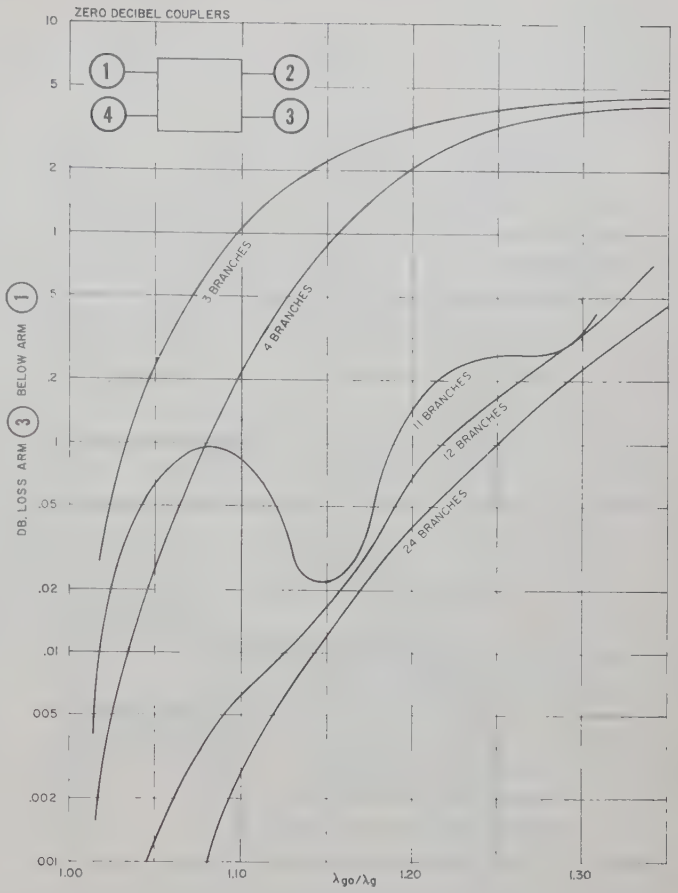


Fig. 6—Zero decibel couplers of 3, 4, 11, 12, and 24 branches.

Length $L/2$ of unity impedance waveguide

$$\begin{bmatrix} \frac{1}{\sqrt{1+t^2}} & \frac{jt}{\sqrt{1+t^2}} \\ \frac{jt}{\sqrt{1+t^2}} & \frac{1}{\sqrt{1+t^2}} \end{bmatrix} \qquad t = \tan\frac{\pi L}{\lambda_g}.$$

Note that when $L=P=\lambda_g/4$ then $t=g=1$.

The even mode matrix for the coupler above is therefore

$$M_{e(n+2)} = \frac{1}{1+t^2}\begin{bmatrix} 1-tga & j(t+ag) \\ jt & 1 \end{bmatrix} \times \begin{bmatrix} \frac{1-t^2-tcg}{1+t^2} & \frac{j(2t+cg)}{1+t^2} \\ \frac{j(2t-t^2cg)}{1+t^2} & \frac{1-t^2-tcg}{1+t^2} \end{bmatrix}^n \times \begin{bmatrix} 1 & j(t+ag) \\ jt & 1-tga \end{bmatrix}. \tag{5}$$

The first matrix is that of an end even mode stub followed by a length $L/2$ of line. The second matrix is that of a length of line followed by a center even mode stub followed by a length of line. The third matrix is that of a length of line followed by an end even mode

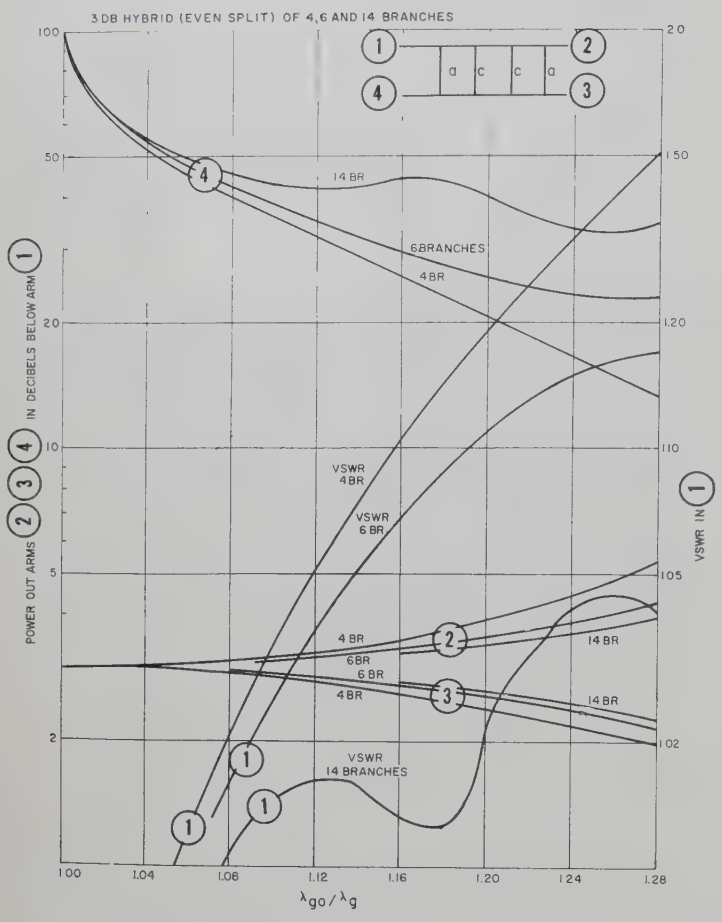


Fig. 7—Three decibel couplers 4, 6, and 14 branches.

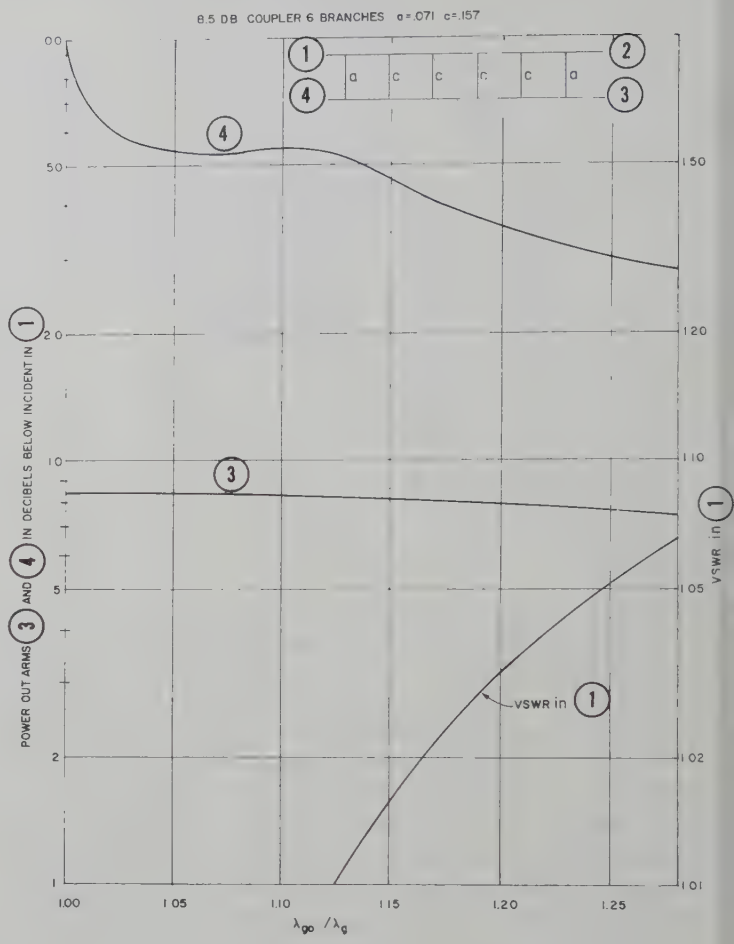


Fig. 8—8.5-db coupler of six branches (see example in text).

stub. The quantity $1/\sqrt{1+t^2}$ is factored out of both the first and third matrix. The matrix product is that of the first matrix times the second matrix raised to the $n$th power where $n$ is the number of center elements times the third matrix. From this matrix product, given $t$, $g$, $a$, $c$, and $n$, the quantities $\Gamma_e/2$ and $T_e/2$ can be computed. The matrix for the odd mode is formed by substituting $-1/g$ for $g$ everywhere in the even mode matrix. From this $\Gamma_0/2$ and $T_0/2$ can be calculated. Thus the amplitudes out each arm can be found.

This computation was programmed for an IBM 650 digital computer. The quantities $a$, $c$, $n$, $P/\lambda_{g0}$, and $L/_{g0}$ (where $\lambda_{g0}$ is the design guide wavelength) are the data fed into the computer. The ouput is the voltage standing-wave ratio to be expected in arm (1) and the power out arms (2), (3), and (4), expressed in decibels below incident power in arm (1), assuming matched loads in arms (2), (3), and (4). In a single run, the values of $a$, $c$, and $n$ are kept constant but the values of $t$ and $g$ must be computed over again for each value of $\lambda_{g0}/\lambda_g$. For a given set of input data the program was arranged so that thirty values of $\lambda_{g0}/\lambda_g$ would be chosen. The limits on them and distance between them can be varied as desired.

The time required to perform the calculation for each value of $\lambda_{g0}/\lambda_g$ varied from about 4 seconds for a value of $n$ equal to 1, to about 11 seconds for $n$ equal to 22. In raising the center matrix to the $n$th power ordinary matrix multiplication was used to retain flexibility. If a lot of work for very high values of $n$ were to be done, the program could be modified to reduce computer time.

Some calculated results are shown in the next few figures. Fig. 6 shows results to be expected for zero decibel couplers [complete transfer of power from arm (1) to arm (3) at the design frequency]. These plots show the power loss in decibels going from arm (1) to arm (3) as a function of $\lambda_{g0}/\lambda_g$. This abscissa would be $f/f_0$ if the couplers were made of coaxial lines and $a$ and $c$ the characteristic admittances. For this graph the lengths of line $L$ and $P$ are a quarter wavelength at midband so the response will be arithmetically symmetrical about the value of $\lambda_{g0}/\lambda_g=1$. That is to say, for example, the insertion loss from the input at arm (1) to the output at any arm will be the same at a value of $\lambda_{g0}/\lambda_g=1.20$ as it would be for $\lambda_{g0}/\lambda_g=0.80$. Therefore only one side of the curves need be plotted. The curves shown are for couplers of 3, 4, 11, 12, and 24 branches

with the values of $a$ and $c$ as shown in Table I. The results for the three arm coupler agree with those already plotted.[3]

Fig. 7 shows the results calculated for branch guide hybrids which give even power split. In this graph the power out arms (2), (3), and (4), expressed in decibels below incident power, is plotted as a function of $\lambda_{g0}/\lambda_g$. The input VSWR to be expected looking into arm (1) is also plotted. These curves are for couplers of 4, 6, and 14 branches with the values of $a$ and $c$ given in Table I.

Fig. 8 shows the results calculated for the 8.5-db coupler discussed earlier as an example. Fig. 9 shows the results to be expected if the length of the branch guides is reduced to 0.22 $\lambda_{g0}$ while the distance between them is maintained at 0.25 $\lambda_{g0}$ and all factors remain the same as in Fig. 8. The curves, of course, will not be symmetrical about the $\lambda_{g0}/\lambda_g = 1$ value.

In the practical application of the above calculations it is seen that the longer the coupler is the broader the band that can result. As the sizes of the coupling slots decrease in size the discontinuity effects get less and less so that the performance approaches the theoretical value closer and closer. Thus the effect of more slots and longer length is doubly beneficial. The theoretical performance becomes better and the actual performance approaches the theoretical.

### Acknowledgment

The author expresses his appreciation to Thomas A. Weil who programmed and ran the computer.

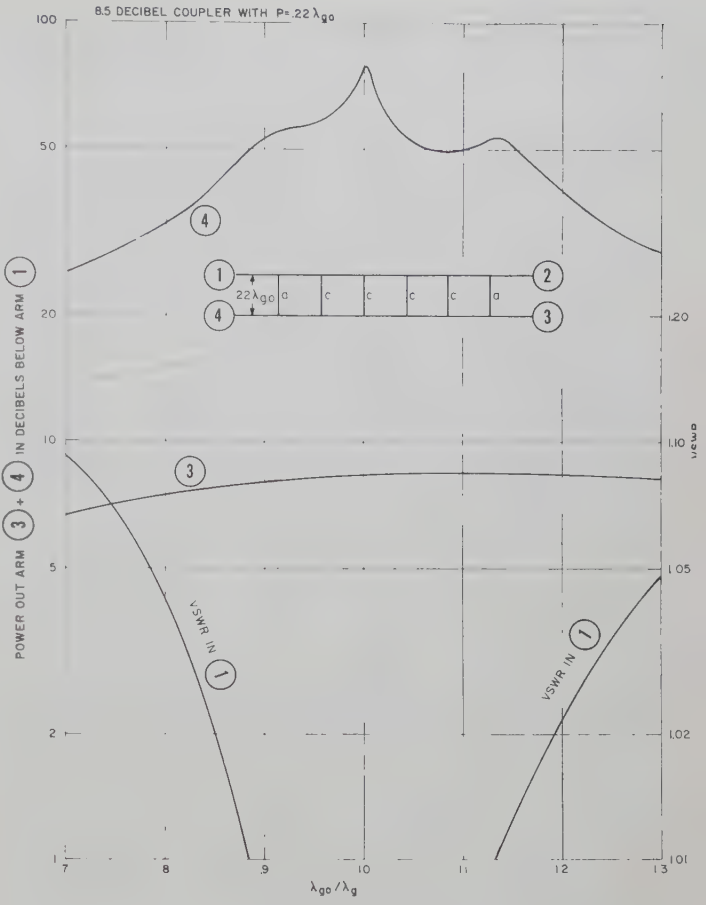


Fig. 9—8.5-db coupler with $P$ reduced.

# Coupled-Transmission-Line Directional Couplers*

J. K. SHIMIZU† AND E. M. T. JONES†

*Summary*—**Formulas are presented for the design of coupled-transmission-line directional couplers that are rigorous for any value of coupling. Two basic types are treated in detail; the simplest is one-quarter wavelength long at the center of its frequency band, while the other is three-quarter wavelength long. The quarter-wavelength type can be used over an octave of frequencies with approximately constant coupling, while the three-quarter-wavelength type can be used equally well over more than two octaves. For example, a −3-db coupler of the first type has a variation of ±0.3 db over a 2:1 band, while the second type has the same variation over a 4.5:1 band. Theoretically both types should have infinite directivity at all frequencies. The experimental results for models of these directional couplers have been found to conform very closely to the theoretical coupling functions, while the directivity, although usually good, is limited by discontinuity effects and constructional tolerances.**

* Manuscript received by the PGMTT, March 4, 1958; revised manuscript received, May 20, 1958. The work reported in this paper was supported jointly by the Signal Corps under Contract DA 36-039 SC-63232 and by the Air Force Cambridge Res. Ctr. under Contract AF 19(604)-1571.

† Stanford Res. Inst., Menlo Park, Calif.

## Introduction

SEVERAL investigators have recently pointed out that coupled transmission lines can be made into directional couplers having excellent wide-band performance, with infinite directivity and constant input impedance theoretically available at all frequencies

and for all degrees of coupling.[1–5] The basic directional coupler of this type is shown schematically in Fig. 1(a), and is seen to consist simply of a pair of coupled transmission lines. As shown, the amplitude of the coupled wave varies approximately sinusoidally with frequency, with maximum coupling occurring when the length of the coupling region is an odd multiple of a quarter wavelength. Usually, a coupler of this type is designed to be one-quarter wavelength at the center of its frequency band, and hence it will be referred to as the *quarter-wavelength* directional coupler. A wider bandwidth with more uniform coupling may be achieved when three basic couplers are connected in cascade as shown in Fig. 1(b) to form a *three-quarter-wavelength* directional coupler. With the center quarter-wavelength coupler more tightly coupled than the outer quarter-wavelength couplers, a maximally flat or equal-ripple coupling response may be obtained. The direction of coupling with coupled transmission lines is backward rather than forward. Thus, if a signal is fed into one port, the coupled signal emerges from the adjacent port, and the diagonally opposite port is isolated. For example, if Port 1 is energized, the coupled wave emerges from Port 2, and no signal is present at Port 3. The power emerging from Port 4 in the case of an ideal, lossless structure is simply the input power minus the coupled power.

Design formulas for the quarter-wavelength and three-quarter-wavelength directional couplers are given. Also, the measured performance of a number of couplers is presented showing close agreement with theory. The formulas given here apply to all types of TEM-mode transmission lines. However, the design information is particularized to the shielded-strip type of transmission line.

## Design Formulas for Quarter-Wavelength Directional Couplers

The principal results of the theoretical analysis of the coupled-transmission-line directional couplers presented by Jones and Bolljahn[6] are reproduced here for completeness.

They show that when all the ports of the directional coupler as shown in Fig. 1(a) are terminated in its characteristic impedance, $Z_o$, the coupled voltage, $V_2$,

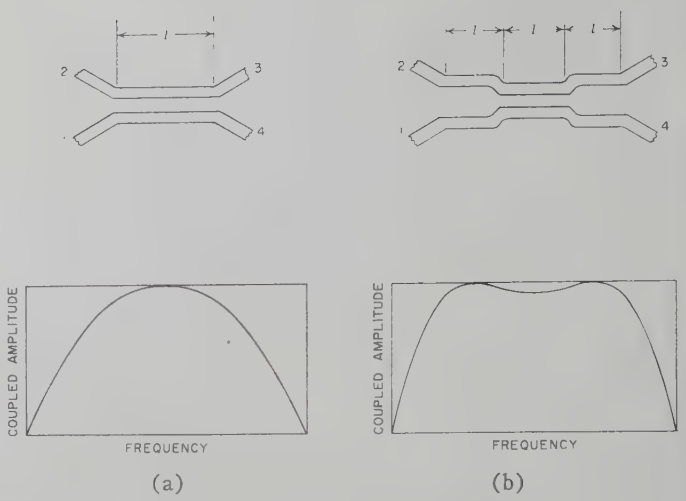


Fig. 1—(a) Quarter-wavelength and (b), three-quarter-wavelength coupled-transmission-line directional couplers.

at Port 2 produced by the applied voltage, $V_1$, at Port 1 is equal to

$$\frac{V_2}{V_1} = \frac{jk \sin\theta}{\sqrt{1-k^2}\cos\theta + j\sin\theta} \tag{1}$$

while the voltage, $V_4$, at the end of the straight-through arm at Port 4 under these conditions is

$$\frac{V_4}{V_1} = \frac{\sqrt{1-k^2}}{\sqrt{1-k^2}\cos\theta + j\sin\theta}. \tag{2}$$

The voltage, $V_3$, at Port 3 is zero for all frequencies. Here $\theta$ is the electrical length of the coupled-line region.

The midband amplitude coupling factor, $k$, is given in terms of the even and odd characteristic impedances, $Z_{oe}$ and $Z_{oo}$, as

$$k = \frac{Z_{oe} - Z_{oo}}{Z_{oe} + Z_{oo}}, \tag{3}$$

while the characteristic impedance $Z_o$ is expressed in terms of the even and odd characteristic impedance as

$$Z_o = \sqrt{Z_{oe}Z_{oo}}. \tag{4}$$

Here $Z_{oe}$ is the even or unbalanced impedance, which is equal to the characteristic impedance of one strip to ground when each strip is at the same potential. The impedance $Z_{oo}$ is the odd or balanced impedance, which is equal to the characteristic impedance of one strip to ground when the strips are at equal but opposite potentials with respect to ground.

## Analysis of the Slot-Coupled Strip-Line Directional Coupler

Fig. 2 shows a slot-coupled strip-line configuration that is particularly suited for weak-coupling applications. The degree of coupling is easily controlled from about −20 db to as low a value as may be desired through the choice of the slot width. For this cross section, the even and odd-mode characteristic imped-

[1] W. L. Firestone, "Analysis of transmission line directional couplers," Proc. IRE, vol. 42, pp. 1529–1538; October, 1954.
[2] B. M. Oliver, "Directional electromagnetic couplers," Proc. IRE, vol. 42, pp. 1686–1692; November, 1954.
[3] R. C. Knechtli, "Further analysis of transmission-line directional couplers," Proc. IRE, vol. 43, pp. 867–869; July, 1955.
[4] E. F. Barnett, P. D. Lacy, and B. M. Oliver, "Principle of directional coupling in reciprocal systems," *Proc. Symp. Modern Advances in Microwave Techniques*, sponsored by Polytechnic Inst. of Brooklyn, Microwave Res. Inst., Brooklyn, N. Y., vol. 14, pp. 251–268; November, 1954.
[5] G. D. Monteath, "Coupled transmission lines as symmetrical directional couplers," *Proc. IEE, London*, pt. B, vol. 102, pp. 383–392; May, 1955.
[6] E. M. T. Jones and J. T. Bolljahn, "Coupled-strip-transmission-line filters and directional couplers," IRE Trans. on Microwave Theory and Techniques, vol. MTT-4, pp. 75–81; April, 1956.

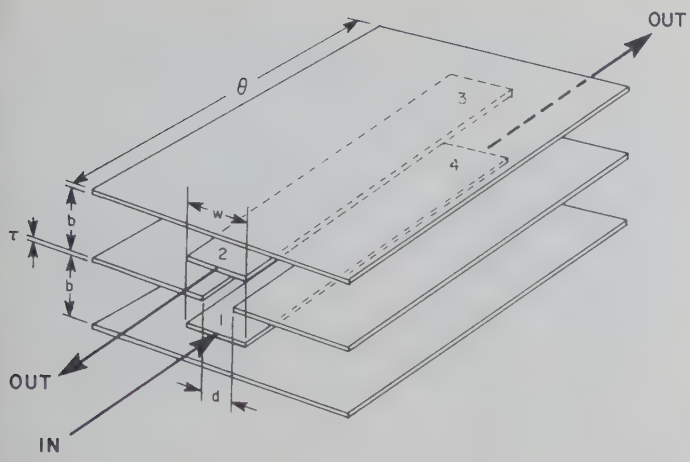


Fig. 2—Slot-coupled strip-line directional coupler.

ances would be difficult to compute rigorously, and therefore an approximate method valid for weak coupling has been used. This method, based on Bethe's[7] small-aperture theory, leads to the following formula for the voltage coupled to Port 2:

$$\frac{V_2}{V_1} = \left(\frac{d^2 E_s^2 Z_o \sqrt{\epsilon_r}}{1920 V^2} \sin \frac{2\pi l}{\lambda}\right) \exp j\left(\frac{\pi}{2} - \frac{2\pi l}{\lambda}\right) \quad (5)$$

where, in MKS units,

$d$ = width of the coupling slit
$\lambda$ = wavelength in the strip line
$l$ = length of the coupling slit
$E_s$ = electric field existing normal to the coupling slit in the absence of the slit
$Z_o$ = characteristic impedance of the strip line
$V_1$ = voltage from one strip to ground
$\epsilon_r$ = relative dielectric constant of the medium filling the cross section of the strip line.

Examination of (5) shows that maximum signal is coupled to Port 2 when the slit is a quarter wavelength long. The exact expression for $E_s$ is

$$E_s = \frac{\pi}{b} \frac{V_1}{K\left(\operatorname{sech} \frac{\pi}{2} \frac{w}{b}\right)} \quad (6)$$

where $K$ is a complete elliptic integral of the first kind. When the width of the strips $w$ is much greater than the separation $b$ of the ground planes

$$E_s \approx \frac{2V_1}{b}. \quad (7)$$

When the coupling aperture has a finite thickness $\tau$, it acts as a waveguide below cutoff having an attenuation $\alpha$ of approximately

[7] H. A. Bethe, "Lumped Constants for Small Irises," Radiation Lab., Mass. Inst. Tech., Cambridge, Mass., Rep. 43-22; March, 1943.

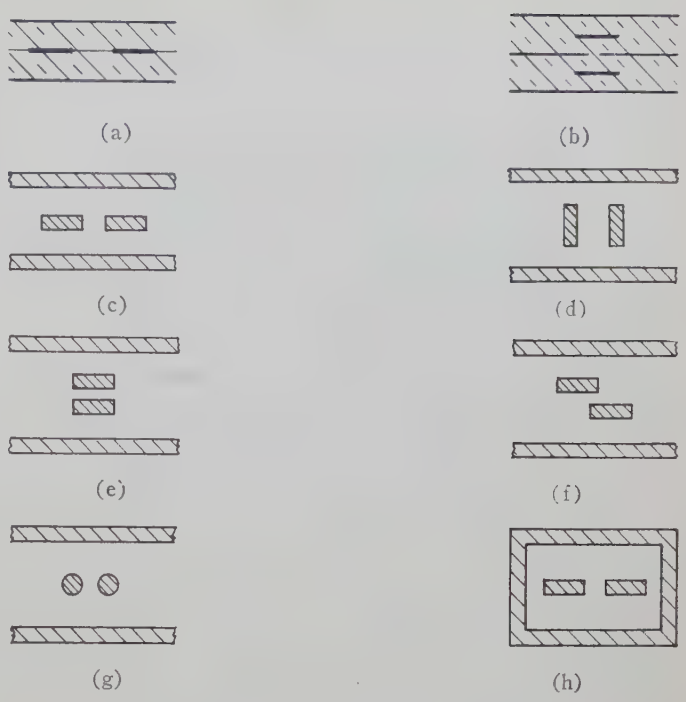


Fig. 3—(a)–(b) Loosely coupled types of directional-coupler cross sections. (c)–(h) Tightly coupled types of directional-coupler cross sections.

$$\alpha = \frac{27.3\tau}{d} \text{ (decibels)}. \quad (8)$$

For the usual values of $\tau$ and $d$ encountered in practice the attenuation through the aperture is not negligible, and it is well to apply (8) as a correction to (5). For loose coupling the characteristic impedance of this strip-line coupler will be practically the same as that of a single strip line of the same dimensions.

## Experimental Quarter-Wavelength Directional Couplers

Experimental data on a number of quarter-wavelength coupled-strip-line directional couplers are presented. Some of these models utilize the photo-etched cross sections of Fig. 3(a) and 3(b), which are particularly useful for loose coupling (*i.e.*, less than about −8 db) but which, for tighter coupling, require impractically small spacings between the coupled strips. Six other cross sections that are practical for tighter coupling are shown in Fig. 3(c)–(h). Cross sections (c), (d), and (e) have been used successfully in 3-db directional couplers. The cross section (h) was used in a three-quarter-wavelength directional coupler to be described in the next section.

### *Loosely Coupled Models*

Two experimental directional couplers having the cross section of Fig. 3(a) were constructed of copper-clad Teflon-impregnated Fiberglas cloth (GB-116-T) manufactured by Continental Diamond Fiber Company. This material has a nominal relative dielectric constant of 2.8 and a loss tangent of 0.003 at 1000 mc.

The strip pattern was cut with a sharp knife on one surface of one sheet, and the unwanted foil was stripped off. The copper foil on the mating surface was removed completely, but on the outer surfaces of the sandwich the foil was left intact to serve as the ground planes. In production, of course, the photo-etching technique would generally be preferred. The design formulas, which apply to all degrees of coupling, are (3) and (4). These relate the coupling factor $k$ and the characteristic impedance $Z_o$ of the connecting lines to the even and odd-mode characteristic impedances $Z_{oe}$ and $Z_{oo}$. The strip widths and spacings of the two models were computed under the assumption of zero strip thickness, so that Cohn's nomograms[8] could be used. If the thickness had been taken into account, slightly different results might be expected. The actual dimensions of the finished models were measured accurately, and are given in Table I. From these dimensions, the theoretical center frequency, midband coupling, and characteristic impedance of the couplers were computed and are included in the Table. In this calculation, the relative dielectric constant was assumed to be 2.80, and the strip thickness was assumed to be zero.

TABLE I

DIRECTIONAL COUPLER CHARACTERISTICS

| Plate Spacing $b$ (inch) | Strip Width $w$ (inch) | Strip Spacing $s$ (inch) | Length of Coupling Region $L$ (inch) | Center Frequency (kmc) | Theoretical Midband Coupling (db) |
|---|---|---|---|---|---|
| 0.123 | 0.0498 | 0.0081 | 0.56 | 2.84 | − 8.9 |
| 0.123 | 0.0597 | 0.028 | 0.57 | 2.9 | −15 |

Fig. 4(a) and 4(b) shows a comparison between the theoretical and experimental values of coupling of these models as a function of frequency.[9] It is seen that the coupling at midband is almost exactly that predicted by theory, while the deviations at other frequencies are undoubtedly due to constructional irregularities and mismatch effects.

An experimental model of the slot-coupled directional coupler of Fig. 3(b) was designed by means of (5). Four layers of Teflon-impregnated glass cloth were used, with the attached copper foil cut and stripped away as necessary to form the two strips, the three ground planes and the coupling slot. The actual measured plate spacing was 0.122 inch, the strip width 0.220 inch, the slit width 0.0713 inch, and the length of the coupling region 0.57 inch. From these dimensions, the theoretical center frequency was computed to be 2.9 kmc, the midband coupling −31.2 db, and the characteristic impedance of the terminating lines 25.0 ohms. The theoretical and experimental coupling curves plotted in Fig. 4(c) show a discrepancy of only about 0.6 db.[9]

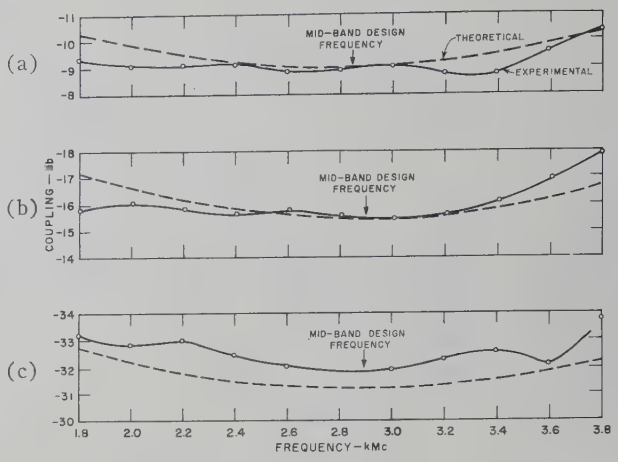


Fig. 4—Measured performance of coupled-strip-line quarter-wavelength directional couplers.

The measured directivities of the three directional couplers averaged about 20 db. Fixed terminations having VSWR's of about 1.1 were used, and therefore better matched terminations (or the use of sliding terminations) would most likely lead to the measurement of higher directivity.

*Models Having 3-db Couplings*

Three types of 3-db strip-line directional couplers have been constructed and tested and their performance described.[10] A summary of the performance of one of these couplers is presented here.

Fig. 5 shows a photograph of the interior of this coupler, and its pertinent dimensions are summarized in Table II. The 50-ohm strip transmission lines are joined to the coupled strips by smooth transitions. Residual reflections are canceled by means of the conducting cylindrical posts placed at the ends of the coupling region. The dimensions of the tapered transition between the 50-ohm strip lines and the Type-N connectors were determined experimentally with the aid of the strip-line standing-wave meter which was constructed at Stanford Research Institute, Menlo Park, Calif. The measured VSWR of the transition in series with a matched pair of Type-N connectors varied from 1.03 to 1.07 over the frequency range 800–1600 mc.

All metal parts of the directional coupler were machined from brass stock. The center conductors were supported at their ends by the Type-N connectors, and small polyfoam supports above and below the coupled lines held them centered between the ground planes. Also, two small polystyrene spacers were placed between the coupled strips to maintain an accurate gap

[8] S. B. Cohn, "Shielded coupled-strip transmission line," IRE TRANS. ON MICROWAVE THEORY AND TECHNIQUES, vol. MTT-3, pp. 32–33; October, 1955.

[9] The actual measured coupling included about 0.5 db of dissipation loss in the connecting strip lines. Therefore, all values of measured coupling were increased by 0.5 db to obtain the coupling that would be measured if the strip lines were lossless. It is the corrected values of coupling that are plotted in Fig. 4.

[10] J. K. Shimizu, "Strip-line 3-db directional couplers," 1957 IRE WESCON CONVENTION RECORD, pt. 1, pp. 4–15.

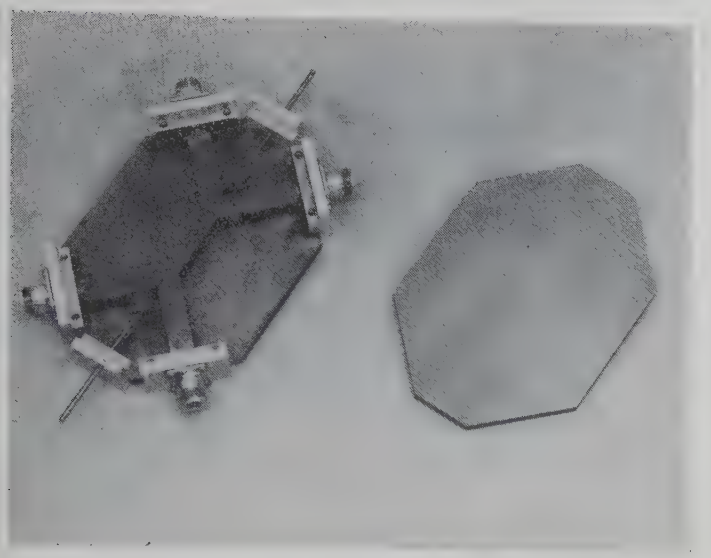

Fig. 5—800–1600 mc 3-db strip-line directional coupler.

TABLE II
DIMENSIONS OF 3-DB DIRECTIONAL COUPLER

| Dimension | Frequency Range (mc) |
|---|---|
| | 800–1600 |
| Center frequency (mc) | 1200 |
| Input impedance-$Z_o$ (ohms) | 50 |
| Theoretical midband coupling (db) | −2.7 |
| Midband coupling factor $k$ | 0.734 |
| $Z_{oe}$ (ohms) | 127.8 |
| $Z_{oo}$ (ohms) | 19.6 |
| Plate spacing $b$ (inch) | 0.500 |
| Strip thickness $t$ (inch) | 0.063 |
| Strip width $w$ (inch) | 0.185 |
| Strip spacing $s$ (inch) | 0.0084 |
| Length of coupling region $l$ (inch) | 2.460 |
| Terminating lines (inch) | $w=0.550$, $t=0.063$ |

spacing. These spacers had no appreciable effect on the electrical performance of the coupler.

The experimental data for this coupler is plotted in Fig. 6. In order to achieve this performance the positions of the matching posts were adjusted for minimum VSWR and maximum directivity at the center frequency of 1200 mc. The coupling response of the coupler shown in Fig. 6 is $-(3\pm0.3)$ db over its 2:1 frequency band. The VSWR of the coupler is less than 1.2 over the band. The VSWR and directivity measurements of the coupler were made with the aid of sliding loads placed on Ports 2 and 4. Hence, these measurements include the mismatch of the coaxial transitions as well as the mismatch of the couplers.

## Theory of the Three-Quarter-Wavelength Directional Coupler

Recently Barnett, Lacy, and Oliver[4] have shown that improved bandwidth can be obtained compared to that of the quarter-wavelength directional coupler by connecting three coupled pairs of lines in cascade in the manner shown in Fig. 1(b). Theoretically, this composite *three-quarter-wavelength* coupler can be made to have

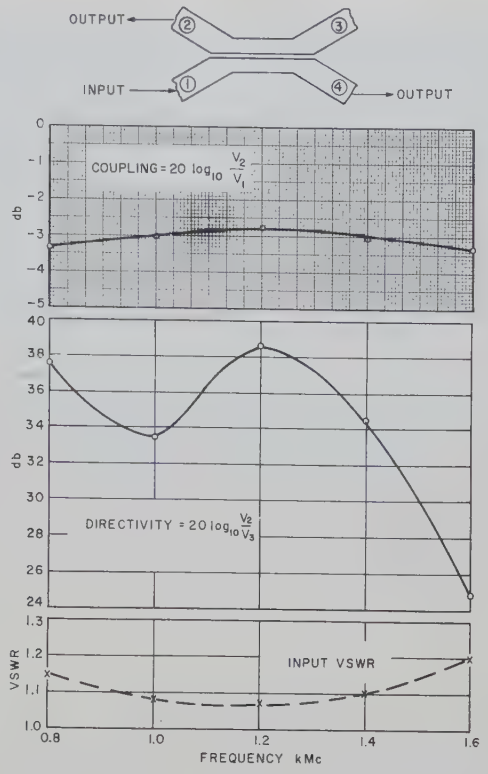


Fig. 6—Experimental performance of the 800–1600-mc 3-db strip-line directional couplers.

infinite directivity and constant input impedance at all frequencies, and for all values of coupling, if each of the cascaded couplers has the same characteristic impedance. The formula given by Barnett, Lacy, and Oliver[4] for the coupling of this directional coupler applies only for weak coupling because of the simplifying assumptions made at the beginning of their analysis. In this section, formulas are given for the three-quarter-wavelength directional coupler that are valid for all degrees of coupling. Also, design information and experimental results are presented for 3-db couplers of this type.

A theoretical analysis of strong coupling is presented by Cohn, Sherk, Shimizu, and Jones.[11] They show that in order for the composite directional coupler to have a perfect match at all frequencies, it is necessary that each individual coupler have the characteristic impedance, $Z_o$, of the transmission lines connected to the coupler. Thus

$$\sqrt{Z_{oo}Z_{oe}} = \sqrt{Z_{oo}'Z_{oe}'} = Z_o. \tag{9}$$

Here, $Z_{oe}$ and $Z_{oo}$ are the even and odd characteristic impedances, with the unprimed and primed values denoting the characteristic impedance of the center and end couplers, respectively, as shown in Fig. 7. Eq. (9) also ensures that the composite directional coupler will have infinite directivity, since each individual coupler

[11] S. B. Cohn, P. M. Sherk, J. K. Shimizu, and E. M. T. Jones, "Strip Transmission Lines and Components," Stanford Res. Inst., Menlo Park, Calif. Final Rep. on SRI Proj. 1114, Contract DA 36-039 SC-63232, DA Proj. 3-26-00-600, SC Proj. 2006A; March, 1957.

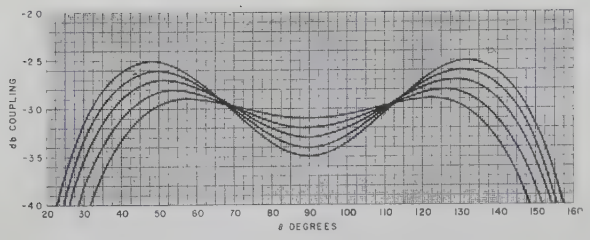


| Coupling Deviation db | k | k′ | $k_0$ | $\frac{k'}{k}$ |
|---|---|---|---|---|
| ±0.1 | 0.8273 | 0.15505 | 0.6998 | 0.18741 |
| ±0.2 | 0.8405 | 0.18367 | 0.6918 | 0.21852 |
| ±0.3 | 0.85241 | 0.21104 | 0.6839 | 0.24758 |
| ±0.4 | 0.86119 | 0.23371 | 0.6760 | 0.27138 |
| ±0.5 | 0.86838 | 0.25373 | 0.6683 | 0.29218 |

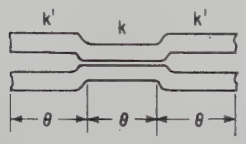


Fig. 7—Equal-ripple response of three-quarter-wavelength directional couplers.

has infinite directivity when it is matched to the connecting transmission lines of characteristic impedance $Z_o$.

Subject to the condition given in (9) and with all the ports of the directional coupler as shown in Fig. 1(b) terminated by $Z_o$, the coupled voltage, $V_2$, at Port 2 produced by the applied voltage, $V_1$, at Port 1 is equal to

$$\frac{V_2}{V_1} = \frac{j\left[\left(\frac{3k_0}{\sqrt{1-k_0^2}} + \frac{2k'}{\sqrt{1-k'^2}} + \frac{k}{\sqrt{1-k^2}}\right)\sin\theta - \left(\frac{k_0}{\sqrt{1-k_0^2}} - \frac{2k'}{\sqrt{1-k'^2}} - \frac{k}{\sqrt{1-k^2}}\right)\sin 3\theta\right]}{\left\{\left[2 - \sqrt{\frac{(1+k)(1-k')}{(1-k)(1+k')}} - \sqrt{\frac{(1-k)(1+k')}{(1+k)(1-k')}}\right]\cos\theta + \left[2 + \sqrt{\frac{(1+k)(1-k')}{(1-k)(1+k')}} + \sqrt{\frac{(1-k)(1+k')}{(1+k)(1-k')}}\right]\cos 3\theta + j\left[\left(\frac{1}{\sqrt{1-k^2}} + \frac{2}{\sqrt{1-k'^2}} - \frac{3}{\sqrt{1-k_0^2}}\right)\sin\theta + \left(\frac{1}{\sqrt{1-k^2}} + \frac{2}{\sqrt{1-k'^2}} + \frac{1}{\sqrt{1-k_0^2}}\right)\sin 3\theta\right]\right\}}. \tag{10}$$

The voltage at Port 3 is zero because each of the individual directional couplers has infinite directivity and the same characteristic impedance $Z_o$ as the terminating lines. By conservation of energy the voltage at Port 4 is

$$\left|\frac{V_4}{V_1}\right| = \left[1 - \left(\frac{V_2}{V_1}\right)^2\right]^{1/2}. \tag{11}$$

Here $\theta$ is the electrical length of the coupled line of each section and $k_0$, $k$, and $k'$ are respectively the midband coupling factor of the three-quarter-wavelength composite directional coupler, the center coupler, and the end coupler.

The midband coupling factor $k_0$ of the three-quarter-wavelength composite directional coupler is given by

$$k_0 = \frac{\frac{Z_{oe}}{Z_{oo}}\left(\frac{Z_{oo}'}{Z_{oe}'}\right)^2 - 1}{\frac{Z_{oe}}{Z_{oo}}\left(\frac{Z_{oo}'}{Z_{oe}'}\right)^2 + 1} \tag{12}$$

while the midband coupling factor of the center coupler is

$$k = \frac{\frac{Z_{oe}}{Z_{oo}} - 1}{\frac{Z_{oe}}{Z_{oo}} + 1} \tag{13}$$

and that of the end couplers is

$$k' = \frac{\frac{Z_{oe}'}{Z_{oo}'} - 1}{\frac{Z_{oe}'}{Z_{oo}'} + 1}. \tag{14}$$

For very weak coupling (10) reduces to

$$V_2 = jV_1(k_1 \sin\theta + k_3 \sin 3\theta)e^{-j3\theta} \tag{15}$$

where $k_1+k_3$ and $k_3$ are the midband voltage coupling factors of the center and end sections, respectively.

One of the most useful forms of the three-quarter-wavelength directional coupler is one that has an equal-ripple frequency variation of coupling. Design information for such couplers is obtained by numerical substitution in (10) and (15).

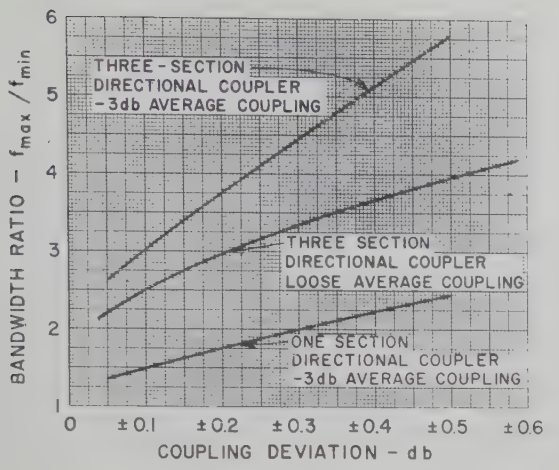


Fig. 8—Bandwidth of various directional couplers.

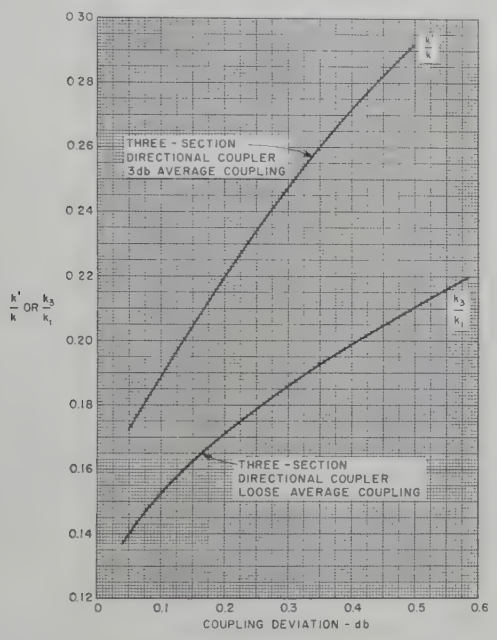


Fig. 9—Design data for three-quarter-wavelength directional couplers.

Fig. 7 shows the variation of coupling with frequency of directional couplers having equal-ripple variations of $\pm 0.1$, $\pm 0.2$, $\pm 0.3$, $\pm 0.4$, and $\pm 0.5$ db. Fig. 8 shows the bandwidth of operation vs coupling deviation for three-quarter-wavelength and quarter-wavelength directional couplers having an average coupling of $-3$ db, and for a three-quarter-wavelength coupler having very loose coupling. The ratio of $k'/k$ and $k_3/k_1$ necessary to achieve this performance with a three-quarter-wavelength coupler is shown in Fig. 9.

It is seen that the $-3$-db three-quarter-wavelength coupler has an extremely wide bandwidth of operation. For example, a bandwidth of 5.8:1 can be obtained for a maximum coupling deviation of $\pm 0.5$ db. Since such a bandwidth is almost unparalleled in microwave components at the present time, it is anticipated that these couplers will find wide application.

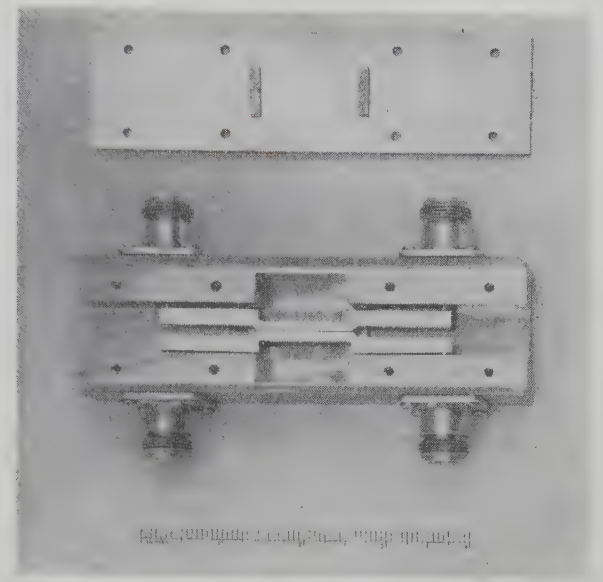

Fig. 10—1.1–3.6-kmc 3-db strip-line directional coupler.

## Experimental Three-Quarter-Wavelength Directional Coupler

A photograph of an experimental 3-db strip-line three-quarter-wavelength directional coupler is shown in Fig. 10. This directional coupler was designed to operate over a 3:1 frequency band centered at 2400 mc with a $\pm 0.1$-db coupling deviation around $-3$ db. Necessary coupling factors, $k$, $k'$, and $k_0$, for the design of this coupler are tabulated in Fig. 7. Examination of the coupling factors $k=0.8273$ and $k'=0.15505$ shows that at midband the coupling of the center coupler is $-1.75$ db and that of the end couplers is $-16.2$ db. The input impedance of this coupler was chosen to be $Z_o=50$ ohms, and the even and odd characteristic impedances of the center and end couplers were computed from (9), (13), and (14) to be $Z_{oe}=162.6$ ohms, $Z_{oo}=15.4$ ohms, $Z_{oe}'=58.5$ ohms and $Z_{oo}'=42.8$ ohms. To achieve reasonable separation between the conductors, the coupling cross section given in Fig. 3(c) was used for the center coupler. However, for the two end couplers, a calculation of the strip dimensions of the cross section given in Fig. 3(c) indicated that the strip widths of the end couplers would have to be approximately five times wider than the center coupler strip widths. In order to reduce this large discontinuity, the cross section of Fig. 3(h) was used for the end couplers. Inspection of the strip cross sections of Fig. 3(c) shows that when conducting side walls are introduced, the dimensions of the coupling slot between the coupled strips need not be altered, but the strip widths must be reduced to maintain the same capacitances to ground. That is, it is only necessary to equate the capacitances of the two cross sections of Fig. 3(c) and 3(h) to each other in order to maintain the same characteristic impedances. Calculations showed that the strip width is reduced to 0.176 inch from 0.488 inch by using the cross section of Fig.

3(h) rather than the one shown in Fig. 3(c), when the side walls are located 0.050 inch away from the strip.

The principal dimensions of the experimental three-quarter-wavelength directional coupler are included in Table III. As may be seen in Fig. 10, each end coupler strip was joined to its terminal by the round center conductor emerging from the coaxial line. The design of this junction was determined experimentally with the aid of the strip-line standing-wave meter. The measured VSWR of the transition in series with a pair of male and female Type-N connectors varied from 1.01 to 1.09 over the frequency range of 1.3 to 4 kmc. To match the junction over this frequency range, it was necessary to extend the strips slightly beyond the junction as shown in Fig. 10. Residual reflections resulting from the steps between the center coupler and end coupler strips were partially canceled by adding a 45-degree transition at each step, and by placing ridges on the ground planes near these points. These matching structures are visible in Fig. 10.

TABLE III

DIMENSIONS OF THREE-QUARTER-WAVELENGTH DIRECTIONAL COUPLER

| | |
|---|---|
| Plate spacing, $b$ | 0.500 inch |
| Strip thickness, $t$ | 0.125 |
| Mid-section strip width, $w$ | 0.107 |
| Mid-section strip spacing, $s$ | 0.0096 |
| End-section strip width, $w'$ | 0.176 |
| End-section strip spacing, $s'$ | 0.135 |
| Spacing between capacitive wall and edge of strip, $s'$ | 0.053 |
| Length of each coupling region, $L$ | 1.110 |

The center conductors and ground planes of this directional coupler were machined from brass stock. The center conductors were supported at their ends by the Type-N connectors. Small polyfoam supports placed above and below the coupled lines held them centered between the ground planes. The gap between the center coupler coupled strips was maintained accurately by means of two small polystyrene spacers.

The experimental data for this directional coupler are plotted in Fig. 11. The coupling response averages $-3$ db with $\pm 0.1$-db variation from 1.1 to 3.6 kmc. The VSWR over this frequency range is under 1.31. The VSWR was measured with the aid of sliding loads placed on Ports 2 and 4, and hence includes the mismatch of the strip-to-coax transition and connector pair between the strip line and the 50-ohm coaxial load, as well as the mismatch of the coupler. Within the coupler, the mismatch due to the steps between the center coupler and end coupler strips is believed to be particularly important.

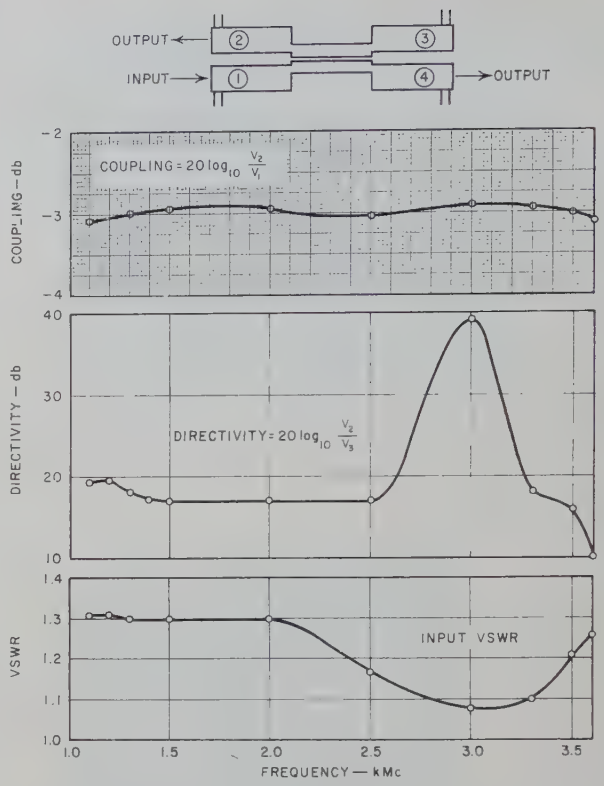


Fig. 11—Experimental performance of 1.1–3.6-kmc 3-db strip-line directional coupler.

The directivity response of this directional coupler, measured with the aid of sliding loads on Ports 2 and 3, varies from 17 to 39 db over the 3:1 band from 1.1 to 3.3 kmc. However, at 3.6 kmc the minimum directivity drops to 10 db. A higher directivity response could certainly be obtained by further work on the various discontinuities.

## CONCLUSION

For all the strip-line directional couplers presented here, very close agreement has been obtained between experiment and theory. The 3-db quarter-wavelength directional coupler has almost constant coupling over a two-to-one frequency band, while the three-quarter-wavelength coupler has almost constant coupling over bandwidths up to 5:1. The various quarter-wavelength directional couplers discussed in this paper have sufficiently good performance to warrant immediate application, while with additional development to improve its directivity, the three-quarter-wavelength model should prove highly useful.

## ACKNOWLEDGMENT

The authors wish to acknowledge the many helpful suggestions received in the course of the work from S. B. Cohn.

# Design of a Full Waveguide Bandwidth High-Power Isolator*

B. J. DUNCAN† AND B. VAFIADES‡

*Summary*—**An analysis of the microwave fields in rectangular waveguide indicates that circular polarization of the *H*-vector components exists at two planes only and the location of these planes is frequency dependent. Also, an examination of Kittel's theory reveals that resonance in ferrites can be made to occur at different frequencies for a constant value of dc magnetic biasing field provided the ferrites are characterized by different values of saturation magnetization. These two effects have been used concurrently in the design of an *X*-band waveguide isolator for operation over a 45 per cent bandwidth, and at high power levels. The theory underlying the design of this isolator is presented. Included is a treatment of the parameters which affect the isolator design. Finally, an operative isolator is described and its experimental characteristics are reported.**

## Introduction

In recent years considerable emphasis has been given to the development of ferrite isolators for microwave applications.[1–6] Isolators have been designed and built for use in low-power narrow band, low-power broadband, and high-power moderate bandwidth applications. However, a description of an isolator designed both for high-power and extremely broad-band application has not yet appeared in the literature. It is the purpose of this paper to describe an isolator of the latter type which operates at gyromagnetic resonance.

In the isolator to be described in this paper, broadbanding is achieved by utilizing ferrites of different saturation magnetization in a constant magnetic biasing field. Each ferrite exhibits a different gyromagnetic resonant frequency and the ferrites are selected in a manner so as to distribute resonance frequencies throughout the required bandwidth of the isolator. Furthermore, each ferrite is located at a position such that it is in a plane of microwave *H*-vector circular polarization at its resonant frequency, and in a region of elliptical polarization at frequencies away from resonance. In this manner, each ferrite exhibits differential attenuation at its resonant frequency and contributes practically no forward (negative) wave magnetic loss at other frequencies. It will be shown that a combination of ferrites operating under these conditions, and in the presence of a single dc magnetic biasing field, will exhibit a large nonreciprocal attenuation over a very broad frequency range while maintaining a very low-forward-wave loss.

The manner in which ferrite location and saturation magnetization affect nonreciprocity over a wide frequency range is treated. Design considerations for the development of a very broad-band *X*-band rectangular-waveguide isolator are presented. Finally an operative high-power 45 per cent bandwidth *X*-band isolator is described and data are presented on its attenuation and VSWR characteristics.

## Design Considerations

The position of *H*-vector circular polarization in rectangular waveguide depends upon the dimensions of the waveguide, operating frequency, and mode of operation. Circular polarization of the microwave *H*-vector components ($H_x$ and $H_z$), as given by Moreno,[7] have been shown to exist in two planes (henceforth referred to as CP planes) for propagation in the dominant $TE_{10}$ mode.[1] The location of the two CP planes with respect to the narrow waveguide walls is given by

$$\frac{x}{a} = \frac{1}{\pi} \tan^{-1} \left[ \left( \frac{\nu}{\nu_c} \right)^2 - 1 \right]^{-1/2} \tag{1}$$

where

$x$ = distance from the narrow waveguide wall,
$a$ = broad dimension of waveguide,
$\nu_c$ = cutoff frequency of waveguide,
$\nu$ = operating frequency.

It follows from (1) that the planes of circular polarization are located equidistant from—and parallel to—the narrow walls of the waveguide. Also these planes are infinitely thin and their location is frequency dependent. The manner in which the location of the CP planes shift

* Manuscript received by the PGMTT, March 10, 1958; revised manuscript received, June 23, 1958.

† Sperry Microwave Electronics Co., Div. of Sperry Rand Corp., Clearwater, Fla.
‡ Microwave Associates, Inc., Burlington, Mass. Formerly at Sperry Gyroscope Co., Div. of Sperry Rand Corp., Great Neck, N. Y.

[1] A. G. Fox, S. E. Miller, and M. T. Weiss, "Behavior and application of ferrites in the microwave region," *Bell Sys. Tech. J.*, vol. 34, pp. 65–103; January, 1955.
[2] S. Weisbaum and H. Boyet, "A double-slab ferrite field displacement isolator at 11 kmc," PROC. IRE, vol. 44, pp. 554–556; April, 1956.
[3] A. Clavin, "High-power ferrite load isolators," IRE TRANS. ON MICROWAVE THEORY AND TECHNIQUES, vol. MTT-3, pp. 38–44; October, 1955.
[4] P. H. Vartanian, J. L. Melchor, and W. P. Ayres, "Broadbanding ferrite microwave isolators," 1956 IRE CONVENTION RECORD, pt. 5, pp. 79–83.
[5] P. H. Vartanian, J. L. Melchor, and W. P. Ayres, "Broadband ferrite microwave isolator," IRE TRANS. ON MICROWAVE THEORY AND TECHNIQUES, vol. MTT-4, pp. 8–13; January, 1956.
[6] M. L. Kales, H. N. Chait and N. G. Sakiotis, "Non-reciprocal microwave component," *J. Appl. Phys.*, vol. 24, pp. 816–817; June, 1953.
[7] T. Moreno, "Microwave Transmission Design Data," McGraw-Hill Book Co., Inc., New York, N. Y., p. 115; 1948.

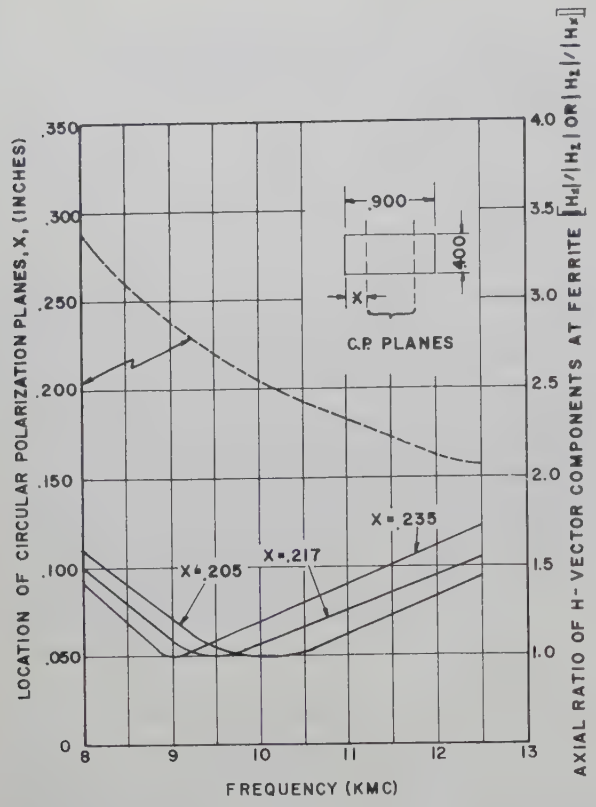


Fig. 1—Frequency dependence of the microwave $H$-vector CP planes in rectangular waveguide. Also shown is the frequency dependence of axial ratio at various points in the waveguide.

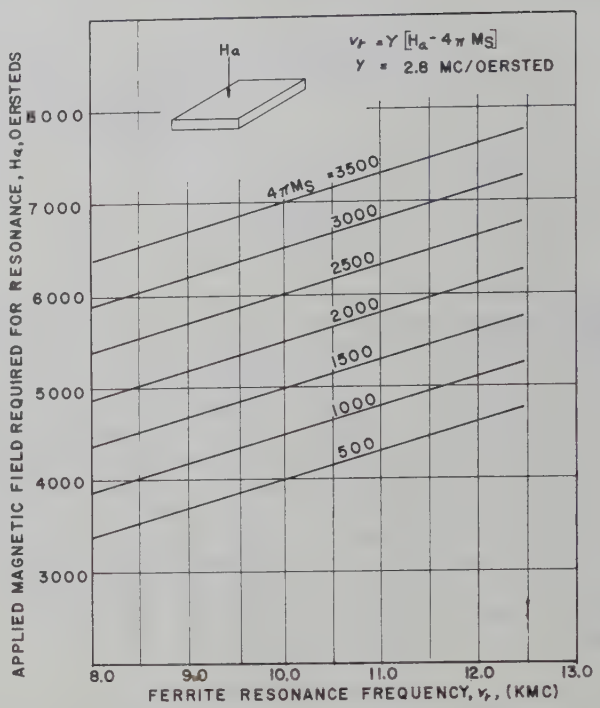


Fig. 2—Frequency dependence of resonance field for ferrites of various $4\pi M_s$.

with frequency is depicted in Fig. 1. The CP planes shift toward the center of the waveguide as cutoff is approached and toward the waveguide narrow walls as frequency is increased It follows that for a given position in the waveguide, true microwave $H$-vector circular polarization will exist at a single frequency only and that at any other frequency an elliptical polarization exists.[1] The degree of ellipticity of the polarization, *i.e.*, the axial ratio of the wave can be obtained as follows

$$AR = \frac{|H_x|}{|H_z|} = \left[\left(\frac{\nu}{\nu_c}\right)^2 - 1\right]^{1/2} \tan\frac{\pi x}{a} \cdot \qquad (2)$$

The microwave $H$-vector axial ratio, *i.e.*,

$$\frac{|H_x|}{|H_z|} \quad \text{or} \quad \frac{|H_z|}{|H_x|}$$

as a function of waveguide position is also shown in Fig. 1 with frequency as a parameter.

In rectangular waveguide the dc magnetic biasing field must of course be oriented perpendicular to the broad waveguide walls in order to obtain optimum nonreciprocal effects in ferrites located in the CP planes. The direction of the applied magnetic field must also be compatible with the direction of propagation to give the desired nonreciprocal effects.

The equation describing gyromagnetic resonance in ferrites shows that for a constant applied dc magnetic field, resonance can occur at only one frequency. Gyromagnetic resonance for a slab of ferrite whose thickness is small compared to a wavelength in the medium can be approximately described by[8]

$$\nu_r = \gamma[H_a - 4\pi M_s] \qquad (3)$$

where $\gamma = 2.8$ mc/oersted (the gyromagnetic ratio of an electron), $H_a$ = external dc magnetic field required for resonance, and $4\pi M_s$ = saturation magnetization of the ferrite.

The dependence of resonance field on frequency as determined using (3) is given in Fig. 2 for various values of $4\pi M_s$. It is evident from the figure that ferrite resonance can be obtained over the full RG-52/U waveguide bandwidth (8.2 to 12.4 kmc) for a constant applied magnetic field by using ferrites with different values of $4\pi M_s$.

## Experimental Characteristics

Using the results derived in the previous section of this paper a broad-band high-power ferrite isolator was designed for operation at $X$-band frequencies. A photograph of the isolator is given in Fig. 3, and its configuration and attenuation characteristics plus VSWR data are given in Fig. 4. Four thin ferrite slabs used in this isolator (Fig. 4) are located flat against the broad walls of rectangular waveguide and each is located in the plane of CP at approximately its resonance frequency. In the isolator design of Fig. 4 the two high $4\pi M_s$ ferrites are located end to end against the top waveguide broadwall whereas the two low $4\pi M_s$ ferrites are similarly located against the bottom waveguide broadwall.

[8] C. Kittel, "On the theory of ferromagnetic resonance absorption," *Phys. Rev.*, vol. 73, pp. 155–161; January 15, 1948.

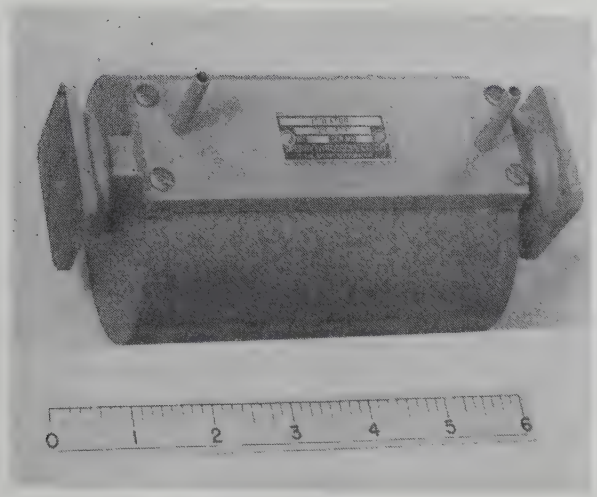

Fig. 3—Assembled version of the $X$-band isolator.

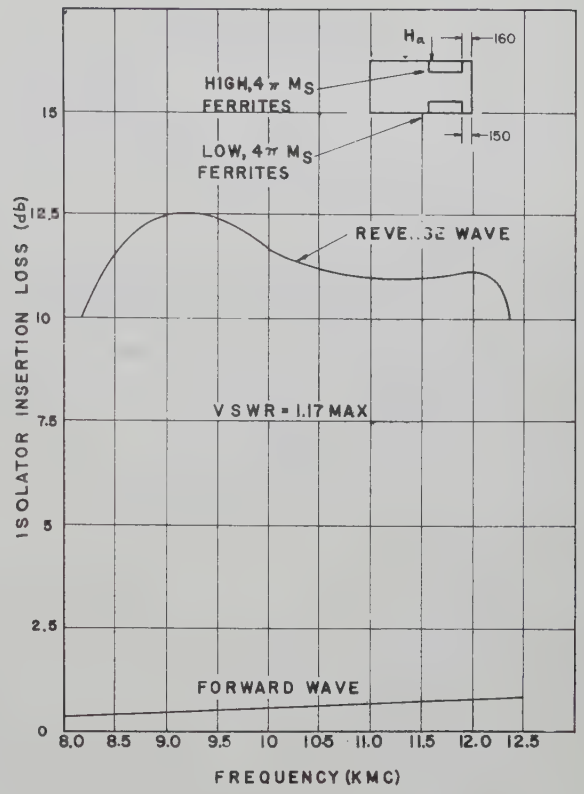


Fig. 4—Physical configuration and attenuation characteristics of the $X$-band isolator.

When located as above in rectangular waveguide, this ferrite configuration offers the advantages over other ferrite shapes of permitting operation at higher peak-power levels without encountering breakdown, and of operating into larger load mismatches without excessive ferrite heating. Also, it can be shown that within the range of values of ferrite saturation magnetization presently available, one of the largest operating bandwidths attainable in high-power rectangular waveguide isolators can be obtained using the isolator configuration depicted in Figs. 3 and 4. Finally, for this configuration the input VSWR can be maintained at a smaller value, and the reverse to forward wave attenuation ratio at a larger value, over the bandwidth than with other configurations presently available and adaptable to high-power use. The presence of all of these desirable features in a single unit gives rise to an isolator which will give satisfactory performance under high-power conditions even when operating into large load mismatches.

The saturation magnetization of the four ferrites employed in the broadband isolator are approximately 2000, 2500, 3300, and 3500 gauss. The resonance frequencies of thin ferrite slabs of the materials as given in Fig. 2 for an applied field of 6500 oersteds are 12.5, 11.5, 9.0, and 8.4 kmc, respectively. The listed ferrites are seen to exhibit resonance frequencies distributed over approximately the desired operating band. An even better distribution would require different value $4\pi M_s$ ferrites which were not immediately available.

Now it is well known in the ferrite art that (3) holds only for the case where the ferrite thickness is small compared both to a wavelength in the medium and the broad dimension of the ferrite. Furthermore, any deviation from these conditions will result in an increase in $\nu_r$ for a constant $H_a$ or a decrease in $H_a$ at a constant frequency. It follows that by varying the ratio of ferrite width to thickness the resonance frequency of a given ferrite can be adjusted within limits as described by Kittel[8] while still maintaining $H_a$ constant. Hence, the dimensions of the ferrite slab used in the isolator were adjusted until it was determined experimentally that the slabs were resonating at the desired frequencies. This shaping of the ferrite slabs resulted in a small deviation from the conditions set forth by Kittel, and a reduction in the $H_a$ required for isolator operation.

Lax[9] has shown that for the ferrite waveguide configuration described herein the location of the CP planes should correspond to those of empty waveguide, and that CP should exist within the ferrite. It was also observed, however, that the presence of the ferrite in the waveguide resulted in an alteration of the location of the planes of circular polarization at each frequency. This can be attributed to the ferrites used in this case being larger than assumed by Lax in his theoretical treatment of this configuration. From Fig. 1 it is seen that the plane of circular polarization for empty waveguide, or waveguide loaded with very thin slabs, shifts from 0.268 inch at 8.2 kmc to 0.158 inch at 12.4 kmc. It has been found experimentally, however, that when ferrite slabs of a practical thickness are used, the best characteristics are obtained when a much smaller shift is assumed. It was further observed that very desirable attenuation characteristics can be obtained with the center of two of the ferrites located at a distance of 0.230 inch from a narrow waveguide wall and the center of the remaining two at a distance 0.210 inch. The ferrites nearest the narrow waveguide wall are, of course, the two ferrites of

[9] B. Lax, "Frequency and loss characteristics of microwave ferrite devices," PROC. IRE, vol. 44, pp. 1368–1386; October, 1956.

smallest $4\pi M_s$ while the ones farthest from the narrow wall are the remaining two ferrites.

The relatively small observed shift of the CP planes as compared to the theoretical empty waveguide can probably be interpreted as being due in part to an effective decrease in the waveguide cutoff frequency caused by the presence of the ferrites and, hence, to a decrease in the shift with frequency of the positions of the CP planes. Also, since ferrites are dielectrics, exhibiting high dielectric constants, it follows that under certain conditions as encountered here they may tend to concentrate the microwave field and hence further reduce the shift of the planes of CP. The magnitude of the effects are, of course, dependent upon the quantity of ferrite present in the waveguide. Similar effects have been observed by other workers including Vartanian[5] who placed an additional dielectric other than ferrite into the waveguide.

An additional important feature of this isolator which aids in maintaining an almost constant reverse attenuation over the entire bandwidth is the use of high $4\pi M_s$ ferrites to obtain differential attenuation at the low end of the frequency band and low $4\pi M_s$ ferrites to achieve the same characteristics at the high end of the band. The need for higher $4\pi M_s$ ferrites to maintain the desired reverse-wave attenuation at the low end of the operating band stems from the decrease in resonance attenuation with frequency for a constant $4\pi M_s$ ferrite and the increase in resonance attenuation with ferrite $4\pi M_s$ for a constant frequency.

A photograph of the 8.2 to 12.4-kmc high-power isolator is shown in Fig. 3 and its configuration; low-power attenuation characteristics and maximum VSWR are depicted in Fig. 4. High-power tests have been conducted on this isolator without the use of liquid cooling which indicates that average powers in excess of 250 watts, with peak powers in excess of 250 kw, can be propagated continuously without deterioration of attenuation below approximately 10 db when looking into a load VSWR of 3:1. Higher microwave power levels can be propagated when the isolator is liquid cooled, or the microwave circuit in which the isolator is located is terminated in a better matched load.

While the effect of ferrite resonance linewidth was not treated in this paper it can play an important role in the design of the broad-band isolators. This effect can generally be compensated for by varying the number of different $4\pi M_s$ ferrites used to cover the desired frequency band and their size, provided extremely broad resonance linewidth ferrites are not used. In the present application ferrites characterized by moderate resonance linewidths were used.

## Conclusions

The design of broad-band isolators in rectangular waveguide can be achieved by using ferrites of different or varying $4\pi M_s$, each of which is located in a plane of microwave $H$-vector circular polarization in rectangular waveguide at its resonance frequency. Under ideal conditions, for a given desired operating bandwidth the values of ferrite $4\pi M_s$ and ferrite waveguide location can be determined with a fair degree of accuracy. In many nonideal conditions the same quantities can be determined to an order of magnitude. By proper selection of ferrite configuration very high-power operation can be effected. Using the information thus derived an extremely broad-band high-power $X$-band rectangular waveguide isolator was constructed which operates over a 45 per cent bandwidth with a forward-wave attenuation of less than 1.0 db and a reverse-wave attenuation in excess of 10 db.

## Acknowledgment

The authors wish to express their gratitude to L. Swern for his generous contributions in technical discussions during the course of this work.

# Correction

Robert E. Collin, author of "A Simple Artificial Anisotropic Dielectric Medium," which appeared on pages 206–209 of the April, 1958 issue of these Transactions, wishes to make the following correction to his paper.

Eq. (13) on page 208 is incomplete and it should be replaced by

$$k_0 S < \frac{2}{\sqrt{\kappa}(1+n_x)}.$$

# Wide-Band Microwave Transmission Measuring System*

J. B. LINKER, JR.†, AND H. H. GRIMM†

*Summary*—A relatively broad-band balanced microwave measurement system has been built using a traveling-wave tube amplifier which permits automatic phase and amplitude transmission measurements to be made simultaneously as a function of frequency over the frequency range 8.7 kmc–9.6 kmc. A phase accuracy of ±1 degree can be achieved for a change of attenuation in the unknown of 24 db. Loss measurements can be made with an accuracy of ±2 per cent. The bridge is built largely of commercially available components and can be easily duplicated. The basic technique is compatible with additional broad-banding efforts as improved components become available, and it will eventually be applicable to all microwave frequencies.

## Introduction

A RELATIVELY broad-band microwave measuring system has been developed which permits rapid search over a wide frequency range at *X* band to meet the growing requirements for impedance, admittance, and transmission measurement in the microwave range. Simultaneous automatic recording of both phase and amplitude response of a general two-port waveguide component as a function of some parameter (such as time, magnetic field, frequency, temperature, etc.) is featured. Of particular note is the accuracy and easy facility with which transmission data as a function of frequency can be obtained. The system is built largely of commercially available components for circuit simplification over previous work[1,2] and also for easy duplication.

## Description of Equipment

### General

A block diagram of the symmetric automatic microwave transmission measuring system is shown in Fig. 1. The system, as used for phase measurements, is built around a traveling-wave tube used in a "frequency offset" application.[1–3] The source of microwave energy is an *X*-band traveling-wave tube whose helix is modulated with a 20-kc sawtooth waveform. This sawtooth serves to phase modulate the $f_0$ signal at a 20-kc rate, causing the output frequency of the traveling-wave tube to be displaced to $f_0+20$ kc. Other frequencies, $f_0$, $f_0-20$ kc, and other sidebands are all at least 20 db below the desired output signal. A ferrite frequency offset generator has been similarly utilized by Dropkin.[4] This signal, $f_0+20$ kc, is fed into two symmetric arms of the measurement system through a Wheeler Hybrid T.[5] (The Wheeler "T" is a quality matched hybrid junction with the necessary electrical and mechanical symmetry to provide a high degree of symmetry and interarm isolation over a 12 per cent frequency band, 8.5–9.6 kmc.) One arm of the measurement system is termed the "reference arm" while the other is the "unknown arm," *i.e.*, the one which contains the unknown in a measurement. Each arm is terminated in a matched load. It is important in broad-band phase measurements that these arms be of the same electrical length. All signals used for measurement are decoupled from the main arms through broad-band waveguide directional couplers. The unknown arm contains both a precision calibrated phase shifter, having small attenuation variation, and a precision attenuator having small phase shift. The phase shifter has only 0.4-db attenuation variation for a 360 degree phase shift range. The attenuator has less than 1 degree phase shift for all values of attenuation up to 40 db. These accuracies hold over an 8.5 to 12.4-kmc frequency range.

### Phase Measurement

For phase measurement, each arm of the measurement system has a symmetrically located crystal mixer. The local oscillator signal, $f_0$, from the klystron is fed symmetrically to each mixer through a Wheeler Hybrid T.[5] Provisions are made for signal level adjustment. Each crystal mixer is a hybrid T balanced mixer. For low signal work, this type of mixer contributes appreciably to the suppression of local oscillator noise. A Hughes *H*-plane folded hybrid T[6,7] is used, fitted with the Microwave Development Laboratories crystal holders, which will take the 2N23D series two-tip 415 crystals, thus permitting choice of mounting polarity. This type of folded hybrid T was chosen because of its high interarm isolation over the frequency range of 8.5 to 9.6 kmc as well as for its mechanical convenience in the

* Manuscript received by the PGMTT, April 21, 1958; revised manuscript received, June 20, 1958. The work for this paper was supported by the United States Air Force.

† General Electric Co., Syracuse, N. Y.

[1] J. B. Linker and H. H. Grimm, "Automatic microwave transmission measuring equipment," *Rev. Sci. Instr.*, vol. 28, pp. 559–563; July, 1957.

[2] E. B. Mullen and E. R. Carlson, "Permeability tensor values from waveguide measurements," PROC. IRE, vol. 44, pp. 1318–1323; October, 1956.

[3] R. C. Cumming, "The Serrodyne frequency translator," PROC. IRE, vol. 45, pp. 175–186; February, 1957.

[4] N. A. Dropkin, "Direct Reading Microwave Phase Meter," Diamond Ordnance Fuze Labs., Washington, D. C., Rep. No. TR-591; April 15, 1958.

[5] E. H. Kraemer and W. A. Elliott, "Model 344 Comparator," Wheeler Labs., Great Neck, N. Y.; Rep. No. 733; February, 1957. (Title Unclassified.)

[6] Microwave Dev. Labs., Wellesley, Mass., Catalog No. 861.

[7] P. A. Loth, Wheeler Labs., Great Neck, N. Y., Rep. No. 443; 1950.

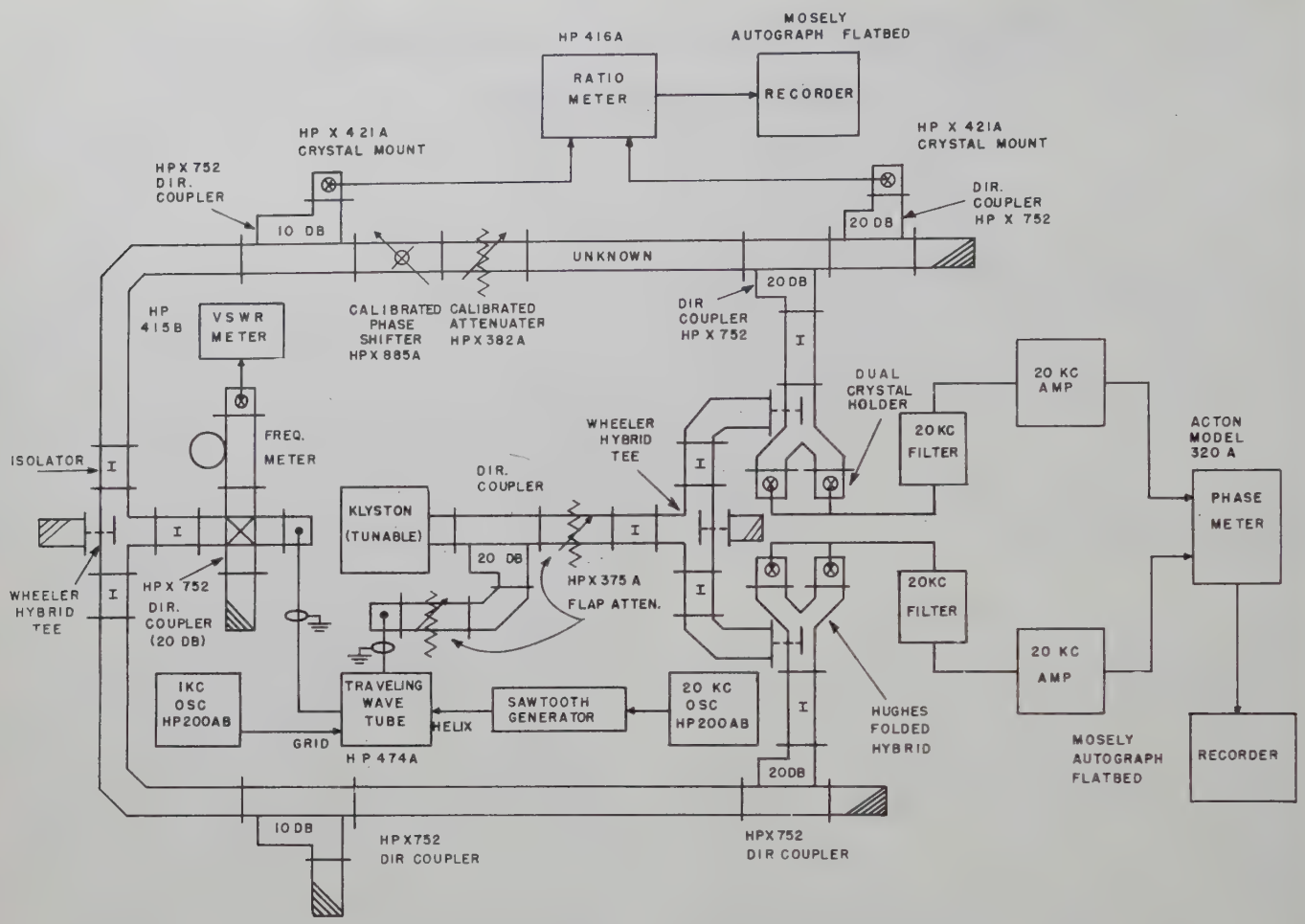


Fig. 1—Symmetric microwave transmission measuring system.

fitting of the crystal holders. The rapid degradation of isolation outside of the 8.5–9.6-kmc frequency range is one of the component properties which limits the frequency range over which the desired precision can be obtained. The available components were adequate for the application requirements to be satisfied by the present equipment. In principle, the single sideband source and the symmetrical arrangement are broad-band techniques. The useful bandwidth depends upon the precision specified and the mechanical symmetry which can be obtained.

In the mixers, then, two 20-kc intermediate frequency signals are generated which are compared in the phase meter for a phase measurement. First, however, each of these two signals is passed through a high-$Q$ 20-kc passive filter to insure a nondistorted waveform which can be used for accurate phase comparison. This is necessary because a "notch" in the IF sinusoidal waveform is caused by the "flyback" of the TWT's helix modulating sawtooth voltage. Wide-band RC coupled amplifiers bring the levels of the two 20-kc signals up to that required by the phase meter. The dc output of the phase meter drives the $y$ axis of the Mosely X-Y-Autograph Recorder, thus giving a continuous record of phase variations as a function of the particular independent variable being used.

### *Attenuation Measurement*

Attenuation (or gain) transmission measurements are easily made by sampling the magnitude of the RF field before and after the unknown by use of the directional couplers. A 1-kc oscillator drives the grid of the traveling-wave tube to amplitude modulate the input signal to the bridge, $f_0+20$ kc. The crystal detector before the unknown provides the 1-kc input to the "incident" channel of a ratio meter while the detector after the unknown feeds the "reflected" channel. The ratio meter automatically measures the change of attenuation of the unknown substantially independent of changes of the input signal level. The recorder output of the ratio meter drives an $x$-$y$ recorder for continuous recording of the amplitude response of the unknown as a function of the varied parameter. The directional couplers can be rearranged for reflectometer measurements.

## Operational Characteristics

### *Fixed-Frequency Measurements*

The curves in Fig. 2 and Fig. 3 illustrate the results obtained from the system in a typical fixed-frequency measurement. These curves, simultaneously recorded, show the phase and attenuation responses of a small rod of ferrite material in round waveguide as a function of a

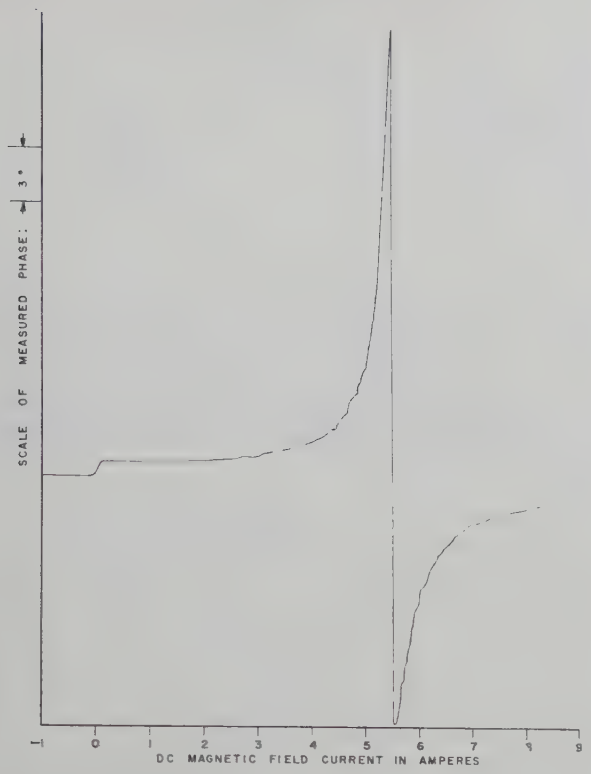


Fig. 2—Phase shift of a ferrite rod in circular waveguide as a function of dc magnetic field for condition of RF circular polarization.

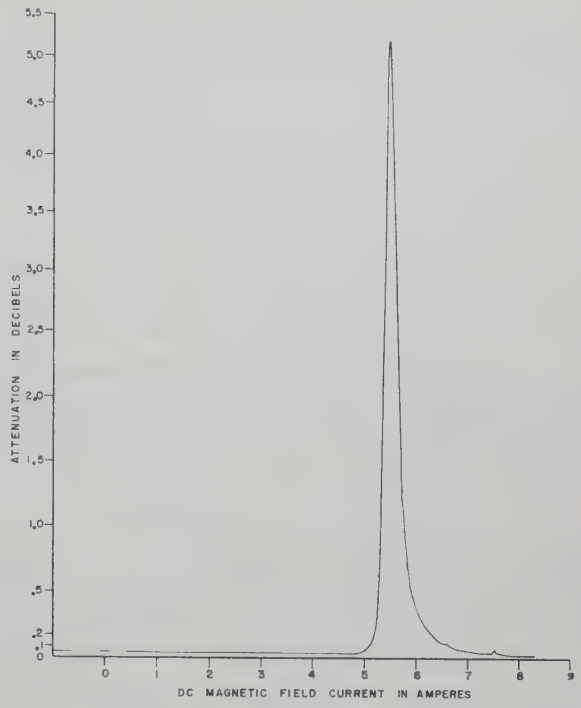


Fig. 3—Attenuation of ferrite rod in circular waveguide as a function of dc magnetic field for condition of RF circular polarization.

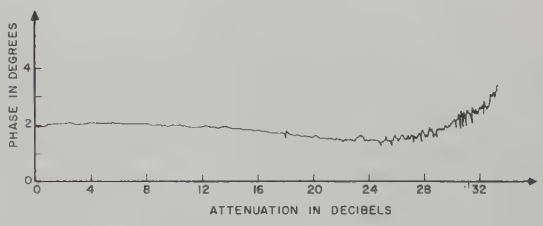


Fig. 4—Measured phase vs dial setting for a Hewlett-Packard X382A precision attenuator placed in unknown arm of measurement system.

longitudinal magnetic field through the rod in one direction. In this case, the microwave signal incident on the sample was circularly polarized. That is, the waveguide "unknown" which was inserted into the arm of the bridge was a piece of round waveguide in a solenoid, preceded and followed by quarter-wave plate sections of round waveguide, each with its rectangular-to-round waveguide transition section. In Fig. 3, the scale of attenuation is shown as calibrated with the sample holder inserted in the "unknown" arm without the ferrite rod. Thus, the displacement of the attenuation curve from zero db represents the minimum insertion loss due to the ferrite rod. In the case of the phase measurement, only the scale is indicated since relative phase shift alone is of significance in a given measurement.

At a fixed frequency, attenuation measurements can be made to within an accuracy of $\pm 2$ per cent of the calibrating attenuator dial reading in decibels. This is the accuracy of the Hewlett-Packard X382A precision calibrated attenuator, which is used to calibrate the system prior to a measurement. The sensitivity may be increased to 0.1 db per inch at any setting of the precision calibrated attenuator. Even at 40-db attenuation, system noise is of the order of 0.02 db. At less than 20-db attenuation, system noise corresponds to less than 0.01 db.

Phase measurements at a fixed frequency can be made with an accuracy of $\pm 2$ degrees. This is essentially the accuracy of the Hewlett-Packard X885A precision calibrated phase shifter (which is 2 degrees from 8.2–10 kmc, and 3 degrees from 10–12.4 kmc). This waveguide phase shifter is used to calibrate the recorders prior to a measurement. In this case, any phase error due to the Acton 320AB Phase Meter, which has a quoted relative accuracy of better than 2 per cent of the differential phase reading, would be avoided. Fig. 4 shows a system phase measurement as a function of the dial setting of a Hewlett-Packard X382A attenuator placed in the "unknown" arm. This shows a maximum variation of 0.5 degree for a 24-db change in level, which is well within the 1 degree accuracy of the attenuator. Although the system sensitivity here limits the dynamic attenuation range to 24 db, this 24-db range can be shifted by resetting the gain of the 20-kc amplifiers.

*Measurements as a Function of Frequency*

The electrical symmetry of this balanced microwave transmission measuring system permits accurate phase measurements as a function of frequency. In Fig. 5, the residual phase response of the system alone is shown when the precision attenuator and phase shifter have been replaced with open waveguide after a calibration

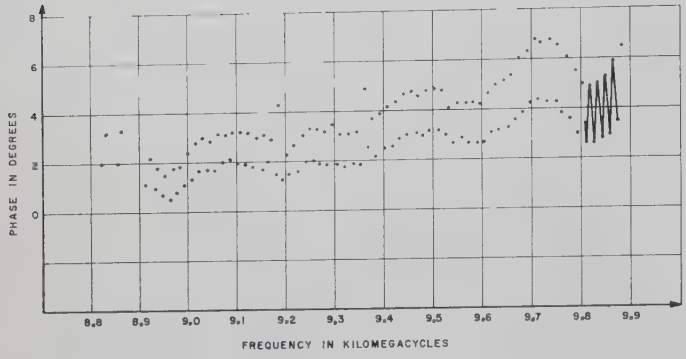


Fig. 5—Residual phase response of symmetric measuring system without calibration phase shifter and attenuator and without padding isolators for mixers.

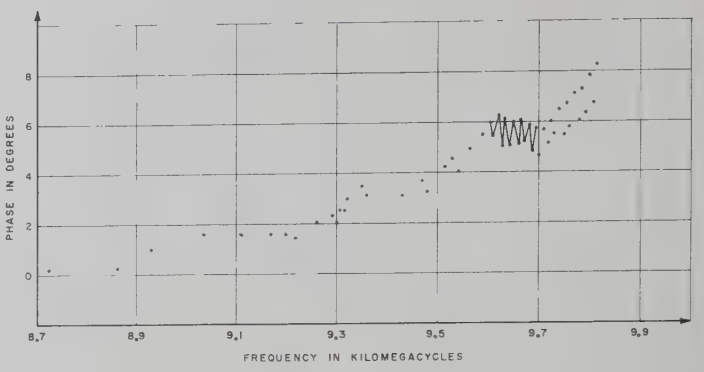


Fig. 6—Residual phase response of symmetric measuring system without calibrating phase shifter and attenuator with padding isolators for mixers.

of the recorders has been made. The calibrating components were removed to improve symmetry in waveguide portions of the system. In Fig. 5, the short period phase variation can be correlated with the reflections from the crystal mixers as a function of frequency. The longer period phase variation (as contrasted with gradual slope) is due to some other discontinuity. Assuming an isolator with a "reverse" reflection coefficient of $\Gamma_I = 1.3$, a reflection coefficient from a discontinuity in open guide would need to be only $\Gamma_d = 1.14$ to give a one degree measured phase error in the system. The gradual slope seen can probably be attributed to an actual small path length differential in the two arms of the system.

When a padding isolator was placed just at the signal input to each of the crystal mixers, the phase vs frequency response shown in Fig. 6 resulted. The undesirable mismatch characteristics (especially those due to the crystals) were reduced, but the path length differential was accentuated (probably due to difference in the isolators). A small phase perturbation device could be used to eliminate the slope of the response shown in Fig. 6, and thus achieve a phase vs frequency response within $\pm 1$ degree for frequency variations from 8.7 to 9.8 kmc. The results shown demonstrate a system phase error of $\pm 2.5$ degrees for frequency variations from 8.7–9.6 kmc, with about half this error for half the frequency range.

Higher accuracy is possible when a phase vs frequency measurement is made on an unknown, if the residual phase shift of the system itself is determined and subtracted from the results. In practice, when less precise results are needed, even the calibrating phase and attenuation components can be left in the unknown arm of the system at the expense of symmetry. In such cases, a correction process (subtraction) would be applied to improve the final data.

## Conclusions

This balanced relatively broad-band microwave transmission measuring system can be used to simultaneously and automatically record the phase and amplitude response of a two-port waveguide device as a function of some chosen parameter, such as magnetic field or frequency. With the present components, automatic phase measurements can be made as a function of frequency from 8.7–9.6 kmc with an accuracy of $\pm 2$ degrees for a change of attenuation in the unknown of from 0–24 db. A method of reducing this error to $\pm 1$ degree has been indicated. Simultaneously, automatic loss measurements can be made with an accuracy of $\pm 2$ per cent. Measurements made at a fixed frequency are quickly accomplished and improved accuracy is achievable.

As a piece of test equipment, this balanced system has a great deal to offer in today's need for accurate and rapid transmission measurements over substantial frequency band. The present work has been confined to the 8.7–9.6-kmc frequency range.

It has been demonstrated that the system has certain accuracies of phase and amplitude in variance in the frequency range of 8.7–9.6 kmc. Fundamentally, this highly symmetrical system has capabilities far in excess of this range. With improvement in bandwidth of waveguide components, such as the hybrid $T$ and isolators, this can be realized. In the meantime, different frequency ranges within the $X$ band can be covered by proper choice of waveguide components. The basic system can easily be applied in other frequency bands.

The system in its present form can be driven by electronically swept microwave sources. Of course, the frequency sweep rates permitted will depend upon both the bandwidth of the receiving components of the system and upon the type of transmission function under examination. Higher speed data accumulation can be engineered into measurement systems of this type as requirements become more stringent.

This system, and modifications of it, are proving to be very useful in antenna phase plotting.

## Acknowledgment

The authors wish to acknowledge the competent technical assistance of Tabor P. Baker.

# A Method for Measuring the Directivity of Directional Couplers*

G. E. SCHAFER† AND R. W. BEATTY†

*Summary*—This method of measuring directivity requires the measurement of the ratio of powers delivered to the side arm when the normal input arm is connected alternately to an adjustable sliding termination and a sliding short circuit. The short circuit is phased to yield maximum and minimum responses and the amplitudes are averaged. Two techniques of adjusting the termination may be used. One procedure requires zero reflection from the termination. The other procedure requires adjustment for a null at the detector and then measurement of the maximum response due to changing the phase of the termination. The inherent errors of the method are analyzed and found to be within the limits—0.01 to 0.00 db in a specific example.

## Introduction

A METHOD to measure directivity of a directional coupler is described. The errors in the method are evaluated and graphs are presented for estimating the total error.

Previously described methods[1,2] required measurement of the combined attenuation of coupling and directivity, the impedance of an auxiliary component, the reversal of the directional coupler, or a combination of these. This method permits measurement of the directivity values up to the entire dynamic range of the attenuation measurement system and completes a measurement by attaching first a short circuit and then an adjustable sliding termination to the same terminal.

## Procedure

The arrangement of equipment is indicated in Fig. 1, with the coupler oriented as in Fig. 2. Preliminary adjustments[3] are made to the tuners shown in Fig. 1 so that: 1) the calibrated attenuator is operated in a matched system, (the condition under which it was calibrated) and 2) the reflection coefficient $\Gamma_{2i}$ (measured at terminal surface 2 of the directional coupler with the normal signal source inactive) has a magnitude less than 0.01.

Procedure 1) is to attach the short circuit and obtain a maximum and minimum amplitude reading by

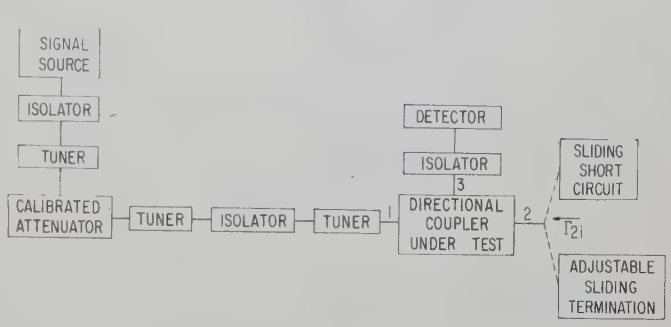


Fig. 1—Arrangement of equipment.

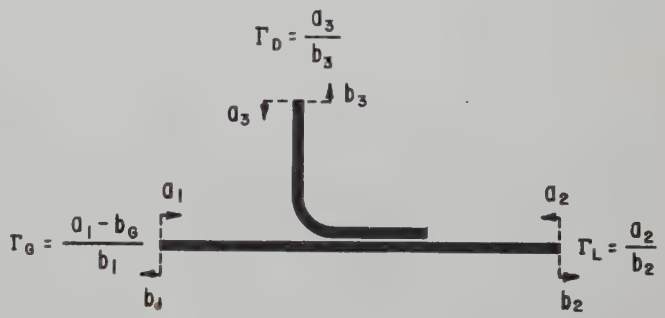


Fig. 2—Representation of directional coupler as a 3-arm junction.

adjusting the phase of the short circuit. The average of these two readings is a reference level and is denoted by $|b_3|_{av}$. An adjustable sliding termination (abbreviated AST in the remainder of the paper) is then attached in place of the sliding short. This AST must be capable of providing zero reflection[4] at the frequency being used. The condition of zero reflection is indicated by no fluctuation in the output level of the detector as the termination is moved along the waveguide. This level is called $|b_3|_0$ and is determined either by the calibrated attenuator or the detector.

$|b_3|_{av}$ is approximately equal to the amplitude of the forward coupled wave, while $|b_3|_0$ is the amplitude of the reverse coupled wave. Therefore, the directivity can be determined to a good approximation by the expression

$$D \approx 20 \log_{10} \frac{|b_3|_{av}}{|b_3|_0}.$$

The adjustment of the AST for $\Gamma_L = 0$ [in procedure 1)] is often tedious. Procedure 2) eliminates this opera-

* Manuscript received by the PGMTT, May 1, 1958; revised manuscript received, June 13, 1958.

† Natl. Bureau of Standards, Boulder, Colo.

[1] C. G. Montgomery, ed., "Techniques of Microwave Measurements," M.I.T. Rad. Lab. Ser., McGraw-Hill Book Co., Inc., New York, N. Y., ch. 14; 1947.

[2] M. Wind and H. Rapaport, "Handbook of Microwave Measurements," Polytechnic Institute of Brooklyn, Microwave Res. Inst., Brooklyn, N. Y., 2nd ed.; 1955.

[3] If the detecting system has sufficient gain, the tuners may be replaced by well-matched broad-band pads with little loss in accuracy. This would simplify the procedure, especially in the case where measurements were to be made at a number of different frequencies.

[4] R. W. Beatty, "An adjustable sliding termination for rectangular waveguide," IRE TRANS. ON MICROWAVE THEORY AND TECHNIQUES, vol. MTT-5, pp. 192–194; July, 1957.

tion and substitutes instead a null adjustment which is readily obtained.[5] (The short circuit measurement remains unchanged from the first procedure and the significance of $|b_3|_{av}$ is the same.) The AST is manipulated to yield a null in the output of arm 3, and is then moved along the waveguide until a maximum response, $|b_3|_T$, occurs. This is approximately twice $|b_3|_0$. The ratio

$$\frac{|b_3|_{av}}{|b_3|_T}$$

can also be used to determine the directivity to a good approximation by the expression

$$D \approx 20 \log_{10} \frac{2|b_3|_{av}}{|b_3|_T}.$$

## Theory

Analysis of this method is accomplished by writing a matrix equation for the three-arm junction representation of a directional coupler

$$b = Sa, \tag{1}$$

(where $S$ is the scattering matrix, and $b$ and $a$ refer respectively to outgoing and incoming wave amplitudes), and solving for the above ratios. The elements of $a$ and $b$ in (1) are displayed in Fig. 2.

The substitution of the appropriate elements into matrix (1) yields a solution for the amplitude of the emergent wave from arm 3,

$$b_3 = -b_g \frac{\begin{vmatrix} S_{12} & 1 - S_{22}\Gamma_L \\ S_{13} & -S_{23}\Gamma_L \end{vmatrix}}{\begin{vmatrix} 1 - S_{11}\Gamma_G & -S_{12}\Gamma_L & -S_{13}\Gamma_D \\ -S_{12}\Gamma_G & 1 - S_{22}\Gamma_L & -S_{23}\Gamma_D \\ -S_{13}\Gamma_G & -S_{23}\Gamma_L & 1 - S_{33}\Gamma_D \end{vmatrix}}, \tag{2}$$

where $b_g$ is the fixed wave amplitude characteristic of the equivalent generator as designated in Fig. 2, and where reciprocity in the form $S_{ij} = S_{ji}$ has been assumed. This may be written in a convenient partition suggested by the form derived by MacPherson and Kerns,[6]

$$|b_3| = \frac{\left| b_g \frac{k}{2} \right|}{\left| \frac{y}{2} + R + r \exp(j\phi) \right|}, \tag{3}$$

where

$$R = \frac{1}{1 - |K\Gamma_L|^2}, \qquad r = |K\Gamma_L| R,$$

$$y = \frac{2\Delta}{KM_{22} - \Delta}, \qquad K = \frac{\begin{vmatrix} S_{12} & S_{22} \\ S_{13} & S_{23} \end{vmatrix}}{S_{13}},$$

$$k = \frac{2S_{13}K}{KM_{22} - \Delta}, \qquad M_{22} = \begin{vmatrix} 1 - S_{11}\Gamma_G & -S_{13}\Gamma_D \\ -S_{13}\Gamma_G & 1 - S_{33}\Gamma_D \end{vmatrix},$$

and

$$\Delta = \begin{vmatrix} 1 - S_{11}\Gamma_G & -S_{12} & -S_{13}\Gamma_D \\ -S_{12}\Gamma_G & -S_{22} & -S_{23}\Gamma_D \\ -S_{13}\Gamma_G & -S_{23} & 1 - S_{33}\Gamma_D \end{vmatrix}.$$

For the arrangement with the short circuit attached, maximum and minimum responses are obtained as the phase of $\Gamma_L$ is shifted. These responses are given by

$$|b_3|\ \max = \frac{\left| b_g \frac{k}{2} \right|}{\left| |r| - \left| \frac{y}{2} + R \right| \right|}, \tag{4}$$

and

$$|b_3|\ \min = \frac{\left| b_g \frac{k}{2} \right|}{\left| |r| + \left| \frac{y}{2} + R \right| \right|}. \tag{5}$$

The average value of these two responses may be written

$$|b_3|_{av} = 1/2(|b_3|_{max} + |b_3|_{min}) = \left| b_g \frac{k}{2} \right| \frac{|r|}{\left| r^2 - \left| \frac{y}{2} + R \right|^2 \right|}. \tag{6}$$

For procedure 1), the AST is adjusted for zero reflection ($\Gamma_L = 0$), and the response may be written

$$|b_3|_0 = \left| b_g \frac{k}{2} \right| \frac{2}{|y + 2|}. \tag{7}$$

The ratio of these two responses is a measure of the directivity and the apparent directivity is given by

$$D_{A1} = 20 \log_{10} \frac{|b_3|_{av}}{|b_3|_0} = 20 \log_{10} \frac{|y+2|}{2} \left( \frac{|r|}{\left| r^2 - \left| \frac{y}{2} + R \right|^2 \right|} \right). \tag{8}$$

In procedure 2), it is convenient to express the response as

$$|b_3| = |b_g| \frac{|k|}{\left| y + \frac{2}{1 + K\Gamma_L e^{-2j\beta l}} \right|}, \tag{9}$$

[5] A similar technique is described by H. C. Poulter in "A note on measuring coaxial coupler directivity," *Hewlett-Packard J.*, vol. 8, pp. 1–4; May–June, 1957.

[6] A. C. MacPherson and D. M. Kerns, "A new technique for the measurement of microwave standing-wave ratios," Proc. IRE, vol. 44, pp. 1024–1030; August, 1956.

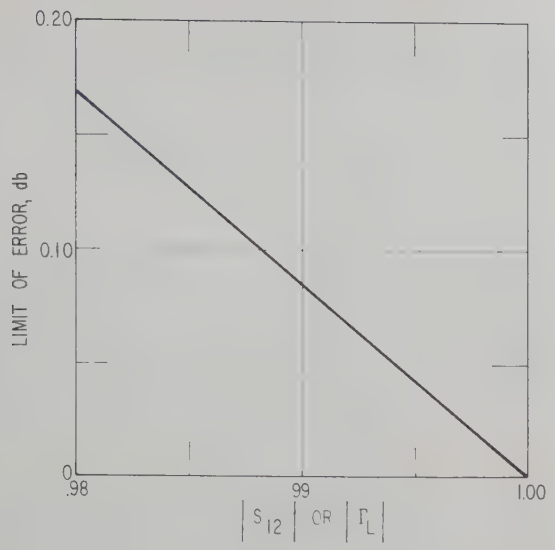


Fig. 3—Limit of error calculated from (17a) (Term 1) and (20).

where $\beta l$ is the electrical length between reference planes of the load and the junction. One adjusts $|\Gamma_L|$ and $l$ to give a null response and it is apparent from (9) that $K\Gamma_L e^{-2j\beta l} = -1$. In deriving the equation for maximum response as $l$ is varied, one considers that the locus of

$$\frac{2}{1 + K\Gamma_L e^{-2j\beta l}},$$

when $|K\Gamma_L| = 1$, is a straight line parallel to the imaginary axis through the point (1, 0) in the complex plane. The maximum response may be written as

$$|b_3|_T = \frac{|b_g k|}{g + 1}, \tag{10}$$

where $g$ is the real part of $y$. Therefore, the apparent directivity may be written as

$$D_{A2} = 20 \log_{10} \frac{2|b_3|_{av}}{|b_3|_T}$$

$$= 20 \log_{10} (g + 1) \left| \frac{|r|}{\left| r^2 - \left| \frac{y}{2} + R \right|^2 \right|} \right|. \tag{11}$$

## Error Analysis

The sources of error can be evaluated by considering the true directivity, defined by

$$D_T = 20 \log_{10} \frac{|S_{23}|}{|S_{13}|}, \tag{12}$$

and evaluating the error in db as

$$\epsilon = D_T - D_A \tag{13}$$

where $D_A$ is given by (8) and (11) for procedures 1) and 2), respectively.

The following three conditions are sufficient to reduce the error to zero:

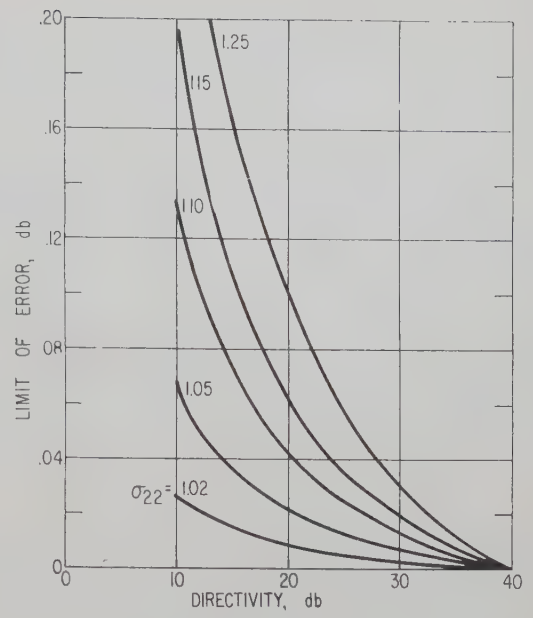


Fig. 4—Limit of error calculated from (17a) (Term 2).

$y = 0$, which reduces the ratios in (8) and (11) to $|K\Gamma_L|$; (14)

$|\Gamma_L| = 1$, which reduces (14) to $|K|$; (15)

$S_{22} = 0$, $S_{12} = 1$, which reduce (15) to $\frac{|S_{23}|}{|S_{13}|}$. (16)

It is assumed that departures from these conditions will be small and are therefore considered as individual cases.

*Case I*

$S_{22} \neq 0$ and $S_{12} \neq 1$, but other conditions are satisfied. Since $D_{A1}$ and $D_{A2}$ reduce to $20 \log_{10} |K|$ in Case I, the error is

$$\epsilon_I = 20 \log_{10} \left| \frac{S_{23}}{S_{12}S_{23} - S_{13}S_{22}} \right|$$

$$= 20 \log_{10} \left| \frac{1}{S_{12}\left(1 - \frac{S_{13}S_{22}}{S_{12}S_{23}}\right)} \right|. \tag{17}$$

One can separate (17) into two terms. If the coupling in decibels is 10 db or more, $S_{12}$ may be eliminated from the second term with little loss of accuracy:

$$\epsilon_I \approx -20 \log_{10} |S_{12}| - 20 \log_{10} \left| 1 - \frac{S_{22}}{\frac{S_{23}}{S_{13}}} \right|. \tag{17a}$$

The magnitude of the contribution from the first and second term is shown in Figs. 3 and 4, respectively. If the coupling in decibels is less than 10 db, the contribution of the second term is appreciably larger than shown in Fig. 4 and it is advisable to employ (17) for a more accurate estimate of the error. (In these cases

where the error caused by assuming $|S_{12}| = 1$ would be large, it would probably be desirable to determine $|S_{12}|$ and make a correction to the measured ratio.)

*Case II*

$y \neq 0$, but other conditions are satisfied. Considerable manipulation of (12) minus (8) and use of the approximation

$$\frac{y}{2} \approx \frac{\Gamma_{2i}}{K}$$

yields for procedure 1),

$$20 \log_{10} \frac{1 - 2\left|\frac{\Gamma_{2i}}{K}\right| - 4|\Gamma_{2i}|^2}{1 + \left|\frac{\Gamma_{2i}}{K}\right|} \leq \epsilon_{II,1}$$

$$\leq 20 \log_{10} \frac{1 + 2\left|\frac{\Gamma_{2i}}{K}\right| - 4|\Gamma_{2i}|^2}{\left|\frac{\Gamma_{2i}}{K}\right|} \quad (18)$$

where $\Gamma_{2i}$ is the reflection coefficient of arm 2, with the inactive generator and detector connected to arms 1 and 3. For the second procedure the limits of error after similar manipulation of (12) minus (11) may be expressed as

$$20 \log_{10} \frac{1 - 2\left|\frac{\Gamma_{2i}}{K}\right| - 4|\Gamma_{2i}|^2}{\left|\frac{\Gamma_{2i}}{K}\right|} \leqq \epsilon_{II,2}$$

$$\leq 20 \log_{10} \frac{1 + 2\left|\frac{\Gamma_{2i}}{K}\right| - 4|\Gamma_{2i}|^2}{1 - 2\left|\frac{\Gamma_{2i}}{K}\right|} . \quad (19)$$

This expression differs from $\epsilon_{II,1}$ only in the denominator.

Fig. 5 shows the limits of error for both procedures 1) and 2) as a function $\sigma_{2i}$, (the VSWR corresponding to $\Gamma_{2i}$). The solid lines indicate the limits of error for procedure 1) and the dashed lines the limits of error for procedure 2). The limiting values for the error as the directivity becomes infinite are indicated on the right-hand side of the graph.

*Case III*

An imperfect short circuit, $|\Gamma_L| \neq 1$, but other conditions are satisfied.

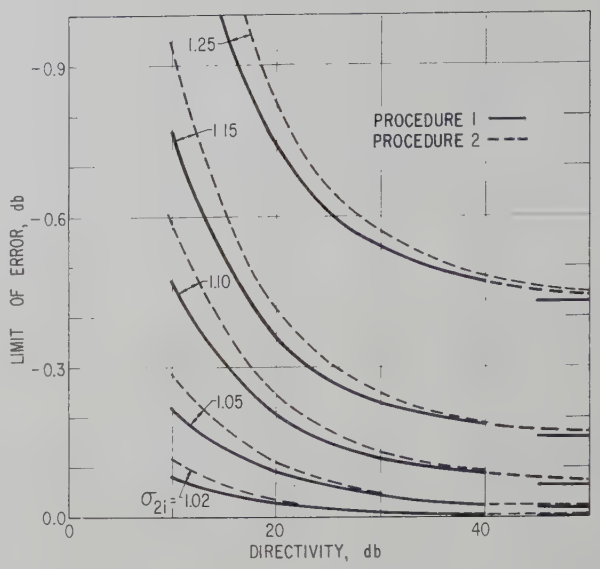


Fig. 5—Limit of error calculated from (18) and (19).

By use of (16) and implications of (17), the error may be written

$$\epsilon_{III} = -20 \log_{10} |\Gamma_L| . \quad (20)$$

This is of the same form as the first term of (17a) and is included in Fig. 3 as an alternate abscissa. This formula applies to both procedures.

The following example shows the limits of error for a case that might be considered typical. For a well-constructed, high directivity, 20-db coupler ($|S_{23}| = 0.1$), the absolute values of the other coefficients are usually

$$|S_{11}| \leq 0.025, \qquad |S_{12}| \approx 0.995,$$
$$|S_{22}| \leq 0.025, \qquad |S_{13}| < 0.001.$$
$$|S_{33}| \leq 0.025,$$

With the preliminary adjustment of $|\Gamma_{2i}|$ to less than 0.01, and use of a short circuit with a reflection coefficient of magnitude greater than 0.995, the limits of error from the above sources are $-0.01$ to $+0.08$. By measuring $|S_{12}|$ and $|\Gamma_L|$, and applying corrections for their departures from unity, the limits of error are reduced to $-0.01$ to 0.00 db. One must also consider the error made in measuring the ratio

$$\frac{|b_3|_{av}}{|b_3|_0} \quad \text{or} \quad \frac{|b_3|_{av}}{|b_3|_T} .$$

Using IF substitution techniques with a below-cutoff standard attenuator, the error may be held to $\pm 0.05$ db with normal precautions. Unless this error is reduced to $\pm 0.01$ db or less, the error in measuring directivity in this example would be limited by the error in measuring the above ratios.

# Development of a High-Power *L*-Band Resonance Isolator*

E. O. SCHULZ-DUBOIS†, G. J. WHEELER‡, AND M. H. SIRVETZ§

*Summary*—Waveguide resonance absorption isolators have been developed for use under high peak and average power conditions at *L* band. Two ferrite materials, one a nickel aluminate ferrite, the other a nickel cobalt ferrite, were developed for this purpose. The characteristics of isolators using these two materials are described.

## Choice of Material

FACED with the problem of developing a high-power isolator for use at about 1300 mc, the resonance-type isolator appeared to be the most promising. Other isolator types which operate off resonance tend to be less feasible at even higher frequencies, at least with ferrite materials presently available.[1]

The principal difficulty in designing a low-frequency resonance isolator is that the applied magnetic fields required for magnetic saturation of the sample and for ferromagnetic resonance are comparable. Thus, care has to be taken to have the sample already magnetically saturated at the resonance field. Otherwise, no distinctive ferromagnetic resonance phenomenon will occur, which is the condition for a satisfactory performance of a resonance isolator. This will be discussed quantitatively.

Although ferrite slabs are used in the practical design, it is somewhat simpler to discuss the relevant facts considering ferrite in disk shape. The sample is mounted in a rectangular waveguide, as shown in Fig. 1, with the dc magnetic field applied normal to its plane. As usual, with respect to its magnetic behavior the disk is approximated by an ellipsoid of revolution. Its dc demagnetizing factor $N_z$ is used for the disk. However, the RF demagnetizing factor $N_x$ is defined by an ellipsoid approximating a disk of twice the original thickness because here the mirror image of the RF $H$ field has to be taken into account. Thus, the sum of the demagnetizing factors is greater than 1.

In order to have the ferrite magnetically saturated, the applied field has to exceed the demagnetizing field,

$$H_{\text{sat}} > 4\pi N_z M_s \tag{1}$$

where $4\pi M_s$ = saturation magnetization.

If the applied field were just equal to the demagnetizing field, there still would be a fair degree of misalignment of the magnetization in some grains of the polycrystalline material due to the magnetic anisotropy. The degree of misalignment is proportional to the anisotropy field, $H_{\text{anis}}$, and decreases as the applied field increases. Thus, it is reasonable to define a saturation field

$$H_{\text{sat}} = 4\pi N_z M_s + H_{\text{anis}} \tag{1a}$$

remembering that this applied field will reduce the misalignment of magnetization in individual grains to a certain degree. Experience has shown that in fairly dense polycrystalline material the ferromagnetic resonance linewidth is of the order of the anisotropy field.

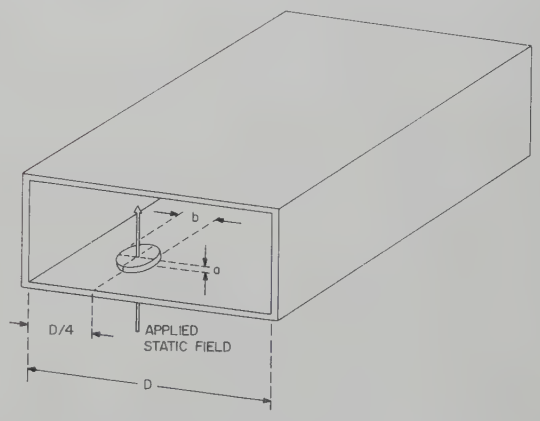


Fig. 1—Illustrating geometry of resonance isolator employing ferrite disk.

The field necessary for resonance is given by Kittel's equation[2]

$$H_{\text{res}} = \omega/\gamma + 4\pi(N_z - N_x)M_s. \tag{2}$$

where $\omega$ = frequency and $\gamma$ = gyromagnetic ratio.

If ferromagnetic resonance is to take place in a saturated ferrite, the resonance field (2) has to be greater than the saturation field (1a) or

$$\omega/\gamma > 4\pi N_x M_s + H_{\text{anis}}. \tag{3}$$

Given the frequency of operation, this condition can be satisfied by choosing a ferrite material with a) small gyromagnetic ratio $\gamma$, b) small saturation magnetization $M_s$, c) small magnetic anisotropy $H_{\text{anis}}$, and by selecting a flat disk geometry such that there is d) a small demagnetizing factor $N_x$. Inspecting the ferrite materials

* Manuscript received by the PGMTT, May 16, 1958; revised manuscript received, June 27, 1958.

† Bell Telephone Labs., Murray Hill, N. J.; formerly with Raytheon Manufacturing Co., Waltham, Mass.

‡ Sylvania Electric Co., Mountain View, Calif.; formerly with Raytheon Manufacturing Co., Waltham, Mass.

§ Raytheon Manufacturing Co., Waltham, Mass.

[1] B. Lax, "Frequency and loss characteristics of microwave ferrite devices," PROC. IRE, vol. 44, pp. 1368–1386; October, 1956.

[2] C. Kittel, "Interpretation of anomalous Larmor frequencies in ferromagnetic resonance experiment," *Phys. Rev.*, vol. 71, pp. 270–271; February, 1947.

TABLE I
SUMMARY OF FERRITE PROPERTIES

| Ferrite | $NiO(Fe_2O_3)_{0.50}(Al_2O_3)_{0.45}$ | $(NiO)_{0.975}(CoO)_{0.025}(Fe_2O_3)$ |
|---|---|---|
| Saturation magnetization, $4\pi M_s$ (gauss) | 300 | 3000 |
| Curie temperature, $T_c$ (°C) | 260 | 590 |
| Linewidth, $\Delta H$, measured at 10 kmc with spherical samples (oersteds) | 825 | 200 |
| Linewidth, $\Delta H^*$, defined as twice the high field half linewidth, measured with thin disks at 1.2 kmc (oersteds) | 780 | 380 |
| Gyromagnetic ratio, $\gamma$, measured at 10 kmc with spherical samples (mc/gauss) | 2.0 | 3.2 |
| Thermal conductivity, $k$, at 100°C, (cal/sec cm. °C) | 0.01 | 0.04 |

presently available and excluding those with a Curie temperature close to room temperature, there appear to exist two classes of ferrites satisfying condition (3) at 1300 mc.

The first class consists of certain members of the family of nickel aluminate ferrites. They have been studied in detail by Gorter[3] and by Maxwell and coworkers.[4,5] If we write the generic formula as $NiAl_xFe_{2-x}O_4$, the pertinent data may be summarized as follows.

1) The Curie temperature drops proportionally to $x$, from 590°C for $x=0$ to 200°C for $x=1$, which is about the limit of usefulness.

2) The saturation magnetization drops from a value of 3000 gauss for $x=0$ to zero at $x=0.625$ (magnetization compensation point), and then rises again to a maximum value at $x=1$. This maximum value at $x=1$ depends somewhat on the processing and in our case is about 500 gauss.

3) The effective $g$ factor is equal to 2.3 at $x=0$, increases with increasing $x$, and reaches very large values just below the compensation point. Above compensation $g$ drops to an approximately constant value of 1.5.

4) The polycrystalline linewidth is large near the compensation point, because the anisotropy energy remains finite as the magnetization goes to zero and the effective anisotropy field becomes very large.[6]

Suitable materials for application in $L$-band resonance isolators may be found for values of $x$ greater than required for magnetic compensation. Conditions a) and b) of small gyromagnetic ratio and saturation magnetization are then met. The anisotropy turns out to be sufficiently small for the purpose. Also, it is not even necessary to choose a very flat geometry because of the small magnetization.

The properties of one such material,

$$NiO(Fe_2O_3)_{0.50}(Al_2O_3)_{0.45},$$

are given in Table I. The resonance isolator data to be given below were obtained with it. The low value of $4\pi M_s$ is a consequence of high porosity in this particular material; when corrected to zero porosity the value of $4\pi M_s$ becomes 500 gauss. The linewidth may be decreased to 600 oersteds by firing the material to high density. After these measurements were completed, it was found that relatively high density materials with measured magnetization of 500 gauss and linewidth below 300 oersteds could be obtained by rather slight compositional and processing variations which did not affect adversely the other properties.

The second type of material that has been investigated is exemplified by nickel ferrite modified by a small cobalt substitution such as to cancel the first order anisotropy at the operating temperature. Sirvetz and Saunders[7] have shown that a decrease in polycrystalline linewidth from 400 oersteds to less than 200 oersteds is achieved by means of a 2.5 mole per cent substitution of cobalt for nickel. The ferrite does not satisfy the first two conditions: the gyromagnetic ratio has practically the free electron value and the saturation magnetization is essentially that of nickel ferrite. However, condition c) of small magnetic anisotropy is fulfilled, and condition d) may be satisfied by choosing a very flat geometry so that the small demagnetizing factor $N_x$ can compensate for the large magnetization. The properties of this material are also given in Table I.

## PERFORMANCE OF THE NICKEL ALUMINATE FERRITE ISOLATOR

### *Isolator and Magnet Geometry*

The typical design of such an isolator is shown in Fig. 2. Fig. 3 is a photograph of one version of the isolator which demonstrates the placement of the Alnico V magnets. Reduced height waveguide is used because it is easier to maintain the biasing $H$ field over the smaller gap. Also, the effectiveness of the ferrite is increased because in reducing the height the RF $H$ field within, the ferrite increases. The reduction in height is limited by the onset of arcing which should be avoided at the peak power used. In practice, half-height guide, $1\frac{5}{8}\times 6\frac{1}{2}$ inches, is used without difficulty at least up to 2.5 megw.

The optimum biasing field at room temperature is about 800 gauss. As a consequence of the large reson-

[3] E. W. Gorter, "Saturation magnetization and crystal chemistry of ferrimagnetic oxides," *Philips Res. Reps.*, vol. 9, pp. 403–443; November, 1954.

[4] L. R. Maxwell and S. J. Pickard, "Magnetization in nickel ferrite-aluminates and nickel ferrite-gallates," *Phys. Rev.*, vol. 92, pp. 1120–1126; December, 1953.

[5] T. R. McGuire, "Magnetic resonance absorption in nickel ferrite-aluminates," *Phys. Rev.*, vol. 91, p. 206; July, 1953.

[6] E. Schlomann and J. R. Zeender, "Ferromagnetic resonance in polycrystalline nickel ferrite aluminate," *J. Appl. Phys.*, vol. 29, pp. 341–343; March, 1958.

[7] M. H. Sirvetz and J. H. Saunders, "Resonance in polycrystalline nickel-cobalt ferrites," *Phys. Rev.*, vol. 102, pp. 366–367; April 15, 1956.

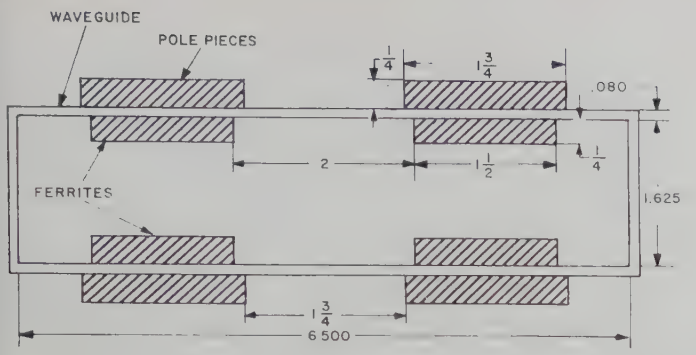


Fig. 2—Dimensions of the $L$-band isolator using nickel aluminate ferrite.

Fig. 3—Photograph of the $L$-band isolator using nickel aluminate ferrite.

ance linewidth, no great homogeneity is required. Therefore, it is possible to have ferrite slabs at the four possible positions within the guide despite the resulting inhomogeneities in the biasing field. The applied biasing field actually is made somewhat lower, between 700 and 750 gauss, beause the device will work at elevated temperatures due to the power dissipated in the ferrite. At higher temperatures the saturation magnetization decreases and so does the field necessary for resonance.

The ferrite dimensions used are determined experimentally as a compromise between various factors. The best figure of merit is achieved with ferrites having a small and flat cross section. The dissipation of power absorbed in the ferrite is also favored by this geometry: that is, small thickness and large area in contact with the guide wall. On the other hand, a large reverse attenuation per unit length of the isolator requires a large ferrite cross section.

Using the ferrite cross-sectional dimensions shown, slabs $\frac{1}{4}\times 1\frac{1}{2}$ inches, an isolation of 10 db was obtained in a length of 15 inches while the insertion loss was 1 db or slightly less. With reduction of ferrite thickness to $\frac{1}{8}$ inch the isolation decreased to one half the above value, but the back-to-front ratio increased from 10 to a value of 15 to 18. Improvement in back-to-front ratio thus involves an increase in length while decreasing thickness for a given amount of isolation, but if lower peak powers were being considered, waveguide of smaller height could be used and the improved back-to-front ratio could be obtained without such a large increase in length.

It seems worth mentioning that the reverse loss per unit length of this isolator can be predicted reasonably well by waveguide perturbation theory. In this theory the change of the wave vector $k$ (in empty guide, $k=2\pi/\lambda_g$) due to perturbations in the waveguide cross section is calculated. The procedure is quite analogous to cavity perturbation theory where the change in resonant frequency is computed. Empty guide RF $H$ field is assumed, in particular circularly polarized field inside the ferrite. Magnetic loss is introduced in the form $\mu''+\kappa''=8\pi M_s/\Delta H$. The reverse loss calculated in this way agrees with the experimental data to within 20 per cent. Good agreement should be expected considering the boundary conditions. The RF $H$ field is tangential to the broad face of the ferrite, hence should be the same inside the ferrite as in empty guide.

*Figure of Merit*

The figure of merit is defined as the ratio of reverse attenuation to insertion loss (back-to-front ratio). For this number Lax,[1] under a number of assumptions, arrived at a theoretical upper limit:

$$F = (2\omega\tau)^2. \tag{4}$$

Here $\tau$ is the relaxation time. The underlying assumptions are: a) the ferrite is magnetically saturated; b) the insertion loss is due to magnetic losses only; c) the loss with applied resonance dc field, but with the nonresonant circular RF excitation, is given by a Lorentzian tail-off of the resonance absorption described by the relaxation time $\tau$; d) the perturbation approach is valid and, especially, the RF $H$ field inside the ferrite is circularly polarized. The relaxation time may be correlated with the observed ferromagntic resonance linewidth. Then the upper limit for the figure of merit reads

$$F = (4\omega/\gamma\Delta H)^2. \tag{4a}$$

Inserting the data for nickel aluminate ferrite, the limiting figure of merit would be 10.5. Experimental figures lie in the range from 10 to 18. The reason for this discrepancy seems to be that the basis of arriving at the theoretical limit is questionable. Most important probably is the fact that the line shape is not Lorentzian. At 10 kmc, the line is found to be asymmetric, with the slope at the low field side larger than that at the high field side. In fact, the assumption of Lorentzian shape far from resonance seems to have no firm theoretical foundation, even for single crystals where distortions due to anisotropy, etc., are absent. It appears that at present there is no reliable basis for estimating a limiting figure of merit under the given circumstances.

*Dielectric Losses*

Since the ferrite fills an appreciable fraction of the waveguide cross section for an appreciable length, dielectric losses would adversely influence the figure of merit of the isolator if they exceeded a certain value. In this case it may be estimated that microwave resistivity of the ferrite should be higher than $10^4$ ohm-cm.

It is known that in ferrites such as considered here, conduction is caused by the presence of divalent iron

ions. In order to keep the resistivity high, the ferrite is made slightly iron deficient and is fired at a rather low temperature (1250°C) in oxygen. Cavity measurements of complex dielectric constant at 10 kmc show that indeed the microwave resistivity of this ferrite is higher than $10^4$ ohm-cm.

*Bandwidth*

From the plot shown in Fig. 4 of attenuation vs applied field, it appears that small changes in applied field and, by the same token, of operating frequency, do not appreciably change the performance of the isolator. This is indeed the case. No special provisions were necessary to achieve a satisfactory performance over a 10 per cent band (1250 to 1350 mc).

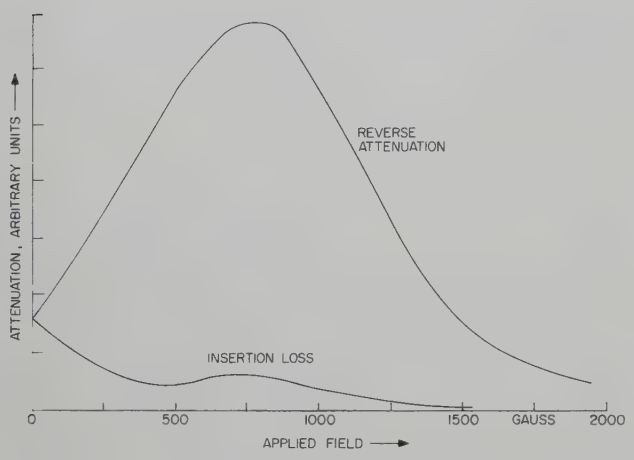


Fig. 4—Typical performance of resonance isolator employing nickel aluminate ferrite.

*Peak Power Performance*

At high-power levels there occur nonlinear phenomena in ferrites which tend to deteriorate the performance of devices operating satisfactorily at low-power levels. For single crystals, the onset of nonlinearities has been explained by Suhl[8] theoretically in terms of instabilities leading to growth of spin wave amplitudes. In this isolator geometry, nonlinearities should set in at an RF $H$ field

$$h = \Delta H_o(2\Delta H_k/4\pi M_s)^{1/2}. \quad (5)$$

Here $\Delta H_o$ and $\Delta H_k$ are the intrinsic linewidths of the uniform precession and of spin waves with wave number $k$, respectively. In applying this result to polycrystalline material, it is difficult to estimate these intrinsic linewidths. But even if they are twenty times smaller than the observed macroscopic linewidth, it turns out that this field hardly can be realized in this isolator with the highest power levels presently attainable. In practice no deterioration in performance has been noted at peak powers of 2 megw in the forward direction (1.5 to 1 mismatch) or with 1.5 megw in the reverse direction.

[8] H. Suhl, "The theory of ferromagnetic resonance at high signal powers," *J. Phys. Chem. Solids*, vol. 1, pp. 209–227; 1957.

*Average Power Handling*

In addition to the nonlinearities mentioned, heating of the isolator due to the energy absorbed in the ferrite can lead to deterioration of the performance at high power levels. Assuming uniform absorption of power throughout the ferrite cross section, the inner surface will be warmer than the one adjacent to the wall by

$$\Delta T = Qd/2Ak \quad (6)$$

with a parabolic distribution in between. Here $Q$ = total power absorbed, $d$ = ferrite thickness, $A$ = total ferrite area, and $k$ = thermal conductivity. Where a large fraction of the power is being absorbed in the reverse direction $\Delta T$ is, of course, a function of position along the length of the ferrite and the above formula must be modified. If $\alpha$ is the fraction of energy absorbed, it is only required to multiply $\Delta T$ as given above by $\ln \alpha/(1-\alpha)$ to get the maximum temperature rise at the end of the ferrite nearer to the load. With absorption of a few hundred watts, this computed temperature gradient only amounts to a few degrees. This is so because the imaginary part of the suceptibility, $8\pi M_s/\Delta H$, is small in this ferrite and hence the absorption per unit area is small.

The present isolator is operated without external cooling. Practically no heating is observable in the application for which it was designed where the total dissipation is of the order of 150 watts, most of this due to forward insertion loss. When 580 watts was applied in the reverse direction (over 500 watts dissipated), the waveguide temperature rose to 115°C, but the isolation was still 10 db. It seems clear that with external cooling and good thermal contact between ferrite and waveguide, power dissipation of up to 5 kw could be realized.

## Performance of the Nickel Cobalt Ferrite Isolator

*Isolator and Magnet Geometry*

The design of this isolator is shown schematically in Fig. 5. The waveguide height is reduced further to one inch without the danger of arcing because samples are very thin.

As was shown in the introduction, this is necessary because the transverse demagnetizing factor $N_x$ has to be small. A typical ratio of width to thickness of the ferrite slabs is 15.

The field required for resonance is about 3000 gauss. It has to be rather homogeneous in order to have the magnetization aligned perpendicular to the slab plane. This is demonstrated in Fig. 6. There, the attenuation shown by the isolator is measured as a function of applied field while the isolator guide is tilted slightly with respect to the homogeneous applied field. It is seen that even small misalignments of ferrite with field are detrimental to its performance, the tolerance being about 0.3 degrees. It is safe to say that the tolerable degree of inhomogeneity of the applied field is of the same order. The difficulty of constructing the magnet and aligning it with the isolator within close toler-

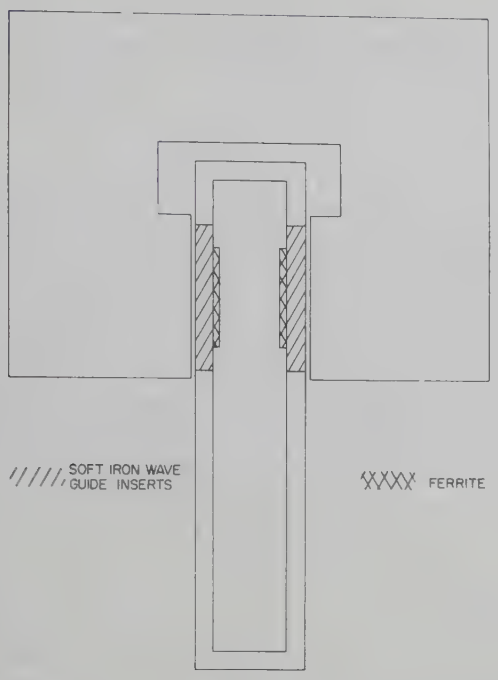


Fig. 5—Schematic cross section of low-frequency isolator with nickel cobalt ferrite.

ances is considerably reduced by making the pole pieces part of the isolator guide rather than of the magnet.

The required high degree of magnetic field homogeneity makes it impossible to use two magnets with opposing fields side by side as in the nickel aluminate ferrite isolator. Thus, only two of the four possible ferrite locations are used in this isolator.

The total length of this isolator can be kept small. In order to achieve the same reverse attenuation, 10 db, it can be about five inches long. This can be understood on the basis of the attenuation per ferrite volume which is proportional to the imaginary part of the resonance susceptibility, $8\pi M_s/\Delta H$. This quantity is much greater for nickel cobalt ferrite.

The reverse loss per unit length of this isolator was computed by waveguide perturbation theory. The agreement with the measured value was better than 10 per cent. A better agreement than in the nickel aluminate ferrite case should be expected since the higher aspect ratio of this ferrite justifies the perturbation approach even more.

*Figure of Merit*

The measured ratio of reverse attenuation to insertion loss is of the same order or greater than the value obtained from (4a) which is 24. Again, this agreement is probably not too significant because the theoretical basis of (4a) is not too realistic.

The most important limitation of the figure of merit in this isolator is the competition of magnetic saturation with ferromagnetic resonance. This was shown by experiments in which further reduction of thickness by grinding the ferrite samples results in further improvement of the figure of merit. Another check is the observation that for higher frequencies the insertion loss is lower.

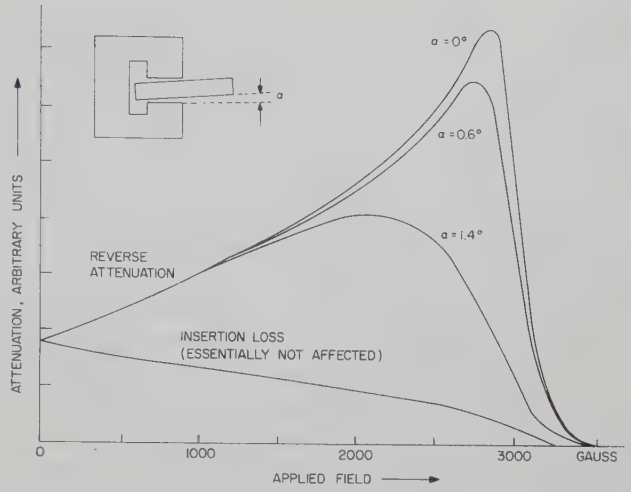


Fig. 6—Demonstrating the effect of misaligning magnet and isolator on reverse attenuation of nickel cobalt ferrite isolator.

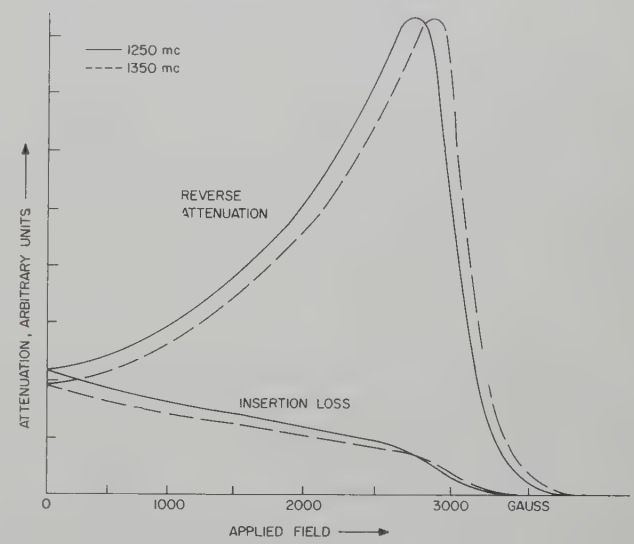


Fig. 7—Reverse attenuation and insertion loss of typical nickel cobalt ferrite isolator at two frequencies as a function of applied field.

For a typical ratio of ferrite width to thickness of 15, the figure of merit at 1200 mc may be 15 increasing to over 30 at 1300 mc.

*Bandwidth*

This isolator works satisfactorily over a 10 per cent band without special provisions. The curves of absorption vs applied field are given in Fig. 7 for 1250 and 1350 mc. With properly chosen applied field the isolation is practically constant over this band. The insertion loss, as mentioned before, however, tends to be somewhat greater at the lower frequency.

*Dielectric Losses*

The fraction of waveguide cross section occupied by ferrite is small. From electrostatic arguments, the electrical field within the ferrite is reduced by some factor greater than 10. Therefore, the dielectric loss tangent tolerable for this isolator is considerably larger than for the one described first. In terms of resistivity, about $10^2$ ohm-cm could be tolerated. The actual microwave

resistivity of this ferrite is somewhat higher. In manufacturing the ferrite material, it is rather fortunate that the requirement of resistivity is not very stringent. Thus, all attention can be concentrated on obtaining a narrow ferromagnetic linewidth. Experience has shown that narrow lines can only be obtained in dense material. Consequently, the processing and firing parameters are optimized with respect to producing a very dense ferrite ceramic.

*Peak Power Performance*

In nickel cobalt ferrite, having high magnetization $M_s$ and small linewidth $\Delta H$, the onset of nonlinearities should occur at comparatively low power levels. To be specific, if the linewidths to be used in (5) are assumed one fifth of the macroscopic linewidth, the nonlinearities should set in below 1 megw.

This seems reasonable in view of some preliminary experiments. Although it was not possible to make very extensive high-power measurements with this isolator, it was found that in the range of 300 to 500 kw the reverse attenuation was about 35 per cent lower than at low powers and was substantially independent of power in this range. The figure of merit did not decrease drastically. So this isolator still might be useful even at high power. One would have to make up for the loss in reverse attenuation by greater length of the isolator.

*Average Power Handling*

With respect to average power dissipation, the two isolators are about equivalent. In the nickel cobalt ferrite isolator, considerably more power is absorbed per volume of ferrite, but heat conduction is enhanced by the higher thermal conductivity of this denser material and by the smaller thickness. With provisions for efficient cooling of the guide wall, it should be possible to dissipate about 5 kw without difficulties.

## Conclusions

In this work two distinct and, in a sense, rather extreme approaches have been taken. In the first a low magnetization material, a nickel aluminate ferrite, was developed especially for the purpose. Although its linewidth was greater than might have been desired, it gave an adequate ratio of isolation to insertion loss for many high-power applications. For example, in amplitron systems,[9] the isolator should provide isolation equal to the amplification of the amplitron in order to reduce the VSWR seen by the driver tube to the value given by the antenna mismatch. Typically, 10 db of isolation is required, and 1 db of insertion loss is ordinarily permissible.

One major advantage of nickel aluminate ferrite is that its low saturation magnetization permits operation with relatively small biasing fields. This is particularly important since pressurization is frequently not available in high power systems, and the magnet gap is consequently large. The fact that the isolation per unit ferrite volume if relatively small is to a great extent overcome by the fact that the geometrical conditions are not very stringent. That is, the transverse demagnetizing factor need not be very small, and a relatively large fraction of the waveguide cross section may be utilized.

The Curie temperature of the nickel aluminate ferrite is rather low, which might appear to be a disadvantage where large amounts of power must be dissipated, but in practice this turns out to be a minor consideration. In high-power systems forced flow liquid cooling will nearly always be available to provide waveguide temperature well below 100°C. Since it has been shown that the temperature difference across the ferrite thickness may be kept small even for several kilowatts of dissipation, there seems to be no strong reason to require a Curie temperature in excess of about 200°C. Finally, it should be noted that no evidence of degradation has been observed at peak powers of 1 to 2 megw. There seems to be every reason to expect good behavior at considerably higher power levels.

The second approach consisted of the use of a material, nickel cobalt ferrite, which had high Curie temperature, high saturation magnetization, and small linewidth. As predicted from the linewidth, a better ratio of isolation to insertion loss was found than could be obtained with the nickel aluminate ferrite. On the other hand, an inconveniently large magnetic field was needed with extremely stringent requirements on accuracy and uniformity as computed on a percentage basis.

In the initial stages of this work it was felt that the high Curie temperature would be very advantageous. Materials like the low magnetization magnesium aluminate ferrites, which were then available for $L$-band use, had Curie temperatures of the order of 100°C and were quite unsuitable for high-power applications. Since the development of the nickel aluminate ferrites, with Curie temperature in excess of 200°C, the importance of the high Curie temperature of nickel cobalt ferrite has been greatly decreased, as explained above. Indeed, the advantages may in practice prove to be rather illusory. Since the resonance field, as given by Kittel's formula, is very nearly equal to the saturation magnetization, rather slight temperature rises, relative to the Curie temperature, will produce significant changes in resonance fields; that is, changes corresponding to an appreciable fraction of the linewidth. With respect to behavior at high peak powers, the present evidence is not clear and experiments are under way to study peak power effects under conditions where heating is negligible. It is expected that nonlinear effects will become important at lower levels than for the nickel aluminate ferrite and some evidence of this may already have been obtained at about 500 kw.

[9] W. C. Brown, "Description and operating characteristics of the planiotron—a new microwave tube device," Proc. IRE, vol. 45, pp. 1209–1222; September, 1957.

# High-Power Microwave Filters*

JOSEPH H. VOGELMAN†

*Summary*—In order to obtain filters capable of handling very high power, the use of radial lines and uniform line discontinuities was investigated as the most promising approach. In this connection, it was necessary to consider the equivalent circuit and interaction for *H*-type radial line mated at each end to uniform $TE_{10}$ waveguide for taper angles of 45°. It was found that the equivalent circuit was valid for taper angles of 45°, and that for engineering design purposes the interaction could be neglected. The author utilized the 45° tapers and the uniform lines to design a high-power microwave filter capable of handling 700 kw at 10 pounds pressure in 0.900 by 0.400 ID waveguide. The design procedure for a multielement filter is described utilizing a partly graphical approach.

## Introduction

SINCE the introduction of radar in the inventory of the United States Air Force, the problem of spurious radiation from the high-power transmitters and the interfering effects on other radars and on communications has been growing in magnitude. As the power of the radar transmitters increased and the frequency spectrum became increasingly crowded, the mutual interference between radars at the same site or between radars and communication reached critical proportions. Since 1948 a major effort has been underway to reduce the deleterious effects of interference. Pulse radar transmitters have been found to radiate relatively large power at spurious frequencies far removed from the operating frequency. These frequencies frequently occur in the assigned operating band of other radars and communications equipments. Accordingly, it is essential to eliminate the spurious radiation at the transmitter. To remove the spurious radiation, the various filters described in the literature by Cohn [5]–[7], Fano [4] and others were examined for their power handling capability. Since the radars in use transmit peak power of the same order of magnitude as the breakdown power of the waveguide, any filter used may not have dimensions smaller than the normal waveguide itself. An examination of the literature and tests of the more promising types indicated that the designs available were not capable of passing the radar transmitter power without breakdown of serious corona and arcing. A new approach was required. The first filter considered consisted of a series of steps similar to that described by Cohn [5] with the exception that the minimum height of the constricted step was made equal to the normal waveguide height.

This type of filter failed to meet the power handling requirement because of the large gradient at the corners of the steps. Since the author had built feed horns with flared outputs which handled large radar power, it appeared that a filter section made up of flared walls would have promise of handling high peak power. The author built in 1953 [3] a filter section consisting of a waveguide of rectangular cross section whose narrow dimensions were expanded through a taper and then contracted through another taper to its original dimensions. The two tapers were separated by a short length of enlarged uniform line [Fig. 1(a)]. The four discontinuities between the uniform and radial lines have a frequency dependence similar to a heavily loaded resonant cavity. Since the taper to uniform line is a more gradual change than a step, this type filter should have a considerably smaller gradient in the vicinity of the discontinuity, and it should be capable of handling high power. The resultant structure was experimentally examined for its transmission characteristics and found to exhibit the properties of a low *Q* band-pass filter. When tested for power handling, it was found to have approximately the same peak power capacity as the uniform waveguide with the normal *E*- and *H*-plane bends when tested at the frequency of minimum insertion loss. This new microwave circuit offered interesting possibilities. The research to be described was undertaken to investigate and apply this circuit form.

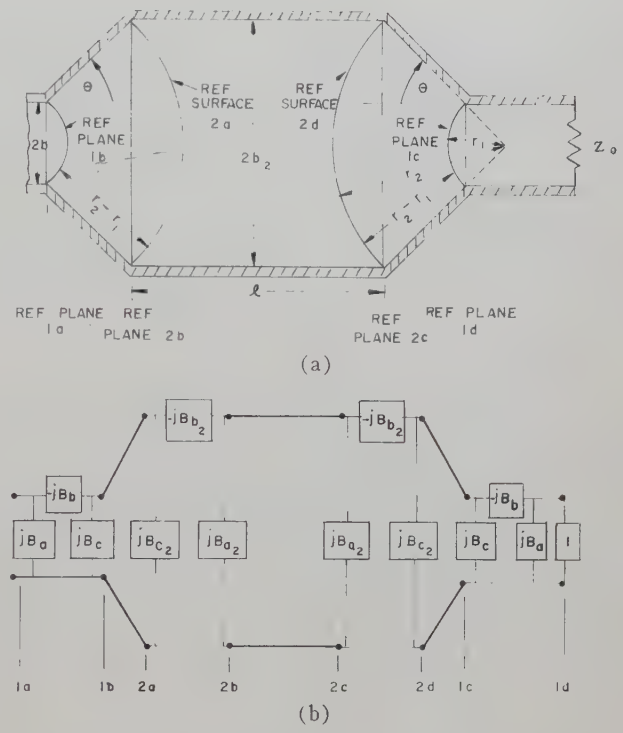


Fig. 1—Physical dimensions and equivalent circuit of a filter section. (a) Physical structure. (b) Equivalent circuit.

* Manuscript received by the PGMTT, May 16, 1958; revised manuscript received, June 30, 1958. The work for this paper was done in partial fulfillment of the requirements for the D.E.E. degree, Polytechnic Inst. Brooklyn, Brooklyn, N. Y., June, 1957.

† Directorate of Communications, Rome Air Dev. Ctr., Griffiss Air Force Base, Rome, N. Y.

### Purpose

The main purpose of the research program was intended to furnish adequate analytic description to permit designing and using this microwave circuit in practical applications. The problem resolved itself into two parts:

1) To determine if the equivalent circuit of the "Waveguide Handbook" [1] accurately described the discontinuity between a uniform and an $E$-plane radial line for taper angles as large as 45°, and if the *interaction* between two adjacent discontinuities in the radial line was small enough to be considered negligible for engineering design purposes.

2) To utilize analytic and experimental properties of tapered sections to derive a rationale for the design of tapered section band-pass and band elimination filters.

### Equivalent Circuit of One Discontinuity

The equivalent circuit of the discontinuity resulting from the junction of an axially symmetrical radial line with a uniform waveguide is identical with that resulting from an asymmetrical junction of a radial line having the same angle with respect to the axis and a uniform line of half the height (Fig. 2). The resulting admittances for the equivalent circuit are given by the following equations [1] (normalized to the rectangular waveguide characteristic admittance):

$$B_a = \frac{2\pi b}{\lambda_g \theta} \ln \frac{\theta}{\sin \theta} \tag{1}$$

$$B_b = \frac{\lambda_g}{\pi b} \frac{\sin \theta}{\theta} \frac{\sin \theta}{1 - \dfrac{\sin 2\theta}{2\theta}} \tag{2}$$

$$B_c = \frac{2b}{\lambda_g}\left[0.577 + \psi\left(\frac{\theta}{\pi}\right)\right] \tag{3}$$

$$\psi(\theta/\pi) = \frac{d \ln \Gamma((\theta/\pi) + 1)}{d(\theta/\pi)} .$$

(See Cohn [2].)

Experiments were set up to confirm these results by obtaining experimentally the equivalent circuit and comparing the results.

### Interaction Between Adjacent Radial Line Discontinuities

The first experimental results confirmed the accuracy of the equivalent circuit within 1 per cent and established a method for examining experimentally combinations of discontinuities resulting from the junction of uniform and $H$-type radial waveguides. The second set of experiments and analysis was intended to investigate the interaction between two adjacent discontinuities along the radial line, resulting from higher order modes in this line and to determine the effect of neglecting it for design purposes. The taper angle, $\pi/4$, between the radial wall and the waveguide axis was selected as a compromise between maximum power handling capacity and magnitude of the discontinuity. The discontinuity capacitance increases while the power handling capacity decreases as the angle increases.

These measurements served to provide a basis for proceeding with the design of the filters, considering the interaction as negligible. The validity of this conclusion was confirmed by the correlation between the design calculations and the measured results. [3]

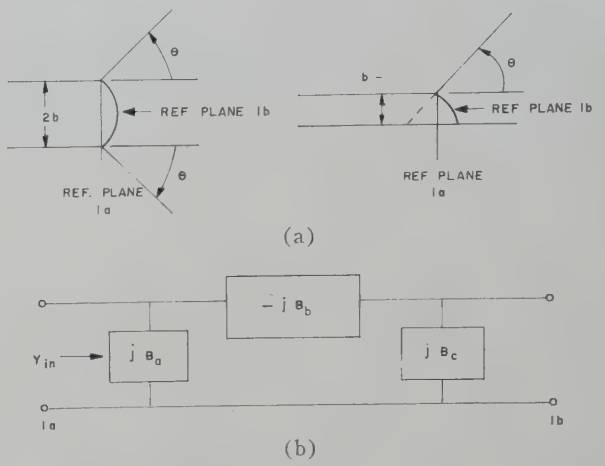


Fig. 2—Junction of uniform and radial line. (a) Physical structure. (b) Equivalent circuit.

### The Single Filter Section

A single filter section consisting of two $H$-type radial lines connected by an enlarged uniform rectangular waveguide will be examined for its characteristics. It will form the fundamental element of a multisection filter design capable of passing high power in one band while providing large loss in the attenuation band.

### Equivalent Circuit of a Single-Filter Section

The physical structure to be considered and its equivalent circuit are shown in Fig. 1. Using this equivalent circuit, the equations which describe the insertion loss can be found in terms of the various parameters forming the equivalent circuit. It should be noted that the specific circuit element values change with frequency, and new values are needed for each frequency of operation.

Since $H$-type radial line and $H_{10}$ rectangular waveguide operation must be described in terms of the waveguide wavelength, a normalizing procedure will be used to make the results generally applicable. Accordingly all dimensions will be normalized to the waveguide wavelength and the parameters $x$ and $y$ as defined by (4a) and (4b) will be used as the variables describing the dimensions of the structure:

$$x = 2\pi r_1/\lambda_g \tag{4a}$$

$$y = 2\pi r_2/\lambda_g \tag{4b}$$

where $r_1$ and $r_2$ are defined in Fig. 1.

TABLE I

NORMALIZED SUSCEPTANCES FOR EQUIVALENT CIRCUIT OF UNIFORM TO RADIAL LINE DISCONTINUITY

| $\theta/\pi$ | $B_a'(\theta)$ | $B_b'(\theta)$ | $B_c'(\theta)$ | $B_c'(-\theta)$ |
|---|---|---|---|---|
| .01 | .00016396 | 3049.6531 | .00016313 | −.00016584 |
| .02 | .00065824 | 759.7244 | .00064789 | −.00066740 |
| .03 | .00147872 | 337.8503 | .00144733 | −.00151013 |
| .04 | .00262640 | 190.0859 | .00254990 | −.00270293 |
| .05 | .00409865 | 121.6865 | .00395448 | −.00425326 |
| .06 | .00589397 | 84.5335 | .00564338 | −.00616219 |
| .07 | .00800834 | 62.1331 | .00761140 | −.00843337 |
| .08 | .01043897 | 47.5935 | .00984880 | −.01106986 |
| .09 | .01318222 | 37.6255 | .01234537 | −.01409215 |
| .10 | .01623377 | 30.4951 | .01509045 | −.01747868 |
| .11 | .01958816 | 25.2195 | .01808371 | −.02124986 |
| .12 | .02324054 | 21.2069 | .02129302 | −.02540972 |
| .13 | .02718508 | 18.0839 | .02472897 | −.02994920 |
| .14 | .03141512 | 15.6059 | .02836850 | −.03486843 |
| .15 | .03592419 | 13.6067 | .03221347 | −.04018163 |
| .16 | .04070486 | 11.9704 | .03622296 | −.04587536 |
| .17 | .04574965 | 10.6141 | .04042975 | −.05196453 |
| .18 | .05105015 | 9.4775 | .04477440 | −.05844997 |
| .19 | .05659785 | 8.5155 | .04927646 | −.06531394 |
| .20 | .06238383 | 7.6940 | .05392453 | −.07255361 |
| .21 | .06839860 | 6.9870 | .05868744 | −.08018519 |
| .22 | .07463217 | 6.3740 | .06355095 | −.08820714 |
| .23 | .08107431 | 5.8392 | .06852173 | −.09650639 |
| .24 | .08771443 | 5.3697 | .07358761 | −.10534803 |
| .25 | .09454171 | 4.9552 | .07871368 | −.11447916 |
| .26 | .10154433 | 4.5876 | .08393175 | −.12398616 |
| .27 | .10871084 | 4.2599 | .08915963 | −.13384062 |
| .28 | .11602911 | 3.9666 | .09445423 | −.14406030 |
| .29 | .12348653 | 3.7030 | .09975445 | −.15461454 |
| .30 | .13107048 | 3.4651 | .10507142 | −.16554699 |
| .31 | .13876802 | 3.2498 | .11039236 | −.17677381 |
| .32 | .14656568 | 3.0542 | .11570450 | −.18833816 |
| .33 | .15444990 | 2.8760 | .12095765 | −.20023248 |
| .34 | .16240676 | 2.7131 | .12619550 | −.21244845 |
| .35 | .17042214 | 2.5639 | .13140382 | −.22494899 |
| .36 | .17848181 | 2.4267 | .13652381 | −.23775218 |
| .37 | .18657103 | 2.3004 | .14157095 | −.25081902 |
| .38 | .19467518 | 2.1838 | .14653297 | −.26416757 |
| .39 | .20277919 | 2.0758 | .15139772 | −.27778706 |
| .40 | .21086781 | 1.9757 | .15615323 | −.29166617 |
| .41 | .21892595 | 1.8827 | .16078772 | −.30576255 |
| .42 | .22693804 | 1.7960 | .16528960 | −.32009385 |
| .43 | .23488851 | 1.7152 | .16964753 | −.33461420 |
| .44 | .24276176 | 1.6396 | .17388165 | −.34937896 |
| .45 | .25054171 | 1.5687 | .17791877 | −.36430560 |
| .46 | .25821271 | 1.5023 | .18177938 | −.37941344 |
| .47 | .26575877 | 1.4399 | .18548491 | −.39465644 |
| .48 | .27316376 | 1.3811 | .18896210 | −.41008308 |
| .49 | .28041166 | 1.3256 | .19226473 | −.42561485 |

If an arbitrary admittance $Y_L = A_L + jB_L$ is used to terminate the circuit at reference plane (1d) of Fig. 1, then the input admittance at reference surface (1c) normalized to the radial line characteristic admittance at $r_2$, defined by (5),

$$\frac{Y_{\text{radial}}}{Y_{\text{uniform}}} = \frac{\sin\theta}{\theta}, \tag{5}$$

is given by the expressions [3]

$$Y_{1c} = A_{1c} + jB_{1c} \tag{6a}$$

$$A_{1c} = \frac{\theta}{\sin\theta} \frac{A_L(B_b')^2}{x^2A_L^2 + (B_b^2 - x^2B_a' - xB_L)^2} \tag{6b}$$

$$B_{1c} = \frac{\theta}{\sin\theta}\left[xB_c' + \frac{B_b'(B_a' + xB_L)(B_b' - xB_L - x^2B_a') - A_L^2xB_b'}{x^2A_L^2 + (B_b' - x^2B_a' - xB_L)^2}\right] \tag{6c}$$

where $B_a'$, $B_b'$ and $B_c'$ are obtained as follows by substituting in (1), (2), and (3):

$$b = x\frac{\lambda_g \sin\theta}{2\pi}. \tag{7}$$

We obtain

$$B_a = x\frac{\sin\theta}{\theta}\ln\frac{\theta}{\sin\theta} = xB_a'(\theta) \tag{8a}$$

$$B_b = \frac{1}{x}\frac{2}{\theta}\frac{\sin\theta}{1 - (\sin 2\theta)/2\theta} = \frac{1}{x}B_b'(\theta) \tag{8b}$$

$$B_c = x\frac{\sin\theta}{\pi}\left[0.577 + \psi\left(\frac{\theta}{\pi}\right)\right] = xB_c'(\theta). \tag{8c}$$

From

$$b_2 = y\frac{\lambda_g \sin\theta}{2\pi} \tag{9a}$$

$$\theta_2 = -\theta \tag{9b}$$

$$\psi\left(\frac{\theta_2}{\pi}\right) = \psi\left(\frac{-\theta}{\pi}\right) = \psi\left(1 - \frac{\theta}{\pi}\right) - \frac{1}{1 - (\theta/\pi)}. \tag{10}$$

Substituting (9a), (9b), and (10) in (7), (8a), (8b), and (8c), we obtained the following relationships used in the computations (normalized to rectangular waveguide of height $b_2$):

$$B_{a_2} = -y\frac{\sin\theta}{\theta}\ln\frac{\theta}{\sin\theta} = -yB_a'(\theta) \tag{11a}$$

$$B_{b_2} = -\frac{1}{y}\frac{2}{\theta}\frac{\sin\theta}{1 - (\sin 2\theta)/2\theta} = -\frac{1}{y}B_b'(\theta) \tag{11b}$$

$$B_{c_2} = y\frac{\sin\theta}{\pi}\left[0.577 + \psi\left(1 - \frac{\theta}{\pi}\right) - \frac{1}{1 - \theta/\pi}\right] = yB_c'(-\theta) \tag{11c}$$

where $B_a'(\theta)$, $B_b'(\theta)$, $B_c'(\theta)$, and $B_c'(-\theta)$ are tabulated in Table I.

In the case of a single filter section terminated in a matched waveguide (*i.e.*, a normalized real terminating admittance of unity value) the above equations reduce to

$$Y_{1c} = A_{1c} + jB_{1c} \tag{12a}$$

$$A_{1c} = \frac{\theta}{\sin\theta}\frac{(B_b)^2}{x^2 + (B_b' - x^2B_a')^2} \tag{12b}$$

$$B_{1c} = \frac{\theta}{\sin\theta}x\left[B_c' + \frac{B_a'B_b'(B_b' - x^2B_a') - B_b'}{x^2 + (B_b' - x^2B_a')^2}\right]. \tag{12c}$$

At reference surface (2d), the input admittance normalized to the radial line characteristic admittance at $r_2$ is

$$Y_{2d} = A_{2d} + jB_{2d} \tag{13a}$$

$$A_{2d} = \frac{A_{1c}\zeta(x, y)[1 + \text{ct}\,(x, y)\ \text{Ct}\,(x, y)]}{A_{1c}^2 + [\text{Ct}\,(x, y) - B_{1c}]^2} \tag{13b}$$

$$B_{2d} = \zeta(x_1 y)\ \frac{[\text{Ct}\,(x, y) - B_{1c}][B_{1c}\,\text{ct}\,(x, y) + 1] - A_{1c}^2\,\text{ct}\,(xy)}{A_{1c}^2 + [\text{Ct}(x, y) - B_{1c}]^2}\,. \tag{13c}$$

The radial functions are defined

$$\text{ct}(x, y) = \frac{J_1(x)N_0(y) - N_1(x)J_0(y)}{J_0(x)N_0(y) - N_0(x)J_0(y)} \tag{14a}$$

$$\text{Ct}(x, y) = \frac{J_1(y)N_0(x) - N_1(y)J_0(x)}{J_1(x)N_1(y) - N_1(x)J_1(y)} \tag{14b}$$

$$\zeta(x, y) = \frac{J_0(x)\text{N}_0(y) - N_0(x)J_0(y)}{J_1(x)N_1(y) - N_1(x)J_1(y)}\,. \tag{14c}$$

The admittance at reference plane (2c), normalized to the enlarged waveguide, is given by

$$Y_{2c} = A_{2c} + jB_{2c} \tag{15a}$$

$$A_{2c} = \frac{(\sin\theta/\theta)A_{2d}(B_b')^2}{y^2((\sin\theta/\theta)A_{2d})^2 + [B_b' + y^2B_c'(-\theta) + y(\sin\theta/\theta)B_{2d}]^2} \tag{15b}$$

$$B_{2c} = -yB_a' + \frac{B_b'[yB_c'(-\theta) + (\sin\theta/\theta)B_{2d}][B_b' + y^2B_c'(-\theta) + y(\sin\theta/\theta)B_{2d}] - yB_b'((\sin\theta/\theta)A_{2d})^2}{y^2((\sin\theta/\theta)A_{2d})^2 + [B_b' + y^2B_c'(-\theta) + y(\sin\theta/\theta)B_{2d}]^2}\,. \tag{15c}$$

$Y_{2c}$ is computed and tabulated in Table II for $\theta = 45°$. At reference plane (2b), the input admittance normalized to the enlarged uniform waveguide is given by

$$Y_{2b} = A_{2b} + jB_{2b} \tag{16a}$$

$$A_{2b} = \frac{A_{2c}(1+\tan^2\phi)}{(A_{2c}^2+B_{2c}^2)\tan^2\phi - 2B_{2c}\tan\phi + 1} \tag{16b}$$

$$B_{2b} = \frac{(A_{2c}^2+B_{2c}^2-1)(-\tan\phi) + B_{2c}(1-\tan^2\phi)}{(A_{2c}^2+B_{2c}^2)\tan^2\phi - 2B_{2c}\tan\phi + 1} \tag{16c}$$

$$\phi = 2\pi l_1/\lambda_g \tag{16d}$$

where $l_1$ is shown on Fig. 3.

The input admittance at reference plane (2a), normalized to the enlarged uniform waveguide, is

$$Y_{2a} = A_{2a} + jB_{2a} \tag{17a}$$

$$A_{2a} = \frac{A_{2b}(B_b')^2}{y^2A_{2b}^2 + (B_b' - y^2B_a' + yB_{2b})^2} \tag{17b}$$

$$B_{2a} = yB_c'(-\theta) + \frac{yA_{2b}^2B_b' - B_b'(yB_a' - B_{2b})(B_b' - y^2B_a' + yB_{2b})}{y^2A_{2b}^2 + (B_b' - y^2B_a' + yB_{2b})^2}\,. \tag{17c}$$

Using the normalizing relationship equation (5), the input admittance normalized to the radial line at reference plane (1b) is

$$Y_{1b} = A_{1b} + jB_{1b} \tag{18a}$$

$$A_{1b} = \frac{(\theta/\sin\theta)A_{2a}\zeta(x, y)[1 + \text{Ct}\,(x, y)\ \text{ct}\,(x, y)]}{((\theta/\sin\theta)A_{2a})^2 + [\zeta(x, y)\ \text{ct}\,(x, y) - (\theta/\sin\theta)B_{2a}]^2} \tag{18b}$$

$$B_{1b} = \frac{[\zeta(x, y) + (\theta/\sin\theta)B_{2a}\,\text{Ct}\,(x, y)]\,[\zeta(x, y)\text{ct}\,(x, y) - (\theta/\sin\theta)B_{2a}) - ((\theta\sin\theta)A_{2a})^2\,\text{Ct}\,(x, y)]}{((\theta/\sin\theta)A_{2a})^2 + [\zeta(x, y)\ \text{ct}\,(x, y) - (\theta/\sin\theta)B_{2a}]^2}\,. \tag{18c}$$

It is now possible to obtain the input admittance in the normal waveguide of the over-all filter using the normalizing relationship equation (5) at reference plane (1a).

$$Y_{1a} = A_{1a} + jB_{1a} \tag{19a}$$

$$A_{1a} = \frac{(\sin\theta/\theta)A_{1b}(B_b')^2}{x^2((\sin\theta/\theta)A_{1b})^2 + (B_b' - x^2B_c' - x(\sin\theta/\theta)B_{1b})^2} \tag{19b}$$

$$B_{1a} = xB_a' + \frac{B_b'(B_c' + (\sin\theta/\theta)B_{1b})(B_b' - x^2B_c' - x(\sin\theta/\theta)B_{1b}) - xB_b'((\sin\theta/\theta)A_{1b})^2}{x^2((\sin\theta/\theta)A_{1b})^2 + (B_b' - x^2B_c' - x(\sin\theta/\theta)B_{1b})^2}\,. \tag{19c}$$

From the input admittance we obtain over-all insertion loss of the filter section:

$$\frac{P_{\text{out}}}{P_{\text{in}}} = a = \frac{4A_{1a}}{(1 + A_{1a})^2 + B_{1a}^2}\,. \tag{20}$$

## Design Procedure

The procedure and examples to be indicated here will assume tapers of 45° (between wall of radial line and center line), since this is considered the most useful compromise between power handling capacity and

TABLE II

INPUT ADMITTANCE OF 45° STEP-DOWN TAPER WITH MATCHED OUTPUT

| y \ x | 0.5 | 0.6 | 0.7 | 0.8 | 0.9 | 1.0 | 1.1 |
|---|---|---|---|---|---|---|---|
| → 0.6 | 1.203338 | | | | | | |
| 0.7 | 1.400145 | 1.171531 | | | | | |
| 0.8 | 1.584169 | 1.336229 | 1.149481 | | | | |
| 0.9 | | | | 1.133411 | | | |
| 1.0 | | | | 1.257456 | 1.122035 | | |
| 1.1 | | | | 1.376837 | 1.232227 | 1.113286 | |
| 1.2 | 1.892920 | 1.797739 | 1.646330 | 1.485810 | 1.339045 | 1.212427 | 1.106944 |
| 1.3 | | | | | | | |
| 1.4 | | | | | | | |
| $A_{2c}$ 1.5 | | | | | | | |
| 1.6 | 1.436203 | 1.601366 | 1.680624 | 1.681639 | 1.627135 | 1.540339 | 1.440697 |
| 1.7 | | | | | | | |
| 1.8 | | | | | | | |
| 2.0 | .956902 | 1.139597 | 1.303417 | 1.434964 | 1.524405 | 1.567949 | 1.568651 |
| 2.4 | .686599 | .818574 | .952227 | 1.083890 | 1.207538 | 1.316435 | 1.402999 |
| 2.8 | .555438 | .647212 | .741529 | .839086 | .938822 | 1.039214 | 1.136668 |
| 3.2 | .505724 | .570511 | .635659 | .703110 | .773405 | .847202 | .923858 |
| 3.6 | .514265 | .557999 | .600448 | .644019 | .689656 | .738529 | .790976 |
| 4.0 | .582900 | .603380 | .622911 | .643958 | .667319 | .693994 | .724410 |
| 4.4 | .738647 | .720488 | .707358 | .700096 | .698189 | .701612 | .710193 |
| → 4.8 | 1.047913 | .947917 | .875883 | .823862 | .786338 | .760096 | .743106 |
| → 0.6 | −.0155465 | | | | | | |
| 0.7 | −.0483493 | −.0160211 | | | | | |
| 0.8 | −.123856 | −.0382917 | −.0170323 | | | | |
| 0.9 | | | | −.0191752 | | | |
| 1.0 | | | | −.0300653 | −.0210976 | | |
| 1.1 | | | | −.0632006 | −.0280343 | −.0229026 | |
| $B_x$ 1.2 | −.778274 | −.459627 | −.247148 | −.120734 | −.0541517 | −.0269147 | .0249325 |
| 1.3 | | | | | | | |
| 1.4 | | | | | | | |
| 1.5 | | | | | | | |
| 1.6 | −1.202105 | −.984238 | −.748404 | −.528785 | −.347814 | −.212308 | −.120243 |
| 1.7 | | | | | | | |
| 1.8 | | | | | | | |
| 2.0 | −1.098445 | −1.053025 | −.967434 | −.846537 | −.703159 | −.552165 | −.409345 |
| 2.4 | −.816035 | −.845162 | −.853190 | −.836469 | −.794072 | −.726502 | −.638047 |
| 2.8 | −.505030 | −.562132 | −.608420 | −.641609 | −.659958 | −.661280 | −.643980 |
| 3.2 | −.193129 | −.265097 | −.329102 | −.384583 | −.431033 | −.467416 | −.492219 |
| 3.6 | +.118990 | +.0328891 | −.0439492 | −.112515 | −.173470 | −.227077 | −.272838 |
| 4.0 | +.432248 | +.327315 | +.236413 | +.156395 | +.0852311 | +.0214090 | −.0355494 |
| 4.4 | +.737174 | +.606920 | +.499452 | +.407806 | +.327947 | +.256887 | +.193178 |
| → 4.8 | +.980700 | +.831424 | +.713496 | +.615469 | +.531509 | +.457437 | +.391136 |

| y \ x | 1.2 | 1.3 | 1.4 | 1.5 | 1.6 | 1.7 | 1.8 |
|---|---|---|---|---|---|---|---|
| → 1.3 | 1.102315 | | | | | | |
| 1.4 | 1.184604 | 1.099170 | | | | | |
| 1.5 | 1.264938 | 1.174456 | 1.096732 | | | | |
| 1.6 | 1.341129 | 1.248624 | 1.166336 | 1.095743 | | | |
| $A_{2c}$ 1.7 | | | | | 1.095495 | | |
| 1.8 | | | | | 1.155230 | 1.095610 | |
| 2.0 | 1.535852 | 1.480423 | 1.412644 | 1.341301 | 1.271392 | 1.206468 | 1.148527 |
| 2.4 | 1.462342 | 1.492353 | 1.494659 | 1.474178 | 1.436856 | 1.389098 | 1.336240 |
| 2.8 | 1.227035 | 1.305527 | 1.367826 | 1.410693 | 1.433332 | 1.436809 | 1.423382 |
| 3.2 | 1.002140 | 1.080043 | 1.154927 | 1.223157 | 1.281993 | 1.328638 | 1.360688 |
| 3.6 | .846932 | .906034 | .967494 | 1.029482 | 1.090638 | 1.148711 | 1.200977 |
| 4.0 | .758646 | .796790 | .838723 | .883641 | .931199 | .980305 | 1.029519 |
| 4.4 | .723529 | .741489 | .763899 | .790229 | .820372 | .853773 | .889868 |
| → 4.8 | .733640 | .730716 | .733574 | .741467 | .754008 | .770671 | .791189 |
| → 1.3 | −.0267145 | | | | | | |
| 1.4 | −.0260050 | −.0283318 | | | | | |
| 1.5 | −.0381399 | −.0260197 | −.0300578 | | | | |
| 1.6 | −.0638222 | −.0348989 | −.0261142 | −.0314047 | | | |
| 1.7 | | | | | −.0326896 | | |
| $B_{2c}$ 1.8 | | | | | −.0260868 | −.0334130 | |
| 2.0 | −.285833 | −.187433 | −.115042 | −.0666671 | −.0382406 | −.0256887 | −.0257226 |
| 2.4 | −.536137 | −.429640 | −.327248 | −.236580 | −.161207 | −.102821 | −.0615519 |
| 2.8 | −.608091 | −.554937 | −.487734 | −.412044 | −.333050 | −.256506 | −.187408 |
| 3.2 | −.504372 | −.502659 | −.486625 | −.456893 | −.414759 | −.362990 | −.305088 |
| 3.6 | −.310386 | −.338874 | −.357444 | −.365389 | −.362252 | −.348144 | −.323434 |
| 4.0 | −.0860780 | −.130078 | −.167284 | −.197094 | −.219146 | −.232962 | −.237769 |
| 4.4 | +.135687 | +.0838508 | +.0373597 | −.00355278 | −.0389994 | −.0686821 | −.0918718 |
| → 4.8 | +.331088 | +.276328 | +.226202 | +.180699 | +.139349 | +.102214 | +.0697134 |

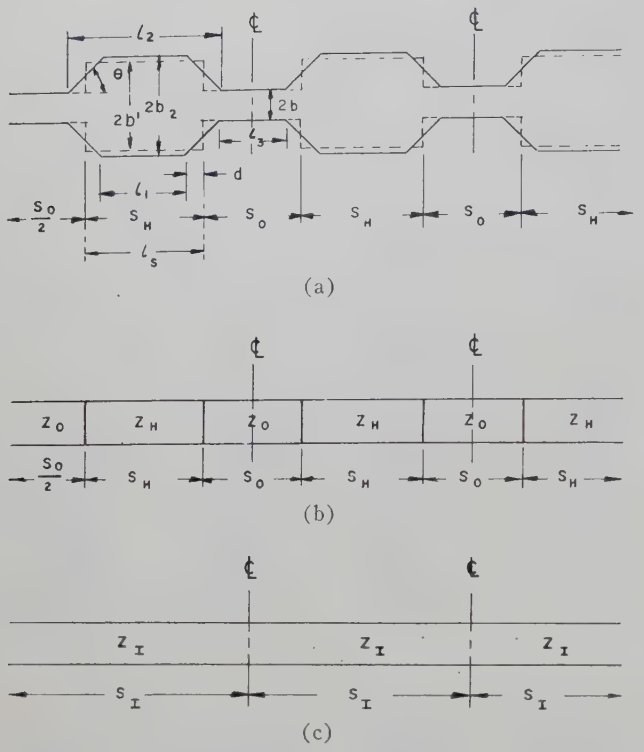


Fig. 3—Physical dimension. (a) Equivalent circuit. (b) Equivalent iterative cell. (c) Multiple section filter.

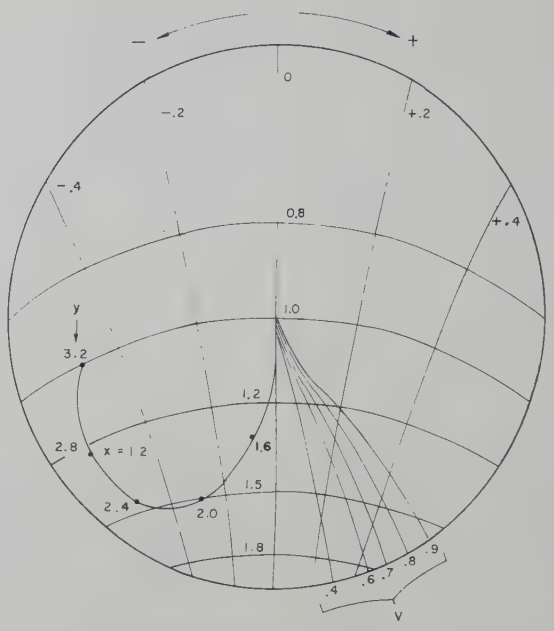


Fig. 4—Plot of input admittance for taper terminated in match ($x=1.2$) as a function of $y$.

maximum effective discontinuities. Since $(r_2-r_1)$ and $l_1$ are independent variables, the frequencies of minimum and maximum insertion loss can be specified to obtain two sets of simultaneous equations (5) to (20) which can be solved to give the required length and height. While the preceding statement is true in principle, the actual reduction to practice is not practical without a high-speed computer since the equations are complex combinations of Bessel and transcendental functions. The problem can be solved without a computer, however, by the use of equivalent steps which will considerably simplify the design procedure and calculations, and produce fairly accurate results.

It can be shown that for every radial line section terminated at each end in a uniform waveguide, there exists an equivalent step which is a function of frequency [3]. The design procedure can then be carried out using uniform waveguide of enlarged $E$-plane dimensions (guide height) connected by steps, and the equivalent taper section can be determined to complete the design.

A plot of the input admittance of a step-down taper terminated in a match obtained from Table II will show that the VSWR in general varies inversely with the frequency. "Step-down" denotes the case where the wave propagates from a larger to smaller guide. As $y$ is made larger, the VSWR gets smaller (Fig. 4), and only at one point on each curve (one frequency), can the magnitude of the admittance be approximated by the ratio of the heights. This characteristic introduces another computational problem when iterative sections are used to design a filter. While the frequency response of a single section can be computed directly from the radial line equation, the computation of an iterative structure of a number of sections is virtually impossible without the use of a high-speed, large capacity digital computer. To overcome the need for a large computer, the concept of the equivalent step is introduced to permit the use of the simplified equivalent circuit and equivalent iterative cell of Fig. 3. By means of the equivalent step, a design procedure for an iterative filter becomes possible.

## The Equivalent Step

Since we have normalized the radial line relationships in terms of $x$ and $y$ as previously defined by (4a) and (4b), we will similarly normalize the step characteristics to $U$ and $V$.

$$U = b'/b \tag{21}$$

where $2b'$ is the height of the enlarged equivalent waveguide (Fig. 3) and $2b$ is the height of the standard waveguide.

$$V = b'/\lambda_g = Ub/\lambda_g \tag{22}$$

Since the standard size guide is the same for both the input to the taper section and the equivalent step section, the ratio of $V$ to $U$ can be expressed in terms of $x$:

$$\frac{V}{U} = x\,\frac{\sin\theta}{\pi}\,. \tag{23}$$

For 45° tapers, we get

$$\frac{V}{U} = 0.22508x. \tag{24}$$

The output radial line section, the equivalent step, and their equivalent circuits are shown in Fig. 2.

The normalized input admittance in the large guide at the step of a step down terminated in a load $Y_L$, normalized to the output guide, is given by the expression

$$Y = (b'/b)Y_L + jB/Y_{01} \tag{25}$$

where $B/Y_{01}$ is the discontinuity susceptance due to the step normalized to the output guide [10].[1] If a matched output load is considered, then (25) reduces to

$$Y = b'/b + jB/Y_{01} = U + jB/Y_{01}. \tag{26}$$

Thus, if we plot on a Smith Chart the input admittance for the step down with matched output, the value of $U$ can be determined directly since it is identical with the conductance (real part) of the admittance.

One can always select a step designed by $U$ and $V$ with an insertion VSWR equal to that of a specific taper. The input admittance plotted on a Smith Chart for either the taper or step will move around the constant VSWR circle in the same manner when the input reference planes are moved identical electrical distances. The input admittance for the step is specified in the plane of the step. The input admittance for the taper is specified at the junction of the enlarged waveguide and the radial line. The angular displacement on the constant VSWR circle between the two input admittances corresponds to the distance in fractions of a waveguide wavelength between the taper and the equivalent step.

In order to permit graphical computation of a filter, the input admittances for a family of selected step down tapers have been computed on a digital computer from (5) to (15), and are tabulated in Table II. The input admittances for the step (step down) have been plotted on Fig. 4 for selected values of $V$ with $U$ as the continuous variable. These are the curves to the right of the real axis on the Smith Charts. The input admittance of a step of height ratio $U$ can be found where the conductance curve, equal in magnitude to $U$, intersects the curve for the appropriate $V$. The plotted curves correspond to $V=0.4$, 0.6, 0.7, 0.8, and 0.9 going from the real axis to the right. For selected values of $y/x$ the input admittance can be plotted with $x$ as the continuous variable. The insertion VSWR curve which intersects with the input admittance curve of a fixed step down increases as the frequency increases ($x$ grows larger). The taper, however, shows a generally decreasing VSWR as $x$ and $y$ increase. The insertion VSWR must be the same for the taper and its equivalent step, and this equivalent step will be a valid approximation only over a narrow frequency band. However, for very small steps and corresponding tapers, the bandwidth, over which the step is a valid approximation, will be larger as the step gets smaller. For a given step the susceptance increases if the wavelength is made shorter. The taper, however, acts like an impedance matching structure between the larger and smaller height waveguides, and the match gets progressively better for shorter wavelengths.

[1] See Marcuvitz [1], pp. 307–309.

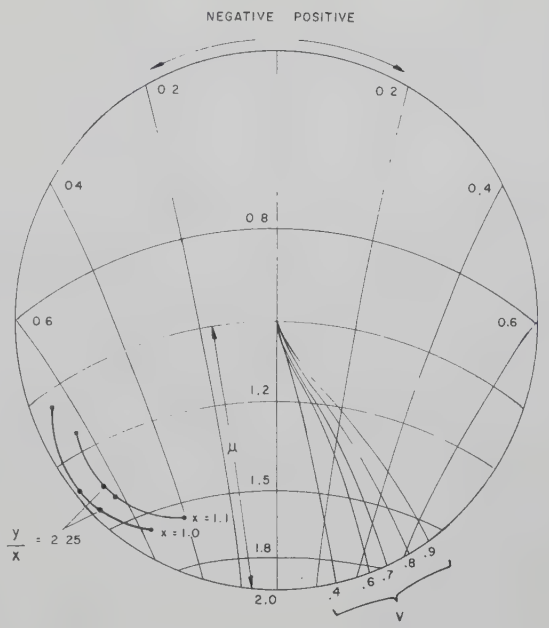


Fig. 5—Plot of input admittance for taper terminated in match ($x=1.1$, $x=1.0$) as a function of $y$.

## Procedure for Determining Equivalent Step

The procedure for determining equivalent steps can best be described by an illustrative example. This approach is not necessary for a single section, but will be used later in the design of an iterative filter.

A requirement is given for a section of a filter that has a maximum insertion loss at 10,320 mc and a zero insertion loss at 9500 mc. The pass band is to be essentially symmetrical. From the frequencies we readily compute the waveguide wavelengths in the standard 1 inch$\times\frac{1}{2}$ inch rectangular waveguide (0.900$\times$0.400 inches ID). A frequency of 9500 mc corresponds to a waveguide wavelength of 4.451 cm and 10,320 mc to a waveguide wavelength of 3.762 cm. From the waveguide wavelengths and the height of the standard waveguide (1.016 cm), the values of $x$ are obtained from (4b). For 9500 mc, $x=1.014$; and for 10,320 mc, $x=1.2$. The values of input admittance from Table II have been plotted on a Smith Chart (Fig. 4). From this curve and Table II the desired value of $y/x$ can be determined. A value of $y=2.70$ is selected which will give the maximum discontinuity at $x=1.2$. This gives a value of $y/x$ of 2.25. The next step in the procedure is to obtain the equivalent step from the value of the discontinuity, $Y_{2c}$, resulting from a matched output step-down taper of $y/x$ of 2.25 at $x=1.014$. This may be calculated by means of (5), (11), (13), and (15) or graphically by plotting from Table II the values for $x=1$ and $x=1.1$ as $y$ varies from 2 to 2.8. This is shown on Fig. 5. From the plotted value of $Y_{2c}$, a constant VSWR circle is drawn so as to intersect the input admittance curves of the equivalent output matched step.

The values on the constant VSWR circle are:

$V = 0$ $U = 1.94$

$V = 0.4$ $U = 1.875$

$V = 0.6$ $U = 1.78.$

From (24), we find that the relationship between $U$ and $V$ for $x = 1.014$ should be $V/U = 0.22823$ for identical output waveguides for both step and taper. From the values of $V$ and $U$, we find respectively the ratios $V/U$ of 0, 0.21333, and 0.33708. Since $U$, $V$ and $V/U$ are monotonic and continuous over the region of interest, the desired value $U$ and $V$ along the constant VSWR circle can be found to give the required ratio of $V/U$. $V/U = 0.22823$ lies between that corresponding to $V = 0.4$, $U = 1.875$ and $V = 0.6$, $U = 1.78$. Linear interpolation gives a value of $U = 1.86$ and a corresponding $V = 0.425$ which prove to be the desired values corresponding to $V/U = 0.22823$. If the first linear interpolation had resulted in a value of $V/U$ different from that required, interpolation could have been repeated between the two new values of $V/U$ on either side of the desired value. From the values of $U$ and $V$, we find from the Smith Chart the input admittance of the output matched step to be $1.86 + j.32$. The phase angle traversed in going from the input admittance of the taper $A_{2c} + jB_{2c}$ to the input admittance of the equivalent step $A_{2b} + jB_{2b}$ is the distance ($d$) toward the generator from reference plane (2c) of the taper to the plane of the equivalent step discontinuity. The equivalent step may now be used to obtain the line length ($l_1$) required to give a match at $\lambda_g = 4.451$. From the Smith Chart, this is found to be $\lambda_g/2$ plus $0.038\lambda_g$, *i.e.*, $0.538\lambda_g$ for the equivalent step. To obtain the spacing required for the taper section, the distance ($d$) traversed along the constant VSWR circle is found to be $0.0805\lambda_g$. Since the equivalent step and the taper are symmetrical about the same center line the length of the enlarged uniform waveguide is obtained from the following relationship (Fig. 3):

$$l_1 = l_s - 2d. \tag{27}$$

In this example $l_1$ is found to be $0.377\lambda_g = 1.500$ cm. All the necessary dimensions have now been obtained, *i.e.*, $b_2 = 2.286$ cm, $l_1 = 1.500$ cm and $\theta = 45°$.

The insertion loss may now be calculated at any frequency by finding $\lambda_g$ and $x$ in turn, and obtaining graphically the equivalent step and the distance, $d$ (traversed in going from the taper input admittance to the equivalent step input admittance). Using (27) where $l_1$ is the physical length of the enlarged waveguide between tapers, $l_s$ can be obtained. The Smith Chart can be used to obtain the input admittance $A_{2a} + jB_{2a}$, due to the equivalent step at a distance $l_s$ toward the generator from the plane of the step. The input admittance $Y_s$ in the standard guide of the matched output filter section can be obtained from the relationship

$$Y_s = \frac{1}{U}\left[A_{2a} + j(B_{2a} + B_{2b})\right] \tag{28}$$

$$Y_s = A_s + jB_s. \tag{29}$$

The insertion loss $\alpha_s$ can be obtained from

$$a_s = \frac{4A_s}{(1 + A_s)^2 + B_s^2}. \tag{30}$$

The values of insertion loss obtained by the equivalent step method for the single section previously considered are plotted on Fig. 6 together with the curve obtained from plotting the insertion loss using (5) through (20). The measured insertion loss is also plotted on the same curve. This shows that the equivalent step is a fairly good approximation.

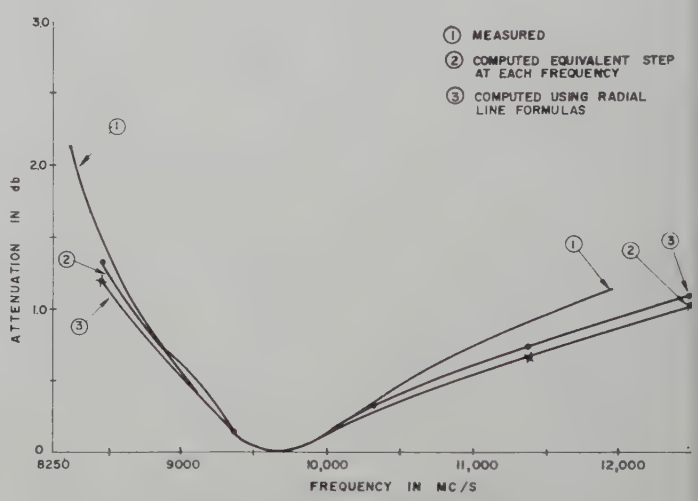


Fig. 6—Comparison of computed and measured insertion loss for single filter section.

## The Multiple Section Filter

To obtain high-power microwave filter structures to meet specific requirements, a number of sections are required. The multiple section procedure follows from the procedure for a single section. Using Fig. 3(a), the multiple section filter can be described in terms of the taper angle $\theta$ and the lengths $l_1$, $l_2$, and $l_3$. From the single taper section, using the procedure previously described, the equivalent step parameters $U$, $V$, and $d$ may be found for each frequency. From these the values $Z_H$, $S_H$, and $S_O$ are determined by the relationships

$$S_H = l_1 + 2d \tag{31}$$

$$S_O = l_3 + 2(b_2 - b)\cot\theta - 2d \tag{32}$$

$$Z_H/Z_O = U = b'/b \tag{33}$$

where $Z_H$ and $Z_O$ are the characteristic impedances shown in Fig. 3.

The following relationships developed by J. W. E. Griemsmann will give the equivalent iterative cell, corresponding to the equivalent step structure [Fig. 3(b) and 3(c)]. The normalized equivalent impedance is

$$\left(\frac{Z_I}{Z_O}\right)^2 = \frac{\tan\left[\beta(S_O/2)+\tan^{-1}\left((Z_H/Z_O)\tan\beta(S_H/2)\right)\right]}{\tan\left[\beta(S_O/2)+\tan^{-1}\left((Z_O/Z_H)\tan\beta(S_H/2)\right)\right]} \quad (34)$$

and the phase change per section $\beta S_I$ is then

$$\cos\beta S_I = \cos\beta S_H \cos\beta S_O - \tfrac{1}{2}\left((Z_H/Z_O)+(Z_O/Z_H)\right)\sin\beta S_H \sin\beta S_O \quad (35a)$$

$$\beta = 2\pi/\lambda_g. \quad (35b)$$

Using the results of (34) and (35) the reciprocal of the insertion loss can be obtained for $n$ sections at the specified frequency (or waveguide wavelength) by [4]

$$\frac{1}{a_n} = \frac{P_{\text{in}}}{P_{\text{out}}} = 1 + \frac{1}{4}\left(Z_I - \frac{1}{Z_I}\right)^2 \sin^2 n\beta S_I. \quad (36)$$

Since taper sections cannot be approximated directly by change in impedance alone, the above procedure for finding the equivalent iterative cell requires the determination of the equivalent step sections at each frequency.

## Design Procedure and General Considerations

A band-pass band-elimination filter suitable for this type of high-power structure is specified in terms of the lower cutoff frequency, the upper cutoff frequency, the width of the attenuation band at the high-frequency end, and the steepness of the rise of insertion loss just beyond the cutoff frequencies of the filter.

The cutoff wavelength of the standard uniform waveguide used in the structure determines in large measure the slope of the insertion loss at the lower end of the pass band. If the specified lower frequency cutoff is close to the guide cutoff, this characteristic can easily be used to achieve the required low-frequency slope. In general, spurious responses will exist in the filter structure due to the repetitive nature of the waveguide circuit elements. The locations of these spurious responses depend on the steepness of the rise of the insertion loss just beyond the cutoff frequency of the filter and on the electrical lengths of the various circuit elements used in the filter. Since the pass band may repeat at half the waveguide wavelength of the design pass band, it is necessary to use various devices to increase the width of the rejection band at the high end. One convenient method of eliminating spurious responses under such circumstances is to design a composite filter made up of several dissimilar filters so that the pass bands are the same but the frequency of infinite insertion are sufficiently different so that the spurious pass band of one filter coincides with the rejection band of another.

## Illustrative Examples

The design procedure can be considered in terms of a specific filter. The problem is to design a 1 inch $\times \frac{1}{2}$ inch waveguide filter with a pass band from 8200 to 10,100 mc, with an insertion loss of greater than 25 db below 8100 mc and also between 10,200 and 10,850 mc. This specification is in keeping with the expectation of a spurious pass band at half the design waveguide wavelength, so only one filter need be designed. If a broader rejection band had been specified, additional dissimilar filters would be needed. Converting the specifications to waveguide wavelength gives us the cutoff wavelengths of 6.088 and 3.902 cm, respectively, and the 25-db insertion loss waveguide wavelengths of 6.303, 3.837, and 3.468 cm, respectively.

From the above values, wavelengths of infinite insertion loss and the wavelengths of zero insertion loss must be selected. For the high-frequency rejection band a central wavelength should be selected, *i.e.*, 3.700 cm (10,400 mc). To obtain the desired low-frequency cutoff and slope of insertion loss, the frequency of zero insertion loss must be selected in combination with the height of the enlarged waveguide to give the desired symmetry. Since the filter to be designed has a very large pass band, it is necessary to use a taper section $y/x$ ratio which shows a relatively slow variation of impedance with wavelength. Examination of Table II shows $y/x=2$ has a curve of the required type. It is now necessary to find $x$ (4a) corresponding to the cutoff wavelengths and the infinite insertion wavelengths. The cutoff wavelengths give values of $x$ of 0.741 and 1.157, respectively. The wavelength for infinite insertion loss gives a value of $x$ of 1.220. A central value of $x=1.0$ ($\lambda_g=4.514$ cm) is selected as the wavelength of zero insertion loss. The 25-db points occur at values of $x$ of 0.716 and 1.302, respectively.

For minimum insertion loss in the pass band (where the pass band is broad) using identical sections, each section is matched at the center frequency (zero insertion loss). Using the procedure outlined in the single-filter section, we find the equivalent step corresponding to $y/x=2$ and $x=1$. The resultant values are $U=1.82$, $V=0.4$, and $d=0.0381\lambda_g$. From the Smith Chart, the length $l_s$ is found to be $\lambda_g/2$ plus $0.039\lambda_g$, *i.e.*, $l_s=0.539\lambda_g$ $=2.433$ cm. Eq. (27) is used to obtain the value of the length of the enlarged waveguide $l_1$. This value is found to be 1.761 cm. The next step in the procedure is the determination of the distance between the sections [$l_3$ of Fig. 3(a)] to give the desired rejection band. For the upper rejection band the 25 db insertion loss wavelengths are 3.837 cm ($x=1.176$) and 3.468 cm ($x=1.302$), respectively. Select a second cutoff at 3.30 cm. The procedure is to find the value of $S_O$ from (34), which will make $(Z_I/Z_O)^2$ infinite at the first cutoff wavelength of 3.902 cm and zero at 3.30 cm, corresponding to the limits of the attenuation band of the filter. To do this, it is necessary to find the equivalent step using the procedure given before corresponding to $x=1.157$ and 1.368, respectively, and determining $U$, $V$, and $d$ for each. Using (31), $S_H$ is obtained for each value of $x$. The following equations can now be used to obtain the value of $S_O$ for the lower and upper frequencies ($x=1.157$ and $x=1.368$), respectively:

$$\beta \frac{S_O}{2} = -\tan^{-1}\left((Z_O/Z_H)\tan\beta(S_H/2)\right) + n\pi \qquad (37)$$

$$\beta \frac{S_O}{2} = -\tan^{-1}\left((Z_H/Z_O)\tan\beta(S_H/2)\right) + n\pi \qquad (38)$$

where $Z_H/Z_O$ is defined by (33). The results of (37) and (38) when inserted in (32) should give approximately the same value of $l_3$. If this is not the case, the original choices of $y/x$ and of the zero insertion loss wavelength must be modified. For a fixed zero insertion loss wavelength, the larger $y/x$ will result in greater rejection bandwidth, but the lower frequency cutoff will go to higher frequency. This can be compensated by lowering the frequency of zero insertion. $S_O$ at the lower cutoff of $\lambda_g = 6.088$ should satisfy (30). In this case, the conditions of (37) and (38) are satisfied by $l_3 = 0.785$ cm for the cutoff wavelengths of 6.088, 3.902, and 3.300 cm.

The design is essentially complete. From $y/x$ we determine $b_2 = 2.032$ cm. The values $l_1 = 1.761$ cm and $l_3 = 0.785$ cm have been determined and $\theta = 45°$ has been specified for maximum power. It now remains to determine the total number of sections to be used in the filter to achieve the desired steepness of the rise of the insertion loss. Fig. 7 shows the insertion loss characteristics of 6, 15 and 21-section filters designed and built as outlined above. The 15-section unit almost meets the 25-db steepness requirement, and the 21-section unit has a steeper slope than specified. The cutoff frequencies occur as computed but the insertion loss in the pass band shows several peaks which do not agree. These may be due to machining tolerances or misalignments. When the rejection band is not too broad, an approximation which has been found empirically to be of relatively good accuracy is to select $S_O$ which satisfies the following relationship at the infinite insertion loss wavelength:

$$S_O = \tfrac{1}{3}\lambda_{g\infty}. \qquad (39)$$

The insertion loss of a multiple section filter in the pass band can be calculated from (31) through (36) using the equivalent step determined at each frequency by the method outlined in the single-filter section.

## Summary of Procedure

The following steps are required to design a high-power filter with a specified pass band and rejection band.

1) Determine cutoff wavelengths for lower and upper ends of pass band and for upper end of rejection band.
2) Determine $x$ as defined by (4b) for each cutoff wavelength.
3) Select value of $y/x$ having desired type of frequency response.
4) Select wavelength of zero insertion loss to give symmetrical filter.

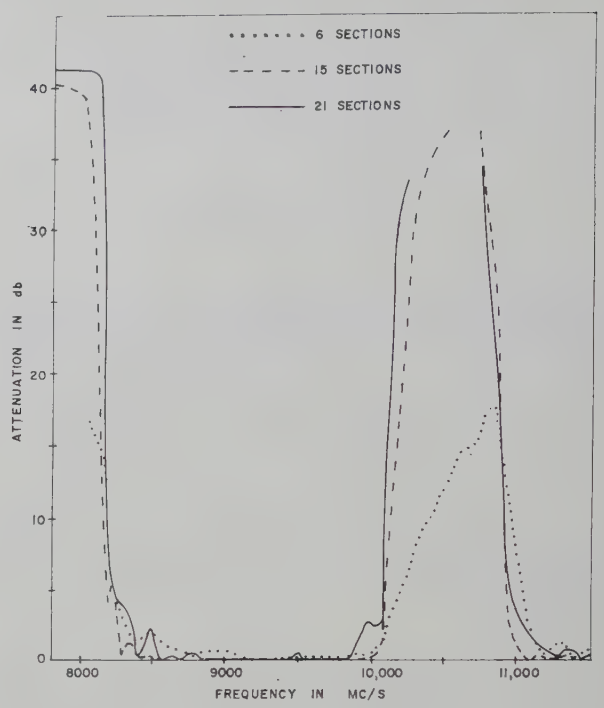


Fig. 7—Insertion loss of 6, 15, and 21-section filters.

5) Determine equivalent steps corresponding to taper of height $y/x$ for zero insertion wavelength.
6) Find $S_H$ length of step section which gives match at the wavelength of zero insertion loss.
7) Using (31) find $l_1$.
8) For the cutoff wavelengths on either side of the rejection band, find the equivalent steps corresponding to each, and calculate $S_H$ from (31).
9) For the longer cutoff wavelength compute $S_O$ from (37) and for the shorter cutoff wavelength from (38).
10) In each case, compute $l_3$ from (32).
11) If $l_3$ is not approximately equal in the two cases, choose a new value of $y/x$ and repeat process.
12) Find equivalent step for the cutoff wavelength at the lower end of pass band and check that computed $S_O$ satisfies (38). If it does not, the wavelength of zero insertion loss should be modified accordingly.
13) Compute $b_2$ from $y/x$ and $b_1$, *i.e.*, $y/x = b_2/b_1$.
14) Select number of sections in accordance with the required steepness of rise of insertion loss.

## Power Handling Capability

The power handling capacity of a waveguide structure is an inverse function of the maximum electric field gradient in the structure. To compare the power handling capacities of waveguide structures of equal width in the $TE_{10}$ mode, it is necessary to examine the relative gradients in the structures. Using the method of curvilinear squares, the gradients have been obtained for the static equivalent of a radial line mated at both ends to uniform lines, and a step between uniform lines of dif-

ferent heights. The relative gradients have been determined by comparison at the 0.05 potential points relative to the smaller uniform line.

The results indicate a ratio of 3.0/1.8 for the gradient of the step compared to the 45° taper section. This analysis predicts a substantially larger power handling capacity for filters made up of taper sections. A series of measurements were made on single step and single taper sections of equal height with spacings between discontinuities to produce a low VSWR to obtain a comparison of power handling capacity. The measurements were made at 9450 mc using a magnetron of in excess of 700 kw of peak power in 1 inch by $\frac{1}{2}$ inch waveguide (normal average unpressurized breakdown power of 400 kw depending on humidity and ionization present). The power handling capacities of a 6-section and a 15-section radial line filter were also measured. The last filter section consisted of a step and a taper combined to give a relatively good VSWR at 9450 mc. Each filter was measured unpressurized, with 10 pounds per square inch pressure, and with 15 pounds pressure. The results were in keeping with the predictions from the comparison of the gradients in the two types of structures. The measured results follow in Table III.

TABLE III

| Type of structure | Enlarged waveguide to std. waveguide ratio | Power when arcing started | | |
|---|---|---|---|---|
| | | No pressure | 10 lbs. pressure | 15 lbs. pressure |
| Single taper section | $b_2/b = 2.25$ | 340 kw | *700 kw | |
| Single step section | $b_2/b = 2.25$ | 40 kw | 90 kw | 140 kw |
| Six section taper filter | $b_2/b = 2.0$ | 140 kw | *700 kw | |
| Fifteen section taper filter | $b_2/b = 2.0$ | 250 kw | *700 kw | |
| Single section step and taper | $b_2/b = 3.5$ | 90 kw | 90 kw | 240 kw |

No arcing occurred at maximum available power.

## Discussion of Experimental Filters

The performance of the filter structure (Fig. 7) designed by using the preceding method, is very close to the expected performance. The 21-section filter was made in 2 parts, to fit the limits of the milling equipment available. One part consisted of 15 sections while the other consisted of 6 sections. An analytic computation of the 15-section filter, using the method outlined in the discussion of the multiple section filter, showed agreement within the actual machining tolerances except for the small insertion loss peaks from 8200 to 8500 mc. The measured insertion loss was within 0.1 db of the computed values in the pass band except at the low-frequency end. In the case of the 6-section filter there was a more marked disagreement between the measured insertion loss and the computed insertion loss below 9000 mc. This disagreement is also found when the 2 parts are put together to form the 21-element filter. Physical measurement of the individual sections of the 6-section filter was not possible without disassembly, but external measurement indicated a total length which was 0.010 inch beyond the tolerances shorter than specified. This would suggest that one or more of the individual sections differed considerably from the design dimensions. The structure would no longer be exactly iterative and the computed results would not be directly applicable. Both the high insertion loss section filter and the normal filter were subjected to 700 kw of peak power with 10 pounds pressurization without any sign of breakdown.

## Bibliography


[1] N. Marcuvitz, "Waveguide Handbook," M.I.T. Rad. Lab. Ser., McGraw-Hill Book Co., Inc., New York, N. Y., vol. 10, pp. 322–323; 1951.

[2] E. Jahnke and F. Emde, "Tables of Functions," Dover Publications, New York, N. Y., 4th ed., p. 16; 1945.

[3] J. H. Vogelman, "High Power Filters," D.E.E. dissertation, Polytechnic Inst. Brooklyn, Brooklyn, N. Y.; 1957.

[4] G. L. Ragan, "Microwave Transmission Circuits," M.I.T. Rad. Lab. Ser., McGraw-Hill Book Co., Inc., New York, N. Y., vol. 9, pp. 643–715; 1948.

[5] Radio Res. Lab. Staff, "Very High Frequency Techniques," McGraw-Hill Book Co., Inc., New York, N. Y., vol. 2, pp. 674–678; 1947.

[6] S. Cohn, "Analysis of wide-band waveguide filter," Proc. IRE, vol. 37, pp. 651–656; June, 1949.

[7] S. Cohn, "Design relations for the wide-band waveguide filter," Proc. IRE, vol. 38, pp. 799–803; July, 1950.

[8] J. Greene, "Corrugated-waveguide band-pass filters," *Electronics*, vol. 24, pp. 117–119; July, 1951.

[9] E. N. Torgow, "Broadband waveguide filters," Polytechnic Inst. Brooklyn, Brooklyn, N. Y., Rep. R-447-55, PIB-377; October, 1955.

[10] C. G. Montgomery, R. W. Dicke, and E. M. Purcell, "Principles of Microwave Circuits," M.I.T. Rad. Lab. Ser., McGraw-Hill Book Co., Inc., New York, N. Y., vol. 8, pp. 187–188; 1948.

# A Method of Calculating the Characteristic Impedance of a Strip Transmission Line to a Given Degree of Accuracy*

RUDOLF G. DE BUDA†

*Summary*—**The calculation of the characteristic impedance of the strip transmission line TEM-mode can be reduced to the solution of a two-dimensional potential equation with the strip cross section determining the boundary conditions.**

**Usually this potential equation is solved by conformal mapping, but only the most simple shapes permit exact mapping. Approximations may require considerable work and their accuracy is uncertain.**

**This paper describes an alternative numerical method which is particularly suitable for boundaries consisting of any number of straight lines and right angles.**

**It is based on relaxation methods, but by using also variational principles it derives an approximate value for the impedance, and an upper and lower bound with a difference as small as desirable.**

IN the last few years, strip transmission line has become increasingly popular for use in transmission lines, filters, mixers, and other components in the kilomegacycle range. For all these applications, values of the characteristic impedance $Z$ of the strip are required, but are often difficult to obtain with good accuracy.

It is the purpose of this paper to describe a new method of numerical calculation which is accurate and simple to use for any strip cross section.

The strip, having a conductor insulated from ground, supports a TEM wave if the medium is homogeneous. The calculation of a TEM field reduces to that of a 2-dimensional Laplace equation with boundaries given by the strip cross section, and the propagation constant depends only upon the medium.[1-2]

Based on this, the characteristic impedance $Z$ is expressed by:

$$Z = \sqrt{\frac{L}{C}} = \frac{\sqrt{\mu\epsilon}}{C} \tag{1}$$

$$C = -\epsilon \oint_H \frac{\partial \phi}{\partial n}\, ds, \tag{2}$$

$$\phi \cdots \text{solution of } \Delta\phi = \frac{\partial^2 \phi}{\partial x^2} + \frac{\partial^2 \phi}{\partial y^2} = 0$$

for the given boundary condition.

The integration extends along the "hot" conductor.

$C$ may be identified with the capacity of the strip per unit length; but it might also be used to solve related problems in which the potential equation defines other physical quantities, like magnetic flux, fluid flow, or heat flux.

In order to obtain $C$, approximation methods, based on estimates for the "fringe" capacity were first introduced.[2,3] Later a number of workers used conformal mapping,[4-13] but only few cases, usually assuming infinitely thin conductors, can be calculated in closed form; even they lead to rather complicated expressions in elliptic functions. Otherwise approximations must be made to obtain usable results.

We note that the main effort of the conformal method is directed toward solving the Laplace equation point by point, or in other words, to describe the electromagnetic field in every point of the cross section. This field is usually of no interest by itself, but a close approximation of the field seems necessary to obtain a close value for $C$.

Variational methods[14] are known to be numerically useful for just such a type of problem and very recently

* Manuscript received by the PGMTT, May 19, 1958.

† Canadian General Electric Co. Ltd., Toronto, Can.

[1] S. A. Schelkunoff, "Electromagnetic Waves," D. Van Nostrand Co., Inc., New York, N. Y., ch. 8–9; 1951.

[2] F. Assadourian and E. Rimai, "Simplified theory of microstrip transmission systems," PROC. IRE, vol. 40, pp. 1651–1657; December, 1952.

[3] S. B. Cohn, "Characteristic impedance of the shielded strip transmission line," IRE TRANS. ON MICROWAVE THEORY AND TECHNIQUES, vol. MTT-2, pp. 52–55; July, 1954.

[4] R. H. T. Bates, "The characteristic impedance of the shielded slab line," IRE TRANS. ON MICROWAVE THEORY AND TECHNIQUES, vol. MTT-4, pp. 28–33; January, 1956.

[5] W. H. Hayt, "Potential solution of a homogeneous strip line of finite width," IRE TRANS. ON MICROWAVE THEORY AND TECHNIQUES, vol. MTT-3, pp. 16–18; July, 1955.

[6] W. Magnus and F. Oberhettinger, "Die Berechnung des Wellen widerstandes einer Bandleitung mit kreisfoermigen bzw. rechteckigem Aussenleiterquerschnitt," *Arch. Elektr.*, vol. 37, p. 380; 1943.

[7] K. G. Black and T. J. Higgins, "Rigorous determination of the parameters of microstrip transmission lines," IRE TRANS. ON MICROWAVE THEORY AND TECHNIQUES, vol. MTT-3, pp. 93–113; March, 1955.

[8] N. A. Begovich, "Capacity and characteristic impedance of strip transmission lines with rectangular inner conductors," IRE TRANS. ON MICROWAVE THEORY AND TECHNIQUES, vol. MTT-3, pp. 127–133; March, 1955.

[9] D. Park, "Planar transmission lines," IRE TRANS. ON MICROWAVE THEORY AND TECHNIQUES, vol. MTT-3,pp. 8–12, April, 1955; pp. 7–11, October, 1955; vol. MTT-4, p. 130, April, 1956; vol. MTT-5, p. 75, January, 1957; p. 163, April, 1957.

[10] B. A. Dahlman, "A double ground plane strip line system for microwaves," *Proc. IEE*, pt. B, vol. 102, pp. 488–492; July, 1955.

[11] B. Vural, J. Cappon, and J. C. Rennie, "Development and Design of a Wideband Microwave Mixer Using Microstripline Components," CGE Rep. RQ57EE6, presented at the Canadian IRE Conference, Toronto, Ont., Can.; October 16, 1957.

[12] E. Fubini, W. Fromm, and H. Keen, "New techniques for high Q strip microwave components," 1954 IRE CONVENTION RECORD, pt. 8, pp. 91–97.

[13] J. M. C. Dukes, "Characteristic impedance of airspaced strip transmission line," PROC. IRE, vol. 43, p. 876; July, 1955.

[14] P. M. Morse and H. Feshbach, "Methods of Theoretical Physics," McGraw-Hill Book Co., Inc., New York, N. Y., vol. 2, ch. 9–4, p. 1108; 1953.

they have been applied to certain TEM structures, as for instance trough lines.[15–18] They permit a good estimate even if a relatively crude trial function is substituted into a "stationary integral." However, variational methods have two disadvantages. Good trial functions must permit easy numerical work, they should contain a large number of parameters which can be chosen arbitrarily, and they should cover a fairly general case. Such functions are not always easily found. Also, the calculated approximation is actually an upper bound for the stationary integral, but little advantage is obtained from this fact as long as no lower bound is known.

In this paper it is intended to derive two stationary integrals, which give both an upper and a lower bound for the characteristic impedance $Z$. Both integrals permit relatively easy numerical evaluation when trial functions obtained by a process similar to relaxation are used.

We shall consider the region $R$ of the complex plane which is bounded by curves $G$ and $H$, corresponding to the cross sections of ground plate and "hot" conductor, and by the two sides of cuts $F_i$ which are introduced with the purpose of making the region $R$ of the complex plane simply connected. This is illustrated in Fig. 1.

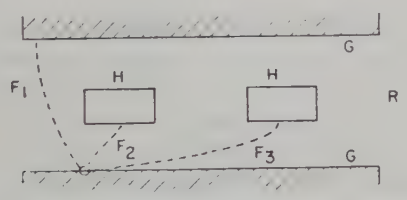


Fig. 1—Strip cross section, showing construction of the simply connected region $R$.

In this region $R$ we shall define a potential function $\phi$ and a stream function $\psi$ as follows:

The potential function $\phi$ is defined by:

$$\phi = 0 \text{ on } G \tag{3a}$$

$$\phi = 1 \text{ on } H \tag{3b}$$

$$\phi \text{ and } \frac{\partial \phi}{\partial n} \text{ are continuous across the cuts } F \tag{3c}$$

$$\Delta\phi = 0 \text{ in } R. \tag{4}$$

Because of (3a)–(3c) the expression $\phi(\partial\phi/\partial n)$ will be equal to the integrand on $H$, disappear on $G$, and cancel on both sides of $F$. Consequently, we may express $C$ by

$$\frac{C}{\epsilon} = -\oint_H \frac{\partial \phi}{\partial n}\, ds = -\oint_{F,G,H} \phi \frac{\partial \phi}{\partial n}\, ds. \tag{5}$$

The subscript $F, G, H$, indicates that the integration extends along the whole contour of the simply connected region $R$. On (5) we may apply the Gauss Theorem, and using (4) we obtain

$$\frac{C}{\epsilon} = \iint_R (\nabla\phi)^2 dA \tag{6}$$

with the notation

$$(\nabla\phi)^2 = \left(\frac{\partial\phi}{\partial x}\right)^2 + \left(\frac{\partial\phi}{\partial y}\right)^2$$

(because this is a two-dimensional problem) and:

$$dA = dxdy.$$

The stream function $\psi$ is defined as the conjugate function to $(\epsilon/C)\phi$, or in other words by the Cauchy-Riemann equations:

$$\frac{\partial\phi}{\partial x} = \frac{C}{\epsilon}\frac{\partial\psi}{\partial y} \tag{7a}$$

$$\frac{\partial\phi}{\partial y} = -\frac{C}{\epsilon}\frac{\partial\psi}{\partial x} \tag{7b}$$

from which it follows immediately that $\psi$ too is a solution of the Laplace equation:

$$\Delta\psi = 0 \tag{8}$$

and

$$(C/\epsilon)^2(\nabla\psi)^2 = (\nabla\phi)^2. \tag{9}$$

$\psi$ is uniquely determined except for an additive constant, which may be chosen arbitrarily.

The boundary conditions for $\psi$ follow from those for $\phi$, (3a)–(3c)

$$\text{on } G \text{ and } H\text{:} \quad \frac{\partial\psi}{\partial n} = 0 \tag{10a}$$

$$\text{on } F_i\text{:} \quad \frac{\partial\psi}{\partial n} \quad \text{continuous.} \tag{10b}$$

Across $F_i$ the function $\psi$ will be discontinuous. (The cuts $F_i$ have been introduced for this purpose: otherwise $\psi$ could not be uniquely defined.) However, the "jump" of $\psi$ will have a constant value along the cut $F_i$. We shall denote this constant by writing $F_i$ as index to the function $\psi$:

$$\text{along } F_i\text{: } \psi/_{12} = \psi_{F_i} = \text{constant.} \tag{10c}$$

We consider now only those cuts $F_h$ which lead from $G$ to $H$. For these cuts we shall calculate the expression $\sum\psi_{F_h}$ as follows: If we integrate along a closed curve around $H$:

$$\oint_H \frac{\partial\psi}{\partial s}\, ds$$

[15] R. M. Chisholm, "The characteristic impedance of trough and slab lines," IRE Trans. on Microwave Theory and Techniques, vol. MTT-4, pp. 166–172; July, 1956.

[16] R. E. Collin, "The characteristic impedance of a slotted coaxial line," IRE Trans. on Microwave Theory and Techniques, vol. MTT-4, pp. 4–8; January, 1956.

[17] N. Tomcio, "The Characteristic Impedance of a Transmission Line Consisting of a Ribbon in a Rectangular Trough," University of Toronto, Toronto, Ont. Can., Dept. of Elec. Eng. Res. Rep.; 1954.

[18] J. D. Horgan, "Coupled strip transmission lines with rectangular inner conductors," IRE Trans. on Microwave Theory and Techniques, vol. MTT-5, pp. 92–99; April, 1957.

this integral does not disappear, because of the discontinuities $\psi_{F_h}$. However,

$$\oint \frac{\partial \psi}{\partial s} ds + \sum \psi_{F_h} = 0. \tag{11}$$

Substituting from (7) and (2) we see

$$-\frac{C}{\epsilon}\frac{\partial \psi}{\partial s} = \frac{\partial \phi}{\partial n}$$

$$\sum \psi_{F_h} = -\oint \frac{\partial \psi}{\partial s} ds = -\frac{1}{-C/\epsilon}\oint_H \frac{\partial \phi}{\partial n} ds = 1. \tag{12}$$

(Provided that consistent sign conventions are used, *e.g.*, counterclock integration, crossing $F_h$ from 1 to 2, normal direction pointing outside from conductor.) Usually there will be only one hot conductor, and one cut $F$, and the sum $\sum \psi_{F_h} = 1$ will have only one term. However, (13) will be derived to cover also the case of several conductors, which of course may be used to support a number of TEM modes. Some such structures have been recently described.[18–20]

Finally we express $C/\epsilon$ by $\psi$, substituting (9) into (6):

$$\frac{C}{\epsilon} = \frac{1}{\iint_R (\nabla \psi)^2 dA}. \tag{13}$$

While (13) as well as (6) seems to be unnecessarily more complicated than (2) we note as previously shown[14] that both area integrals are stationary. Consequently, even crude approximations of $\phi$ and $\psi$ will give close upper bounds for the area integrals, and with it upper and lower bounds for $Z$. The approximations have to fulfill the same boundary conditions as $\phi$ and $\psi$ and they must be continuous; they need not be solutions of the Laplace equations. We may formulate:

a) If a function $U$ is continuous and if it takes the values $U=1$ along the hot conductor(s) and $U=0$ along ground, then $U$ may be used as trial function to calculate an upper bound for $C$ by

$$\frac{C}{\epsilon} \leqq \iint_R (\nabla U)^2 dA. \tag{14}$$

The equal sign holds only if $\Delta U = 0$.

b) If a function $V$ is continuous in a simply connected region $R$, which is obtained by arbitrary cuts $F_i$ from the part of the complex plane which is bounded by the conductor and ground plate cross section, and if the jump in $V$ across any cut $F_i$ is, for this particular cut, a constant $V_{F_i}$, and if the sum

$$\sum_h V_{F_h} = 1,$$

(the summation extending over all cuts leading from ground to a hot conductor), then $V$ may be used as trial function to calculate a lower bound for $C$ by

$$\frac{C}{\epsilon} \geqq \frac{1}{\iint_R (\nabla V)^2 dA}. \tag{15}$$

The equal sign holds only if $\Delta V = 0$.

Physically the integrals (6) and (13) are twice the electrostatic energy ($\frac{1}{2}CU^2$) for unit potential drop, and twice the electromagnetic energy ($\frac{1}{2}LI^2$) for unit current in the conductor(s); both are expressed by the energy density of the respective fields. The stationary character of the integrals may be explained by noting that any approximation of the field introduces additional space charges or currents which can only increase the total energy.

The lower bound is then obtained from $L$ by eliminating $Z$ from

$$Z = \frac{\sqrt{\epsilon\mu}}{C} = \sqrt{\frac{L}{C}}. \tag{1}$$

However, because of the importance of the relations (14) and (15) they will be derived separately in Appendix II; this will also give a better understanding of the restrictions in the choice of $U$ and $V$.

The bounds obtained by the integrals are remarkably close if we construct suitable trial functions. This will be done now for $U$; the construction of $V$ is completely analogous. As (14) and (15) can be used to check the accuracy of the result, we may feel free to choose the trial functions not so much for close approximation of the field but for numerical convenience:

a) We chose a Cartesian grid of square mesh with $N$ meshes of side length $h$ which is conveniently located with regard to boundaries and symmetry lines.

b) Within each square $k$ of the grid, we define a different trial function $U_k(x, y)$ as the bilinear expression:

$$U_k(x, y) = B_{k1} \cdot xy + B_{k2} \cdot x + B_{k3} \cdot y + B_{k4}.$$

$U_k$ is a potential function with four available parameters $B_k$, which shall be chosen in such a way that $U_k$ interpolates linearly between the (arbitrarily chosen) values of $U$ at the grid corners, which we shall name "grid values." Then the functions $U_k$ will join continuously across the grid lines.

c) The function $U$, which is constructed to be equal to each $U_k$ in its square, is then a continuous function and suitable as trial function.

[19] S. B. Cohn, "Shielded coupled-strip-transmission line," IRE TRANS. ON MICROWAVE THEORY AND TECHNIQUES, vol. MTT-3, pp. 29–38; October, 1955.

[20] E. M. T. Jones and J. T. Bolljahn, "Coupled-strip-transmission-line filters and directional couplers," IRE TRANS. ON MICROWAVE THEORY AND TECHNIQUES, vol. MTT-4, pp. 75–81; April, 1956.

This trial function contains the arbitrarily chosen grid values as independent parameters which shall be chosen later so that a minimum condition will be fulfilled. Therefore, it is logical to express by these grid values the contribution of the $k$th square to the stationary integral. Substituting gives at first an expression in $B_k$;

$$\iint_R (\nabla U)^2 dA = \sum_{k=1}^{n} \iint_{R_k} (\nabla U_k)^2 dxdy$$

$$\iint_{R_k} (\nabla U_k)^2 dxdy$$

$$= \int_{-h/2}^{+h/2} \int_{-h/2}^{+h/2} [(B_{k1}y + B_{k2})^2 + (B_{k1}x + B_{k3})^2] dydx$$

$$= h^2 \left[ \frac{h^2 B_{k1}^2}{6} + B_{k2}^2 + B_{k3}^2 \right] \tag{16}$$

but we wanted to express the integrals in terms of the grid values $U_{k1}$, *etc.*

After further substituting and rearranging, the final equation may be written in two forms:

$$\iint (\nabla U)^2 dA = \sum \left[ \tfrac{1}{6}(U_1 - U_2 + U_3 - U_4)^2 + \tfrac{1}{2}(U_1 - U_3)^2 + \tfrac{1}{2}(U_2 - U_4)^2 \right] \tag{17}$$

$$= \sum \tfrac{1}{6}\left[ (U_1 - U_2)^2 + (U_2 - U_3)^2 + (U_3 - U_4)^2 + (U_4 - U_1)^2 + 2(U_1 - U_3)^2 + 2(U_2 - U_4)^2 \right]. \tag{18}$$

Eq. (17) is useful for numerical evaluation as shown in Appendix I. However, (18) is helpful in understanding the additional restrictions we can impose on the grid values so that the integral becomes a minimum.

It is of course desirable to use such grid values that the integral (14) has the lowest possible value. As this integral in any case must be larger than $C$, the lowest integral gives also the lowest error. In (18) the terms in the brackets contain twice the squares of the changes of $U$ along the diagonals, but only once the square of the change along the side of the mesh. However, the same amount again is contributed by the side of the next mesh square, as shown in Fig. 2.

Consequently each grid value $U_{k1}$ contributes with equal weight the squares of the eight differences between $U_{k1}$ and its eight neighboring grid values, to the quadratic terms of the sum (18). The minimum of these 8 terms is obtained when the grid value $U_{k1}$ is the arithmetic mean of its 8 surrounding grid values. This gives one linear equation. Similar equations are desirable for all other grid values. This results in a system of linear equations which has only the one solution corresponding to the lowest value which the upper bound for $C$ can take if any function defined for the given grid is used as trial function.

If the number of grid values is large, these equations may be solved by the relaxation methods introduced and described in detail by Southwell and his coworkers[21–23] except that conventional relaxation is based on the average of only four neighboring values and is of little known accuracy. Also, because our integrals cancel the first-order error, the relaxation must be carried out only to one or two digits accuracy for our case, so that there is less numerical work than in a conventional relaxation.

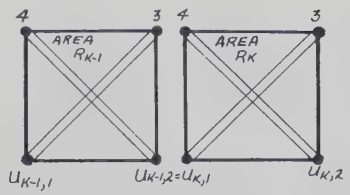


Fig. 2—Each value $U_{k1}$ is the average of eight surrounding values.

## Conclusion

In conclusion we may describe the numerical method as follows:

1) Make a low accuracy relaxation plot for unity potential drop.
2) Repeat the plot, but for unity potential discontinuity.
3) Square the differences $(U_1 - U_2 + U_3 - U_4)$, etc., and summate for both plots according to (17). The normalized impedance must then lie between the inverse of the sum of the first plot and the sum of the second plot.

## Appendix I

### Example

Suppose we have the symmetrical strip of the cross section, Fig. 3, and we want its impedance for the odd mode. Because of conventional symmetry considerations and the availability of a solution for one strip (due to Bates[4]) shown in Fig. 4, we have to solve numerically only for twice the piece of cross section which is shown enlarged in Fig. 5, covered by a grid of ten meshes and bounded by equipotential and symmetry lines. The field and the characteristic impedance for the cross section, as shown in Figs. 5–7, will be evaluated numerically. This is intended as an example, illustrating the

[21] D. R. Hartree, "Numerical Analysis," Clarendon Press, Oxford, Eng., ch. 10; 1952.
[22] R. V. Southwell, "Relaxation Methods in Theoretical Physics," Oxford University Press, Oxford, Eng.; 1946.
[23] E. M. Grad, "Solution of electrical engineering problems by Southwell's relaxation method," *Trans. AIEE*, vol. 71, pt. 1, pp. 205–214; July, 1952.

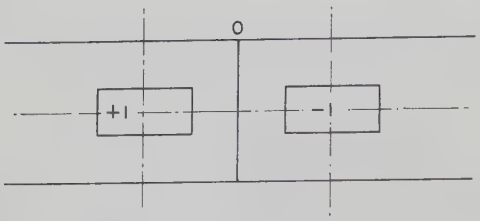


Fig. 3—Double conductor strip.

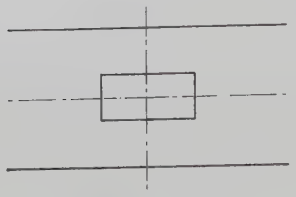

Fig. 4—Strip solved by Bates.[4]

numerical work required. Fig. 6 shows a very rough approximation of the potential at the corners of the grid, which we call "grid values." Each "grid value" is obtained from the condition that it must be approximately the average of its eight neighboring grid values; approximately means accurate within one or two digits. With some practice the grid values may be just written down without further calculation.

Fig. 7 shows a similar plot, except that equipotential and symmetry lines are interchanged. Decimal points are omitted in both plots. Their proper location is given by the requirement that Fig. 6 shows a field with unity potential drop, and Fig. 7, a field with unity sum of potential discontinuities. For each mesh, we calculate the following expressions in its 4 grid values $U$:

$$(U_1 - U_2 + U_3 - U_4)^2, \quad (U_1 - U_3)^2, \quad (U_2 - U_4)^2$$

and add these terms for all $N$ mesh squares, according to (17) as tabulated and evaluated in Table I.

As our approximation is still very crude, we consider it to fit a similar plot evaluating the left half of Fig. 4. This plot need not be worked out because we obtain its results from the Bates solution[4] which, in this particular case, gives $Z_B = 51.5$ ohms. The (with 377 ohm) normalized values for the impedance and admittance of the left half may be added to the values of our plot as if we had obtained them by continuing our plot into the Bates region.

The results of the numerical calculation are two values, one larger than $377/Z$, the other larger than $Z/377$ (the normalized impedance of the strip). This can be rewritten as $Z = 48.6$ ohms with an accuracy just shown to be better than $\pm 2$ per cent. A more refined plot with 40 meshes and 2 digit accuracy has been worked out and gave $Z = 48.5$ ohms $\pm 0.8$ per cent. This illustrates that it is not difficult to get good results.

## Appendix II

For proof of (14) write $U$ as sum of the correct solution $\phi$ and an error $\phi'$,

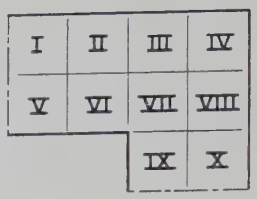


Fig. 5—Detail of Fig. 3, showing numbered mesh.

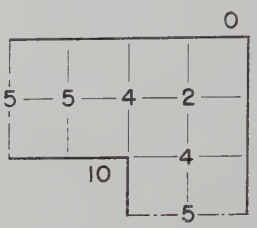


Fig. 6—Relaxation solution for the "grid values" of Fig. 5. Each grid value is approximately the average of the eight neighboring grid values.

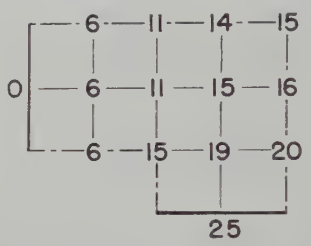


Fig. 7—Relaxation solution for the grid values of Fig. 5 after interchanging equipotential and symmetry lines.

$$U = \phi + \phi'.$$

The boundary conditions for the error $\phi'$ are:

$$\phi' = 0 \text{ on } G$$

$$\phi' = 0 \text{ on } H$$

$$\phi' \text{ and } \frac{\partial \phi'}{\partial n} \text{ continuous across } F.$$

We note that the last condition is not very stringent, as the location of the cuts $F$ is arbitrary. Consequently,

$$\oint_{FGH} \phi' \frac{\partial \phi}{\partial n} ds = 0$$

and, using again Gauss' theorem and (4) this becomes

$$\iint \nabla\phi \nabla\phi' dA = 0$$

for any $\phi'$ which only fulfills the boundary conditions and is continuous and of limited variation so that the Gauss theorem can be used. Expanding the expression on the right side of (14), we get

$$\iint_R (\nabla U)^2 dA$$

$$= \iint_R (\nabla\phi)^2 dA + 2 \iint_R \nabla\phi \nabla\phi' dA + \iint_R (\nabla\phi')^2 dA,$$

TABLE I

NUMERICAL EVALUATION OF $Z$

| Mesh | $(U_1-U_2+U_3-U_4)^2$ | $(U_1-U_3)^2$ | $(U_2-U_4)^2$ | $(V-V_2+V_3-V_4)^2$ | $(V_1-V_3)^2$ | $(V_2-V_1)^2$ | Square terms of final equation |
|---|---|---|---|---|---|---|---|
| I | 0 | 5 | 25 | 0 | 36 | 36 | |
| II | 1 | 25 | 16 | 0 | 25 | 25 | |
| III | 4 | 16 | 4 | 1 | 9 | 16 | |
| IV | 4 | 4 | 0 | 0 | 0 | 4 | |
| V | 0 | 25 | 25 | 0 | 36 | 36 | |
| VI | 1 | 36 | 25 | 16 | 25 | 81 | |
| VII | 16 | 64 | 0 | 0 | 0 | 64 | |
| VIII | 4 | 16 | 4 | 0 | 9 | 25 | |
| IX | 1 | 36 | 25 | 16 | 36 | 100 | |
| X | 1 | 25 | 16 | 1 | 25 | 36 | |
| | 3)32 | 272 | 140 | 3)34 | 201 | 423 | Sum up:— |
| | 11 | | | 11 | | | $\frac{1}{3}\sum(\ )^2+\sum(\ )^2+\sum(\ )^2$ |
| | 272 | | | 201 | | | |
| | 140 | | | 423 | | | |
| | 423 | | | 635 | | | |
| | 4.23 | | | 0.0635 | ← | | —Restore decimal point |
| | 3.66 | ← | | | | | —Add known solution for remaining half of field |
| | — | | 377 | 0.0683 ← | | $Z$ | |
| | 7.89 | > | $Z$ | 0.1318 | > | 377 | $\sqrt{\mu/\epsilon}=377\ \Omega$ |

The 2 inequalities give: $Z=48.6\ \Omega\pm 2$ per cent
A more refined plot with half the mesh size and 2 digit accuracy gives: $Z=48.5\ \Omega\pm 0.8$ per cent

and substituting (6) gives

$$\iint_R (\nabla U)^2 dA = \frac{C}{\epsilon} + \iint_R (\nabla \phi')^2 dA \qquad (19)$$

from which (14) follows immediately. Regarding accuracy, (19) shows also how the error in $C$ depends on the error of the approximation $U$ of the potential function $\phi$. Finally we may drop the requirements for limited variation; otherwise the integrals would not even be finite, much less a minimum.

For proof of (15) write $V$ as sum of the correct solution $\psi$ and an error $\psi'$:

$$V = \psi + \psi'$$
$$\sum_n V_{F_h} = 1$$
$$\sum_n \psi_{F_h}' = 0 \qquad (20)$$

in which $V_{F_h}$ and $\psi_{F_h}'$ denote the jump of $V$ and $\psi'$ across the cuts $F_h$ (which are crossed when circling all $H$ boundaries).

We now have to calculate

$$\oint_{FGH} \psi' \frac{\partial \psi}{\partial n}\, ds.$$

Because $\partial\psi/\partial n = 0$ on $G$ and $H$ (10a) this becomes:

$$\oint_{FGH} \psi' \frac{\partial \psi}{\partial n}\, ds = \sum_i \int_{F_i} \psi_{F_i}' \frac{\partial \psi}{\partial n}\, ds$$
$$= \sum_i \left( \psi_{F_i}' \int_F \frac{\partial \psi}{\partial n}\, ds \right).$$

Substitute from (7)

$$\frac{C}{\epsilon} \int_{F_i} \frac{\partial \psi}{\partial n}\, ds = \int_{F_i} \frac{\partial \phi}{\partial s}\, ds.$$

This integral can have only two values:

$= 0$ if $F_i$ connects two boundaries of equal potential, or

$= 1$ if $F_i$ connects from a $G$ boundary to an $H$ boundary

Only the latter ones are crossed by the contour around all $H$ conductors; therefore only these terms contribute to the sum, which we indicate by changing the index from $i$ to $h$:

$$\oint_{FGH} \psi' \frac{\partial \psi}{\partial n}\, ds = \sum_i \psi_{F_i}' \int_{F_i} \frac{\partial \psi}{\partial n}\, ds$$
$$= \frac{1}{C/\epsilon} \sum_h \psi_{F_h}' \int_{F_h} \frac{\partial \phi}{\partial s}\, ds = \frac{1}{C/\epsilon} \sum_h \psi_{F_h}' = 0.$$

If $\psi'$ is continuous and of limited variation we can apply the Gauss theorem and get

$$\iint_R \nabla\psi \nabla\psi' dA = 0$$

for any function $\psi'$ which need only fulfill (20). From this follows

$$\iint_R (\nabla V)^2 dA = \frac{1}{C/\epsilon} + \iint_R (\nabla \psi')^2 dA$$

which gives us (15) immediately.

## APPENDIX III

This Appendix deals with the convergence of the bounds when evaluated by relaxation methods.

For all practical purposes, it will be sufficient to calculate the upper and lower bounds, which give directly

the total possible errors and, if necessary, to go to one finer plot. However, this can be repeated to any given accuracy; in other words, it is sufficient to refine the plot if the difference between the bound and the correct value is to be made smaller than any given value. This shall now be shown briefly.

The error in (19) consists of two parts: 1) Error due to incomplete relaxation, 2) Inherent error due to size of the grid.

The first error is essentially numerical and shall not be of concern here. It is assumed that a sufficiently accurate relaxation is available. For the second error, however, we will assume that we know the exact solution $\phi$ and we will take arbitrarily the values of the exact solution as grid values $U_{k1}$ etc., and get

$$U_k = \phi_k.$$

With (19) this error becomes

$$\iint (\nabla\phi')^2 dA.$$

But on the grid corners $\phi_k' = 0$; and because $\phi$ is continuous and differentiable the integral, and with it the error for this arbitrarily chosen plot, will disappear in the limit if the grid is made sufficiently fine.

Of course the plot for which it was just proved that its error can be made negligible is not the plot obtained by relaxation. However, it is a pleasant feature of the variational method as compared to conventional relaxation that this does not really matter because the error due to the completely relaxed plot must be still smaller than the error from any other plot. This completes the proof.

# Ferrite Line Width Measurements in a Cross-Guide Coupler*

DONALD C. STINSON†

*Summary*—**Theoretical and experimental results are presented to show that the line width and the $g$ factor of a spherical ferrite sample can be measured in a cross-guide coupler. The method is much easier to instrument than the usual cavity method and the measurements are much easier to perform. Experimental verification with a cavity perturbation system indicates that the measured quantities are sufficiently accurate for most purposes.**

## Introduction

RECENT work by the author with ferrite directional couplers indicated that such devices[1] might be useful in measuring the line width and the $g$ factor of ferrites. Earlier unpublished work by the author in this field showed that such devices were not practical for measuring the components of the susceptibility tensor of a ferrite sphere because of the extreme sensitivity that was required in the detecting system. However, the measurement of the line width and the $g$ factor depends upon relative power measurements. Thus, it was felt that the couplers offered considerable promise of yielding accurate data with a minimum of effort. A second method was also desirable in order to verify data on line widths and $g$ factors obtained with a cavity-perturbation system. It was not intended that the new method be highly accurate, but rather that it be simple and capable of yielding reliable comparative data during the development of optimum manufacturing techniques.

The method chosen is extremely simple and uses a cross-guide directional coupler with a round, centered hole in the common broad wall. The wall thickness at the coupling aperture is about half the normal waveguide wall thickness and the hole is of such a diameter that the coupling is 40–50 db. For the $X$-band test coupler presently used, the hole diameter is $\frac{1}{8}$ inch and the wall thickness at the hole is 0.020 inch. The $X$-band test coupler is illustrated in Fig. 1. The two waveguides are soldered together and an access hole is provided for inserting the sample into the coupling hole. The fit of the cover plate on the access hole is not critical since any leakage of power through it is unimportant in relative power measurements of this type as long as the leakage power remains constant while the measurements are being taken. The ferrite sample is glued symmetrically in the coupling hole with Duco Cement, which had no noticeable effect on the measurements. However, the placement of the sample in the coupling hole had some effect on the level of the coupled power but no noticeable effect on the line width or the $g$ factor.

The usual method for measuring the microwave susceptibility and the effective $g$ factor of a ferrite depends upon the complex frequency perturbation of a resonant cavity. The method is quite popular but fairly difficult to instrument. It also has other disadvantages:

* Manuscript received by the PGMTT, May 27, 1958; revised manuscript received, July 11, 1958.

† Lockheed Missile Systems Div., Sunnyvale, Calif.

[1] D. C. Stinson, "Ferrite directional couplers with off-center apertures," IRE TRANS. ON MICROWAVE THEORY AND TECHNIQUES, vol. MTT-6, pp. 332–333; July, 1958.

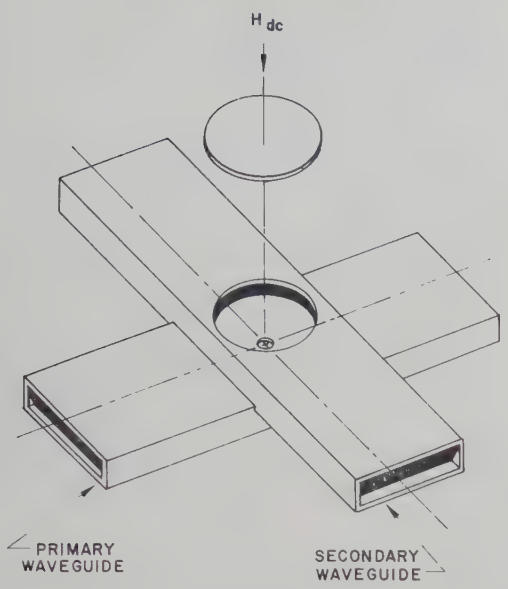


Fig. 1—Cross-guide directional coupler.

1) it requires familiarization with cavity-coupling techniques and $Q$-measuring techniques; 2) it does not permit one to vary frequency easily; 3) it requires a high-$Q$ cavity, which is often expensive; 4) it requires a rather extensive amount of accessory equipment. Another disadvantage is that the amplitude of the microwave magnetic field in the vicinity of the ferrite is much larger. Thus, it is quite easy to exceed the critical field necessary for the excitation of spin waves.[2] This limitation becomes important when measuring the narrow line widths possessed by many of the garnet-structure ferrites. Regardless of these disadvantages, the cavity-perturbation technique is required in a large number of experiments because of its extreme accuracy and because of its susceptibility to a great many refinements. However, it is felt that the cavity technique can be dispensed with for the routine measurement of the line width and the $g$ factor of microwave ferrites. This is especially true where one is concerned with comparative data among a large number of ferrite samples. In such a situation, saving time is more important than obtaining very accurate data. In view of these considerations, it is felt that the cross-guide coupler method should be extremely useful to anyone who desires information which may be obtained quickly and easily concerning the line width of ferrites, *e.g.*, ferrite manufacturing organizations.

The technique for measuring line widths of ferrites using a cross-guide coupler is easily developed from the theory of coupling through apertures containing ferrites. This theory[3] was formulated recently in fairly general terms and can be used directly. The theory which will require a little more attention is that dealing with the magnetization of the ferrite sample. This is developed fully in the Appendix.

[2] H. Suhl, "The nonlinear behavior of ferrites at high microwave signal levels," PROC. IRE, vol. 44, pp. 1270–1284; October, 1956.

[3] D. C. Stinson, "Coupling through an aperture containing an anisotropic ferrite," IRE TRANS. ON MICROWAVE THEORY AND TECHNIQUES, vol. MTT-5, pp. 184–191; July, 1957.

## Coupling Theory

The theory which was developed for coupling through an aperture containing a ferrite assumes an aperture which is small compared with the guide wavelength and a ferrite sample which is small compared with the wavelength inside it. Fortunately, experimental data[4,5] indicate that these restrictions are not too severe. Thus, the theoretical results can be quite useful in obtaining qualitative information concerning many ferrite coupling problems. In the present paper, these restrictions create no special problem since only small samples and small apertures are considered.

The coupling expressions derived from the foregoing theory for coupling between waveguides contained terms relating to both the electric and magnetic susceptibilities. However, it was shown that one could remove the electric susceptibility term by terminating the primary waveguide in a short located so as to annul the electric field at the aperture, *i.e.*, a multiple of a half guide wavelength from the aperture. Thus, the coupling expression for a collinear coupler contained only the diagonal magnetic susceptibility while the coupling expression for a cross-guide coupler contained only the nondiagonal magnetic susceptibility. Also, for the cross-guide coupler there is no coupled power in the absence of the applied magnetostatic field. For the collinear coupler, there is coupled power in the absence of the applied magnetostatic field. In view of this fact, the cross-guide coupler is considered more suitable for line width measurements since extremely small samples may be used. In practices, garnet-structure ferrite spheres 0.030 inch in diameter have been quite adequate for measurements at $X$-band frequencies.[6] Even smaller samples could be used if the sensitivity of the detecting system were increased. The present system uses a conventional waveguide detector mount and a standing wave indicator.

The expression for the coupled power in db in the cross-guide coupler for a centered aperture and with a short located in the primary waveguide so as to annul the electric field at the aperture is

$$C^{\pm} = C_0' + 20 \log \left| \chi_{xy} \right| \qquad (1)$$

where $C_0' = 20 \log \left[2\pi d^3 (3ab\lambda_g)^{-1} F_H\right]$; $\chi_{xy}$[7] is the nondiagonal magnetic susceptibility of the ferrite sample in the coupling aperture; $d$ is the diameter of the aperture; $a$ and $b$ are the wide and narrow dimensions, respectively, of the rectangular waveguide; $\lambda_g$ is the guide wavelength; and $F_H$ is a quantity which measures the attenuation due to finite aperture thickness. The expression (1) and all of the quantities involved are

[4] *Ibid.*, Figs. 2, 6, and 7.

[5] Stinson, footnote 1.

[6] The effect on the line width and the $g$ factor of the sample size and the surface roughness of the sample will be reported in a WESCON paper.

[7] The susceptibility used here is defined in terms of the external microwave magnetic field. However, data obtained using external rather than intrinsic quantities are satisfactory as mentioned by E. G. Spencer, L. A. Ault, and R. C. LeCraw, "Intrinsic tensor permeabilities on ferrite rods, spheres, and disks," PROC. IRE, vol. 44, pp. 1311–1317; October, 1956. See p. 1314.

more completely defined elsewhere.[8] MKS units are used throughout. Since relative measured values are of interest, we consider only the magnitude of the magnetic susceptibility, $|\chi_{xy}|$. By measuring the line width of $|\chi_{xy}|$, it is possible to obtain useful comparative information among ferrite samples. However, it would be desirable to measure the true line width which is normally defined in relation to the absorptive component, $\chi_{xy}'$, where $\chi_{xy}'$ is the real part of $\chi_{xy}$. Thus, since the line width measured using (1) is not the true line width of the material, we need to derive a relation concerning the values of the magnetostatic field and the amplitude of $|\chi_{xy}|$ when $\chi_{xy}'$ is half its maximum value. This is carried out in the Appendix. The result is that

$$|\chi_{xy}(H_{3,4})|\,|\chi_{xy}(H_1)|^{-1} = 2^{-1/2}$$

when

$$[\chi_{xy}'(H_{2,5})][\chi_{xy}'(H_0)]^{-1} = \tfrac{1}{2}; \tag{2}$$

where the expression $\chi_{xy}(H_i)$ means the value of $\chi_{xy}$ when the applied magnetostatic field has the value $H_i$. The relations in (2) are illustrated in Fig. 2. When the results of (2) are applied to (1), the measured line width, $\widetilde{\Delta H}$, and the $g$ factor can be obtained simply by measuring the magnetostatic field values at the two 3-db points and at the peak of the coupled power curve. The $g$ factor and the measured line width are obtained from

$$\begin{aligned} \widetilde{\Delta H} &= H_4 - H_3 \\ g &= 2H_r H_1^{-1}(1 - \tfrac{1}{2}\lambda_1^2) \\ \lambda_1 &= \widetilde{\Delta H}(2H_1)^{-1} \end{aligned} \tag{3a}$$

where $H_r = \omega[\mu_0\gamma_0'(1+\lambda_1^2)^{1/2}]^{-1}$ and $\mu_0\gamma_0' = 2.210 \cdot 10^5$ met/amp-sec. If one uses CGS units, the expression for $H_r$ in oersteds is $H_r = f(2.8)^{-1}(1+\lambda_1^2)^{-1/2}$, where $f$ is the operating frequency in megacycles. If the reduced damping constant is very small, the expression for the $g$ factor simplifies to

$$g = 2H_{r0}H_1^{-1} \quad \text{for} \quad \lambda_1 \ll 1 \tag{3b}$$

where

$$H_{r0} = \omega(\mu_0\gamma_0')^{-1}. \tag{3c}$$

The following measurement procedure for obtaining $H_1$, $H_3$, and $H_4$ has been found satisfactory. The magnetostatic field is first increased until the peak of the coupled power curve is obtained. This peak output is set at an arbitrary reference level by an ordinary variable attenuator and a calibrated variable attenuator in the primary arm. The calibrated attenuator is set at 3 db. The calibrated attenuator is then set at zero db and the magnetostatic field value is decreased considerably below the resonance value. The magnetostatic field is next increased until the coupled power reaches the prescribed reference level. The field value obtained is $H_3$ in Fig. 2. The magnetostatic field is further increased until the reference level is reached but with the calibrated attenuator set at 3 db. This field value is $H_1$. The field value $H_4$ is obtained by setting the calibrated attenuator at zero db again and increasing the magnetostatic field until the reference level is reached. In this method hysteresis effects are avoided by always increasing the magnetostatic field.

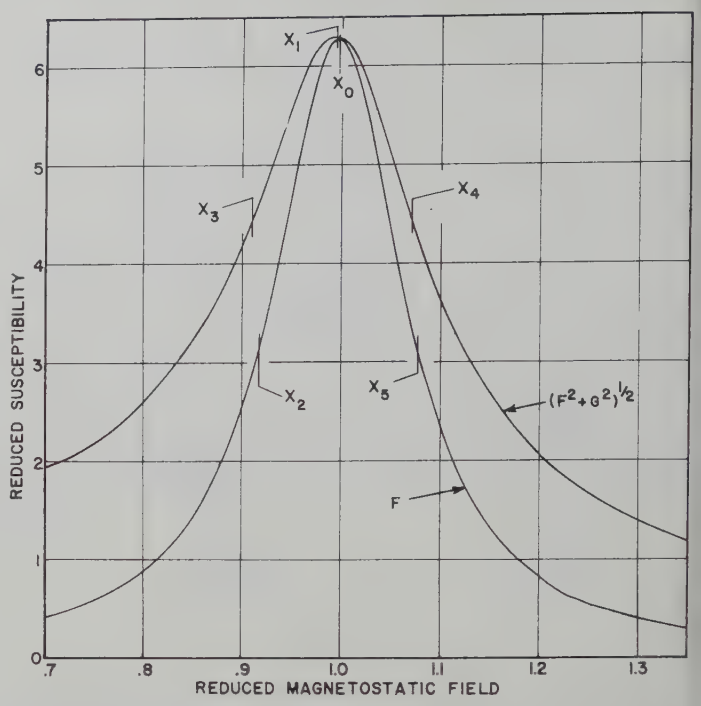


Fig. 2—Relation between the magnitude of the complex nondiagonal susceptibility and the magnitude of its absorptive component as a function of the applied magnetostatic field, all quantities in reduced units.

## Experimental Results

The theoretical basis for the foregoing expressions rests upon the usual equation of motion of the magnetization[9] with the Landau-Lifshitz form of damping.[10] Since this theory is adequate for a small-signal analysis, it is felt that measurements of line width and $g$ factor performed with the cross-guide coupler should compare favorably with measurements performed using the cavity technique. The results of such comparative measurements are shown in Table I. The cavity system available for line width measurements was not too refined and consequently accurate to about $\pm 10$ per cent, since errors are contained both in the value of the magnetostatic field and the measured $Q$. The error associated with the coupler measurements was about $\pm 5$ per cent, since the 3-db points of the coupled power curves can be measured more accurately than the $Q$ of the cavity. One question which arises is whether there is an error in the measurements because of the nonuniform fields in the coupling aperture. However, it is felt that this problem is not significant since the tangential magnetic fields in the aperture are identical

[8] Stinson, footnote 3, (14), (22), and (28).

[9] C. L. Hogan, "The microwave gyrator," *Bell Sys. Tech. J.*, vol. 31, pp. 1–31; January, 1952.

[10] H. G. Beljers, "Measurements on gyromagnetic resonance of a ferrite using cavity resonators," *Physica*, vol. 14, pp. 629–641; February, 1949.

TABLE I

Comparison of Ferrite Parameters Measured in Cavity and Cross-Guide Coupler

| Material | Cavity $\Delta H$ oersteds | Coupler $\Delta H$ oersteds | Diameter, inches | $H_1$ oersteds | $\lambda_1$ | Coupler $g$ factor |
|---|---|---|---|---|---|---|
| General Ceramics R-1 | 535 | 473 | 0.046 | 3063 | 0.07725 | 2.16 |
| Raytheon R-151 | 450 | 476 | 0.040 | 3150 | 0.0756 | 2.10 |
| Lockheed 26-1 | 60 | 58 | 0.030 | 3326 | 0.00873 | 1.99 |
| Lockheed 26-2 | 60 | 60 | 0.030 | 3324 | 0.00904 | 1.99 |
| Lockheed 26-5 | 60 | 56 | 0.030 | 3326 | 0.00843 | 1.99 |
| Lockheed 24A | 150 | 176 | 0.030 | 3225 | 0.0273 | 2.05 |
| Lockheed 26A | 75 | 76 | 0.030 | 3290 | 0.01155 | 2.02 |
| Lockheed 26A1 | 145 | 169 | 0.030 | 3228 | 0.0262 | 2.05 |

with those of the undisturbed system with no ferrite present.[11] Thus, the perturbing effect of the ferrite on the aperture fields can be reduced to a negligible amount by using a ferrite sample considerably smaller than the aperture and by using a very small aperture wall thickness. This affirmation is substantiated by the correspondence between the cavity and coupler line width measurements presented in Table I. Further corroboration is offered in Fig. 3 with theoretical and experimental curves of coupled power vs the magnitude of the applied magnetostatic field. The experimental coupling curve was obtained using the cross-guide coupler with a centered aperture 0.124 inch in diameter, a short located so as to annul the electric field at the aperture, and a LMSD 26C YIG sphere 0.060 inch in diameter. The theoretical curve was obtained by calculating 10 log $(F^2+G^2)$ from (4a) and (4b) in the Appendix and setting the peak value equal to zero db. The value of $\lambda_1$ was calculated from (3a) using the measured values of $\widetilde{\Delta H}=55.5$ oersteds and $H_1=3313$ oersteds. The value of $g$ was calculated from (3b) using a value of $H_{r0}=3315$ obtained from (3c). With an operating frequency of 9272.3 mc, the calculated values were $g=2.0012$ and $\lambda_1=0.0084$. The error between the theoretical and experimental curves is less than 1 per cent, which is better than the accuracy of the magnet calibration.

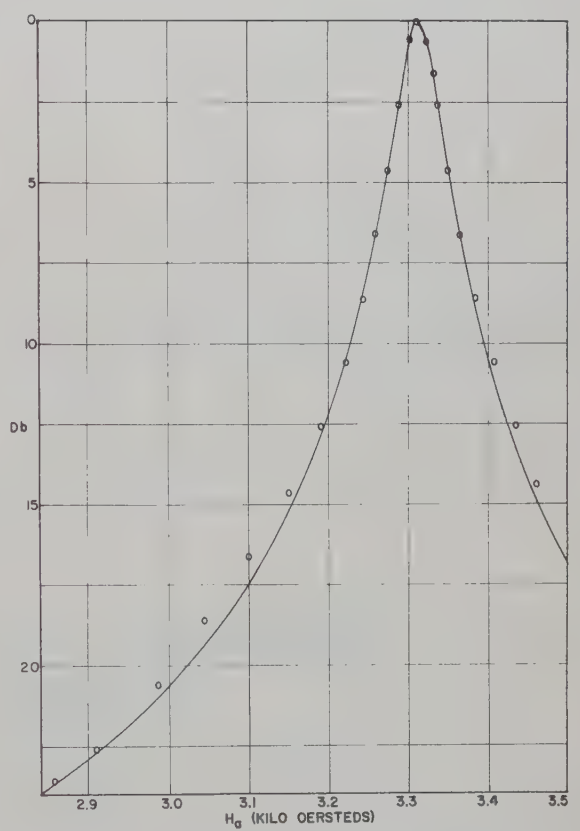


Fig. 3—Comparison of theory and experiment for the coupled power in a cross-guide coupler as a function of the applied magnetostatic field. Theoretical curve calculated for $\lambda_1=0.0084$—based upon measured values of $\widetilde{\Delta H}=55.5$ oersteds and $H_1=3313$ oersteds. Experiment performed at 9272 mc.

## Appendix

### Microwave Magnetic Susceptibilities

The expressions for the magnetic susceptibilities of a ferrite sphere as a function of the applied magnetostatic field and with the saturation magnetization, damping constant, and $g$ factor as parameters has been derived elsewhere.[12]

The quantities of interest are the following:

$$\chi_{xy}' = EF$$
$$\chi_{xy}'' = EG \qquad (4a)$$

where

$$\chi_{xy} = \chi_{xy}' + j\chi_{xy}''$$
$$E = \gamma'\mu_0 M\omega^{-1}$$
$$F = c/b$$
$$G = -c'/b$$
$$c = 2\lambda_1 x(1+\lambda_1^2)^{-1/2}$$
$$c' = 1 - x^2$$
$$b = x^4 - 2x^2[1 - 2\lambda_1^2(1+\lambda_1^2)^{-1}] + 1$$
$$x = \gamma'\mu_0 H\omega^{-1}(1+\lambda_1^2)^{1/2}. \qquad (4b)$$

[11] C. J. Bouwkamp, "Diffraction theory," *Rep. Prog. Phys.*, vol. 17, pp. 32–100; 1954. See p. 78.
[12] Stinson, footnote 3, see Appendix.

In the above expressions, $\gamma'$ is the magnitude of the magnetomechanical ratio, $\mu_0$ is the magnetic inductive capacity of free space, $M$ is the saturation magnetization, $\lambda_1=\lambda/M$ is a reduced damping constant, and $H$ is the applied magnetostatic field. The problem is that of determining the values of $x$ for which $\chi_{xy}'$ is maximum and one half of its maximum value and the values of $x$ for which $|\chi_{xy}|$ is maximum and $2^{-1/2}$ of its maximum value. Although this is a rather involved analytical procedure using the above expressions, a graphical solution can be obtained quite easily. In the present case, this was accomplished by calculating the values of $F$ and $(F^2+G^2)^{1/2}$ as a function of $x$ with a computer for values of $\lambda_1$ of 0.125, 0.100, 0.080, and 0.070. The results were then plotted as a function of $x$ and the aforementioned values of $x$ were obtained from the curves, one of which is shown in Fig. 2 for $\lambda_1=0.080$. The following values were obtained for $x$ in this manner:

$$x_0 = 1 - \lambda_1^2/2, \qquad F_{\max} = F_0 \,@\, x = x_0$$

$$\left.\begin{aligned} x_2 &= 1 - \lambda_1 - \lambda_1^2/2, \\ x_5 &= 1 + \lambda_1 - 3\lambda_1^2/5, \end{aligned}\right\} \quad F_0F_{2,5}^{-1} = 2 \,@\, x = x_2, x = x_5 \quad (5a)$$

$$x_1 = 1 - \lambda_1^2 \qquad (F^2 + G^2)_{\max} = A_1 \,@\, x = x_1$$

$$x_3 = 1 - \lambda_1 - \lambda_1^2$$

$$x_4 = 1 + \lambda_1 - 3\lambda_1^2/2, \quad A_1A_{3,4}^{-1} = 2 \,@\, x = x_3, x = x_4 \quad (5b)$$

where the $x_i$'s are defined in Fig. 2. The true line width in terms of $x$ is given as

$$\Delta x = x_5 - x_2 = 2\lambda_1 - \lambda_1^2/10.$$

The measured line width in the coupler in terms of $x$ is

$$\widetilde{\Delta x} = x_4 - x_3 = 2\lambda_1 - \tfrac{1}{2}\lambda_1^2. \quad (6)$$

Thus, if one measures in the coupler the line width $\widetilde{\Delta x}$, the value obtained is 2 per cent larger than the true line width $\Delta x$, if the reduced damping constant is 0.10. As the reduced damping constant decreases below 0.10, the measured line width approaches the true line width even more closely. The actual expression for the reduced damping constant can be obtained from (5b), (6), and (4b) as

$$\Delta\widetilde{H}H_1^{-1} = \tfrac{1}{2}(4\lambda_1 - \lambda_1^2)(1 - \lambda_1^2)^{-1}$$

where $\Delta\widetilde{H}=H_4-H_3$. This expression reduces to the following for $\lambda_1$ small:

$$\lambda_1 = \tfrac{1}{2}\Delta\widetilde{H}/H_1. \quad (3a)$$

The expression for the $g$ factor can be obtained from (5a), (5b), and (4b) as:

$$g = 2H_rH_1^{-1}(1 - \lambda_1^2)(1 - \tfrac{1}{2}\lambda_1^2)^{-1} \simeq 2H_rH_1^{-1}(1 - \tfrac{1}{2}\lambda_1^2).$$

ACKNOWLEDGMENT

The author wishes to thank L. Freiberg and M. Fisher for performing the cavity measurements and J. Novak for performing the coupler measurements and grinding the samples. Thanks are also extended to the Magnetic Properties Group of the Solid-State Electronics Department for supplying the YIG samples.

# Applications of Directional Filters for Multiplexing Systems*

FRANKLIN S. COALE†

*Summary*—The design of microwave multiplexing systems for frequency channelization of a broad-band microwave spectrum is complicated by problems such as off-resonance mismatch and mutual interaction between adjacent filters. By employing directional filters as basic building blocks, it is possible to construct multiplexing filters with a perfect input match since the input VSWR of a directional filter is theoretically unity both at resonance and off-resonance. Less insertion loss of a manifold may be obtained by the use of directional filters than with conventional band-pass filters. Curves giving the predicted response of a manifold containing $n$ elements are presented for single-tuned and double-tuned directional filters. An asymmetrical response shape is obtained which has a midband insertion loss related to the separation of adjacent channels.

An experimental model consisting of a five-channel multiplexer has been constructed utilizing double-tuned-circular-waveguide directional filters.

* Manuscript received by the PGMTT, May 28, 1958; revised manuscript received, June 20, 1958.

† Microwave Engineering Labs., Palo Alto, Calif.

## INTRODUCTION

MICROWAVE filters are used extensively in separating or combining signals of different frequencies. It is desirable in some applications to divide the frequency band into many narrow channels which are spaced in such a way that complete coverage is obtained; *i.e.*, any signal within the frequency band will be within the pass band of one or more filters. Most multiplexers of this variety have consisted of a number of filters loosely coupled to a transmission

line (hereafter referred to as a manifold). Loose coupling has been necessary because of the off-resonant mismatch associated with most band-pass filters. When a great many filters are connected on a manifold it is possible to obtain a large mismatch at some frequency within the bandwidth of the system due to the quasi-periodic nature of the manifold. Tighter coupling to the manifold produces correspondingly greater off-resonance mismatch in addition to mutual interaction between filters.

By employing filters which have a constant input impedance (a unity input VSWR) as basic building blocks, it is possible to construct multiplexing filters with a perfect input match. Filters of this type called "directional filters" have been the subject of a number of recent papers.[1–7] A directional filter is a four-port network having the response shown in Fig. 1. A typical band-pass response is obtained between arms 1 and 4; a band rejection response, between arms 1 and 2; arm 3 is isolated from the input. Ideally, the input VSWR is unity both at resonance and off-resonance. This paper will consider the application of directional filters to multiplexing systems where adjacent bands of frequencies are separated in the manner illustrated in Fig. 2.[8]

In particular the point at which adjacent bands overlap will be chosen to be the half-power points. The filters will be placed in the manifold in the order of increasing frequency.

## Theory of Single-Tuned-Directional Filter Manifolds

The response of the $n$th filter of a multichannel filter system containing single-tuned-directional filters may be obtained by forming a product of the band-rejection response of the $n-1$ filters (between the input and the $n$th filter) and the single filter may be given in terms of a normalized wavelength $\Omega$ and a normalized quality factor $Q$ where

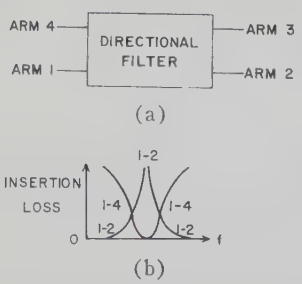


Fig. 1 Response of a directional filter.

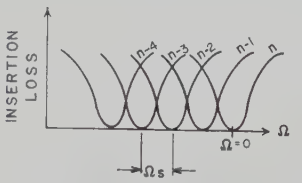


Fig. 2—Method of placing filters on a manifold.

$$\Omega = \frac{\lambda_{g0}}{\lambda_g} - 1$$

$$Q = Q_L\left(\frac{\lambda}{\lambda_g}\right)^2.$$

$\lambda_{g0}$ is the resonant guide wavelength of the directional filter, $\lambda_g$ and $\lambda$ are the guide wavelength and free space wavelength of the input signal. $Q_L$ is the loaded $Q$ of the cavity. It will be assumed that the unloaded $Q$ is infinite and that the cavity is loaded only by the coupling apertures.

If a signal of frequency corresponding to $\Omega$ and magnitude 1 is incident at arm 1 of a directional filter the following voltages exist at the other arms.[5]

$$E_1 = 1 \tag{1a}$$

$$E_2 = \frac{2\Omega Q}{(1 + 4\Omega^2Q^2)^{1/2}} \tag{1b}$$

$$E_3 = 0 \tag{1c}$$

$$E_4 = \frac{1}{(1 + 4\Omega^2Q^2)^{1/2}}. \tag{1d}$$

If one assumes that the $Q$'s of adjacent filters do not vary appreciably from one another and also that there is a fixed separation of the resonant frequencies by an amount corresponding to $\Omega_s$ as shown in Fig. 2 where

$$\Omega_s = \frac{\lambda_{gK}}{\lambda_{gK-1}} - 1,$$

then the output from arm 4 of the $n$th filter is given by the product

$$E_n = E_{4_n}E_{2_{n-1}}E_{2_{n-2}} \cdots E_{2_1}.$$

Writing this in terms of $Q$, $\Omega$ and $\Omega_s$ this expression becomes

$$E_n = \frac{1}{(1 + 4\Omega^2Q^2)^{1/2}} \prod_{\substack{a=1 \\ a\neq 1}}^{n-1} \frac{2[\Omega + a\Omega_s]Q}{[1 + 4(\Omega + a\Omega_s)^2Q^2]^{1/2}}. \tag{2}$$

[1] F. S. Coale, "A traveling-wave directional filter," IRE Trans. on Microwave Theory and Techniques, vol. MTT-4, pp. 256–260; October, 1956.

[2] S. B. Cohn and F. S. Coale, "Directional channel-separation filters," Proc. IRE, vol. 44, pp. 1018–1024; August, 1956.

[3] S. B. Cohn and F. S. Coale, "Research on Design Criteria for Microwave Filters," Stanford Res. Inst., Menlo Park, Calif., Third Quart. Prog. Rep. under Signal Corps Contract No. DA 36-039 SC 64625, Project 1331; September 15–December 15, 1955.

[4] E. M. T. Jones, F. S. Coale, O. Heinz, J. K. Shimizu, and S. B. Cohn, "Research on Design Criteria for Microwave Filters," Stanford Res. Inst., Menlo Park, Calif., Fourth Quart. Prog. Rep. under Signal Corps Contract No. DA 36-039 SC-64625, Project 1331; December 15–March 15, 1956.

[5] S. B. Cohn, E. M. T. Jones, and F. S. Coale, "Research on Design Criteria for Microwave Filters," Stanford Res. Inst., Menlo Park, Calif., Sixth Quart. Prog. Rep. under Signal Corps Contract No. DA 36-039 SC-64625, Project 1331; July 15–November 15, 1956.

[6] C. E. Nelson, "Ferrite-tunable microwave cavities and the introduction of a new reflectionless, tunable microwave filter," Proc. IRE, vol. 44, pp. 1449–1455; October, 1956.

[7] C. E. Nelson, "Circularly polarized microwave cavity filters," IRE Trans. on Microwave Theory and Techniques, vol. MTT-5, pp. 136–147; April, 1957.

[8] The problem of cascaded inputs and outputs has been previously treated by Cohn, Jones, and Coale, *op. cit.*

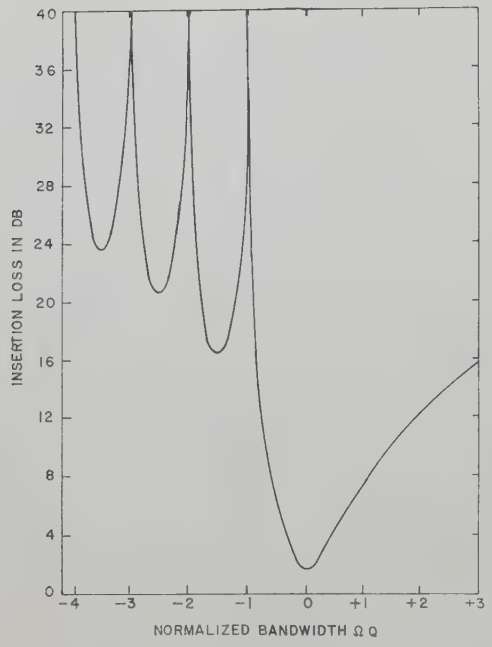


Fig. 3—Response of a single tuned directional filter manifold.

In general this expression may not be simplified and one must resort to numerical computation. If the value of $\Omega_s$ is given such that the responses of the filters intersect at their half-power points a curve shown in Fig. 3 results where insertion loss is plotted against $\Omega Q$. At the resonant frequency of a single directional filter a zero exists in the output response as measured between arms 1 and 2. Hence zeros will be expected in the response of $E_n$ at the resonant frequencies of the $(n-1)$ filters. At frequencies greater than the resonant frequency of the $n$th filter no zeros will exist (except at $\infty$) and a smooth monotonically decreasing curve is obtained which approaches the insertion loss curve of a single directional filter. The insertion loss at resonance may be deduced from (2) by setting $\Omega=0$

$$E_n|_{\Omega=0} = \prod_{a=1}^{n-1} \frac{2a\Omega_s Q}{[1+4a^2\Omega_s{}^2Q^2]^{1/2}}.$$

If one allows $n$ to approach $\infty$ and employs the relation

$$\frac{\sin \pi z}{\pi z} = \prod_{a=1}^{\infty}\left(1-\frac{z^2}{a^2}\right),$$

the following expression is found

$$\text{I.L.} = -10\log\left[\frac{\pi}{2\Omega_s Q \sinh\left(\frac{\pi}{2\Omega_s Q}\right)}\right]. \quad (3)$$

Such a curve is shown in Fig. 4 as a function of insertion loss in db vs the normalized bandwidth, $\Omega_s Q$. For a value of $\Omega_s Q=1$ (corresponding to filters whose responses overlap adjacent filter responses at the 3-db points), an insertion loss of at least 1.66 db is expected.

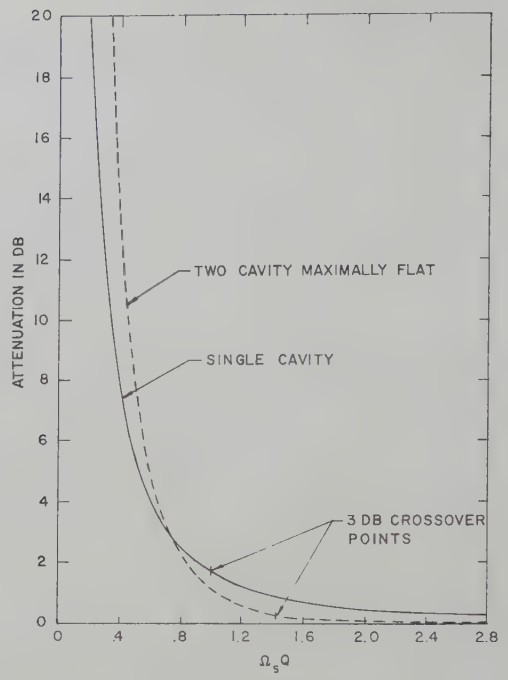


Fig. 4—Insertion loss of single and double tuned directional filter manifolds as a function of the $Q$-band separation constant $\Delta$, $Q$.

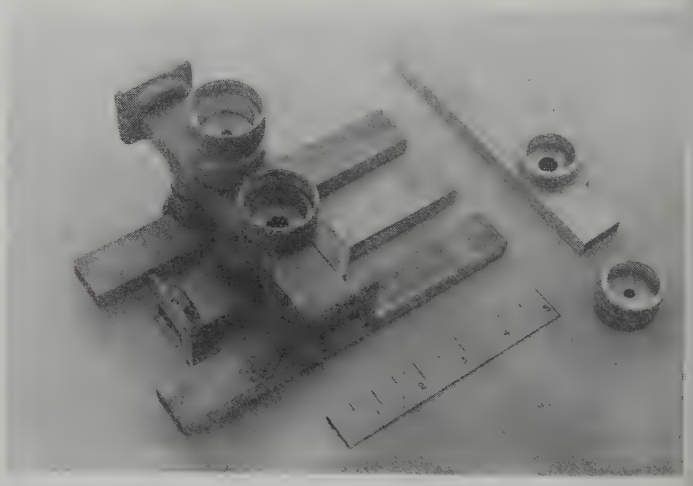

Fig. 5—Photograph of $X$-band experimental multiplexer.

## Theory of Double-Tuned-Directional Filter Manifolds

The use of double-tuned-directional filters creates considerable sharper skirts on the band-pass response. The output response of the double-tuned-directional filter is given by[9]

$$E_4 = \frac{2K}{[(K^2+1)^2+8\Omega^2Q^2(1-K^2)+16\Omega^4Q^4]^{1/2}} \quad (4)$$

(assuming $\Omega \ll 1$) where $K$ is the coefficient of coupling normalized to the critical coefficient of coupling, and $Q$ is the loaded $Q$ of a single cavity; the $Q$'s of the two

[9] This result is similar to that derived by Cohn, Jones, and Coale, *op. cit.*, and may be deduced from equations given in F. E. Terman, "Radio Engineers' Handbook," McGraw-Hill Book Co., Inc., New York, N. Y., sec. 3, para. 5, pp. 154–163; 1943.

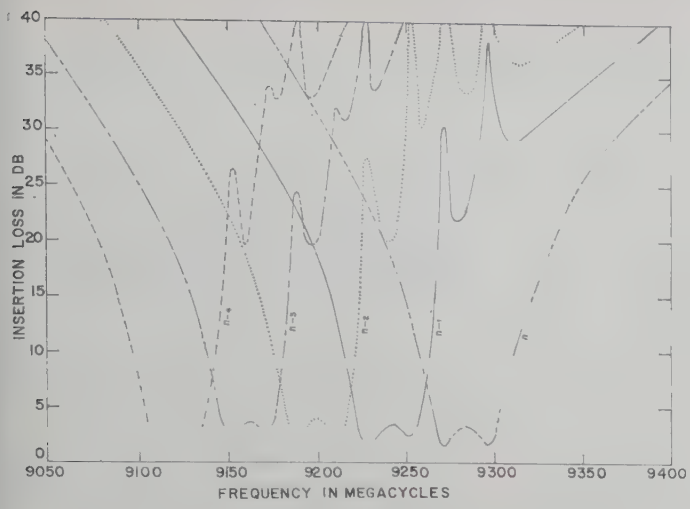


Fig. 6—Insertion loss of experimental multiplexer as a function of frequency.

cavities are assumed equal. $E_2$ is the complementary response of $E_4$ and given by

$$E_2 = \frac{K^2 - 1 - 4\Omega^2 Q^2}{[(K^2+1)^2 + 8\Omega^2 Q^2(1-K^2) + 16\Omega^4 Q^4]^{1/2}} . \quad (5)$$

The output response of the $n$th filter of the manifold is given by

$$E_n = \frac{2K}{[(K^2+1)^2 + 8\Omega^2 Q^2(1-K^2) + 16\Omega^4 Q^4]^{1/2}} \prod_{\substack{a=1 \\ n\neq 1}}^{n-1} \frac{-4Q^2(\Omega + a\Omega_s)^2 + K^2 - 1}{[(K^2+1)^2 + 8(\Omega + a\Omega_s)^2 Q^2(1-K^2) + 16Q^4(\Omega + a\Omega_s)^4]^{1/2}} . \quad (6)$$

Similar curves may be obtained as in the single tuned filters but double zeros exist where single zeros existed before. For the maximally flat case ($K=1$) the output voltage becomes:

$$E_n = \frac{1}{[1 + 4\Omega^4 Q^4]^{1/2}} \prod_{\substack{a=1 \\ n\neq 1}}^{n-1} \frac{-2Q^2(\Omega + a\Omega_s)^2}{[1 + 4(\Omega + a\Omega_s)^4 Q^4]^{1/2}} \quad (7)$$

and $E_n$ at $\Omega=0$ yields the insertion loss formula

$$\text{I.L.} = -10 \log \left[ \frac{\pi^2/(2Q^2\Omega_s^2)}{\sinh^2 \frac{\pi}{2Q\Omega_s} + \sin^2 \frac{\pi}{2Q\Omega_s}} \right]. \quad (8)$$

This is plotted in Fig. 4. Due to the sharper skirts of the double-tuned filter one should expect much less insertion loss than in the case of the single-tuned filter. The 3-db crossover point occurs at $Q\Omega_s = \sqrt{2}$ which corresponds to an insertion loss of 0.26 db.

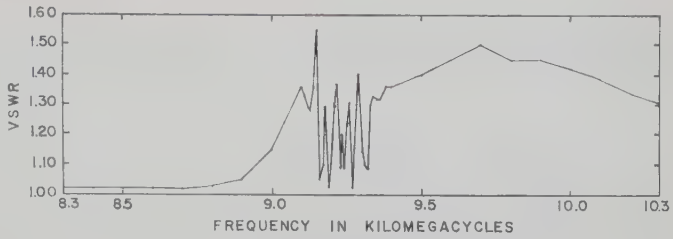


Fig. 7—VSWR of experimental multiplexer as a function of frequency.

## Experimental Results

A five-channel multiplexer was constructed in the $X$-band region and is shown in Fig. 5. The particular design of the circular waveguide directional filters is given in the literature.[2-4] The bandwidth of each output response was approximately 40 mc. The curves are shown for the cavities in the reverse order, *i.e.*, the highest frequency cavity was placed first in the line. A curve showing the electrical performance is given in Figs. 6 and 7. It may be shown that if an elliptically polarized wave rather than a circular wave exists in the cavity that the input VSWR is not unity, nor is there a perfect band rejection response. Due to the particular manner of construction it is impossible to cause perfect circular polarization since the positions of coupling holes between the waveguide manifold and the circular cavities were not varied from filter to filter. Other causes for the rather high VSWR are due to inaccurate tuning of the cavities. The criterion chosen was response shape rather than input VSWR.

## Conclusion

The use of directional filters in the design of complete-coverage multiplexers realizes maximum electrical performance. The theory presented in this paper has been substantiated by experiment.

# Correspondence

## Coaxial Isolator Utilizing Yttrium-Iron Garnet*

The inherently narrow ferromagnetic resonance line width attainable with yttrium-iron garnet (YIG) material permits building isolators with greatly improved characteristics at the lower microwave frequencies. An isolator utilizing YIG designed for operation in the UHF range has been reported.[1] This letter describes a coaxial isolator designed to operate at $2250 \pm 50$ mc employing yttrium-iron garnet.

A $\frac{3}{8}$-inch diameter, 50-ohm coaxial line was half filled with a high dielectric constant material (Stycast Hi-K-15) with $2\frac{1}{2}$-inch tapers on the ends and the YIG rods placed on the interface; the magnetic biasing field was parallel to the interface in the manner reported by Duncan, *et al.*[2] Two YIG rods of square cross section ($0.070 = 0.070 \times 2.450$ inches long with $\frac{1}{4}$-inch tapers on the ends) were located on both sides of the inner conductor. With a permanent magnet biasing field adjusted for resonance at 2250 mc, isolator characteristics as shown in Fig. 1 were obtained.

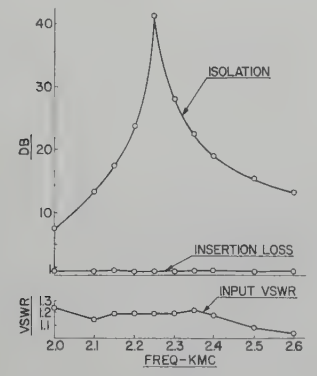


Fig. 1—Characteristics of yttrium-iron garnet coaxial isolator.

By replacing the permanent magnet with an electromagnet and adjusting the biasing field for maximum reverse attenuation at each frequency, the maximum reverse attenuation as a function of frequency was obtained as shown in Fig. 2. All measurements were made in the milliwatt power range. Since this material evidenced such reasonable isolation-to-insertion loss ratios in the 1-kmc region, additional work was initiated and is presently in progress to develop an isolator for this frequency range.

This material was prepared by the Magnetics Research Group of the Solid State Electronics Department of Lockheed Missile Systems Division, and had a measured

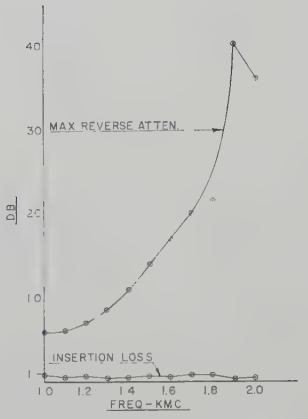


Fig. 2—Maximum reverse attenuation of coaxial isolator vs frequency by varying biasing field.

density of 98 per cent of theoretical maximum, a Curie temperature of 318°C, and a measured X-band line width of 60 oersteds.

L. Freiberg
Lockheed Missile Systems Div.
Sunnyvale, Calif.

## A Broad-Band Microwave Coaxial Connector with Capacitive RF Coupling and Isolated DC Returns*

### Introduction

A modified type N connector for passing RF while grounding the center conductor of the coaxial line has been reported by McLaughlin and Dunn.[1] This device is useful for many applications but in microwave measurements it is sometimes necessary to have a high pass filter with a different dc voltage connected to each side of the filter. One such situation occurs in the connection of the input terminal of a microwave tube at one dc potential to a signal generator at essentially ground potential. Such a filter has been made with a type N connector having a series capacitance in the center conductor and a high resistance wire connected to one side of the split center conductor and passing through a small hole in the outer conductor. Since the resistance wire has very little effect on the RF properties, very little difference would be observed by having a dc return to both sides of the split center conductor. The capacitance consists of parallel plates separated by an insulator with a large dielectric constant. From 1.5 to 10 kmc the connector has less than 3 db insertion loss and a VSWR less than 1.5. The dc current rating of the resistance wire is 100 ma and the dc voltage breakdown between two faces of capacitance is greater than 1500 volts.

### Physical Properties

The center conductor of a type N(UG29 B/U) connector is severed and insulated with dielectric material to form a blocking condenser which will pass RF but not direct current. The capacitance should be made as large as possible for low impedance at the operating frequency. Various materials were tested and the best results were obtained by inserting a piece of ceramic obtained from an ordinary Erie 0.001 $\mu$f disk ceramic condenser. It was estimated that the dielectric constant of this type ceramic was in the order of 100, which greatly exceeds the dielectric constant of the usual construction materials. With a piece of ceramic having a diameter of 0.168 inch and a thickness of 0.040 inch the inserted capacitance was 7 to 12 $\mu\mu$f at 1 mc and the dc working voltage was greater than 1500 volts. The dc path was formed by placing a fine Karma alloy resistance wire inside a small teflon tubing and feeding this unit through a $\frac{1}{16}$-inch diameter hole in the outer conductor in such a way that the Karma wire overlapped the teflon tubing and was pressed against the center conductor by screwing on a bakelite cap. With this arrangement the insulation between the Karma wire and the outside conductor was also greater than 1500 volts. The bakelite cap also formed the terminal for the dc connection. A drawing of the modified connector is shown in Fig. 1.

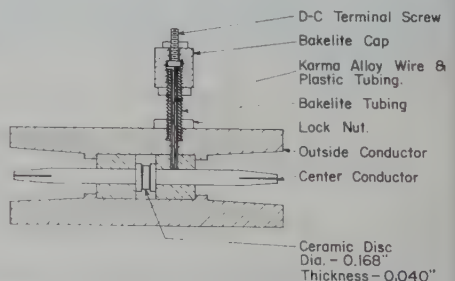


Fig. 1—Microwave coaxial capacitance using an N-type connector fitted with one dc connection and a series capacitance in the center conductor.

The Karma alloy wire was used because it was readily available in small sizes and has excellent mechanical properties. Its physical properties were as follows:

| | |
|---|---|
| Karma alloy wire | 0.0012 inch diameter |
| Resistivity of wire | 521.5 ohms per foot |
| Resistance of dc path | 30–40 ohms |
| Current carrying capacity | 100 ma |

The specifications of the unit were selected to satisfy our own requirements but could be suitably modified to allow for a different breakdown voltage or frequency bandwidth for other applications.

* Received by the PGMTT, June 27, 1958.
[1] F. R. Morgenthaler and D. L. Fye, "Yttrium garnet UHF isolator," Proc. IRE, vol. 45, pp. 1551–1552; November, 1957.
[2] B. J. Duncan, L. Swern, K. Tomiyasu, and J. Hannwacker, "Design considerations for broad-band ferrite coaxial line isolators," Proc. IRE, vol. 45, pp. 483–490; April, 1957.

* Received by the PGMTT, July 18, 1958.
[1] J. W. McLaughlin and D. A. Dunn, "Wide band dc return connector," IRE Trans. on Electron Devices, vol. ED-4, pp. 310–311; October, 1957.

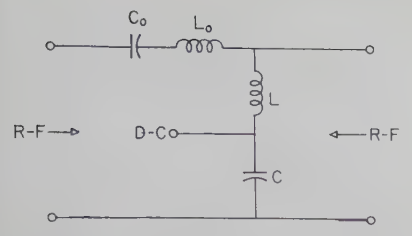


Fig. 2—Schematic diagram of a microwave coaxial capacitance of the type employed. Only one dc voltage is applied in this device but another terminal is possible.

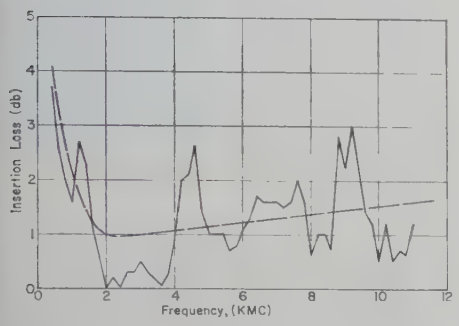


Fig. 3—Experimental measurement of insertion loss of the microwave N-type coaxial capacitance with one dc terminal, showing also the probable value of the connector loss. The connector has a sharp low frequency cutoff and a very gradual high frequency cutoff.[2]

### RF Properties

The connector is really a band-pass filter[2] with a sharp low frequency cutoff and a gradual upper frequency cutoff so that it makes an excellent high-pass filter in the range from 1.5 to 10 kmc. A schematic diagram of the equivalent circuit is shown in Fig. 2. In this case $C_0$ represents the capacitance in the center conductor, $L$ represents the inductance of the Karma alloy resistance wire, $C$ represents the capacitance between this wire and the external shield, and $L_0$ is the natural series inductance between the capacitance $C_0$ and the dc resistance path. As $L_0$ approaches zero this becomes a high-pass filter.

The connector loss was measured by the insertion loss method. The power delivered to a matched load from a matched generator was detected with and without the "connector" inserted in the line. The ratio of these powers thus gave the insertion loss directly. As a result of this method the readings were sensitive to the VSWR at the terminals of the connector. The insertion loss varied from 0.01 to 3 db for the frequency range 1.5 to 10 kmc, as shown in Fig. 3.

The dashed average line on Fig. 3 indicates the probable value of the insertion loss across the band in the absence of reflections. Even though the device is a pass band filter the attenuation of the pass band apparently rises very slowly on the high frequency end making the device very broadband.

The VSWR of the connector, which may be of more interest than the insertion loss for some considerations, is shown in Fig. 4.

[2] W. P. Mason, "Electro-Mechanical Transducers and Wave Filters," D. Van Nostrand Co., Inc., New York, N. Y., p. 52; 1948.

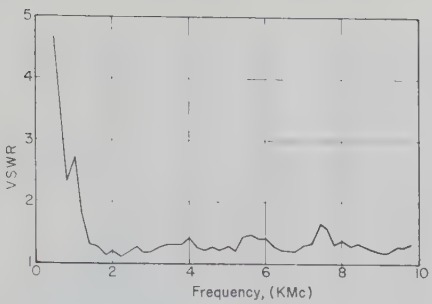


Fig. 4—Experimental measurement of VSWR of the microwave N-type coaxial capacitance with one dc terminal

The VSWR is less than 1.50 between 1.5 and 10 kmc.

No direct measurement was made to determine the radiation loss through the Karma wire terminal, but it was noted that placing a grounded copper shield $\frac{1}{2}$-inch long around the terminal caused less than a 2 per cent difference in the VSWR reading when the dc terminal was grounded or open circuited.

C. M. Lin
R. W. Grow
Electronics Labs.
Stanford University
Stanford, Calif.

## The Cutoff Wavelength of Trough Waveguide*

### Introduction

The trough waveguide,[1] although in use for several years, is not widely known and has received only little attention in the literature. This waveguide was suggested by E. G. Fubini, and its fundamental mode may be compared to that of a TE mode in symmetrical strip transmission line. The configuration is shown in Fig. 1. This type of

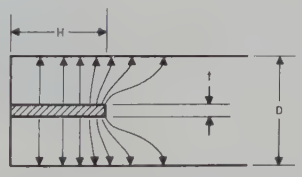


Fig. 1—Trough waveguide.

waveguide has several advantages, which include:

1) broad frequency range, because the cutoff frequency of the second mode is approximately three times that of the dominant mode;
2) low-reflection, broad-band transitions to TEM lines, easily made by an end-on connection of the center conductor of a coaxial line to a point on the center vane;[2]
3) line measurements, made with a minimum of disturbance because of the open side;
4) simple control of the propagation characteristics, possible by changing the center vane;
5) economical fabrication.

The application of this waveguide to line-source radiators has been investigated extensively by Rotman and Karas and excellent results have been obtained.[3]

A derivation of the cutoff wavelength for a TE mode in symmetrical strip transmission line in the case of a zero-thickness center strip was obtained independently by Jasik[4] and Oliner.[5] In both instances the result was based on the analogous $E$-plane bifurcation in rectangular waveguide, and this result applies also to the trough waveguide. In any actual waveguide, however, the center vane must have a finite thickness. It is of interest, therefore, to know how the cutoff wavelength depends on this parameter.

### Derivation of the Approximate Cutoff Wavelength

By the transverse resonance procedure, the cutoff wavelength is given by

$$\lambda_c = 4(H + d) \tag{1}$$

where $d$ is the distance from the physical edge of the center vane to the effective open circuit point. In the case of $t=0$, we have[4,5]

$$d = \frac{D}{\pi} \ln 2 + \frac{\lambda_c}{2\pi}\left[S_1\left(\frac{2D}{\lambda_c}\right) - 2S_1\left(\frac{D}{\lambda_c}\right)\right], \tag{2}$$

where

$$S_1(x) = \sum_{n=1}^{\infty}\left(\arcsin\frac{x}{n} - \frac{x}{n}\right).$$

We may relate $d$ to an equivalent fringing capacitance which, because $d$ is frequency dependent, will also be frequency dependent.

In the case of thick center vane let us consider the equivalent fringing capacitance from one edge of the vane. This is given by

$$C_f = 0.0885\epsilon \frac{d}{\frac{1}{2}(D - t)}, \ PF/\text{cm}, \tag{3}$$

so that

$$\frac{d}{D} = \frac{1}{2} \cdot \frac{C_f}{0.0885\epsilon}(1 - t/D), \tag{4}$$

and from (1), we have

$$\frac{\lambda_c}{D} = 4\frac{H}{D} + \frac{2C_f(1 - t/D)}{0.0885\epsilon}. \tag{5}$$

The second term on the right side of (5) is

* Received by the PGMTT, July 21, 1958.

[1] Airborne Instruments Lab., Mineola, N. Y., Advertisement, Proc. IRE, vol. 44, p. 2A; August, 1956.

[2] H. S. Keen, "Scientific Report on Study of Strip Transmission Lines," Airborne Instruments Lab., Mineola, N. Y., Rep. No. 2830-2; December 1, 1955.

[3] W. Rotman and N. Karas, "Some new microwave antenna designs based on the trough waveguide," 1956 IRE Convention Record, pt. 1, pp. 230–235.

[4] H. Jasik, private communication to E. G. Fubini; July 30, 1953.

[5] A. A. Oliner, "Theoretical developments in symmetrical strip transmission line," *Proc. Symp. Modern Advances in Microwave Techniques*, Polytechnic Inst. of Brooklyn, Brooklyn, N. Y., pp. 379–402; November, 1954.

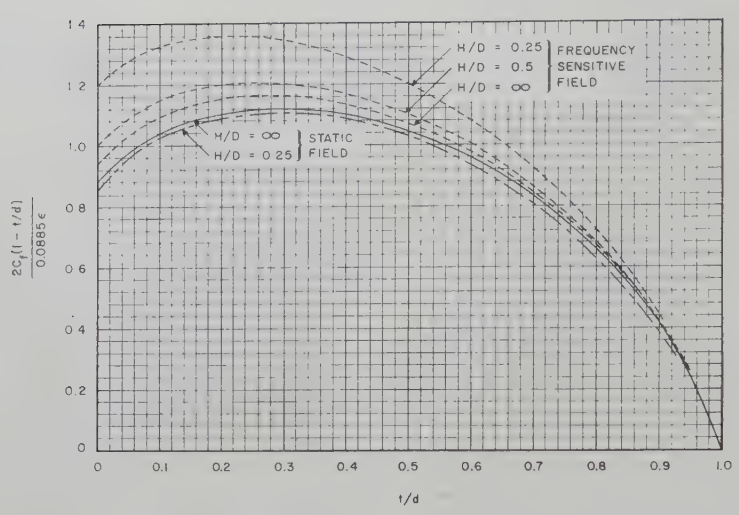


Fig. 2—Normalized fringing capacitance from one edge of trough waveguide center vane.

readily evaluated for *wide* vanes and a *static* field, in which case[6]

$$\frac{2C_f(1-t/D)}{0.0885\epsilon} = \frac{4}{\pi}\ln\left(\frac{2-t/D}{1-t/D}\right) - \frac{2t}{\pi D}\ln\left(\frac{1-[1-t/D]^2}{[1-t/D]^2}\right). \quad (6)$$

This term is plotted in Fig. 2 (solid curve) and for most applications this curve together with (5) will provide sufficiently accurate results.[7]

## Corrections to the Approximate Solution

One correction which must be made to the solution obtained above is that due to the assumption of the semi-infinite width of the center vane used in deriving (6). The exact value of the static fringing capacitance may be found, but not in closed, explicit form. Consider the strip transmission line of width $2H$, thickness $t$, and ground-plane spacing $D$, then the capacitance per unit length is given by

$$C = 4(C_b + C_f), \quad (7)$$

where

$$C_b = \frac{0.0885\epsilon H}{\frac{1}{2}(D-t)}$$

is one-half the parallel plate capacitance to one ground plane, neglecting fringing, and $C_f$ is the fringing capacitance from one corner of the center strip. Thus

$$\frac{2C_f(1-t/D)}{0.0885\epsilon} = \frac{C(1-t/D)}{0.177\epsilon} - \frac{4H}{D}. \quad (8)$$

Now $C$ may be evaluated[8] from the relations

$$C = \frac{100\sqrt{\epsilon}}{3Z_0} = 1.1\,\pi\sqrt{\epsilon}K'(k)/K(k)$$

$$2H = \frac{2K(k)}{\pi}\left[\frac{k^2\,sn\,(u)\,cn\,(u)}{dn\,(u)} - zn(u)\right] \quad (9)$$

$$t/D = \frac{u}{K(k)} - \frac{2K'(k)}{\pi}\left[\frac{k^2\,sn\,(u)\,cn\,(u)}{dn\,(u)} - zn\,(u)\right]$$

where

$K(k)$ is the real quarter period of $sn(u)$,
$K'(k)$ is the imaginary half period of $sn(u)$,
$sn(u)$, $cn(u)$ and $dn(u)$ are Jacobian elliptic functions,
$zn(u)$ is the Jacobian zeta function.

This evaluation is very tedious, but fortunately the resulting correction is small for all practical cases. The dot-dash curve in Fig. 2 shows the result for the case $H/D = 0.25$ and, since the deviation from the solid curve ($H/D$ large) will be less for larger values of $H/D$, we may conclude that this correction term is negligible for all practical cases.

A correction which is of greater significance is that required to account for the frequency sensitive portion of the fringing capacitance. Neglect of this term in the case $t=0$ results in an error of less than 4 per cent in the cutoff wavelength for $H/D$ greater than 0.5, and the error vanishes as $H/D$ approaches infinity. It does not seem reasonable to expect this term to be strongly dependent on $t/D$. It certainly would not have a pole at $t/D=1$ and, therefore, the second term on the right hand side of (5) will vanish as $t/D$ approaches unity. An estimate of the effect of frequency sensitivity of the fringing capacitance can be obtained by assuming that it does not depend on $t/D$. With this assumption the dashed curves in Fig. 2 are obtained.

From these considerations it is seen that in practical cases, such as a thin, wide center vane, or a thick, narrow center vane, the approximate solution is satisfactory.

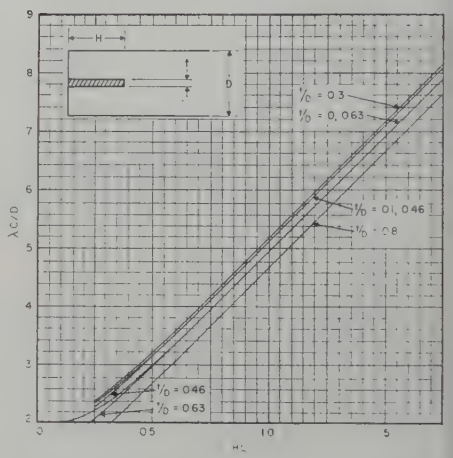


Fig. 3—Cutoff wavelength of trough waveguide.

For convenience, the value of the cutoff wavelength is plotted in Fig. 3 as a function of the waveguide dimensions. It should be pointed out that the curves for $t/D=0.1$ and 0.46 are identical as are those for $t/D=0.0$ and 0.63. The estimated frequency-dependent correction has been used in this calculation. At $\lambda_c/D=2$ the higher mode spectrum becomes continuous and a TM mode may also exist.[5] The curves may be extrapolated to larger values of $H/D$, but are in doubt in the region $H/D<0.5$. Curves for other values of $t/D$ are readily obtained from Fig. 2, as is the sensitivity of waveguide wavelength to changes in vane thickness.

K. S. Packard
Airborne Instruments Lab.
Mineola, N. Y.

[6] J. J. Thomson, "Recent Researches in Electricity and Magnetism," Clarendon Press, Oxford, Eng.; 1893.

[7] This result has been obtained independently by A. A. Oliner, "Leaky Waves on Asymmetric Trough Waveguides." Microwave Res. Inst., Polytechnic Inst. of Brooklyn, Brooklyn, N. Y., Memo. No. 36; October 31, 1957.

[8] R. H. T. Bates, "The characteristic impedance of the shielded slab line," IRE Trans. on Microwave Theory and Techniques, vol. MTT-4, pp. 28–33; January, 1956.

# Contributors

Victor J. Albanese (A'48–SM'55) was born on February 2, 1927, in New York, N. Y. He received the B.E.E. degree in 1947 and the M.E.E. degree in 1949 from the Polytechnic Institute of Brooklyn, Brooklyn, N. Y.

V. J. Albanese

From 1947 to 1949, he was a research assistant at the Microwave Research Institute. From 1949 to 1951, he was a member of the antenna group at Airborne Instruments Laboratory, Mineola, N. Y., where he worked on the development of flush-mounted antennas and associated components for jet aircraft. In 1951, he joined the engineering staff of the W. L. Maxson Corp., New York, N. Y. He became a project engineer in 1953, responsible for RF component development for electronic countermeasures systems.

He has been associated with the Bogart Manufacturing Corp., Brooklyn, N. Y., since 1955, and currently holds the position of assistant chief electronics engineer in charge of research and development.

He has been a member of the evening teaching staff at the Polytechnic Institute of Brooklyn since 1951.

Mr. Albanese is a member of Tau Beta Pi, Eta Kappa Nu, and Sigma Xi.

❖

Lawrence K. Anderson (S'55) was born on October 2, 1935, in Toronto, Ont., Canada. He received the B.E. degree in engineering physics from McGill University, Montreal, Que., Canada, in 1957.

L. K. Anderson

He has been employed for the last three summers by the Radio and Electrical Engineering Division of the National Research Council of Canada. At the present time Mr. Anderson is studying at Stanford University, Stanford, Calif., where he holds an appointment as a research assistant in the Microwave Laboratory.

❖

Carlos M. Angulo (S'50–A'52–M'52–SM'56) was born in Pinto (Madrid), Spain, in 1921. He received the degree of Ingeniero de Telecomunicacion from the Escuela Oficial de Telecomunicacion in Madrid, Spain, in 1946; the M.E.E. degree in communication engineering in 1951 and the D.E.E. in electro-physics in 1955, both from the Polytechnic Institute of Brooklyn.

From 1946 to 1948, he worked as an assistant technical director of Transradio Espanola S. A. in Madrid in radio telegraphy and radio telephony. In 1947 he became a research associate of the Spanish Council of Scientific Research in Madrid and worked in electroacoustics.

C. M. Angulo

He joined the Polytechnic Institute of Brooklyn as a research associate in 1949 and as instructor of electrical engineering in 1950; his research during this period was in microwaves. He became an assistant professor of engineering in 1952 and associate professor in 1955 at Brown University, Providence, R. I., where he is at present doing research in antennas and propagation, and teaching.

During the summer of 1956, he was a visiting research associate professor at the Control Systems Laboratory of the University of Illinois, working in propagation problems.

Dr. Angulo is a member of Tau Beta Pi, Sigma Xi, and the American Association for the Advancement of Science.

❖

Robert W. Beatty (S'43–A'45–M'50–SM'53) was born in York, Pa., on May 31, 1917. He received the B.S. degree in electrical engineering in 1939 from George Washington University, Washington, D. C., and the S.M. degree in electrical communication in 1943 from the Massachusetts Institute of Technology, Cambridge, Mass. From 1940 to 1942, he was associated with the Naval Research Laboratory in work on underwater sound and radio direction finding. He was a staff aid at the M.I.T. Radar School in 1943 and served in the U. S. Naval Reserve from 1943 to 1946. He has had several years experience in the field of consulting radio engineering for the radio broadcast industry. Since 1948, he has been associated with the National Bureau of Standards, Boulder, Colo., working in the field of microwave standards, and is Chief of the Microwave Circuit Standards Section.

R. W. Beatty

Mr. Beatty is a member of Sigma Tau, Theta Tau, RESA, and chairman of Commission I of the U.S.A. National Committee of the International Scientific Radio Union.

William S. C. Chang was born in Kiangsu, China, on April 4, 1931. He received the B.S.E. degree in 1952 and the M.S.E. degree in 1953 from the University of Michigan, Ann Arbor, Mich. He continued to study at Brown University, Providence, R. I., where he received the Ph.D. degree in electrical engineering in 1957. At Brown University he was associated with the theoretical research on dielectric antennas. At present, he is a research associate at the Stanford Electronics Laboratories, Stanford, Calif., engaged in the research of solid-state masers.

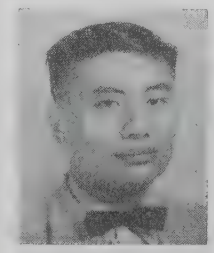

W. S. C. Chang

Dr. Chang is a member of Sigma Xi and Tau Beta Pi.

❖

Franklin S. Coale (A'53) was born in Plainfield, N. J., on February 16, 1931. He received the B.S. degree in engineering physics from Lehigh University, Bethlehem, Pa., in 1952, subsequently taking postgraduate work in applied mathematics at New York University, New York, N. Y. In 1953, he joined the Sperry Gyroscope Company, Great Neck, N. Y., as an associate engineer in microwave components and antennas engineering. He became a research engineer in the Microwave Group of the Antenna Systems Laboratory at Stanford Research Institute, Menlo Park, Calif., in 1955, and in December, 1957, he joined Microwave Engineering Laboratories, Inc., Palo Alto, Calif., as a senior engineer. He is presently engaged in research and development on filters, multiplexers, and solid-state physics.

F. S. Coale

Mr. Coale is a member of the American Physical Society and the Research Society of America.

❖

Rudolf G. de Buda was born in Vienna, Austria, on January 21, 1924. He attended the University in Vienna where he received the degree of Dipl. Ing. in electrical engineering (communications) and the Ph.D. degree in mathematics. He went to Canada in 1951, and joined the Canadian General

Electric Company, Ltd., and until 1954 he worked at its Davenport and Guelph Works as design engineer of power transformers.

R. G. de Buda

In 1954, he transferred to the Electronic Equipment and Tube Department of the same company in Toronto, where he now works as an engineering consultant.

Dr. de Buda is a member of the Association of Professional Engineers of Ontario.

❖

B. J. Duncan, for a photograph and biography, please see page 115 of the January, 1958, issue of these Transactions.

❖

Kazuo Fujisawa was born on August 24, 1921, in Tokyo, Japan. At Osaka University, he graduated from the Faculty of Engineering in 1943, finished the graduate course in 1948, and received the Ph.D. degree in engineering in 1955.

K. Fujisawa

He was appointed assistant professor of Osaka University in December, 1948. In July, 1954, he transferred to Kobe University, Kobe, Japan, where he was appointed professor in April, 1955.

Since 1948, he has been engaged in research on microwave electronics.

Dr. Fujisawa is a member of the Institute of Electrical Communication Engineers of Japan.

❖

Robert V. Garver (A'57) was born on June 2, 1932, in Minneapolis, Minn. He attended the University of Maryland, College Park, Md., where he was awarded the Bachelor of Science degree in physics in 1956. In 1956 he became affiliated with the Microwave Development Section of Diamond Ordnance Fuze Laboratories, Washington, D. C., where he has been working on microwave semiconductors.

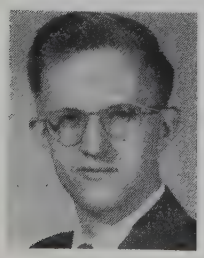

R. V. Garver

Mr. Garver is a member of the American Physical Society.

❖

Edward L. Ginzton (S'30–A'40–SM'46–F'51) was born in Russia on December 27, 1915, and came to the United States in 1929. He received the B.S. and M.S. degrees in electrical engineering from the University of California, Berkeley, Calif., in 1936 and 1937, respectively. He received the E.E. degree in 1938, and the Ph.D. degree in 1940 from Stanford University, Stanford, Calif.

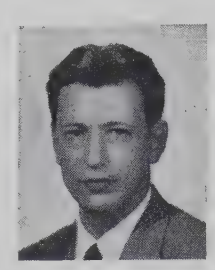

E. L. Ginzton

He is now a professor of applied physics and electrical engineering at Stanford University, and Director of the Microwave Laboratory there.

He has been a member of the Board of Directors of Varian Associates, Inc., Palo Alto, Calif., since that company's organization in 1948, and was appointed an assistant to the chairman of the Board in 1957.

Dr. Ginzton is a member of Sigma Xi, Tau Beta Pi, and Eta Kappa Nu.

❖

Henry H. Grimm (A'44–M'52) was born in Annville, Pa., on March 29, 1913. He received the A.B. degree in physics and mathematics in 1935 from Lebanon Valley College, at Annville, and the M.A. degree in physics in 1936 from the University of Pennsylvania. From 1936 to 1941 he taught high school science and mathematics at New Cumberland, Pa.

H. H. Grimm

During 1941 to 1943 he was a graduate student and instructor in the physics department of Pennsylvania State University. From 1943 to 1946 he was employed on countermeasures development as a physicist in the Special Projects Laboratory at Wright Field, Dayton, Ohio. He worked from 1946 to 1951 as a physicist specializing in electronic standards and microwave research at the Naval Research Laboratory.

Since 1951 he has been associated with the Electronics Laboratory of General Electric Company, Syracuse, N. Y., where he has worked in the fields of high-power coherent radar, countermeasures, ferrites, and low noise microwave amplifiers. He is now a consulting engineer in the Antenna and Microwave Component Division.

Mr. Grimm is a member of RESA.

❖

Mrs. M. A. Harper was born in Washington, D. C., on July 28, 1929. She was a student at George Washington University, Washington, D. C. She then was employed by the National Bureau of Standards, and attended the NBS graduate school.

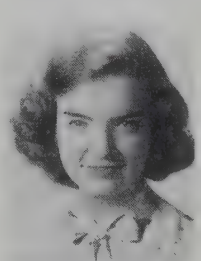

M. A. Harper

Since the activation of the Diamond Ordnance Fuze Laboratories in 1953, Mrs. Harper has been engaged in research and development work on microwave components.

Archibald Hendry (S'50–A'52–M'58) was born on April 1, 1929, in Newcastle, Ont., Canada. He received the B.S. degree in physics from Queen's University, Kingston, Ontario, in 1952.

A. Hendry

He has been employed in the Radio and Electrical Engineering Division of the National Research Council of Canada, in Ottawa, Ontario, since 1952, where he has been engaged in the study of low-noise amplifiers and the development of microwave radar receivers.

❖

Edward M. T. Jones (S'45–A'51–SM'56) was born in Topeka, Kan., on August 19, 1924. He received the B.S. degree in electrical engineering from Swarthmore College, Swarthmore, Pa., in 1944 and the M.S. and Ph.D. degrees in electrical engineering from Stanford University, Stanford, Calif., in 1948 and 1950, respectively.

E. M. T. Jones

He was a radar maintenance officer in the U. S. Navy from 1944 to 1946. From 1948 to 1950 he was a research associate at Stanford University, and in 1950 he joined the staff of the Stanford Research Institute, Menlo Park, Calif., where he is now head of the microwave group of the electromagnetics laboratory.

Dr. Jones is a member of Sigma Tau and RESA.

❖

J. Burton Linker, Jr. (S'48–A'49–M'56) was born in Durham, N. C., in 1923. He received the B.S. degree in physics from the University of North Carolina in 1944. He then entered the service and trained at Harvard University and the Massachusetts Institute of Technology radar schools, to become a naval electronics officer. After the war he returned to graduate school and received the M.S. degree in electrical engineering from the College of Engineering of the University of North Carolina. Since 1949 he has been associated with the Electronics Laboratory of the General Electric Company, Syracuse, N. Y.

J. B. Linker, Jr.

He has been concerned with advanced development in color television for two years, and with problems related to missile electronic guidance systems for five years. During the past two years he has

worked in the field of microwave measurements, with particular emphasis on the measurement of ferrite characteristics. He became a professional registered engineer in the State of New York in 1955 and graduated from the three-year advanced engineering program at General Electric in 1958.

Mr. Linker is an associate member of Sigma Xi and a member of RESA and Eta Kappa Nu.

❖

William P. Peyser (SM'52) was born on April 15, 1918, in New York, N. Y. He received the B.S. degree from the College of the City of New York in 1939 and continued there for one year of graduate study in chemistry and education.

W. P. Peyser

He was a civilian coordinator of instruction at the Army Air Force Radio School, Scott Field, Ill., from 1941 to 1944. While serving with the U. S. Navy from 1944 to 1946, he also was a student at the Bellevue Radio Materiel School, Naval Research Laboratories, Washington, D. C.

He joined Airborne Instruments Laboratory, Mineola, N. Y., in 1946 as a project engineer in the Special Devices Group, where he contributed to the development of a UHF swept frequency voltage standing-wave-ratio indicator and a VHF airborne direction-finding antenna.

From 1953 to 1956 he was with the Bogart Manufacturing Corp., Brooklyn, N. Y., as supervisor of engineering in charge of development programs in microwave components and assemblies.

He returned to the Airborne Instruments Laboratory in January, 1957, and was assigned to the Department of Special Systems and Components. He is now group leader in the Reconnaissance Systems Department and is active in the field of passive countermeasures.

Mr. Peyser has been on the evening teaching staff of the Polytechnic Institute of Brooklyn since September, 1955.

❖

John Reed (A'48–SM'53) was born in Cambridge, Mass., on March 9, 1922. He received the B.S. degree in applied physics from Massachusetts Institute of Technology in 1943, and for two years thereafter was on the staff of the M.I.T. Radiation Laboratory in the Radio Frequency Components Group. After graduate study at Cornell University he joined the Submarine Signal Company in 1947 and then transferred to the Raytheon Manufacturing Company in 1948, where he is currently employed as consultant on microwave problems.

J. Reed

Henry J. Riblet (M'55) was born on July 21, 1913, in Calgary, Canada. He received the Ph.D. degree from Yale University in 1939 and then taught mathematics for three years at Adelphi College and at Hofstra College on Long Island. He joined the M.I.T. Radiation Laboratory in 1942 and at the close of the war was in charge of one of the three development sections of the Antenna Group. From 1946 to 1948 he headed the VHF group at the Submarine Signal Company. He is presently at the Microwave Development Laboratories, Inc., of which he was a cofounder.

H. J. Riblet

Dr. Riblet is a member of the American Mathematical Society and the American Physical Society.

❖

George E. Schafer (SM'57) was born in Lincoln, Neb., on April 27, 1922. He received the B.A. degree in physics from Macalester College, St. Paul, Minn., in 1943, the M.A. degree in physics from the University of Minnesota, Minneapolis, in 1949, and the Ph.D. degree in physics from the University of Colorado, Boulder, in 1958.

G. E. Schafer

He served as a weather officer in the Air Force from 1943 to 1946, taught physics from 1948 to 1950, and joined the National Bureau of Standards, Boulder, Colo., in 1951. He is presently engaged in work on microwave attenuation and field strength standards.

Dr. Schafer is a member of the American Physical Society, American Association of Physics Teachers, Colorado and Wyoming Academy of Science, RESA, and Sigma Xi.

❖

Erich O. Schulz-DuBois was born in Frankfurt, Germany, on March 17, 1926. He received the Dr. phil. nat. degree in physics in 1954, at the J. W. v. Goethe University in Frankfurt, where he carried out microwave investigations of gas discharges. He then accepted a position as research associate with the solid-state physics group at Purdue University, Lafayette, Ind., and worked on paramagnetic resonance in irradiated semiconductors. In 1956, he joined the Raytheon Manufacturing Company, Waltham, Mass., where he was engaged in the development of ferrite materials and devices.

Schulz-DuBois

At present, he is a member of the technical staff at Bell Telephone Laboratories, Murray Hill, N. J., where he is participating in the development of solid-state maser devices.

❖

James K. Shimizu (S'51–A'52–M'57) was born in San Diego, Calif., on October 28, 1924. He received the B.S. degree in electrical engineering in 1950 from Indiana Technical College, Fort Wayne, Ind. He received the M.S. degree in electrical engineering in 1952 from the University of Notre Dame, Notre Dame, Ind.

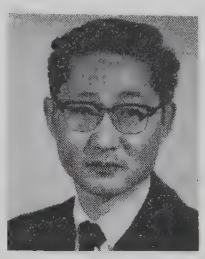

J. K. Shimizu

While at Notre Dame he was a teaching fellow in the Electrical Engineering Department, and was also employed as a research assistant for the Office of Air Research. In 1952 he joined the staff of the Stanford Research Institute, Menlo Park, Calif., where he has been working on research and development of various microwave antennas and components.

Mr. Shimizu is a member of the Scientific Research Society of America.

❖

Marshall H. Sirvetz was born in Lynn, Mass., in 1924. In 1950 he received the Ph.D. degree in chemical physics from Harvard University, Cambridge, Mass., where he did work in microwave spectroscopy. After spending two years at Brookhaven National Laboratory, Long Island, he joined the Research Division of Raytheon Manufacturing Company, Waltham, Mass., in March, 1953.

M. H. Sirvetz

His present work deals with the microwave properties and applications of ferrites and with solid-state microwave amplifiers.

❖

L. Solymar was born on January 24, 1930, in Budapest, Hungary. In 1952 he received the diploma of Electrical Engineer from the Technical University of Budapest, where from 1952 to 1953 he was assistant to the professor.

L. Solymar

From 1953 to 1956 he was a research engineer at the Research Institute of Telecommunication, Budapest, and was engaged in antenna theory and design. In 1956 he became a research en-

gineer at the Standard Telecommunication Laboratories Ltd., Enfield, Middlesex, England, where he was concerned with various topics in microwave transmission.

❖

Edward G. Spencer (SM'57) was born on July 21, 1920, in Lynchburg, Va. He received the B.S.E. degree in physics from George Washington University and the M.A. degree in physics Boston University. He did further graduate work at the Massachusetts Institute of Technology and the University of Maryland. From 1943 to 1946 he was engaged in microwave radar research at the Naval Research Laboratory.

E. G. Spencer

From 1946 to 1949, he was associated with the Cambridge Air Force Research Laboratory, and from 1949 to 1953 with the Naval Research Laboratory. During this time he worked in microwave spectroscopy of gases and paramagnetic and nuclear magnetic resonance of solids. In 1953, he joined the National Bureau of Standards, Ordnance Electronics Division, which is now the Diamond Ordnance Fuze Laboratories. In March, 1958, he became associated with Bell Telephone Laboratories. He is engaged at present in microwave physics research.

Mr. Spencer is a member of the American Physical Society.

❖

Donald C. Stinson (S'50–M'57) was born in Malta, Idaho, on December 7, 1925. He received the B.S. degree from Iowa State College in 1947, the M.S. degree from the California Institute of Technology in 1949, and the E.E. degree and the Ph.D. degree from the University of California in 1953 and 1956, respectively.

He spent one year with the General Electric Company as a test engineer, and for three summers he was a member of the technical staff of the Research and Development Laboratories at Hughes Aircraft Company. He is now with the Missile Systems Division of Lockheed Aircraft Corp., Sunnyvale, Calif.

D. C. Stinson

Dr. Stinson is a member of Sigma Xi, Eta Kappa Nu, and Pi Mu Epsilon.

❖

Basil C. Vafiades (A'53) was born in Boston, Mass., on May 14, 1929. He received the B.S. degree in physics from Boston College in 1951, and did graduate study at the Polytechnic Institute of Brooklyn, Brooklyn, N. Y., from 1952 to 1953. From June, 1951, to December, 1956, he was employed by the Microwave Electronics Division of the Sperry Gyroscope Company, Clearwater, Fla., where he was a member of the applied physics group working on microwave devices.

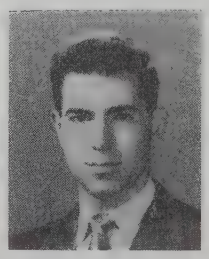

B. C. Vafiades

Since December, 1956, Mr. Vafiades has been with Microwave Associates Inc., engaged in the study of ferrite properties and in the development of high-power gas switching tubes and ferrite devices.

❖

Joseph H. Vogelman (M'44–SM'48) was born in New York, N. Y., on August 18, 1920. He received the B.S. degree in 1940 from the City College of New York, the M.E.E. degree in 1948 and the Dr.E.E. degree in 1957 from Polytechnic Institute of Brooklyn.

In 1945, after several years at the Signal Corps Radar Laboratory at Ft. Hancock and Belmar, N. J., he joined Watson Laboratories, Red, Bank, N. J., and served until 1951 as chief of the Development Branch, responsible for research and development of test equipment and microwave components and techniques. He then joined the Rome Air Development Center, where from 1951 to 1953 he was chief scientist in the General Engineering Laboratory and consultant on UHF and SHF theory and techniques to the U. S. Air Force; from 1953 to 1956, as chief of the Electronic Warfare Laboratory, he directed all research and development in ground based electronic warfare for the Air Force. Since 1956 he has been Technical Director of the Communications Directorate, directing the Air Force research and development effort in ground based and ground to air communications.

J. H. Vogelman

Dr. Vogelman is a member of Sigma Xi, the AIEE and the Armed Forces Communications and Electronics Association.

❖

Gershon J. Wheeler (SM'54) was born on July 11, 1913, in Massachusetts. He has been in the field of microwaves since 1942. From 1950 to 1957 he was with the Raytheon Manufacturing Company in Waltham and Wayland, Mass., where he worked as a consultant on special microwave problems.

G. J. Wheeler

At present, he heads the engineering and development department of Sylvania's Microwave Physics Laboratory, Mountain View, Calif.

Mr. Wheeler is a member of RESA.

# Index to
# IRE Transactions
# on
# Microwave Theory and
# Techniques
# Volume MTT-6, 1958

# Professional Group on Microwave Theory and Techniques

## Index to Volume MTT-6, 1958

### Contents

## Volume MTT-6, Number 4, October, 1958



# Index to Authors

# Index to Subjects

## NOTICE TO ADVERTISERS

•

Effective immediately the IRE TRANSACTIONS ON MICROWAVE THEORY AND TECHNIQUES will accept display advertising. For full details contact Tore N. Anderson, Advertising Editor, PGMTT TRANSACTIONS, 1539 Deer Path, Mountainside, N.J.

## AVAILABLE BACK ISSUES OF IRE TRANSACTIONS ON MICROWAVE THEORY AND TECHNIQUES

| Publication | Prices | | |
|---|---|---|---|
| | Group Members | IRE Members | Non-* Members |
| Vol. MTT-2, No. 3, Sept., 1954 | $1.10 | $1.65 | $3.30 |
| Vol. MTT-3, No. 1, Jan., 1955 | $1.50 | $2.25 | $4.50 |
| Vol. MTT-3, No. 4, July, 1955 | $1.60 | $2.40 | $4.80 |
| Vol. MTT-4, No. 1, Jan., 1956 | $1.65 | $2.45 | $4.95 |
| Vol. MTT-4, No. 3, July, 1956 | $1.25 | $1.85 | $3.75 |
| Vol. MTT-4, No. 4, Oct., 1956 | $1.85 | $2.75 | $5.55 |
| Vol. MTT-5, No. 2, April, 1957 | $1.90 | $2.85 | $5.70 |
| Vol. MTT-5, No. 3, July, 1957 | $1.15 | $1.70 | $3.45 |
| Vol. MTT-5, No. 4, Oct., 1957 | $1.20 | $1.80 | $3.60 |
| Vol. MTT-6, No. 1, Jan., 1958 | $2.65 | $3.95 | $7.95 |
| Vol. MTT-6, No. 2, April, 1958 | $2.50 | $3.75 | $7.50 |
| Vol. MTT-6, No. 3, July, 1958 | $2.00 | $3.00 | $6.00 |

* Colleges, Universities, Subscription Agencies, and All Libraries may purchase at IRE Member rate.

# INSTITUTIONAL LISTINGS

The IRE Professional Group on Microwave Theory and Techniques is grateful for the assistance given by the firms listed below, and invites application for Institutional Listing from other firms interested in the Microwave field.

AIRTRON, INC., 1101 W. Elizabeth Ave., Linden, N.J.
Designers and Producers of Complete Line of Microwave, Electronic and Aircraft Components.

COLLINS RADIO CO., Cedar Rapids, Iowa
Complete Industrial Microwave, Communication, Navigation and Flight Control Systems

LITTON INDUSTRIES, INC., MARYLAND DIV., College Park, Md.
Development and Production of Microwave Antennas and Waveguide Components

MICROWAVE DEVELOPMENT LABS., INC., 92 Broad St., Babson Park 57, Mass.
Designers, Developers and Producers of Microwave Components and Assemblies, 400 mc to 70 kmc

SAGE LABORATORIES, INC., 159 Linden St., Wellesley 81, Mass.
Microwave Engineering Specialists

WEINSCHEL ENGINEERING CO., INC., Kensington, Md.
Attenuation Standards, Coaxial Attenuators and Insertion Loss Test Sets

WHEELER LABORATORIES, INC., 122 Cutter Mill Road, Great Neck, N. Y.
Consulting Services, Research & Development, Microwave Antennas & Waveguide Components

The charge for an Institutional Listing is $50.00 per issue or $140.00 for four consecutive issues. Applications for Institutional Listings and checks (made out to the Institute of Radio Engineers) should be sent to Tore N. Anderson, PGMTT Advertising Editor, 1539 Deer Path, Mountainside, N.J.

*Introducing*

# WR 2100* WAVEGUIDE COMPONENTS...

*WR2100 (21 x 10½")
WRITE FOR DETAILS

**REPRESENTATI**

**WASHINGTON, D. C**
A & M ASSOC.
1145 19th ST., N.W.
WASHINGTON, D. C.

**WASHINGTON**
**OREGON**
AHMCO
BOEING FIELD
KING CTY. AIRPORT
SEATTLE 8, WASH.

**MICHIGAN**
**OHIO**
**W. PENN.**
**E. KENTUCKY**
J. R. DANNEMILLER ASS
3955 LEE ROAD
CLEVELAND 28, OHIO

•

J. R. DANNEMILLER ASS
384 W. 1st ST.
DAYTON 2, OHIO

•

J. R. DANNEMILLER ASS
1204 N. WOODWARD ST.
ROYAL OAK, MICHIGAN

**BOSTON AREA**
ROBERT L. DIAMOND
69B STRATHMORE RD.
BROOKLINE 46, MASS.

**COLORADO**
**NEW MEXICO**
**UTAH**
**WYOMING**
HYTRONIC
MEASUREMENTS, INC.
1295 S. BANNOCK ST.
DENVER 23, COLORADO

**ILLINOIS**
**INDIANA**
**WISCONSIN**
KADELL SALES ASSOC.
5875 N. LINCOLN AVE.
CHICAGO 45, ILLINOIS

**FLORIDA**
**GEORGIA**
**ALABAMA**
**TENNESSEE**
**S. CAROLINA**
J. NEAL CO.
P. O. BOX 50-438
MIAMI 50, FLA.

**CANADA**
RADIONICS, LTD.
8230 MAYRAND STREET
MONTREAL 9, CANADA

**UPPER NEW YORK STAT**
J. D. RYERSON ASSOC., IN
P. O. BOX 1400
SYRACUSE, NEW YORK

**EXPORT**
SZUCS INT'L CORP.
50 BROAD STREET
NEW YORK 4, N. Y.

**CALIFORNIA**
**ARIZONA**
VAN GROOS CO.
21051 COSTANSO ST.
WOODLAND HILLS, CALIF.

•

VAN GROOS CO.
1178 LOS ALTOS AVE.
LOS ALTOS, CALIF.

FXR

F-R MACHINE WORKS, Inc.
Woodside 77, N. Y. • AStoria 8-2800

**PRECISION MICROWAVE EQUIPMENT** • **RADAR COMPONENTS** • **HIGH-POWER MODULATORS** • **ELECTRONIC TEST EQUIPMENT**


*Write T*
for your new